

The Calcium Infrared Triplet as an Indicator for Stellar Activity

Dissertation
zur Erlangung des Doktorgrades
an der Fakultät für Mathematik, Informatik und Naturwissenschaften
des Fachbereichs Physik
der Universität Hamburg

vorgelegt von
Johannes Martin
aus Gifhorn

Hamburg
2017

Gutachter/innen der Dissertation:	Prof. Dr. Jürgen H. M. M. Schmitt Dr. Sandra Jeffers
Zusammensetzung der Prüfungskommission:	Prof. Dr. Jochen Liske Prof. Dr. Peter H. Hauschildt Prof. Dr. Jürgen H. M. M. Schmitt Dr. Sandra Jeffers Prof. Dr. Robi Banerjee
Vorsitzender der Prüfungskommission:	Prof. Dr. Jochen Liske
Datum der Disputation:	20.02.2018
Vorsitzender Fach-Promotionsausschusses Physik:	Prof. Dr. Wolfgang Hansen
Leiter des Fachbereichs Physik:	Prof. Dr. Michael Potthoff
Dekan der Fakultät MIN:	Prof. Dr. Heinrich Graener

Abstract

Cool stars exhibit a chromosphere, classically considered as a thin layer on top of the photosphere. This region is characterized by a number of phenomena created by strong, changing magnetic fields, which we refer to as signs of stellar activity. On stars other than the Sun, they cannot be resolved, and only the effects on a star's spectrum can be measured. Measurements of these activity-related phenomena can be used to find magnetic cycles and rotation periods in stars, including the Sun, and are of great interest, in order to better understand the cause and creation of the magnetic fields, which are thought to stem from a dynamo process. Most activity related studies focused on changes in the Ca II H- & K-lines, two spectral lines of single ionized calcium at about 395 nm. They display prominent emission cores, generated in the chromosphere. Other authors have used the behavior of the H α -line, which is also affected by chromospheric activity. However, the recently launched GAIA satellite and CARMENES missions will obtain many spectra that do not feature all of these lines. In order to still use these spectra for activity studies, we set out to analyze and compare the activity-induced changes in the Ca II Infrared Triplet (Ca II IRT), three calcium lines in the infrared, to those in the Ca II H- & K-lines and the H α -line.

To do so, we analyze several thousand spectra of F, G and K-stars taken by the TIGRE telescope. We carefully subtract spectra without contributions related to magnetic activity in order to obtain the chromospheric excess flux. To perform such a comparison for that large number of spectra, we have developed an automatic routine, which defines the flux scale, performs normalization, rotational broadening, and – if necessary – degrades a spectrum to the lower resolution of the TIGRE spectra. We obtained the excess flux by comparing the spectra of active stars to those of inactive stars of similar type, and performed a second comparison to PHOENIX model spectra. We perform this latter step by developing a new approach of interpolating irregularly sampled model spectra, and used it to fit model spectra to the observed ones. We find the stellar parameters in the process.

The determined excess fluxes show a strong correlation to each other, but also to classical activity indices. We give relations to convert such fluxes into these indices, and vice versa. The correlation between the excess flux in the calcium lines is larger than the one between the excess flux in the H α -line and the Ca II H- & K-lines, suggesting that the Ca II IRT-lines may be better suited for activity studies. This correlation is weakened, but still apparent, when performing the analysis for individual stars only. As we compared with both, spectra of inactive stars and model spectra, we can analyze the basal flux level – the chromospheric emission unrelated to magnetic activity, which is included in the spectra of inactive stars, but not in the model spectra – in detail, though the noise level of the spectra complicates this. We find relations somewhat lower than most cited in the literature, but they are still in good agreement.

Since the excess fluxes are created within active regions of the chromosphere, moving in and out of view on the stellar disk as the star rotates, we can use the determined excess fluxes to find periods in stars, and have demonstrated this for a small sample of stars, confirming literature values in most cases. We present an outlook for applying this method to binary systems, and to gain information regarding the position and movements of active regions on the surface.

Zusammenfassung

Kühle Sterne zeigen eine Chromosphäre, die klassisch als eine dünne Schicht über der Photosphäre beschrieben wird. Dort entstehen einige Phänomene durch starke, dynamische Magnetfelder, die wir als Zeichen stellarer Aktivität sehen. Diese Phänomene können nur auf der Sonnenoberfläche aufgelöst und abgebildet werden, wohingegen auf anderen Sternen nur die Effekte auf das Spektrum des Sterns beobachtet werden können. Aus Messungen dieser Veränderungen können Rückschlüsse z.B. über magnetische Zyklen und die Rotationsperiode gezogen werden. Solche Daten verbessern unser noch immer unvollständiges Verständnis der Prozesse hinter der Struktur und Erzeugung der stellaren Magnetfelder, von denen wir annehmen, dass sie durch Dynamoprozesse entstehen. Die meisten Analysen stellarer Aktivität entstanden durch Beobachtung der Veränderungen in den Ca II H- & K-Linien, zwei Spektrallinien des einfach ionisierten Kalziums, die bei einer Wellenlänge von etwa 395 nm liegen. Diese Linien zeigen einen prominenten Emissionskern, der in der Chromosphäre erzeugt wird, und deren Stärke von der magnetischen Aktivität abhängt. Häufig wird auch das Verhalten der H α -Spektrallinie analysiert, die ebenfalls durch chromosphärische Aktivität beeinflusst wird. Die vor kurzem gestarteten GAIA und CARMENES Missionen werden eine große Zahl Spektren aufnehmen. Sie werden jedoch nicht die Ca II H- & K-Linien, und im Falle von GAIA auch nicht die H α -Linie enthalten. Damit diese Spektren trotzdem für Aktivitätsstudien genutzt werden können, haben wir in dieser Arbeit das Verhalten des sogenannten Ca II Infrared Triplets (Ca II IRT), drei Spektrallinien des einfach ionisierten Kalziums im Infraroten, analysiert, und mit dem der H α - und Ca II H- & K-Linien verglichen.

Dazu haben wir mehrere tausend Spektren von F, G und K-Sternen, die vom TIGRE-Teleskop aufgenommen wurden, untersucht. Wir vergleichen diese Spektren mit solchen ohne den Beitrag einer magnetisch aktiven Chromosphäre, um über die Differenz der beiden Spektren den chromosphärischen Exzessfluss zu bestimmen. Um dies für diese große Zahl Spektren verlässlich tun zu können, haben wir eine automatische Routine entwickelt, welche die Spektren normalisiert, verbreitert, die Flusskala bestimmt, und ggf. Spektren auf die korrekte Auflösung degradiert. Für die Exzessbestimmung haben wir als Vergleich zunächst Spektren inaktiver Sterne verwendet, und anschließend Spektren, die aus PHOENIX Modellatmosphären berechnet wurden. Wir haben dafür ein neues Verfahren zur Interpolation von Modellspektren zwischen stellaren Parametern entwickelt. Mit einem Fit der theoretischen an die beobachteten Spektren können wir die stellaren Parameter der Sterne bestimmen.

Die so bestimmten Exzessflüsse zeigen eine starke Korrelation zueinander und zu den bekannten Aktivitätsindizes. Wir finden Relationen, die Exzessflüsse in Aktivitätsindizes oder umgekehrt umzurechnen. Die Korrelation der Exzessflüsse in den Kalzium-Linien ist größer als die der Exzessflüsse in den Ca II H & K-Linien zum Exzessfluss in der H α -Linie. Diese Korrelation bleibt auch erhalten, wenn als Datengrundlage lediglich die Exzessflüsse eines einzelnen Sterns verwandt werden. Da wir den für die Exzessbestimmung nötigen Vergleich sowohl mit inaktiven Sternspektren, als auch mit Modellspektren durchgeführt haben, können wir durch Vergleich der Ergebnisse auf den basalen Fluß schließen. Dies ist der chromosphärische Fluss, der nicht von magnetischer stellarer Aktivität verursacht wird, und daher in den Spektren inaktiver Sterne enthalten ist, aber nicht in den Modellspektren, die lediglich die Photosphäre abbilden. Diese Bestimmung wird durch das vergleichsweise hohe Rauschen in den Spektren erschwert. Die gefundene Beziehung stimmt – in Anbetracht dieser Fehler – gut mit bekannten Beziehungen aus der Literatur überein.

Da die Exzessflüsse in den aktiven Regionen der Chromosphäre entstehen, die sich durch die Rotation des Sterns über die beobachtete Sternscheibe bewegen, kann aus den gemessenen Werten auch die Rotationsperiode von Sternen bestimmt werden. Wir demonstrieren dies für eine kleine

Auswahl an Sternen, und finden in der Regel Werte, die gut mit den Literaturwerten verträglich sind. Schließlich geben wir noch eine Aussicht darauf, wie dieses Verfahren auf Binärsysteme angewandt werden kann, und wie aus der Analyse der Form des Exzessflusses auf die Position und Bewegung aktiver Regionen auf der Oberfläche geschlossen werden kann.

Contents

1	Introduction	1
2	Magnetic Activity and the TIGRE Telescope	3
2.1	Atmospheric structure	3
2.1.1	The Photosphere	3
2.1.2	The Chromosphere	4
2.2	Activity indices	6
2.2.1	Mount-Wilson S_{MWO} -Index	7
2.2.2	Emission in Ca II lines	8
2.3	Magnetic activity	10
2.3.1	The Ω -effect	10
2.3.2	The α -effect	11
2.4	Time Series and periodicity	12
2.4.1	Rotational periods	13
2.5	TIGRE Telescope	13
2.5.1	Automatic spectra	14
2.5.2	Calibrating the S_{TIGRE} index	14
2.5.3	TIGRE spectra used in this work	15
2.6	TIGRE problems and limitations	16
2.6.1	Defective camera and replacement	16
2.6.2	Resolution	16
2.6.3	Estimates of signal-to-noise ratio and errors	17
2.6.4	Cosmics and other problems	19
2.6.5	Corrupt files	19
2.7	Telluric correction	19
3	Measuring Chromospheric Excess	21
3.1	A new approach and its goals	21
3.2	Normalizing the spectrum and obtaining the continuum	22
3.2.1	Normalizing the Ca II H- & K-lines	23
3.3	Correcting wavelength shifts	23
3.3.1	Limitations	24
3.4	Adding rotational broadening to the comparison spectrum	25
3.5	Degradation of the comparison spectrum	27
3.6	Subtracting spectra and obtaining the excess	28
3.7	Monte-Carlo iterations	30
4	Comparing Active Stars to Inactive Stars	33
4.1	Rationale	33
4.2	Stellar parameters of stars observed by TIGRE	33
4.3	Defining the “inactive” state	34
4.4	Finding a comparison star	35

4.5	Empirical relations for fluxes of stars in inactive state	36
4.6	Outliers and objects not suitable for our method	38
4.7	Resulting excess fluxes and their correlations	39
4.8	Fitted parameters	42
5	Modeling stellar spectra with PHOENIX	47
5.1	Introduction and rationale	47
5.2	Short overview of PHOENIX	48
5.3	Interpolating on irregular grids	49
5.3.1	Determining the grid	50
5.3.2	Partitioning the grid	52
5.3.3	Filling holes	53
5.3.4	Problematic partitions	54
5.3.5	Determining polynomial coefficients	54
5.3.6	Interpolating and extrapolating from model spectra	55
5.3.7	Sanity check: comparing the results	56
5.4	Summary	57
6	Fitting TIGRE spectra with PHOENIX models	59
6.1	Method of the fit	59
6.1.1	Regions to perform the fit in, and those to ignore	60
6.1.2	Fitting normalized spectra	60
6.1.3	Finding the spectral resolution	61
6.2	Performing the fit of PHOENIX model spectra to TIGRE observations	62
6.2.1	Fitting the spectrum with the Levenberg-Marquardt algorithm	63
6.2.2	Fitting the spectrum with a Markov Chain Monte Carlo	66
6.3	Results and comparison	66
6.4	Summary	70
7	Comparing TIGRE Observations to PHOENIX models	73
7.1	Introduction and goals	73
7.2	Differences in the method to Chapter 4	73
7.2.1	Fit of the resolution	74
7.2.2	Automatic determination of the excess region	74
7.2.3	Noise of the comparison spectrum	74
7.2.4	Limitations of the sample	75
7.3	Outliers and objects not suitable for this analysis	75
7.4	Difference in flux scale to Chapter 4	77
7.5	Resulting flux and correlations	78
7.6	Fitted parameters	82
7.7	Comparison to results from Chapter 4	84
8	Converting Activity Indices into one another	85
8.1	Rationale	85
8.2	Methods for finding conversion relations	86
8.2.1	Linear regression	86
8.2.2	Subdividing sample into groups with similar $B-V$	87
8.2.3	Comparison of the two methods	88
8.3	Conversion relations from the result of Chapter 4	89
8.3.1	Activity indices and excess fluxes	89
8.3.2	Converting excess fluxes in one line to the excess flux in another line	92
8.3.3	Conversion of the amplitude of Gaussians fitted to the excess distribution	94
8.4	Conversion relations from result of Chapter 7	95
8.4.1	Activity indices and excess fluxes	95

8.4.2	Estimation of excess fluxes from other excess fluxes	98
8.5	Summary and choice of conversion relations	101
9	Obtaining the Chromospheric Basal Flux	103
9.1	Basal flux relations given in the literature	103
9.2	Finding the basal flux by comparison of our results to literature values	104
9.3	Finding the basal flux from the lower envelope of the chromospheric flux	106
9.3.1	Basal flux for individual lines	107
9.3.2	Combined basal flux in groups of lines	109
9.4	Finding the basal flux by comparison of our results from different comparison sources	110
9.4.1	Comparing the measured values directly	110
9.4.2	Combined lines	111
9.5	Results	113
10	Correlations for Individual Stars and Finding Periods	115
10.1	Correlations for individual stars	115
10.1.1	The effect of stellar parameters on the correlations	117
10.1.2	Correlation for different levels of activity	118
10.1.3	Summary	119
10.2	Measuring periods	120
10.2.1	Lomb-Scargle periodograms	120
10.2.2	String length	121
10.2.3	Wavelets	121
10.2.4	Determining periods of stars from TIGRE observations	123
10.2.5	Periods recovered	126
10.3	Summary	127
11	Summary and Outlook	129
11.1	Summary	129
11.2	Outlook	132
11.2.1	Applying the method to binary systems	132
11.2.2	Applying the method to fast rotators	134
11.2.3	Implementation as part of TIGRE's pipeline	135
11.3	Closing Remarks	137
	Bibliography	143
A	Notes on the IDL Implementation	151
A.1	Measuring chromospheric excess	151
A.2	Interpolating model spectra on irregular grids	152
A.2.1	Using the code	152
A.3	Obtaining conversion relations	156
A.4	Determining stellar parameters from TIGRE spectra and PHOENIX model spectra .	158
B	Additional Information, Figures and Tables	161
B.1	Combining Levenberg-Marquardt and the MCMC approach	172
C	Previously published works	175

Chapter 1

Introduction

On stars, a wide variety of phenomena caused by magnetic activity are observed. These range from spots and faculae to filaments and prominences, which we can directly observe on the Sun, and which create an ever-changing, different view of the solar disk, depending on the wavelength we perform this observation in. Some of the phenomena so observed are created in the chromosphere, a layer on top of the photosphere in a star's atmosphere.

However, the Sun is actually a star showing only low levels of activity, and it is known that for other stars, the level of activity, and therefore the chromospheric emission, is much stronger. Analysis of these stars is therefore a great way of better understanding these phenomena, which will also allow us to learn more about the Sun. The Mount-Wilson survey, started in 1966, has perhaps been the most impactful study performed to understand the long-term behavior of stellar activity, and it relied on the clear, easily distinguished emission cores in the Ca II H- & K-lines. The long-time analysis of these lines has allowed unprecedented studies regarding magnetic cycles in stars.

With modern telescopes, such as the Telescopio Internacional de Guanajuato Robótico Espectoscópico (referred to as "TIGRE"), located in Mexico, such studies are possible as well, with an additional advantage: the spectra taken by this telescope also include the Calcium II Infrared Triplet (Ca II IRT) lines. It has been shown before that those lines are activity tracers as well, and studies have been undertaken to compare their behavior to the Ca II H- & K-lines, e.g. Martínez-Arnáiz et al. [2011b]. Knowledge of this is now more important than ever, as new missions have been launched, such as CARMENES or GAIA, that will take spectra of the Ca II IRT, but not of the Ca II H- & K-lines [Prusti, 2012, Quirrenbach et al., 2014]. These missions are expected to take an extremely large number of spectra, with the GAIA catalog alone including 1 142 679 769 entries, and CARMENES expected to take $\sim 15\,000$ spectra of M-dwarfs in the first three years. Taking these spectra into account for activity studies therefore greatly enhances both the temporal coverage of stars with existing data on their activity, and adds reliable information of a number of stars that so far have no activity-related data at all. However, since those spectra do not include the Ca II H- & K-lines, new indicators to estimate the activity levels are necessary, as well as a relation between those indicators to compare the new ones to the old values, and to add this new data to existing results of other studies.

In this work, we want to make use of the very large amount of data taken by the TIGRE telescope, which simultaneously takes spectra of the Ca II H- & K-lines and Ca II IRT-lines. Analysis of these spectra then makes it possible to understand how the Ca II IRT-lines change dependent on activity, which is indicated from the emission core in the Ca II H- & K-lines. Since these observations are simultaneous, there is no discrepancy of the two indices simply from different moments in the cycle, or from inherent stochastic changes in activity. This is a major advantage of the TIGRE dataset, and is an important improvement on the works from e.g. Busà et al. [2007]. Additionally, we will analyze not only the activity indices, but also the actual chromospheric flux in units of $\text{erg s}^{-1} \text{cm}^{-2}$, which we obtain by careful removal of photospheric effects.

In the next chapter, we give a basic outline of the chromosphere, observed activity phenomena, the creation of the magnetic field, and the TIGRE telescope. In the following Chapter 3, we describe

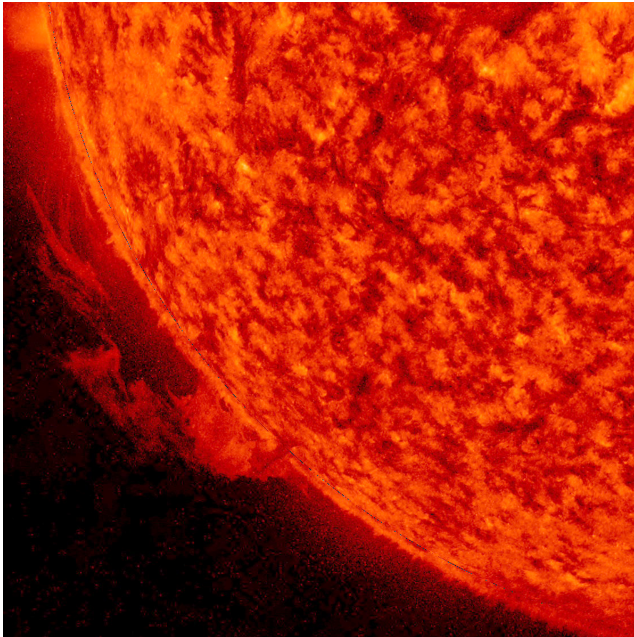


Figure 1.1: **The Sun's chromosphere, showing a prominence, on February 3rd, 2016.** This image was taken from NASA/SDO, and shows the Sun in 304 \AA , which is chromospheric emission from He II.

how we perform the removal of the photospheric contribution. We take inactive stars to show only the photospheric contribution – neglecting the basal flux – and from this determine chromospheric excess fluxes in Chapter 4. To improve this method, we move towards PHOENIX model spectra as true photospheric spectra. To perform the comparison correctly, and to not suffer from incorrectly determined stellar parameters, we first calculate a set of PHOENIX model spectra, and derive a new way of interpolating them in stellar parameter space, even if they are not sampled in a grid-wise fashion. This is described in detail in Chapter 5. Fitting these models to TIGRE spectra in order to obtain the stellar parameters is the focus of Chapter 6. With the best-fitting model determined for each star, we can finally perform the comparison, and determine the excess fluxes, which we show in Chapter 7. Since we have now determined different activity indices, we can find a relation to convert the measurement of one into another, which is useful to supplement existing archival data of one line with new data of another, for example to add to the archival Mount-Wilson data from the new GAIA observations. We show how we perform this conversion in a way to minimize sampling effects in Chapter 8. Carefully contrasting the results of the comparison to inactive models and the results of comparison to model spectra reveals their major difference, which is the basal flux level. We show how we can determine it from our results in Chapter 9. We then check the correlation between the different activity-related indicators and fluxes on the level of an individual star, and determine periods, in Chapter 10. An outlook of further possibilities, as well as a summary of these results, is given at the end in Chapter 11.

Chapter 2

Magnetic Activity and the TIGRE Telescope

In this thesis, we will analyze spectra of stars that show signs of magnetic activity. First, we will discuss the atmospheric structure of the main-sequence stars we consider here, which will lead us to differentiate between the photosphere and the chromosphere. We describe some of the observable physical phenomena that are caused by a star's magnetic field. We continue with a summary of some indices that are in use today to characterize and quantify the level of magnetic activity in a star. We then give a short overview of the dynamo process that is thought to cause the magnetic fields. These activity processes are often observed to vary in cycles. We will discuss such cycles shortly, before we give a description of the instrument that observed the spectra we have used in this work.

2.1 Atmospheric structure

We analyze the light emitted by stars in detail, studying the spectral signatures and spectral lines to figure out tracers for physical processes taking place in the star. Most of the light in the spectra we work with is created in a star's photosphere. However, we are most interested in light that was emitted from the chromosphere, a thin layer on top of the photosphere. We will now describe the photosphere and chromosphere, using the definition given by Hall [2008]. We give a short outline of the various features observed there related to activity.

2.1.1 The Photosphere

When observing the sun with the naked eye (hopefully using a solar filter), we see the region in the atmosphere where the optical depth is $\tau = 1$. It shows granulation, an effect from the energy transport outwards through convection [Strassmeier, 1997], as well as limb-darkening, which is a geometric effect. Towards the limb, the regions that we see the emitted light from at $\tau = 1$ is from greater heights, where there is a lower temperature. Therefore, we measure less light from there, and correspondingly the limb appears darker¹. But it also shows effects from magnetic fields: There may be spots, where the magnetic field suppresses convection, therefore creating these regions with lower temperature. We can also observe bright spots called faculae. We know from magnetograms of the solar disk that these phenomena appear in regions of strong magnetic fields.

The continuum emission is contributed from the photosphere, though it also contributes absorption lines. In Fig. 2.1, we show an image of the sun's photosphere, taken from the Solar Dynamics Observatory (SDO) [NASA/SDO], at a wavelength of $\lambda = 6173 \text{ \AA}$. It shows clearly the granulation, limb-darkening, as well as a well-defined sunspot. The dark core is called the umbra. The spot shown in Fig. 2.1 is larger than the earth, to give a sense of scale. Around the dark center of the spot is the penumbra.

¹If observing with a small filter centered at the right wavelength, we may observe limb-brightening instead!

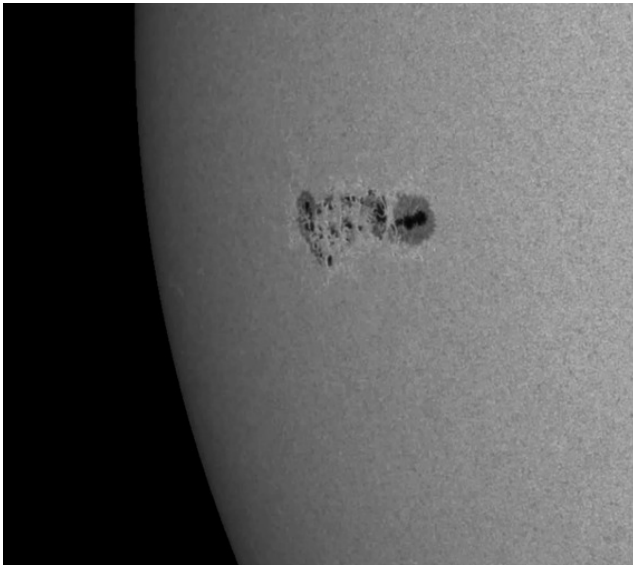


Figure 2.1: **The sun’s photosphere, observed by the SDO.** This shows a segment of an image taken from the SDO Gallery [NASA/SDO], and shows the sun as it appeared on July 7th, 2017.

As these spots can be made out even with simpler means, a lot of historical data reaching back centuries is available on the amount of spots on the sun’s surface. Kepler and Galilei were among the first who analyzed such data. We will see later that this historical data is very interesting as cycles appear in them. Note that for the sun, spots are only observed in a belt around the equator. However, for more active stars, spot configurations that feature large spots near the poles have been found, and are most impressively seen in surface maps from Doppler Imaging (see e.g. Wolter et al. [2008], Huber et al. [2009]). Because spots are created from magnetic fields, they are an indicator for magnetic activity. This activity has an even stronger effect in the chromosphere, the thin layer above the photosphere.

2.1.2 The Chromosphere

In visual light, the chromosphere is hard to make out against the much brighter photosphere, as the contrast is simply too low against the bright continuum emission of the photosphere. However, during a solar eclipse, since the light of the photosphere is blocked, light from other atmospheric structures can be made out, such as the corona, visible as photospheric light is scattered from it, and also the chromosphere, which appears as a violet-pinkish ring that can be made out around the solar disk. Unlike the photosphere, the chromosphere emits light mostly in certain lines, such as the $H\alpha$ -line at $\lambda = 6563 \text{ \AA}$, giving it the pink color. However, most of these chromospheric lines are outside the visible range. Vernazza et al. [1981] derived a temperature-structure of the atmosphere of the sun from models they created, which are cited often to this day. This temperature-structure is shown in Fig. 2.2. When going outwards towards greater heights (right to left in the plot), the temperature first falls to a minimum, here at about 500 km. This point marks the beginning of the chromosphere. From there, the temperature rises again, before it flattens out to a plateau at a temperature of about 6500 K. Then, suddenly, we enter the transition region, where there is a very steep temperature rise upwards at about 2100 km. Past this very thin layer, the corona begins, which is a very wide extended region of thin plasma, with extremely high temperatures of more than one million Kelvin in the case of the sun [Hall, 2008].

Figure 2.2 also marks the formation heights of several lines important to measurements of the chromosphere, among them the Ca II H- & K-lines, the Mg II h and k doublet in the UV and the famous $H\alpha$ -line. Another group of lines that have been used are the Ca II IRT-lines, which are formed in the lower chromosphere [Linsky et al., 1970], and which we will focus on in this work. Hall [2008] defines the chromosphere in a review paper as the region where there is “emission in excess of that expected in radiative equilibrium and [...] where cooling occurs mainly by radiation in strong resonance lines”. There are processes by which mechanical energy is dumped into the

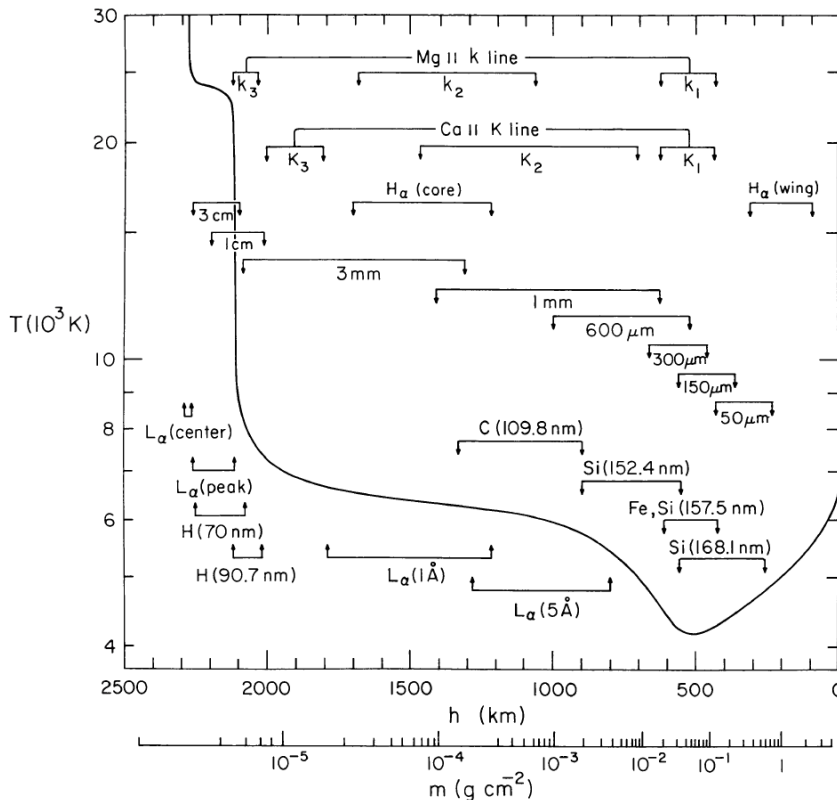


Figure 2.2: **Temperature structure of the Sun, as given by Vernazza et al. [1981].** The temperature structure is plotted against the height, and the formation heights of certain lines are given as well.

chromosphere, which heats up, and ionizes hydrogen as a result. The freed electrons allow collisional radiative cooling, which creates the radiation in the resonance lines [Hall, 2008]. The abrupt end of the chromosphere towards the high temperatures of the corona marks the point where all hydrogen is ionized, and this cooling is no longer possible. Possible processes to put the energy into the chromosphere might be acoustic waves [Biermann, 1948, Schwarzschild, 1948], or a magnetic field created from a dynamo [Babcock, 1961]. Since these processes require surface convection to work, hot stars cannot become too active and will not feature an extended chromosphere. Additionally, their photospheres may already be highly ionized, so that there are already no electrons left at the end of their photosphere to perform the cooling procedure.

Figure 2.3 shows the sun in a $H\alpha$ -filter, taken by the ChroTel telescope². Since the $H\alpha$ -line is one that shows strong radiation from the chromosphere (see Fig. 2.2, from Vernazza et al. [1981]), this figure gives us insight into the chromospheric structure. Clearly visible are thin, dark structures called filaments. They only appear dark against the brighter solar disk. Those that are seen past the limb of the solar disk appear bright against the dark background, and are called prominences. We can also make out regions of bright light, called plages. They are not just visible in the $H\alpha$ -line, but also for example in the Ca II H- & K-lines. These structures are not always visible, and are connected to magnetic activity (see next section). Figure 2.4 shows the chromosphere, as it appears during a time of low magnetic activity (the “quiet state”), and as it appears during more active phases. In Fig. 2.5, an image of the solar disk taken in the Ca II K-line, highlighting the chromosphere, is compared to one in white light, showing the photosphere, taken at the same time. This comparison reveals that the bright, chromospheric plage structures on the right appear at the positions where we observe spots and faculae (mostly visible closer to the limb) in the photosphere. The magnetic structures, and the emission resulting from them, therefore do not appear to be uniformly distributed across the chromosphere, or even the projected disk, but rather to be formed in certain regions of high

²ChroTel is operated by the Kiepenheuer-Institute for Solar Physics in Freiburg, Germany, at the Spanish Observatorio del Teide, Tenerife, Canary Islands. The ChroTel filtergraph has been developed by the Kiepenheuer-Institute in cooperation with the High Altitude Observatory in Boulder, CO, USA.

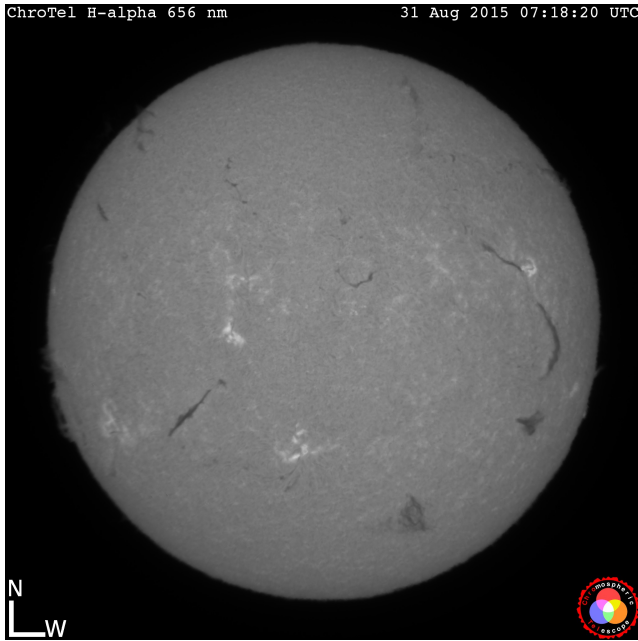


Figure 2.3: **The sun in H α -emission, taken by ChroTel [Bethge et al., 2011].** This image shows the sun on August 31, 2005.

magnetic activity, the position and strength of which varies over time. As singular magnetic regions vanish – either because they have reached the end of their lifetime, or simply because stellar rotation moves them out of view – the resulting emission and the measured activity from this will diminish, too. This can and has been used to determine stellar rotation periods, and we will get back to this in Chapter 10.

The chromosphere is therefore strongly sensitive to magnetic structure, and can be used to obtain information regarding the magnetic structure. Since the chromospheric emission is mostly limited to small spectral line cores, analysis of these spectral regions can be used for such an analysis. Several different indices for stellar magnetic activity have been derived from such observations.

2.2 Activity indices

Here, we give a short overview of some of the most important activity indices in use today. We will focus mostly only on those that we are using in this work: The famous Mount-Wilson S-Index S_{MWO} and the index R'_{HK} , derived from the same spectral lines.

Historically, the first measurement able to be converted into a numerical measurement of the strength of activity was the amount of sunspots. In order to quantify this more reliably, the Wolf sunspot index number, also called the Zürich relative sunspot number, was introduced [Schrijver and Zwaan, 2008]:

$$R = k(10g + f), \quad (2.1)$$

with g as the number of spot groups visible on the disk, and f the number of individual spots. The correction factor k is used to bring measurements from different observers and their instruments into agreement. This number is of course dependent on the number of spots visible to a specific observer. However, by taking a monthly average, much of these effects smooth out, and the resulting index correlates well with less subjective indices.

Over the years, the advances in instrumentation made it possible to observe in other wavelengths, and better filters, so that observations in other spectral ranges, such as the UV, and even X-Rays, as well as detailed spectra from individual lines could be used for analysis of the magnetic activity.

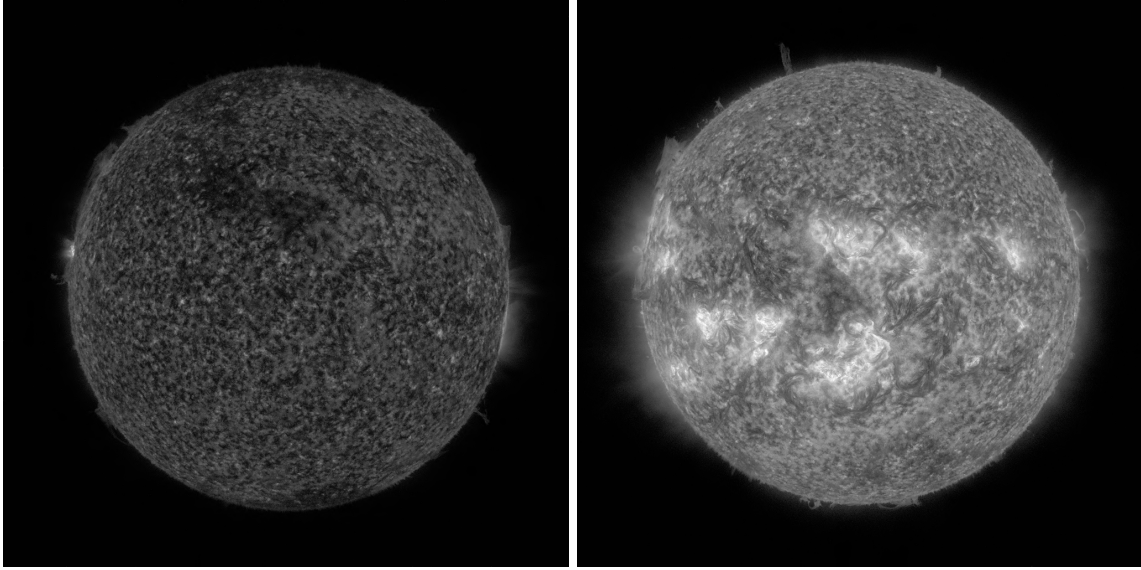


Figure 2.4: **The Sun’s chromosphere, as seen on August 14th, 2017 (left) and on July 5th, 2014 (right).** The image on the left shows the Sun in a quiet state, whereas that on the right shows the Sun at the height of its activity in Cycle 24. Both images show the Sun in 304 Å and are taken from the SDO Gallery [NASA/SDO].

2.2.1 Mount-Wilson S_{MWO} -Index

Possibly the most famous activity index is the Mount-Wilson S-Index S_{MWO} , which is derived from the Ca II H- & K-lines³, two lines at $\lambda = 3968 \text{ \AA}$ and $\lambda = 3934 \text{ \AA}$, respectively. They are formed by the transition from the $4p^2P_{1/2}$ (Ca II H) and $4p^2P_{3/2}$ (Ca II K) states down to the $4s^2S_{1/2}$ state [Shine et al., 1975, Kramida et al., 2015]. These two lines sensitive to chromospheric magnetic activity are perhaps the easiest to observe from the ground. Eberhard and Schwarzschild [1913] noted that for some stars, the Ca II H- & K-lines featured very strong emission cores. The spectra of these lines appear strikingly different dependent on the level of activity, as shown in the comparison in Fig. 2.6, where we compare the spectrum of an “inactive” and an “active” star, using the threshold definition from Henry et al. [1996], which we will explain later in Chapter 4, Sect. 4.3. We can see that the Ca II H- & K-lines are very broad with almost a triangular shape, contaminated by a number of different lines. In the line center, the active star shows a clear peak in both lines, with the peak in the Ca II K-line being a bit higher. We interpret these peaks as chromospheric emission due to magnetic activity, as they would appear as bright regions on the solar disk, which we have seen in Fig. 2.5 corresponds to regions with strong magnetic fields. Wilson and Vainu Bappu [1957] found that the width of this emission W_0 is correlated with the absolute magnitude M of the star. This effect is called the “Wilson-Bappu effect”, and can be formulated as:

$$M = 27.59 - 14.94 \log W_0. \quad (2.2)$$

The lines also show emission reversal: While it is hard to make out in the smoothed spectra shown in Fig. 2.6, there is an apparent “dip” in the very center of the emission peak. These points are often referred to as K_1 (minimum furthest out), K_2 (maximum) and K_3 (minimum in the emission peak center)⁴, and are formed in different parts of the chromosphere (Fig. 2.2), and are therefore subjected to different conditions in the local plasma [Hall, 2008]. Analysis of the position of these points can therefore be used to better understand the local conditions at different points in the

³They are both Fraunhofer lines, which explains the names “H” and “K”. Since Fraunhofer named them in order from red to blue, the Ca II H-line has the *higher* wavelength of the two.

⁴There are two K_1 and K_2 points each, on the red and blue side of K_3 respectively.

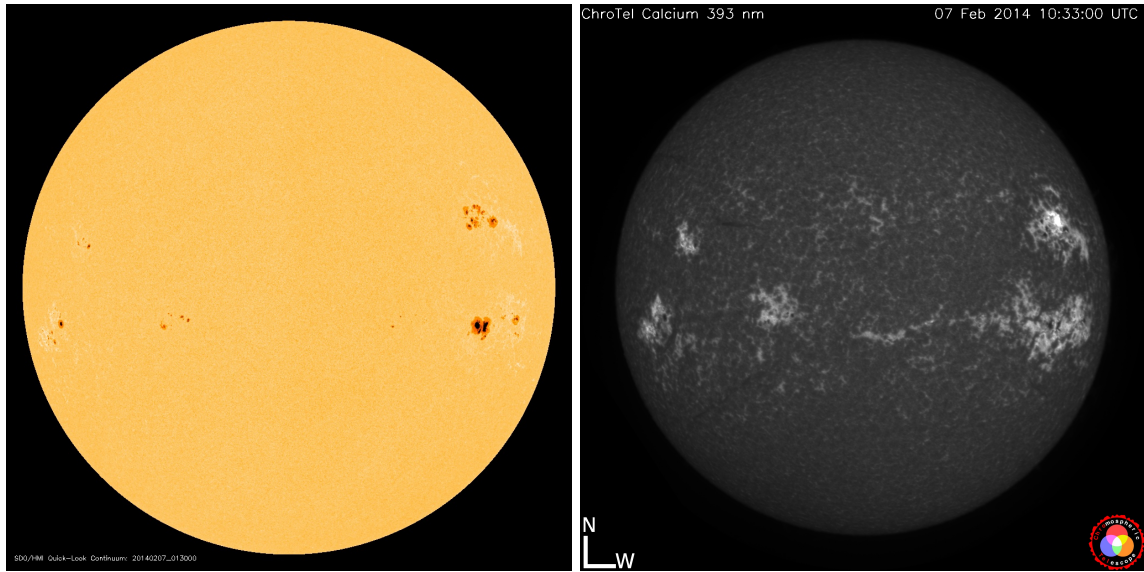


Figure 2.5: The solar disk, as seen on February 7th, 2014 by the SDO/HMI (left) [NASA/SDO], imaging the photosphere in the continuum. On the right, the solar disk imaged in the Ca II K-line, taken by ChroTel [Bethge et al., 2011], showing chromospheric structure.

chromosphere.

Olin Wilson began observing the Ca II H- & K-lines of a number of stars in 1966, with the stated goal of determining if “the chromospheric activity of main-sequence stars vary with time, and if so, how?” [Wilson, 1978], and such observations continued until 2003. The peculiar behavior of the Ca II H- & K-lines on activity was analyzed by defining the so-called S-Index. By comparing the count rate in the center of the lines to the count rate outside the lines in the continuum, they arrived at the numerical value S_{MWO} to describe a star’s activity levels:

$$S_{\text{MWO}} = \frac{N_H + N_K}{N_V + N_R} \alpha. \quad (2.3)$$

Here, N_H and N_K are the count rates inside a triangular, 1.09 \AA -wide bandpass in the center of the Ca II H- and K-line, respectively. N_V and N_R are the count rates in a 20 \AA rectangular bandpass in the continuum, centered at 3901.07 \AA and 4001.07 \AA . The factor α is meant to bring measurements of different instruments into agreement, as different sensitivity at different wavelengths can result in different values for this parameter [Strassmeier, 1997]. To determine α , usually measurements of a set of standard stars are compared. This index is perhaps the most important activity index there is, with a large amount of archival data available for a number of stars, and many authors choosing to quantify activity using this index. However, this value depends on stellar parameters, and therefore is not a good fit to compare the activity levels of stars of different types. Historically, it soon became apparent for the Sun that this index closely follows the sunspot number [White and Livingston, 1981], further cementing it as a useful activity indicator.

2.2.2 Emission in Ca II lines

To eliminate the problem of the dependency on stellar parameters, we must adapt the analyzed parameter. The S-Index simply compares the count rates inside the line and normalizes by those outside, which is a crude estimator for the emitted chromospheric flux as a fraction of the continuum flux. A better estimate is given by the index R'_{HK} , which aims to improve the estimate. The first change is to move from the simple count rates in the triangular bandpasses in the line centers towards

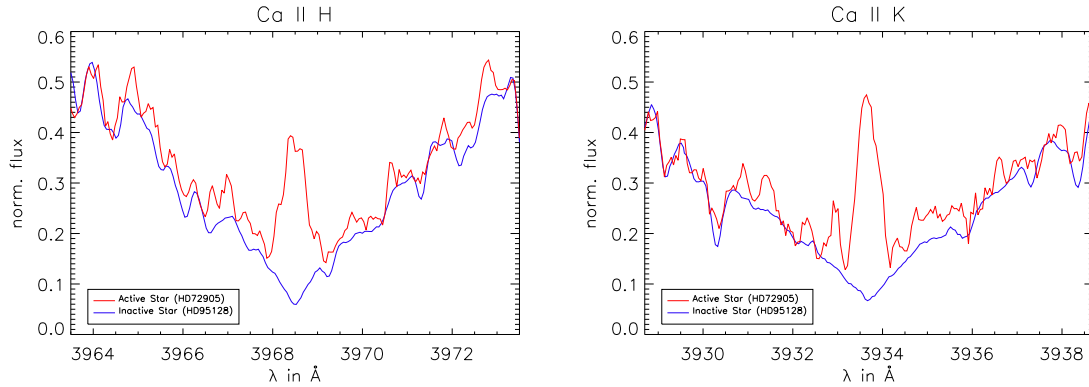


Figure 2.6: **Comparing two spectra taken by the TIGRE telescope (see Sect. 2.5) in the Ca II H & K-lines for an “active” (red line) and an “inactive” (blue line) star.** For clearer illustration, these spectra have been slightly smoothed to reduce the levels of noise, and to make the overall structure clearer.

the actual flux. Performing this step is not trivial, as it is notoriously difficult to measure spectra in real units of physical flux ($\text{ergs}^{-1} \text{cm}^{-2} \text{\AA}^{-1}$). Common ways of converting spectra into those units are by comparing with model spectra, or by scaling relations valid for the Sun. In any case, the actual value given will also depend on the determination of the continuum in the spectrum, as the continuum marks the level that can reliably be estimated. For the Ca II H- & K-lines, determining the continuum from a spectrum is difficult as well, due to their broad shape and the large amount of line contamination (see Chapter 3, Sect. 3.2). However, if such a value F_{HK} has been determined, it can subsequently be normalized by the total flux emitted by the star according to the Stefan-Boltzmann-Law:

$$R_{\text{HK}} = \frac{F_{\text{HK}}}{\sigma T_{\text{eff}}^4}. \quad (2.4)$$

Compared to Eq. (2.3), this index has the advantage of a more “physical” value with F_{HK} , rather than its estimate from count rates, and a better normalization with the Stefan-Boltzmann law in the denominator. However, this index still suffers from some photospheric contribution to F_{HK} . This is undesired, as this contribution is unrelated to the magnetic activity, and therefore an improved index R'_{HK} has been derived that aims to remove this contribution, leaving just the chromospheric stellar flux:

$$R'_{\text{HK}} = \frac{F_{\text{HK}} - F_{\text{HK,phot}}}{\sigma T_{\text{eff}}^4}. \quad (2.5)$$

The difficulty here is to determine the value of the purely photospheric $F_{\text{HK,phot}}$. This can be done e.g. from photospheric model spectra, and several relations to estimate this value exist in the literature, e.g. those determined by Mittag et al. [2013]. This index is usually of the order of $\sim 10^{-4.75}$ for stars starting to show signs of activity [Henry et al., 1996]. While R'_{HK} is much better suited for activity studies, as it does not show the same dependency on stellar parameters as S_{MWO} does, it is harder to determine. However, it is possible to convert a measurement of S_{MWO} to the corresponding value of R'_{HK} , by estimating the conversion from S-Index count rates to physical flux from the star’s spectral class and temperature, or $B - V$ value. In this work, values for R'_{HK} we give have been calculated from the measured S_{MWO} -value using the relations from Mittag et al. [2013], though other such relations are available, e.g. those from Rutten [1984].

At first glance, it would appear that R'_{HK} would reach zero for very inactive stars. However, this is not the case, as we always have $F_{\text{HK}} > F_{\text{HK,phot}}$. The reason for this is that there is always a residual level of chromospheric flux, called the basal flux, which may [Judge et al., 2003, Schrijver and Title, 2003] or may not [Schrijver, 1987] be of magnetic origin. Another possibility is that the mechanisms are both magnetic and acoustic in nature [Hall, 2008]. This flux is about an order of

magnitude lower than the “typical” emission from active stars, but it is distinctively not zero (we will try to estimate the basal flux in several lines in Chapter 9). Following the logic of removing contributions to the flux unrelated to magnetic activity, Mittag et al. [2013] introduced the index R_{HK}^+ , which removes this basal flux component $F_{\text{HK,basal}}$:

$$R_{\text{HK}}^+ = \frac{F_{\text{HK}} - F_{\text{HK,phot}} - F_{\text{HK,basal}}}{\sigma T_{\text{eff}}^4}. \quad (2.6)$$

The authors also give a way to estimate $F_{\text{HK,basal}}$. Unfortunately, this index has not yet caught on, and most authors stick to the more widely-used R'_{HK} . For even remotely active stars, the difference between R'_{HK} and R_{HK}^+ is negligible, however, due to the small contribution of the basal flux. In this work, we will analyze and compare the directly measured flux from chromospheric activity, which we obtain by disentangling this flux from the photospheric contribution, to these activity indices, which serve as our control.

The Ca II H- & K-lines are not the only Ca II-lines sensitive to magnetic activity. The Ca II IRT-lines have also been known as an activity indicator. These three lines at $\lambda = 8498 \text{ \AA}$, $\lambda = 8542 \text{ \AA}$ and $\lambda = 8662 \text{ \AA}$ will be the focus of this work, and we will compare their performance as an indicator to the Ca II H- & K-lines. The Ca II IRT-lines are formed from the transitions of Ca II from the $4p^2P_{1/2}$ to the $3d^2D_{3/2}$ state, and those from the $4p^2P_{3/2}$ to the $3d^2D_{5/2}$ and $3d^2D_{3/2}$ state [Shine et al., 1975, Kramida et al., 2015].

2.3 Magnetic activity

We have already mentioned that the phenomena we have described are caused by underlying stellar magnetic fields. For example, sunspots are regions with very strong magnetic fields, as evidenced by magnetogram images. In fact, these spots mark the points where magnetic flux tubes penetrate the photosphere. The magnetic fields in stars, including the Sun, cannot simply be static, as its lifetime would be too short. Therefore, only a consistently regenerating, dynamic process can explain the observed magnetic fields, not to mention their change that is ultimately observed in the activity related phenomena. This process is not yet fully understood in all details. The most common explanation is given by the $\alpha\Omega$ -dynamo model⁵. This theory was first introduced by Parker [1955]. The magnetic field is postulated to consist of a poloidal component, as well as a toroidal component. The idea behind the dynamo model is that there are underlying processes that turn poloidal fields into toroidal fields, which in this model is called the Ω -effect, and vice versa turning toroidal fields into poloidal ones (the α -effect). By doing so, the magnetic field constantly changes and adapts, keeping the overall magnetic field alive much longer. We will now consider these two effects in more detail, which are thought to happen at the base of the convection zone.

2.3.1 The Ω -effect

The Ω -effect converts a poloidal magnetic field into a toroidal one, and it is heavily dependent on differential rotation. Differential rotation describes the phenomenon that the rotation of a star depends on the latitude. This can directly be observed on the Sun, where spots at the equator have smaller periods than those closer to the pole. As such a star rotates, the hot plasma moves in the ϕ -direction, given the usual definition of spherical coordinates. Due to differential rotation, the regions at the equator are rotating faster. If there was a poloidal magnetic field, then it will now be deformed as the ions that generated the magnetic field move, effectively generating a magnetic field component in the ϕ -direction. The longer this process goes on, the more are the field lines “wound up”, and the stronger the generated toroidal field is. This process is shown in Fig. 2.7. As we have mentioned, it requires a notable amount of differential rotation in order for this effect to create a toroidal field. This can, however, be done with the α -effect as well, which can also perform the opposite conversion.

⁵Depending on which effect dominates, different models are being used. For the $\alpha\Omega$ -model, the α -term is much smaller, but there exists also the α^2 -model, in which the α term dominates, and the $\alpha^2\Omega$, where both α - and Ω -term are of similar magnitude. [Schrijver and Zwaan, 2008]

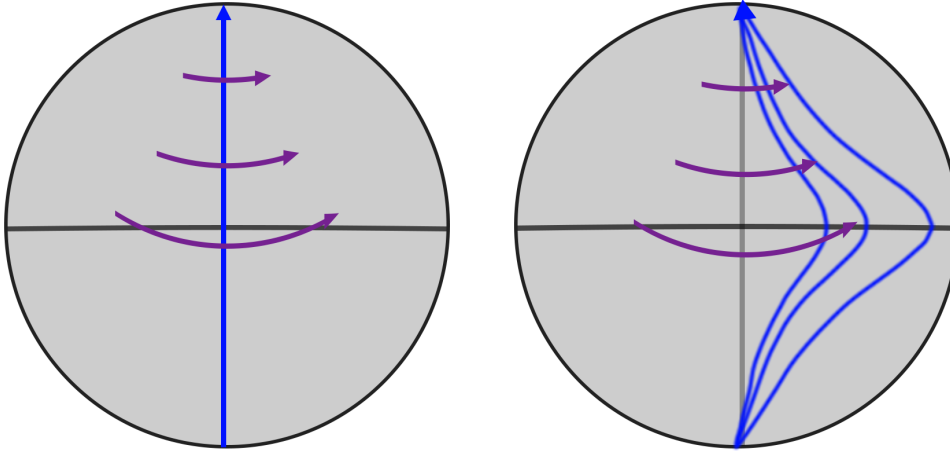


Figure 2.7: **The Ω -effect illustrated.** A purely poloidal magnetic field (blue line, left) is “stretched out” by the differential rotation as parts close to the equator rotate faster than those closer to the pole (shown by violet arrows). The end result is a magnetic field that contains a toroidal component (blue lines, right). Image based on the ones from Lang [2008], Werne [2000].

2.3.2 The α -effect

In this section, we follow the description by Parker [1955].

Consider a hot region of plasma, rising up in the atmosphere, or radially outward in the star’s frame of reference, with a purely toroidal magnetic field $\vec{B} = B\vec{e}_\phi$. Because this system of reference is rotating with the star, this region will be subject to the Coriolis force, which will cause the region to start rotating. The total movement of a fluid element is therefore a combination of a circular movement around a local rotation axis orthogonal to the surface, assumed to be at R_0 in the local $\phi - \theta$ -plane, and a radial component outwards. Assuming infinite conductivity of the fluid, we can set the last part of the magnetohydrodynamics induction equation,

$$\frac{\partial \vec{B}}{\partial t} = \nabla \times (\vec{v} \times \vec{B}) + \eta \nabla^2 \vec{B}, \quad (2.7)$$

to zero. In Eq. (2.7), the parameter η is the magnetic diffusivity. This can be solved using a Cauchy integral, and yields:

$$\vec{B}(\vec{r}(\vec{r}_0, t)) = \left(\vec{B}(\vec{r}_0) \nabla_0 \right) \vec{r}(\vec{r}_0, t), \quad (2.8)$$

where $\vec{r}(\vec{r}_0, t)$ describes the position of a fluid element at time t originally at \vec{r}_0 , and ∇_0 means that we differentiate with respect to \vec{r}_0 .

Parameterizing the movement as a combination of a rotation and a radial component, we then find for \vec{B} :

$$\begin{aligned} B_\theta &= B((R - R_0) - Z) \left(\sin \Psi + \lambda \frac{\partial \Psi}{\partial \lambda} \sin \psi \sin(\psi - \Psi) \right) \\ B_\phi &= B((R - R_0) - Z) \left(\sin \Psi + \lambda \frac{\partial \Psi}{\partial \lambda} \cos \psi \sin(\psi - \Psi) \right) \\ B_R &= B((R - R_0) - Z) Z \sin(\psi - \Psi). \end{aligned} \quad (2.9)$$

Here, λ is the distance to the local rotation axis, ψ is the angle measured from the local θ -direction around that same axis, and Z and Ψ are functions dependent on λ that originate from the movement parameterization. Here, we just note that:

$$Z(\lambda) \propto v_0 t, \quad \Psi \propto w_0 t / a, \quad (2.10)$$

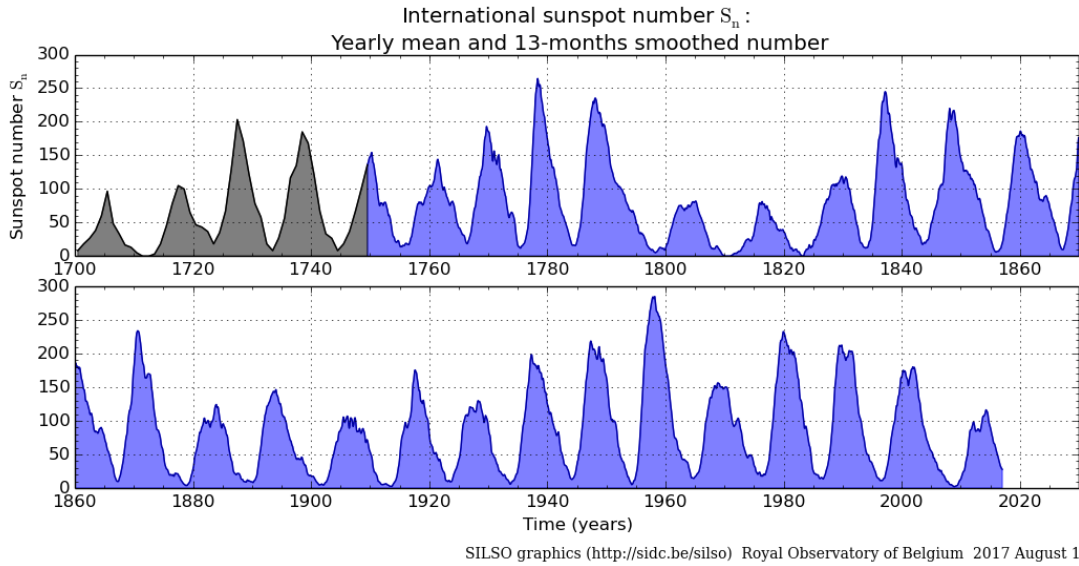


Figure 2.8: **The yearly mean of the sunspot number (gray) and the 13-month smoothed number of sunspots (blue) from about 1700 to today.** A clear periodical signal can be made out. Image from SILSO World Data Center.

where v_0 is a proportionality constant describing the speed of movement in the radial direction, w_0 describing the speed of the local rotation, and a is a parameter describing the depth of the local toroidal field.

The result of Eq. (2.9) shows that the formerly purely toroidal field now shows a component that is poloidal. For example, both B_θ and B_ϕ now include rotated parts of the original field B , creating a poloidal component. Additionally, there is now a radial component as well, moving outwards. The result of these effects is that there now appears to be a “loop” perpendicular to the surface area! This magnetic flux loop shows components circulating around both the (local) θ and the (local) ϕ -direction. Careful consideration on the effects of several such loops, including those created from cool regions falling, shows that this effect creates a net positive magnetic field in the poloidal direction, created from a toroidal one. These effects explain a possibility of keeping the stellar magnetic field “alive”. Additionally, careful models have revealed that this $\alpha\Omega$ -dynamo also explains cycles, as the two components periodically grow and shrink in strength, as shown for example for the sun by [Stix, 1976].

2.4 Time Series and periodicity

Activity related phenomena are not constant, but vary with time, and so do their associated activity indices. For example, if we plot the sunspot number R (Eq. (2.1)), smoothed out over a small time frame to take care of spots leaving the visible surface area, we can make out a very clearly defined period of about eleven years. Due to this periodic increase and decrease of spots (and faculae), the overall irradiance from the sun also varies, therefore the solar constant is actually not a constant. The change in irradiance is only about 0.1 %, however [Fröhlich and Lean, 1998]. Modern measurements of the magnetic field have revealed that the polarity switches from one such cycle to the next, suggesting a 22-year cycle, which is sometimes called Hale’s cycle [Hale and Nicholson, 1925]. Going even further, the sunspot number between 1645 and 1715 was much lower, suggesting a period of very low activity. This period is referred to as the Maunder Minimum [Eddy, 1976]. Such cycles can not only be found in the sunspot number, but also in other activity indices. For example, Baliunas and Soon [1995] analyzed the cycle length of about 100 dwarf stars from the

Mount-Wilson survey, using the S_{MWO} index. They found that for those stars with comparatively low activity levels – similar to the Sun – larger cycle lengths correlated with generally lower levels of chromospheric activity, and lower amplitude in the cycles. They found no cycles shorter than about six years in solar-like stars. Most stars in their sample showed periods between eight and thirteen years: The range the Sun’s activity cycle length also falls into. Performing such searches for other stars, with this and other activity indices, will bring forth important data, which may bring forth better understanding of the dynamo process, as well as understanding the Sun’s cycles better. It has been suggested that the Earth’s temperature is affected by the level of solar activity, which may contribute to Global Warming. A more detailed analysis of this effect as it applies to the UV emission is given by Friis-Christensen and Lassen [1991].

2.4.1 Rotational periods

The eleven year cycle of the Sun is not the only period that can be derived from its activity indices, or observation of spots. From regular observations of the solar disk, the time it takes them to migrate across the disk can be measured. This movement is caused by the rotation of the sun, and takes about 25 days, but is dependent on the latitude due to differential rotation. Since the changes in spectra highlighted in activity indices are localized to active regions, which move across the star’s surface as well, it is possible to obtain the rotational periods from activity indices, as well as the measured chromospheric fluxes. We will describe this process in detail, and demonstrate it with a subset of our available data in Chapter 10.

2.5 TIGRE Telescope

This section gives a short overview of the instrument used to acquire the spectra we have analyzed in this work. It follows the much more detailed overview given in Schmitt et al. [2014].

This work has made extensive use of a large number of spectra from the Telescopio Internacional de Guanajuato Robótico Espectroscópico, or TIGRE for short. This 1.2 m, f/8 telescope has been robotized and is therefore able to obtain spectra completely autonomously. The TIGRE project is a collaboration of astronomers from the Hamburger Sternwarte, the University of Guanajuato, as well as the High Energy Astrophysics group of the University of Liège.

The TIGRE telescope is now stationed near Guanajuato, Mexico, at a height of about 2400 m, after a series of extensive tests have been performed to characterize and optimize the telescope’s performance [Mittag, 2006]. The telescope is a Cassegrain-Nasmyth type, and the signal from one of its foci is fiber-fed to the HEROS spectrograph (Heidelberg Extended Range Optical Spectrograph)⁶ [Kaufer et al., 2001]. This spectrograph features two channels, which cover a wavelength range of about 3800–5700 Å and 5830–8800 Å, respectively⁷. This large wavelength range, covered simultaneously, is a very uncommon selling point for the instrument, and a pivotal advantage that made this work possible. The echelle spectrograph takes spectra with a resolution of roughly $R \approx 20\,000$ (see below).

TIGRE’s main goal is the analysis of stellar activity cycles, with a strong focus on the Ca II H- & K-lines. TIGRE has already proven that it fulfills this goal very well, and papers about searching for periods from TIGRE spectra on the Ca II H- & K-lines have already been published, e.g. Hempelmann et al. [2016], Mittag et al. [2017]. However, TIGRE’s large wavelength range, and the great flexibility from its automatic approach allowed the investigation of different science as well, for example from analyzing Supernovae [Jack et al., 2015b] and Novae [De Gennaro Aquino et al., 2015], to analyses of chemical abundances [Cazorla et al., 2017].

⁶<http://www.lsw.uni-heidelberg.de/projects/instrumentation/Heros/>

⁷A service mission in 2015 improved these wavelength ranges, and they are given as $\lambda_{\text{Blue Channel}} = 3738 - 5748 \text{ \AA}$ and $\lambda_{\text{Red Channel}} = 5767 - 8779 \text{ \AA}$ in the TIGRE newsletter [TIGRE Team, 2015].

2.5.1 Automatic spectra

TIGRE can be operated manually, but it is usually operating fully automatically. The system then performs the initialization setup (opening the dome, etc.), obtains calibration measurements (such as flatfield and bias images), as well as a ThAr spectrum, and finally takes scientific measurements. The choice of the observed star is performed by an automatic scheduling system, which selects a suitable target according to various parameters, such as the target’s visibility and height or priority of the measurement. This scheduling system allows TIGRE to automatically obtain data for several different science projects, including those that require many measurements at particular time intervals to measure periods, or to synchronize observations with those of other instruments (such as X-Ray satellite telescopes). Via various safeguarding measurements, this system also ensures that observations are only performed if it is safe to do so, with weather conditions permitting.

Afterwards, the spectra are reduced fully automatically. TIGRE uses a modified version of the REDUCE code [Piskunov and Valenti, 2002], as described by Mittag et al. [2010]. In short, it creates master calibration images (flatfield, bias) from the several ones taken throughout the night: These are subtracted from the images analyzed in the following steps. It then proceeds to determine the positions of each spectral echelle order from the flat field images. If no errors occurred in those steps, the so-called “blaze spectrum” from the flatfield lamp is extracted. Since a flat response is expected for this, dividing real spectra by this blaze spectrum eliminates differences in the spectrograph’s responsiveness to wavelength (e.g. from different pixel quantum efficiencies). Next, the spectrum of the ThAr lamp is analyzed. Since the positions of the lines in this spectrum are known and well distributed across the range, their positions allow the mapping of pixel positions in each order to wavelength. Finally, the actual science spectra’s wavelength is determined using the previous result, and the S_{TIGRE} -value is determined.

2.5.2 Calibrating the S_{TIGRE} index

TIGRE’s automatic pipeline does not only perform the reduction of spectra. It also performs a rudimentary activity analysis by determining an S-Index S_{TIGRE} . The routine performs this calculation using the blaze-normalized, echelle-order-merged spectra [Mittag et al., 2016], but it does use rectangular bandpasses instead of the triangular ones used in the original definition. This value S_{TIGRE} is saved in the header of the spectra, and can be used for activity studies. The resulting index cannot directly be compared to the S_{MWO} -values. The original definition Eq. (2.3) includes the factor α which is meant to bring values from different systems into agreement. Mittag et al. [2016] have determined this factor by means of a linear regression via 50 comparison stars with S_{MWO} values known from the literature, and found:

$$S_{\text{MWO}} = (0.0360 \pm 0.0029) + (20.02 \pm 0.42) \cdot S_{\text{TIGRE}}. \quad (2.11)$$

Since the intercept of ~ 0.04 is similar to the residuals (at least for stars with $S_{\text{MWO}} \gtrsim 0.17$), this is likely just a statistical artifact, and therefore similar to setting $\alpha = 20.02$ in Eq. (2.3).

The index S_{TIGRE} has not been determined for all TIGRE spectra, or at the very least not included in their header, so we have determined this value ourselves for this work. We used the triangular bandpass for N_H and N_K , and summed up the counts in the wavelength bins included in the respective bandpasses, determined from the non-normalized spectrum, to find $S_{\text{This Work}}$. We must now find the correct transformation of this index to the S_{MWO} -scale, like Mittag et al. [2016] have done. To do this, we take the spectra for which a value S_{TIGRE} is available, convert this to a value S_{MWO} using Eq. (2.11), and compare this value to our value for $S_{\text{This Work}}$. There is a very clear linear relation, a linear fit of which yields:

$$S_{\text{MWO}} = (0.04447 \pm 0.0016) + (24.404 \pm 0.152) \cdot S_{\text{This Work}}. \quad (2.12)$$

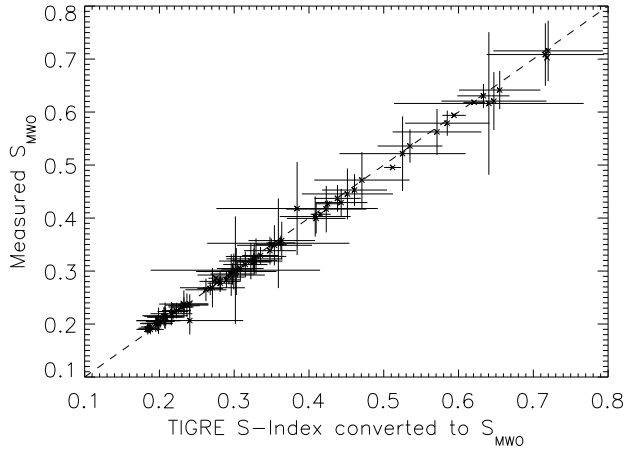


Figure 2.9: **Comparing the S-index determined from Eq. (2.11) (abscissa) to the one calculated from Eq. (2.12) (ordinate).** This plot originally appeared in Martin et al. [2017].

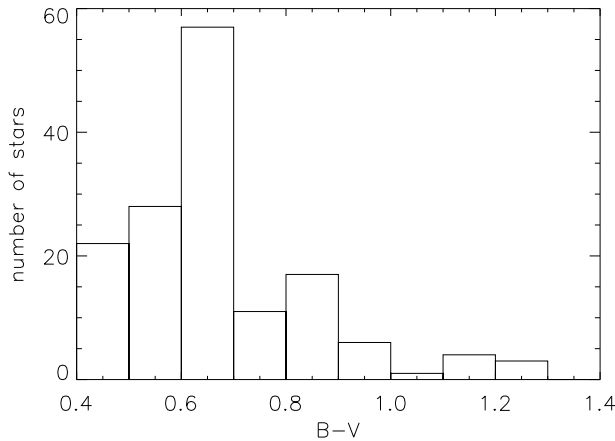


Figure 2.10: **Histogram of the distribution of stars with spectra analyzed in this work.** There are further TIGRE spectra available with $B - V$ outside this range, or of non-main sequence stars, that are not included in this histogram.

Again the intercept is small compared to the residuals, and we find a very similar value⁸ of $\alpha \approx 24$. The resulting values for S_{MWO} from Eq. (2.11) and Eq. (2.12) agree very well, and are shown in Fig. 2.9.

2.5.3 TIGRE spectra used in this work

We performed a search through the TIGRE archive for main sequence stars in late 2015. Those stars, as well as some of their parameters (see Sect. 4.2) have been added to a local database, for quick access to this data. We filter by only allowing F, G and K stars, with a $B - V$ between 0.4 and 1.25. This range was chosen to hold a large selection of both active and inactive stars with good quality spectra (defined as in a reasonable signal-to-noise ratio). Since the data we analyze here was taken for various different projects, the range of signal-to-noise values, exposure time, etc. varies quite a bit. We will give details in the corresponding sections. Here, we note that the stars are not evenly distributed. Figure 2.10 shows a histogram of the distribution in $B - V$. There is a large peak for $B - V$ in between 0.6 and 0.7, quickly tapering off, with only about eight stars with $B - V > 1.0$.

A large part of the spectra analyzed here were recorded for Hempelmann et al. [2016].

⁸The TIGRE pipeline also provides an additional, normalized spectrum. When using these normalized spectra instead, $S_{\text{This Work}}$ increases a small amount, so the value found for α would be slightly lower.

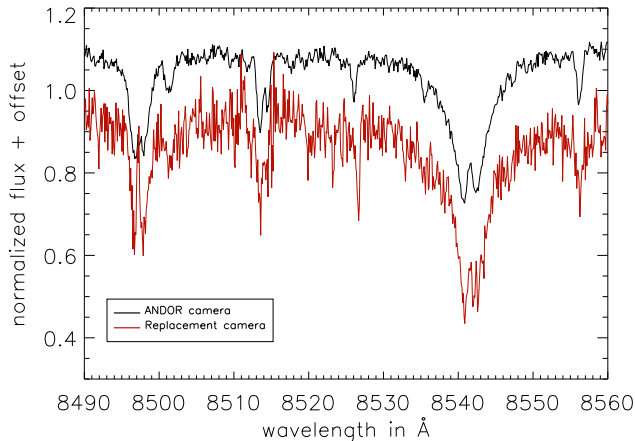


Figure 2.11: Comparing a spectrum of HD 129333 taken with the TIGRE default camera (black) and the replacement camera (red). The quality of the replacement camera spectrum is much worse.

2.6 TIGRE problems and limitations

Unfortunately, the telescope is not completely without issues. While many of them have been fixed, we had to solve or work around some problems in order to use as much of TIGRE’s large archive as possible.

2.6.1 Defective camera and replacement

In 2014, it was discovered that the default TIGRE camera did not cool down its chip correctly. The camera was sent in for repairs, and during that time, replaced by a different camera (FLI ProLine PL09000). This camera, however, performed much worse, showing much higher noise levels, as well as more artifacts, than the default camera, as shown in Fig. 2.11. The quality gap between good and bad spectra varies, and is not always as strongly pronounced as in that example. However, it is difficult to quantify, and the work we plan to perform on these spectra is very sensitive to these changes. For this reason, we have disregarded all spectra taken with this camera, which was in use between December 6th, 2014 and May 15th, 2015. The large amount of TIGRE spectra available allows us to perform such a drastic step.

2.6.2 Resolution

The spectral resolution is defined as:

$$R = \frac{\lambda}{\Delta\lambda}, \quad (2.13)$$

where $\Delta\lambda$ is the measured width of a fictitious, infinitely sharp spectral line measured at λ , which only appears broadened due to the limiting capabilities of the instrument. It can be measured by taking very narrow, known spectral lines. For this purpose, TIGRE is using a number of lines in a ThAr-spectrum, and fits Gaussians to them, in order to determine their width $\Delta\lambda$. The result is stated on the official TIGRE website as $R = 20\,484 \pm 92$ for the red spectral arm and $R = 20\,738 \pm 81$ for the blue spectral arm [Mittag, 2015]⁹. However, these are mean values from the resolution of 28 lines in the blue spectral range and 29 lines in the red.

A byproduct of the automatic reduction are plots revealing more information about a number of parameters, one of which is the determined resolution of the spectrum. Figure 2.12 shows the obtained resolutions for a large number of lines across the spectrum in the red arm. The mean resolution is of a similar value than the one stated on the website. However, it is obvious that the

⁹http://www.hs.uni-hamburg.de/DE/Ins/HRT/hrt_user/spec_redu_info_res.html

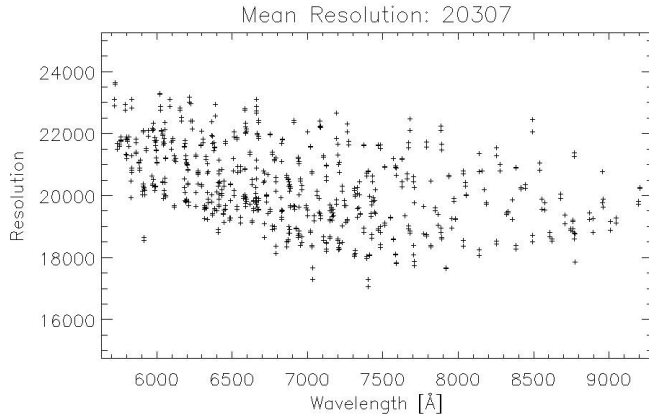


Figure 2.12: **Obtained resolution from the ThAr spectrum for many lines.** This figure is a byproduct of the reduction pipeline written by Marco Mittag. Used with permission. [Mittag, 2015]

resolution differs very strongly from line to line, and that for some lines it goes down¹⁰ as far as 18 000. For some applications, the difference between $R \approx 21\,000$ and $R \approx 18\,000$ must be considered. For example, when fitting a model to the data, the resolution must be known so that the model can be appropriately degraded. If this is done incorrectly due to an overestimated resolution, the spectrum’s lines will appear broader than they really are, which a fit would seek to compensate by varying the stellar parameters, most likely stellar rotational velocity. If the resolution varies as strongly as it does in Figure 2.12, then it must be tuned in the fit as well, separately for all lines that are fitted. We come back to this in the chapter on fitting models (Chapter 6).

This variation in resolution does not appear to be stable in time, as visual inspection of several available plots such as the one in Fig. 2.12 reveals.

2.6.3 Estimates of signal-to-noise ratio and errors

The main part of this work has made use of an extensive number of spectra in an automatic approach. Such an approach was greatly simplified by the information written into a file’s header by the TIGRE pipeline, as this fixed the need for an additional pass through the dataset to determine, for example, the Signal-to-Noise-ratio (SNR). The spectra are delivered as FITS-files, with the header including general information about the spectrum, such as exposure time, location on the sky, and weather conditions. Additionally, the TIGRE pipeline determines some parameters in the course of the reduction from echelle image to spectrum. As the error is determined during this process, one of the parameters available throughout this reduction is the Mean Signal-to-Noise ratio of the spectrum, which is saved in the header named as `MEAN_SNR`. While this is generally reliable, we encountered several cases in which the given ratio differed from what was observed near the lines we are analyzing, as evidenced by a simple visual check.

Spectra with very poor SNR cannot be used to determine accurate information regarding the deviation in line shape expected in the Ca II IRT-lines. In fact, they can potentially introduce artifacts into the sample, which limits the possible conclusions to be drawn from it. However, if it is known that such a spectrum is of low quality, it can either be ignored outright, or the determined parameters can be assigned an appropriately large error, and thus it would not affect the conclusions drawn. The worst case is a poor SNR spectra that has been assigned a high SNR erroneously. In this case, an unrealistic value might be determined that would not carry a correct error, negatively impacting the conclusions. In many cases, these spectra ultimately result in determined values that are clear outliers. If not properly taken care of, those can have a very strong impact on a generated fit compared to a much larger sample of tightly-clustered data.

In this automatic analysis, we have always set a lower limit on SNR – typically twenty – and disregarded spectra with SNR lower than that value. We have carefully visually investigated the spectra

¹⁰The description of the website states “To optimize the figure, only data are plotted into the range from $R=15\,000$ to $R=25\,000$ ” [Mittag, 2015]. This implies that it is possible for individual lines to show lower resolutions, but this seems unlikely given the distribution the points seem to follow in Fig. 2.12.

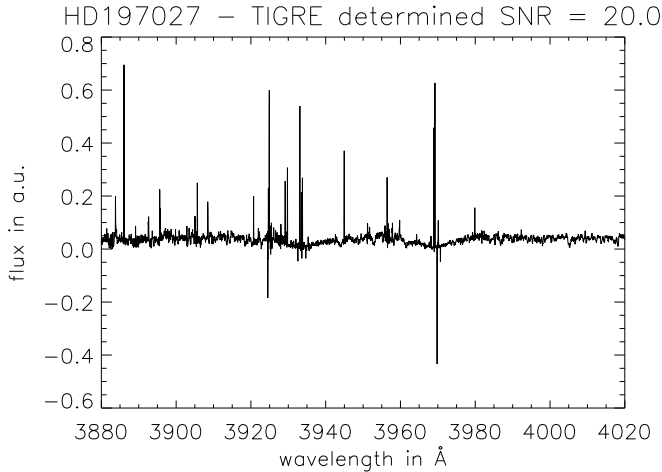


Figure 2.13: **Spectrum with very low SNR in the region of the Ca II H- & K-lines, classified with a Mean SNR of 20** Plotted here is the region of the Ca II H- & K-lines, as taken by TIGRE on October 15th, 2014. Visual inspection makes it clear that this spectrum is more noisy in this region than the given mean SNR of 20.

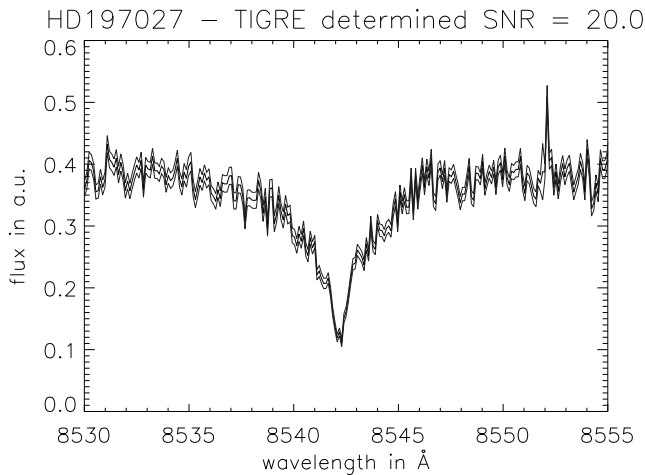


Figure 2.14: **Spectrum with a low SNR in the region of the second Ca II IRT line, classified with a Mean SNR of 20.** Plotted here is the second Ca II IRT line, taken by TIGRE on October 15th, 2014. The thin lines shows the pipeline-determined 1σ -region.

for which we have determined values that are outliers or otherwise unexpected or nonconforming. The most common case of these were spectra with SNR lower than 20 near the lines we are interested in. In Fig. 2.13, the region including the Ca II H- & K-lines of a spectrum from HD 197027, taken on October 15th, 2014 is plotted. The SNR estimated by the pipeline and written in the header is given as 20.0049246883, however, it is very clear that the spectrum is suffering from a great number of artifacts, and only very little actual signal can be seen. In fact, it is difficult to even make out the deep, broad Ca II H- & K-lines! As the pipeline's determined SNR is given as a *mean* SNR, this is an unfortunate case where most regions may very well have a much higher SNR, and only some regions, including those we are interested in, are affected by such low SNR.

This problem affects not only the given value for SNR. The errors in the spectrum as well seem underestimated. Figure 2.14 shows the second Ca II IRT-line of the same spectrum. Here, the situation is better than in the region around the Ca II H- & K-lines, but this region, too, shows a SNR lower than 20 (it is actually closer to ~ 8 near the center and inner wings). In Fig. 2.14, we have also plotted the errors determined by the pipeline. It can be seen that the data fluctuates a lot more than would be expected given those determined errors. We must stress again that this is not (necessarily) an error in the TIGRE pipeline, rather that the mean SNR can in some cases not be meaningful for small regions in the spectrum. In the vast majority of cases, however, TIGRE's SNR estimate is a reliable indicator of the quality of the spectrum. However, in the large sample we are analyzing in this work, some of the spectra had to be disregarded due to the insufficient SNR near the lines of interest.

2.6.4 Cosmics and other problems

Figures 2.13 and 2.14 both show strong artifacts in the form of large peaks with a low width, sometimes of only one wavelength point. As long as those artifacts occur only sporadically, and do not fall into the line cores, they do not pose a threat to the analysis we perform. It is difficult to discern whether these spikes are due to the influx of cosmic particles on the detector, or if they are introduced in the reduction of the echelle images. In any case, they are not caused by stellar activity. Most spectra are not contaminated by such artifacts, and they rarely affect the determined quantities. For this reason, no further actions and filters to remove such artifacts have been used, with one exception: Spectra to be used as comparison have been visually checked to ensure they do not suffer from these effects.

2.6.5 Corrupt files

In this work, a large part of the TIGRE archive has been searched and analyzed. Many files have been accessed, opened and read. In some cases, however, this was not possible as the file was corrupt. Trying to open it therefore triggered an error message.

This is not in itself a problem for this work, as we still have a large number of spectra left to analyze, but it may be of interest to others to know that some spectra that are mentioned in the archive do not exist due to a corrupt file. We found that less than 1% of all files we tried to analyze were corrupt, usually due to an “Invalid BITPIX”, an incorrect or unexpected setting in the file’s header.

2.7 Telluric correction

TIGRE is a ground based telescope. For this reason, the spectra it takes are contaminated by the atmosphere. Elements or compounds in the atmosphere absorb and scatter light, which distorts the recorded spectrum. These effects, caused by spectral lines in the earth’s atmosphere, are called telluric lines. Neither the Ca II IRT-lines, nor Ca II H- & K-lines are strongly affected by telluric lines. The spectral region around the H α -line is affected much more strongly. If the atmospheric composition and its physical parameters (e.g. temperature) at the time of the observation is known, then these effects can be estimated and subsequently corrected. This process is called telluric line correction. For TIGRE, Klocová and Kohl [2015] have adapted the popular Molecfit code [Smette et al., 2015, Kausch et al., 2015] to work with TIGRE spectra. It can correct the telluric contamination using available weather data. To this end, we installed Molecfit on our work machine, and let our code execute a Molecfit call (using the IDL-routine SPAWN). We show the results of this correction for the lines we are investigating here in Fig. 2.15. There is a small effect in the second Ca II IRT-line, and a somewhat stronger one in the H α -line. Generally, however, the telluric contamination is not significant.

Because the effect is rather small for the Ca II IRT-lines and Ca II H- & K-lines, we have not always performed this correction. Such a correction is rather time-consuming: it takes about 3 minutes of computing time per spectrum on our system. For a large sample of roughly 3 000 spectra, that alone amounts to 150 hours. We mention in the text if this step was performed.

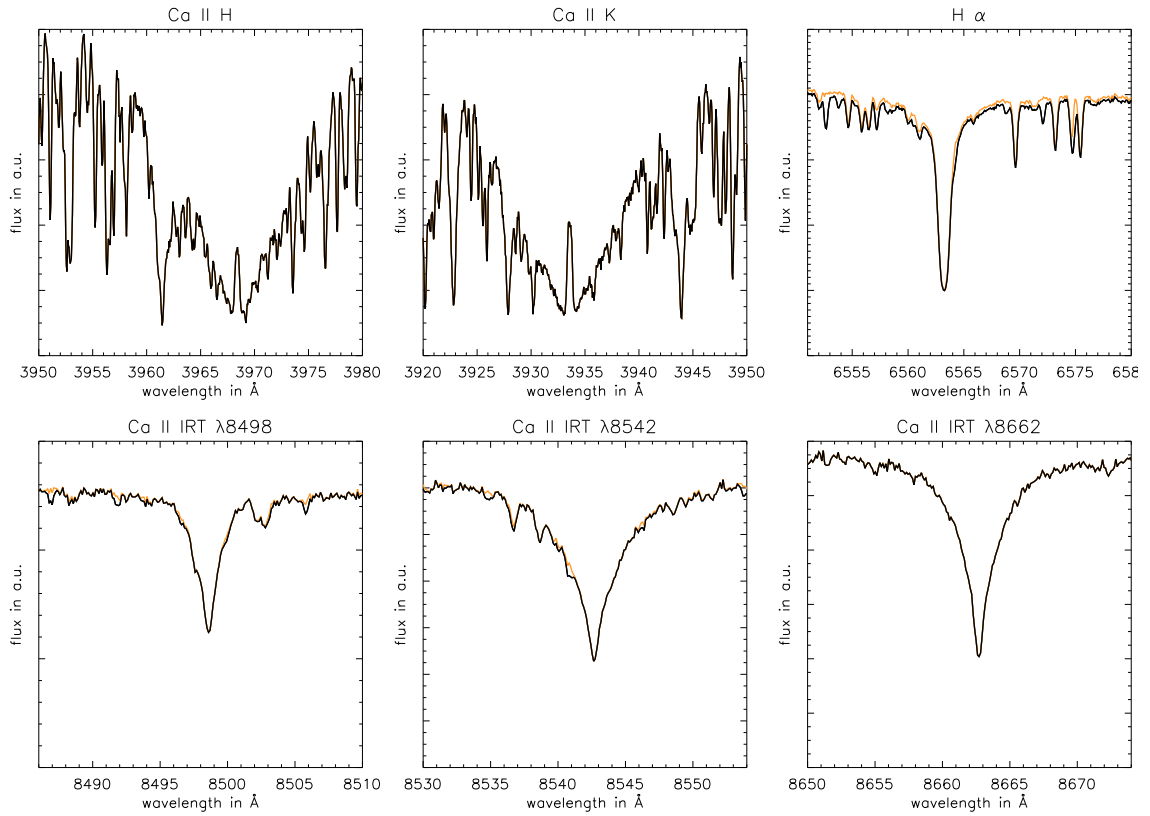


Figure 2.15: **Effect of telluric line correction with Molecfit in the lines we are investigating.** For the Ca II H- & K-lines, the H α -line and the Ca II IRT-lines, we show the effect of telluric line correction using Molecfit in this plot for the spectrum of HD 165341A, obtained on August 27th, 2014. The corrected spectrum is shown in orange only where it differs. The differences are not significant, and almost nonexistent for Ca II H- & K-lines and the first and last Ca II IRT-line.

Chapter 3

Measuring Chromospheric Excess

In this chapter, we describe the algorithm that allowed us to measure the chromospheric stellar flux in certain lines. First, we give a motivation as to why such an algorithm is desirable, and give a short overview on how it works, followed by an extensive description of each of the performed steps, with examples and problem cases shown. Details on the actual implementation in IDL are given in the appendix.

3.1 A new approach and its goals

In this work, we measure the chromospheric excess in the line spectra of active stars. The change in the line profile differs strongly from the Ca II H- & K-lines to the Ca II IRT-lines, as the former show a much larger fill-in up to clear emission cores (Fig. 2.6), which we do not normally observe in the latter, at least not for F, G and K stars. Additionally, we wish to measure this excess in physical units, however, TIGRE spectra are not flux calibrated. This requires us to find a way to convert the measurement into physical units. Finally, we wish to analyze a large sample automatically, as the number of spectra is too large for human intervention, and for reasons of consistency, wish to perform this analysis with just one algorithm.

We have already introduced the S -Index S_{MWO} in Sect. 2.2, which is the ratio of counts in the center of the Ca II H- & K-lines to the counts in the region outside the lines. While this index is easy to measure and very robust, it shows a clear dependence on the spectral type of the star (or equivalently, its temperature or value of $B - V$). This is because of the photospheric contribution to the central line flux, as well as the different continuum outside the lines. For this reason, this index works well for analyzing individual time series, but cannot be used to compare the activity levels of stars with very different temperatures. Therefore, the index R'_{HK} is defined, which subtracts the photospheric contribution to obtain a flux $F_{\text{HK,chrom}} = F_{\text{HK}} - F_{\text{HK,phot}}$ and normalizes the result by σT_{eff}^4 [Linsky et al., 1979]. In this work, we similarly want to find the flux free from photospheric contributions for different lines (Ca II H- & K, Ca II IRT, $\text{H}\alpha$), which we are then free to normalize by σT_{eff}^4 if needed. This has been done before in the literature [Martínez-Arnáiz et al., 2011b, Busà et al., 2007] with promising results. In this work, we make use of the very large TIGRE sample of *simultaneous* observations in the different lines. The large sample allows us to analyze the correlation of these indices in detail – so it is possible for us to estimate the quality of these lines as a stellar activity diagnostic – and their behavior in time: For example, it has been shown that the activity indices derived from the $\text{H}\alpha$ -line and the Ca II H- & K-lines are not perfectly correlated for all stars [Cincunegui et al., 2007, Gomes da Silva et al., 2014]. It is therefore interesting to see the temporal behavior of these indicators, as they may be formed in different parts of the chromosphere [Vernazza et al., 1981].

The algorithm we describe below has been written in IDL and performs all necessary steps to find the chromospheric flux. It does so by subtracting a spectrum that is assumed to be inactive and therefore chromospherically quiet: Therefore, to good approximation, we have $F_{\text{HK}} \approx F_{\text{HK,phot}}$ for

this inactive star. This can be either the observed spectrum of an inactive star, or a model. We perform these two comparisons in Chapter 4 and Chapter 7, respectively. This comparison spectrum is also assumed to be passed in physical units of $\text{erg s}^{-1} \text{cm}^{-2} \text{\AA}^{-1}$, and this scale is used to convert the measured flux to physical units. The steps performed are as follows:

1. Normalizing the two spectra
2. Correcting any wavelength shifts
3. Perform rotational broadening, and if necessary instrumental broadening, of comparison spectrum
4. Subtracting the spectra from each other
5. Integrating the residuals or performing a fit to them

We now describe how these steps are performed in detail, and give examples. Note that this algorithm has been described before in my paper [Martin et al., 2017].

3.2 Normalizing the spectrum and obtaining the continuum

TIGRE spectra are not given in $\text{erg s}^{-1} \text{cm}^{-2} \text{\AA}^{-1}$. The spectra are also not proportional to those units across the entire spectral range. Therefore, two spectra of the same object do not show the same continuum level. However, for our purpose, we need to find the continuum in the spectrum, as this will define our flux scale. We know the flux in physical units at the continuum level from flux-calibrated comparison spectra, if we have those available. Otherwise, Hall [1996] gives relations to determine a star’s continuum level. After normalizing a spectrum, a point at 1.0 will therefore correspond to the value given at that point in the continuum, a point at 0.5 will be at half that flux level, etc. As we wish to compare the flux in the center of spectral lines, we need to normalize the region these lines fall in. We require an approach that works in an automated fashion without user interaction, in a flexible way for any lines a potential user may wish to analyze: For us, these lines will be the Ca II IRT-lines, the Ca II H- & K-lines and the H α -line.

The simplest possible approach is to divide a spectrum by a defined value in its region, such as the maximum or median value. However, this does not return reliable results (see Fig. 3.1). Since we analyze spectra of absorption lines, the median value will usually be below the continuum level (blue dotted line in Fig. 3.1), and create an offset in this way, which we would need to correct. Using the maximum value does not have this problem, but is sensitive to noise, or cosmics, as the maximum value is defined by just one value. This will then result in an incorrect normalization as well (red dashed line in Fig. 3.1). For this reason, we require a better approach, which finds the continuum in a spectrum from all data points.

The idea here is simple, and follows the approach of `top.pro` from the REDUCE package [Piskunov and Valenti, 2002]: In an iterative process, we first fit a polynomial to the region around the spectral line considered. Then, we remove points more than 2.5σ below the fit value and re-fit the remaining points, until a convergence criterion has been reached, or until a certain amount of points has been removed. We use a linear fit and stop the process after 40% of points have been removed. An example of this process for HD 145675 is shown in Fig. 3.2, where for illustration purposes both a different normalization region has been used, and more iterations have been performed than in the actual excess determination. To normalize, the spectrum is subsequently divided by the assumed continuum.

In most cases, where only a small region around the center of a line is fitted, a linear fit to the continuum is suitable. However, if a larger region is fitted, which may be required in regions with very few continuum points, a higher polynomial order fit might be needed. In Fig. 3.3, we show the normalization result for different orders. It’s apparent that if too large orders are chosen, the fitted continuum is following the spectrum and its noise too closely, resulting in a worse normalization with a continuum that is “too curved”.

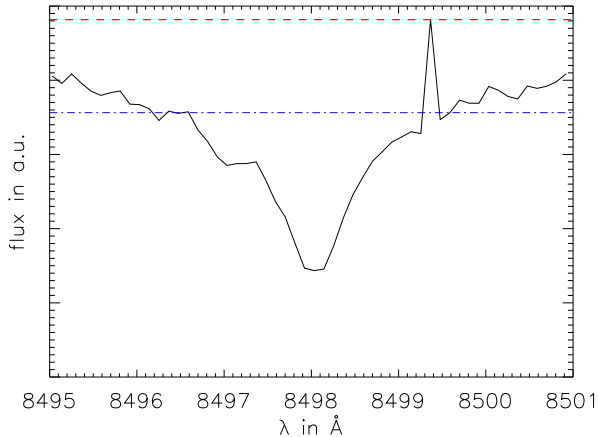


Figure 3.1: **Simple normalization attempts for noisy spectra.** This plot shows the case of normalizing the merged TIGRE-spectra of inactive object HD 145675 with added synthetic noise and an outlier. The simple cases of using the median value (blue dash-dotted line) results in a continuum level that is too low, whereas using the highest value would be too high due to the noise spike (red dashed line).

3.2.1 Normalizing the Ca II H- & K-lines

This general process returns a reliable estimate of the continuum, if a large enough part of the spectrum is passed that contains at least about 60% continuum, and if the spectrum features only absorption lines, as it currently does not handle emission lines. In most cases, the region to be considered is simply the region around a line. However, for the Ca II H- & K-lines, this process can then fail, as the broad, triangular shape with the large amount of absorption lines nearby leaves no points at continuum level near the lines. The estimated continuum level will then be too low. To fix this problem, we use the upper envelope instead of the actual spectrum. This “masks” many of the narrow absorption lines. To help with the problem of the wide line not leaving any continuum on its sides, we consider the original definition of the S_{MWO} -value [Vaughan et al., 1978, Duncan et al., 1991]. There, two 20 Å-wide continuum bands are defined to the “red” and “blue” region of the continuum, centered at 3901.07 Å and 4001.07 Å. We adapted the procedure above to only take into account points in these bandpasses. The difference of using this approach and to simply use the region around Ca II H- & K-lines as we are able to do for the Ca II IRT lines is shown in Fig. 3.4. The result of this approach is satisfactory, but we still note that this normalization – which affects the subsequent conversion to the physical flux scale in units of $\text{erg s}^{-1} \text{cm}^{-2} \text{Å}^{-1}$ – is much easier, and therefore more reliable, for the Ca II IRT lines, which has been noted as an advantage of using the Ca II IRT lines for activity studies [Busà et al., 2007].

This procedure is not meant for spectra with emission lines. For very active stars, the emission cores in the Ca II H- & K-lines lines become so strong that they have a similar effect. This, however, is not a problem when using the two regions defined in the S_{MWO} -definition for normalization, as the emission cores are then simply ignored.

3.3 Correcting wavelength shifts

Stellar spectra feature wavelength shifts. Movement along the line of sight will create a red- or blueshift in the spectra, which has to be corrected. For all stars analyzed in this work, values for this shift were available from SIMBAD [Wenger et al., 2000]. To correct the shift, the wavelength scale is then multiplied by a factor of $(1 \pm v_{\text{radial}}/c)$, with the sign depending on whether the star moves away or towards the observer. An additional shift stems from the relative movement of Earth and star from the Earth’s rotation around the Sun, and the movement of the center of mass. However, the routine used for reading in TIGRE spectra automatically performs this correction. At this point, most wavelength shifts are already corrected. However, in practice, these shifts are rarely perfectly corrected, or other effects create a significant additional shift. For example, in the case of binaries performing a rotation around their center of mass, the wavelength shift from the projection

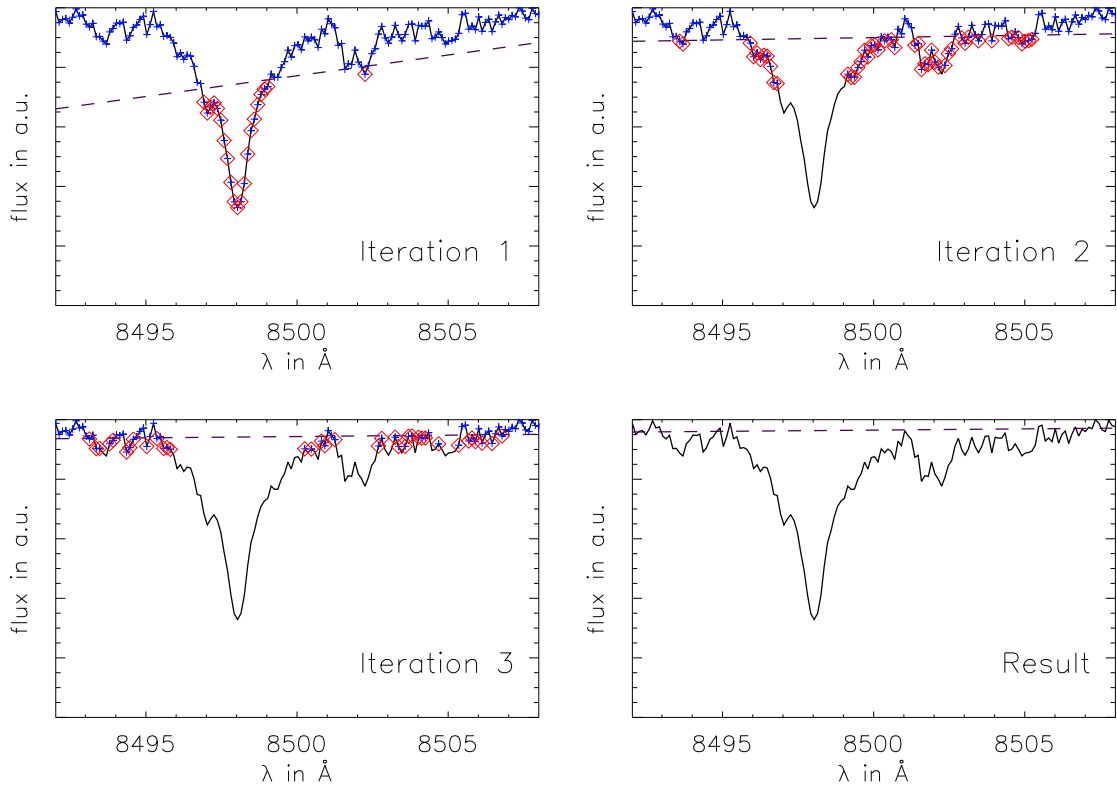


Figure 3.2: **Illustrating the Normalization procedure.** These plots show three iterations and the final result for normalizing a TIGRE-spectrum of HD 145675 with added synthetic noise. In each iteration, the data points shown as blue pluses are fitted to obtain the current best guess of the continuum (violet dashed line). Afterwards, all points below 2.5σ of the continuum are removed for the next iteration (red diamonds).

of that movement along the line of sight will differ in time. However, no matter the cause, our algorithm must be expected to handle these cases and to perform its own wavelength correction to shift comparison and considered spectrum on top of each other. This step is performed using cross correlation. For this to work correctly using the standard procedure of calculating the cross correlation with a Fast Fourier Transform (FFT), however, both spectra need to be sampled on an equidistant wavelength scale. The comparison spectrum is always resampled to such a scale, as this requirement is needed for the instrumental and rotational broadening (as those make use of a FFT as well). The spectrum under consideration is temporarily resampled to the comparison’s wavelength scale. Afterwards, the cross correlation is calculated. This cross-correlation will appear to be a smooth function, however, its true maximum may not have been sampled. We fit a parabola to the five points surrounding the maximum, and use the analytical maximum of that fit as the best-value for the shift. This approach is more reliable with shifts that are less than the wavelength difference in the sampling.

3.3.1 Limitations

This method works very well in almost all cases. Only for HD 22468 (HR 1099), a very active star that shows very strong emission cores, has this method failed. It’s spectra is not “similar enough” to its comparison spectrum, because of the high emission cores, affecting the shift that was determined.

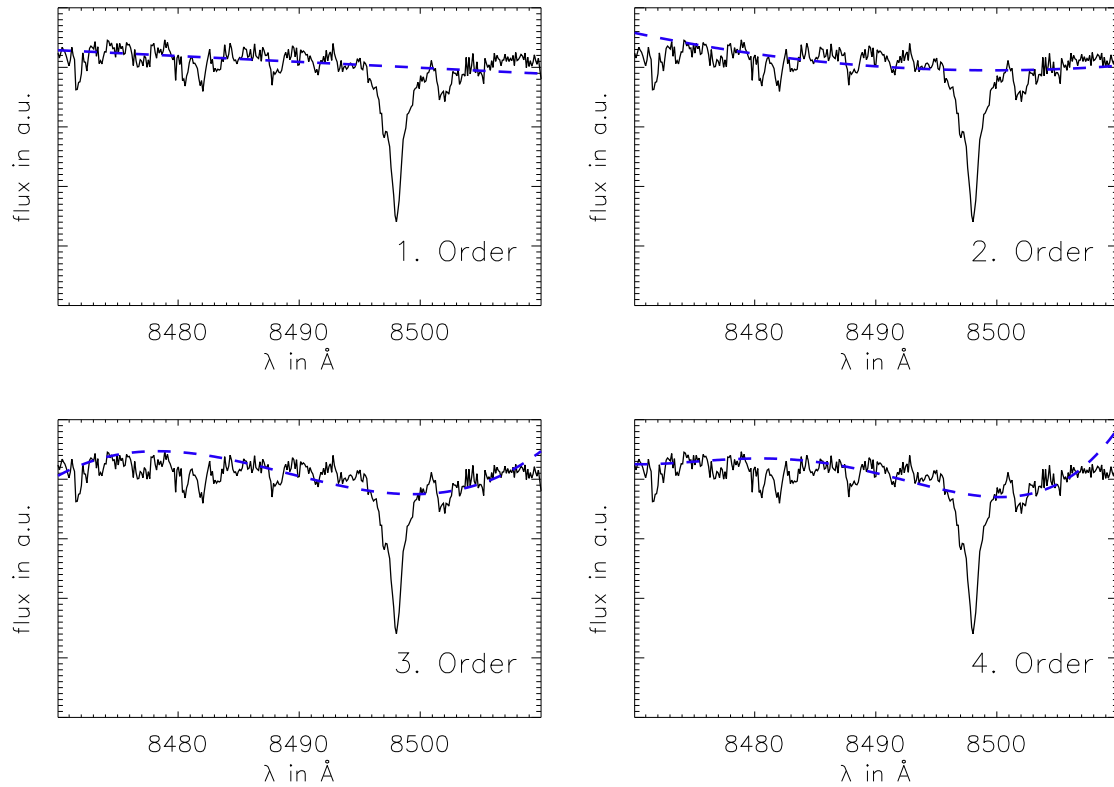


Figure 3.3: **Fitting the continuum with different polynomials.** In this plot, we compare the fitted continuum for different orders for the polynomial fit. If the order is too large, the fit follows the spectrum and its noise “too well”, which results in a continuum that appears “too curved”.

This object’s wavelength shift has therefore not been determined automatically, but by hand. Since no other star has shown problems with the shift, no further efforts to improve on this algorithm has been performed.

3.4 Adding rotational broadening to the comparison spectrum

If a star rotates, spectral lines are broadened. Our procedure compares two spectra with the goal of obtaining the additional flux from the active chromosphere F_{Exc} . We must take care of all other differences in the spectra, so that the only difference in the two spectra is ideally only the additional flux F_{Exc} . Applying our method, we can obtain not only the integrated flux, but also the function $F_{\text{Exc}}(\lambda)$, which describes how the flux is distributed in the line. One reason why this is interesting is that it allows a “light” version of Doppler Imaging (See Sect. 11.2.2). Since we artificially broaden the comparison spectrum to the rotational velocity of the spectrum under consideration, the original comparison spectrum should be free from any rotational broadening itself.

Figure 3.5 shows how rotational broadening works: As the star rotates, sections of it will move away from the observer, whereas other sections will move towards them. The light from sections that move away are redshifted, whereas the contributions of the parts that are moving towards the observer are blueshifted. The rotation axis of the star does not have to be aligned orthogonal to the line of sight. The effects of an inclination of this rotation axis means that the broadening observed stems from only the projected rotational velocity $v \sin i$, which is always smaller than the real rotational velocity of

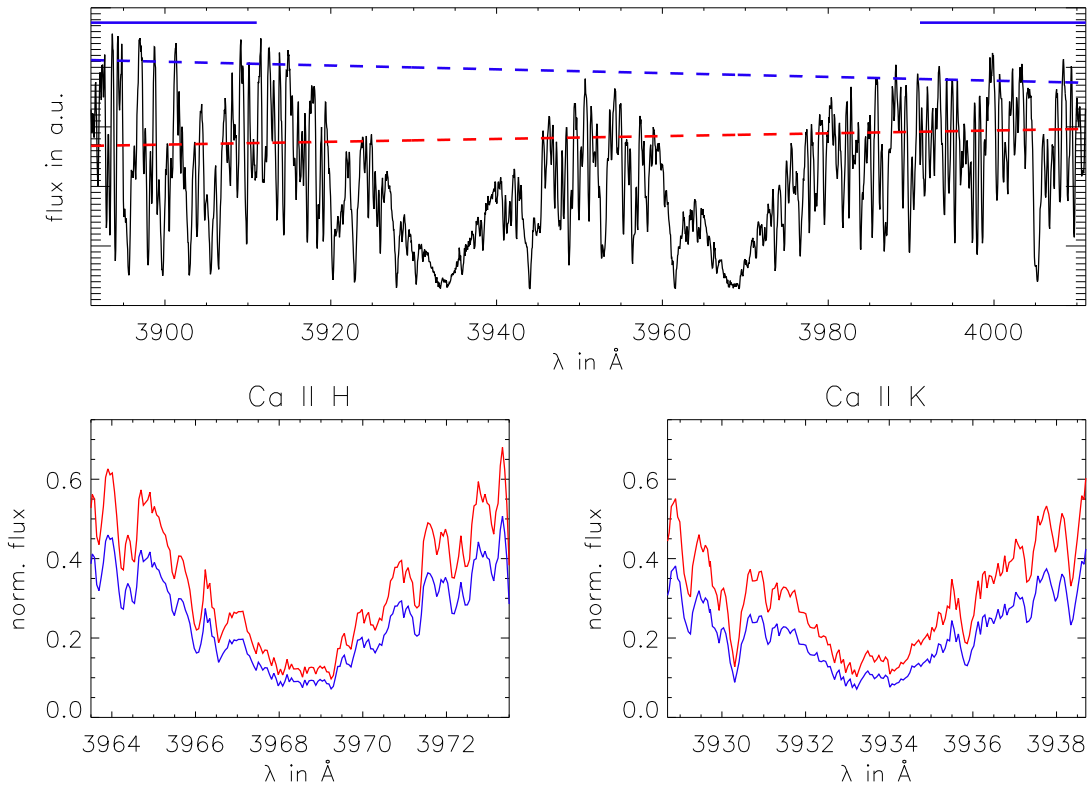


Figure 3.4: **Normalizing the Ca II H- & K-lines by finding the continuum only in particular bands (blue) vs. not limiting the region (red).** The top plot shows the found continuum from using the algorithm without any particularly defined regions (red dashed line), and compares it to the continuum (blue dashed line) that was found by only taking into account the continuum bandpasses defined in the S_{MWO} -definition, shown as blue, horizontal lines. The blue dashed line describes the continuum better. The result of normalizing the Ca II H- & K-lines by the continuum is shown in the lower plots in the colors corresponding to the continuum used. The difference appears mostly as an offset, which affects the determined flux.

the star. Numerically, this broadening is handled by folding the non-broadened comparison spectra with a kernel that describes this broadening. Here, we use the kernel provided by the IDL-function `lsf_rotate`, which is part of the IDL Astronomer’s Library [Landsman, 1993]. It uses the kernel as given in Chapter 17 of Gray [2005]. One of the more important parameters affecting rotational broadening is the limb-darkening coefficient ϵ . Limb-darkening is an effect by which the limb of a stellar disk appears darker than the center of it, which we have briefly described in Sect. 2.1.1. How the brightness varies across the stellar disk is described by limb-darkening laws. The parameter ϵ describes limb-darkening for the simplest approximation of linear limb-darkening. ϵ actually depends on the atmosphere of the star, and therefore on stellar parameters such as temperature, but varies also by wavelength. To accurately model this effect, we interpolate ϵ from the relations given by Gray [2005]. There, they give ϵ as a function of $B - V$ and wavelength. The result is that the kernel used for broadening depends on stellar parameters. This is the reason why our algorithm requires the user to pass a value for $B - V$. Figure 3.6 shows how the kernel changes for different $B - V$. Since the relation $\epsilon(B - V)$ is monotonous, we can estimate the error on ϵ from the error on $B - V$, which is another optional input parameter. For a more detailed review on limb-darkening, we refer to Müller [2016]. Here, we require the comparison spectrum to not show any strong broadening effects already. Neglecting this would result in the comparison spectrum to be broadened too much,

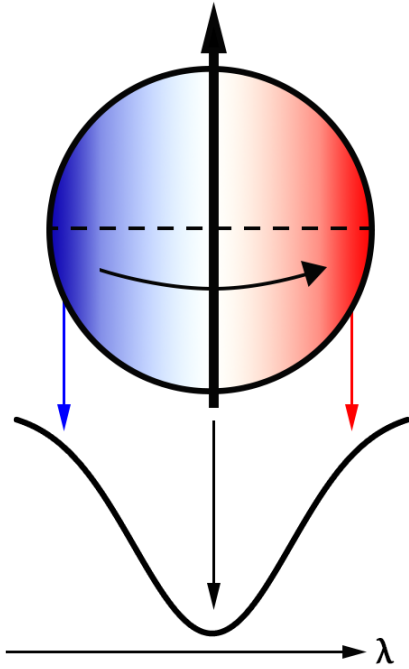


Figure 3.5: **Rotational broadening.** If a star rotates, sections of it will appear to move away from the observer (right), whereas some will move towards them (left). The result is a broadening of the stellar line, as the parts moving away from the observer are redshifted, and those moving towards the observer are blueshifted. This illustration shows the case of the rotational axis being orthogonal to the view direction. In any other case, the broadening effect is lessened, and appears to stem from the projected rotational velocity $v \sin i$, which is lower than the true rotational velocity. This illustration also simplifies the true rotational broadening by ignoring any effects from limb-darkening. Image based on one from Strassmeier [1997].

past the effects the rotational velocity of the star under investigation would yield. This will affect the obtained excess distribution $F_{\text{exc}}(\lambda)$, making it appear as if flux from the line core was shifted towards the wings. This is not a strong limitation in practice, as it has been known that inactive stars tend to be slow rotators [Andretta et al., 2005].

3.5 Degradation of the comparison spectrum

This procedure works regardless if the comparison spectrum stems from a synthetic model, from observed inactive stars or any other source. However, if using a model spectrum, or a high resolution observation, another step is necessary. TIGRE observations have a resolution of roughly 20 000, though the actual resolution varies (see also Sect. 2.6.2). Therefore, lines in TIGRE spectra are intrinsically broadened just due to the finite resolution. Model spectra are usually calculated at a much higher resolution (the ones we are using in Chapter 7 are roughly 500 000). Lines of the model spectra would therefore appear much deeper and more narrow than those in the TIGRE spectra. We therefore need to correct this effect. Broadening due to the finite resolution is done via a kernel that models the instrumental profile, which is a simple Gaussian in our case. The Gaussian's width is adjusted to fix the difference of the two resolutions, and is for the kernel centered around λ to degrade a spectrum to resolution R' [Czesla et al.]¹:

$$k(\Delta\lambda) = \frac{1}{\frac{\lambda}{R'}\sqrt{\pi}} \exp\left(-4\frac{\Delta\lambda^2}{\left(\frac{\lambda}{R'}\right)^2 \cdot \log_{10} 2}\right). \quad (3.1)$$

If the spectrum to be degraded already has finite resolution R_{current} , R' is not the target resolution R_{target} , but must be adjusted:

$$R' = (R_{\text{target}}^{-2} - R_{\text{current}}^{-2})^{-1/2} \quad (3.2)$$

If $R_{\text{current}} \gg R_{\text{target}}$, then to good approximation $R' \approx R_{\text{current}}$. However, if the difference is not as significant, this adjustment becomes very important. This effect is also referred to as instrumental

¹<https://github.com/sczesla/PyAstronomy>

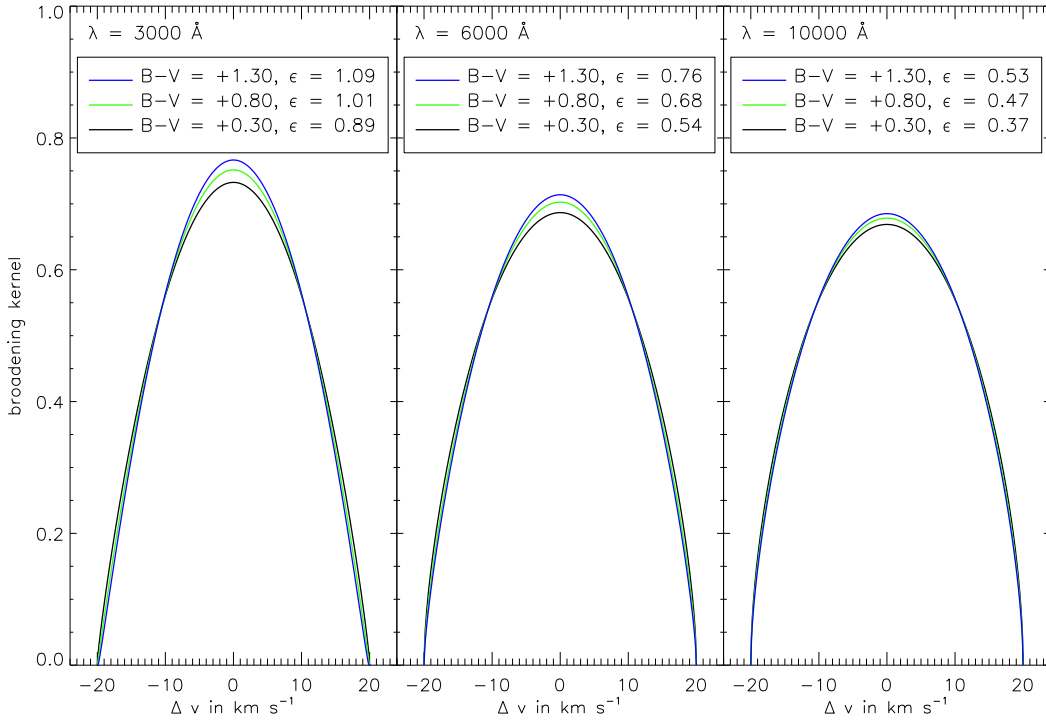


Figure 3.6: **Change in the rotational broadening kernel for different stellar parameters.** The rotational broadening must take limb-darkening into account, which depends strongly on stellar parameters. This plot shows how the kernel the spectra is folded with varies depending on a change in wavelength (left, middle and right plots), or in $B - V$ (colored lines). The resulting value for ϵ was interpolated from wavelength and $B - V$, and is given in the legend as well.

broadening. In order to differentiate it from the effects of rotational broadening, we refer to it as “degradation”.

3.6 Subtracting spectra and obtaining the excess

At this point, our comparison spectrum is guaranteed to be at the same resolution, broadened to the same rotational velocity, and normalized like the spectrum under consideration. If the comparison spectrum was aptly chosen, the only significant difference left is the chromospheric activity contribution. We can now subtract the comparison spectrum from the spectrum under consideration to obtain this contribution. We refer to the thus obtained residuals as excess. Slight differences in stellar parameters in the two stars we are comparing will introduce a slight offset between the two spectra. The same is true for a normalization that has been performed incorrectly, likely due to large errors on the two spectra. To fix these errors, we can make use of the fact that the flux from the active chromosphere is expected to be in the line core [Busà et al., 2007] and shift the line wings on top of each other. As formally, both incorrect stellar parameters and an erroneous normalization would not necessarily create a constant offset across the entire spectral region considered, we perform a linear fit on the excess distribution. For this fit, we ignore points near the line center. Subtracting this linear trend corrects this problem.

We denote the flux that we are left with the excess flux F_{Exc} . For the more active stars, $F_{\text{Exc}}(\lambda)$ is clearly well-defined and often appears close to Gaussian in shape. See Fig. 3.7 for examples. The re-

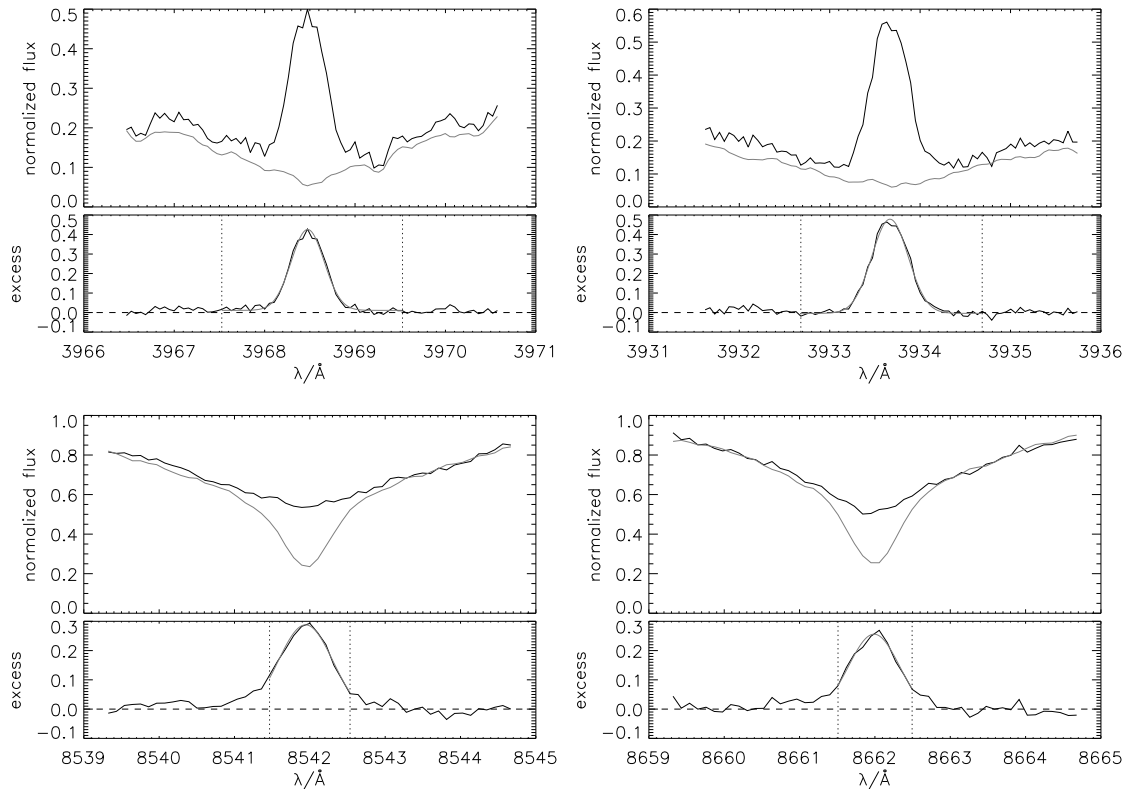


Figure 3.7: **Determined excess flux for a TIGRE spectrum of HD 152391.** For four chromospherically active lines, the excess flux was determined according to the method described in this chapter: Top row: Ca II H- & K-lines, Bottom row: Two of the Ca II IRT lines. The remaining one shows very similar behavior, and was therefore omitted from the plot. The spectrum of the active star HD 152391 (top panel, black) was compared to the inactive object HD 117176 (top panel, gray). The resulting excess distributions are shown in the bottom panels. The dotted vertical lines correspond to 2 \AA in the Ca II H- & K-lines plots or 1 \AA in the others, which correspond to the region the excess was determined during this procedure. Only for very active stars like this one this does not entail the entire excess flux for some lines (bottom row), see Chapter 4 for details. It can be seen that the excess is well determined for most lines.

lation to estimate the continuum flux from Hall [1996], or the flux-calibrated comparison spectrum's continuum provides the physical unit scale that we need to convert this value to $\text{erg s}^{-1} \text{ cm}^{-2} \text{ \AA}^{-1}$ (or $\text{erg s}^{-1} \text{ cm}^{-2}$ if using the integrated excess). Note that for the $\text{H}\alpha$ -line, the determined excess flux differs strongly in shape, with a much wider, and less defined shape, as Fig. 3.8 shows. When comparing a TIGRE spectrum to a model spectrum, we perform an automatic determination of the region to integrate the excess flux in. However, if the comparison spectrum is a TIGRE spectrum as well, the resulting excess flux often becomes too noisy, so that this determination could not be done reliably. We therefore chose to use a fixed width for the integration intervals, using 2 \AA for Ca II H- & K-lines and 1 \AA for all others. The automatic determination assumes a well-defined excess distribution, and then looks for a minimum in the distribution, which corresponds to the point where the small remaining signal becomes lost in the noise².

The excess $F_{\text{Exc}}(\lambda)$ can either be integrated over λ to obtain the total flux from the active chromosphere in that particular line, or it can be fitted, for example by a Gaussian. Fitting a profile

²In the unlikely case that not at least two such minima are found, then the points of 50% line depth are chosen as the limits for the bandpass. In case of several minima, the minima closest to the center maximum, but at least four data points away are picked.

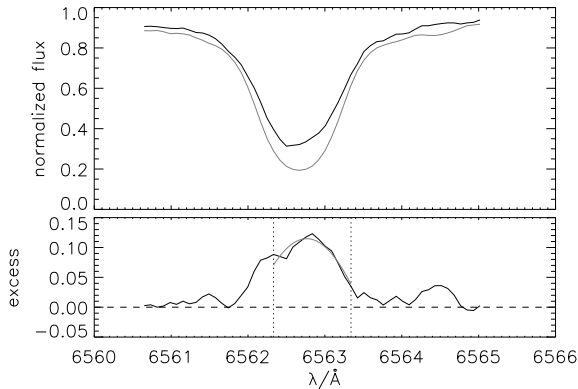


Figure 3.8: **Excess determination for the $H\alpha$ -line.** This plot shows the excess flux determination for the same spectrum as in Fig. 3.7. See caption of Fig. 3.7 for a description of what the various lines represent. It can be seen that the shape of the excess determined here differs from the more Gaussian-like shape of the excess fluxes determined in Fig. 3.7. The wider shape places more of the excess flux outside the marked 1\AA -wide region.

to it has the additional advantage that more information regarding the distribution is retained: the width σ , amplitude A_f and position $\Delta\lambda$ could be used for more detailed studies (e.g. those we outline in Sect. 11.2.2).

We set some limits on the fitted parameters. For example, the amplitude of the fit must be positive, and may not exceed the maximum value of the excess. Tests have shown that single strong noise structures could dominate this fit. In order to fix this, we optionally allow to fit a smoothed version of the excess. More accurately, the excess is then first broadened by a Gaussian kernel using the IDL-routine `GAUSS_SMOOTH`.

Naturally, the flux may be estimated from the Gaussian fit as $F_{\text{Gaussian}} = A_f \sigma \sqrt{2\pi}$. Assuming that the excess profile is indeed Gaussian, this value includes the entire flux in the excess, instead of just the small bandpass used for integrating. For stars with low activity, the amount of flux outside the bandpass is negligible, but for the most active stars in the sample, this amounts to at most 10% of flux lost (see e.g. Sect. 4.8). In these cases, it may be argued that the approach via the fit is better than the direct integration, as it is less affected by noise. Since outside the bandpass, the leftover excess is naturally small (due to the exponential drop-off in the wings), that region is dominated by residual noise (Fig. 3.7). Integrating that region adds more noise than signal to the obtained value. When fitting the Gaussian, only the center region is taken into account, where the signal clearly dominates the noise. The parameters can be reliably determined there, and the behavior in the wings is then defined by the profile function assumed (the Gaussian we are fitting here) for the excess core emission, and the flux contribution from outside the bandpass can safely be estimated this way. The values of the flux estimated from the Gaussian are very similar to those determined from direct integration. As the parameters for the fit are limited to physical values, clearly wrong results, such as a negative amplitude, can never be obtained. This makes the fluxes derived from the fitted Gaussian more desirable than the directly integrated ones for the basal flux determination, which might be very sensitive to the smallest fluxes, see Chapter 9.

We often present the obtained parameters of a group of lines, e.g. the excess flux in the Ca II H- & K-lines. In these cases, the estimated flux and amplitude A have been determined individually for each line, and subsequently added together, with their errors handled according to Gaussian error propagation:

$$A_{f,\text{HK}} = A_{f,\text{H}} + A_{f,\text{K}}, \quad (3.3)$$

and similar equations for the Ca II IRT-lines, or the determined flux as parameter.

3.7 Monte-Carlo iterations

We want to know a reliable error for the excess flux F_{Exc} . To recapitulate, we have used two spectra with known errors, the value used for R' (Eq. (3.2)), which has an error attached to it (we do not know the exact resolution of the spectra to full accuracy), as well as $v \sin i$ with some degree of uncertainty. The latter is often quoted with no error given in the literature, so we often need to

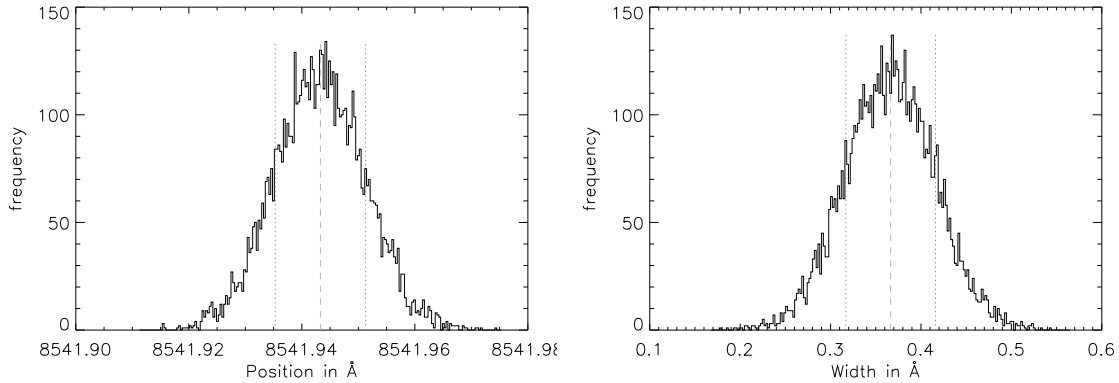


Figure 3.9: **Obtaining the error from the distribution of obtained parameters.** This plot shows the distribution of the position (left) and width (right) from fitting a Gaussian to the excess obtained for the case of the second Ca II IRT line of one observation of HD 152391, which is shown in Fig. 3.7 (bottom left). The distributions appear to be Gaussian. The dashed line corresponds to the best obtained value, with the dotted lines marking the region encompassing 68% of all points, which marks the 1σ -region.

assume an error (we have used 10% in these cases). All these uncertainties are taken into account, as well as subsequent ones from the following steps. For example, after normalizing the spectrum, the error on this normalized spectrum is increased, as the normalization can not be done perfectly. The errors on R' and $v \sin i$ are not handled in an analytical approach, because their errors would be strongly correlated. We use a Monte-Carlo approach to still get a reliable estimate: For a number of iterations N the user may chose (we use $N = 150$), the degradation and rotational broadening-step is performed with a randomly chosen value for R' and $v \sin i$, chosen from within their errors. After each step j , the spectra are subtracted from each other and the excess parameters are obtained. From the errors on the spectra, which we handle by Gaussian error propagation, we find a Gaussian distribution at each step for all parameters $F_{\text{Exc},j}, A_{f,j}, \dots$. We then add a number m (we use $m = 250$) of values for each parameter following that distribution to a list. Therefore, we end up with $N \cdot m$ values in that list for each parameter determined. The distribution these parameters make up allows us to estimate the error. This is done by finding the range covering 68% of all determined points, from which we subsequently estimate a 1σ -error. In most cases, this is indeed valid, because the distribution obtained is Gaussian in shape. Figure 3.9 shows examples for the obtained distributions. However, for some parameters – most notably the fitted width – the obtained distributions are not always Gaussian, which usually indicate unusual behavior. Figure 3.10 shows an example. As the excess is not of Gaussian shape (Fig. 3.8, bottom panel), the Gaussian fit performed resulted in a poor match. For some choices of $v \sin i$ and R' that were sampled during the Monte-Carlo iterations, the excess distribution subsequently differed so strongly from the Gaussian shape that extreme values for the width were necessary. This is mirrored in the histograms (Figure 3.10). Finally, since we limit the range of possible values, for some very noisy spectra, the resulting histograms of fitted parameters are Gaussians with the wings cut at the limits for the fitted parameters. This resulting structure is not a Gaussian either, and while the returned σ may be correct in the sense of 68% of values falling in that range (depending on where that cutoff happened), a smaller value $\Delta x < 2\sigma$ may then be required to find 95% of all values to fall in that range (or a smaller value $\Delta x < 3\sigma$ for 98% of all values, and so on). Therefore, the error given could be interpreted as overestimated, however, it still gives a valid estimation of the *quality* of the obtained value.

This procedure, and this routine, as outlined in this chapter, forms the basis for the following chapters. All measured parameters have been obtained using this procedure. It has been tested

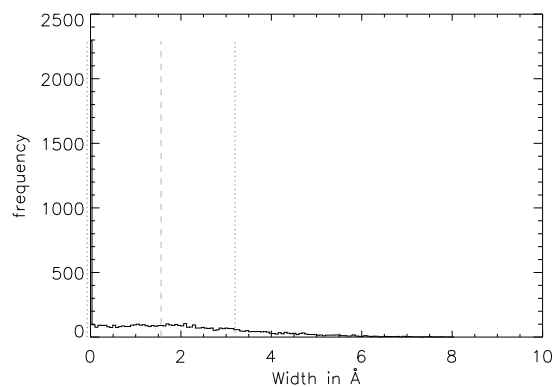


Figure 3.10: **Non-Gaussian distribution of fitted parameter values.** Same as Fig. 3.9, but for the excess determined in the $H\alpha$ -line, shown in Fig. 3.8. The distribution is clearly not Gaussian, which mirrors the fact that the determined excess also did not appear to be Gaussian in shape. A Gaussian was therefore a poor choice for fitting.

extensively, and provides a variety of optional input and keywords to be adaptable for different circumstances and available input. More information regarding the IDL implementation can be found in the Appendix (Sect. A.1).

Chapter 4

Comparing Active Stars to Inactive Stars

With the method described in Chapter 3, we are now ready to determine the excess flux F_{Exc} , and to analyze its suitability as an activity indicator across various spectral types. In this chapter, we compare 2274 spectra of 82 F, G and K main-sequence stars to a spectrum of one of 28 inactive stars. All these spectra have been observed by TIGRE (see Sect. 2.5), therefore, no systematic errors from the use of spectra observed by different instruments are added. We describe the approach of determining which object to compare to and how the flux is determined. We then give relations for the flux in the Ca II IRT lines for the inactive stars, which allows to easily calculate the integrated excess flux F_{Exc} for future spectra, without using the method described in Chapter 3. We then analyze the resulting correlations of the excess fluxes in the different lines. Finally, we briefly analyze the parameters of the Gaussians fitted to the excess flux distributions. A large part of this chapter has previously been published in Martin et al. [2017].

4.1 Rationale

The flux in the center of the spectral lines we are analyzing in this work is composed of several components. For an active star, the flux in the center consists of a photospheric and a chromospheric component. However, the latter is made up of two more components, so that we find for the total observed flux, analogous to the flux in the definition of R_{HK}^+ (Eq. (2.6)):

$$F = F_{\text{phot}} + F_{\text{chrom,basal}} + F_{\text{chrom,act}}, \quad (4.1)$$

where F_{phot} is defined by the stellar parameters and could for example be obtained from analyzing models, and $F_{\text{chrom,act}}$ is the flux in which we are mostly interested in, as it directly relates to stellar activity. When comparing this measured flux to a hypothetical flux that is made up of only the photospheric and basal contribution, the difference will be exactly the flux $F_{\text{chrom,act}}$. Such spectra are provided in the form of very inactive stars to good approximation, as the level of $F_{\text{chrom,act}}$ they show is negligible.

4.2 Stellar parameters of stars observed by TIGRE

As outlined above, we require knowledge of certain stellar parameters of the stars we are analyzing and of the comparison stars. The values for these parameters were mostly taken from the PASTEL catalog [Soubiran et al., 2010], which includes the majority of our stars in their catalog. Missing values were adopted from other sources. Tables B.1 and Table B.2 in the Appendix show the parameters we have used, as well as the corresponding sources. They are already separated into two groups, called “active stars” and “comparison stars”, according to the threshold defined in the next

section. In this work, we do not differentiate between $[M/H]$ and $[Fe/H]$, as those values differ less than the typical error for the main sequence stars under consideration.

Performing the comparison with a poor choice of comparison star will yield incorrect excess flux results. Incorrect stellar parameters could result in such a poor choice. For this reason, we estimate the error from incorrect stellar parameters. It has been found before that for the Ca II IRT-lines, the most significant parameters are T_{eff} and $[M/H]$ [Andretta et al., 2005]. This mirrors the results of our own test, which we present in a later chapter (Chapter 5, Sec. 5.3.1). In Soubiran et al. [2010], the authors give typical discrepancies of catalog values for stars featuring more than one literature value as 1.3% and 0.08 dex, respectively. Using PHOENIX models (see Chapter 5), we can estimate the error in the flux from this discrepancy. Comparing these models shows that a $\approx 2\%$ difference in T_{eff} can be neglected. Furthermore, if we incorrectly use a metallicity that deviates by 0.25 dex from the real value, we can evaluate the resulting error in the flux. To do so, we compare the integrated flux from a PHOENIX model with $T_{\text{eff}} = 5700\text{ K}$, $\log g = 4.40$ and $[M/H] = 0.0$ to one with $[M/H] = 0.25$ (and the same value for the other parameters). The difference in the integrated flux is less than 3%. We therefore conclude that incorrect stellar parameters from the catalog do not strongly affect our results. Additionally, those errors would be statistically distributed around the real values, increasing the scatter, and decreasing the correlation, but not significantly our conclusions.

With this set of stellar parameters, we can pick from the available TIGRE observations those stars that are F, G or K main-sequence stars. As already mentioned, TIGRE spectra are not flux-calibrated. To obtain an excess flux in $\text{ergs}^{-1}\text{ cm}^{-2}$, we must find the correct scale of the continuum level. In this chapter, we use the relation of Hall [1996], where the authors give photospheric surface flux values at the position of a number of spectral lines, for different sets of $B - V$. We interpolate these relations in $B - V$ for each star to find the right value.

4.3 Defining the “inactive” state

First, we need to divide the stars with spectra available into two groups: those stars that are “active” and those that are “inactive”. In reality, this is not a binary switch, but rather there is a continuous level of activity, which forces us to set a threshold value, as described below. After performing this division, every spectrum of all active stars is then compared to a spectrum of an inactive star. Additionally, that comparison star must feature low rotational broadening in order to get a reliable distribution of the excess. Here, we set somewhat arbitrarily the limit at $v \sin i \leq 5\text{ km s}^{-1}$. We can estimate the corresponding broadening to be

$$\frac{\Delta\lambda}{\lambda} = \frac{\Delta v}{c} \Rightarrow \Delta\lambda \approx 0.14\text{ \AA} \quad (4.2)$$

for $\Delta v = 5\text{ km s}^{-1}$. Comparing this to $\Delta\lambda$ from the finite resolution of TIGRE spectra, which is around 0.425 \AA at the position of the Ca II IRT-lines, it becomes clear that those stars rotate slowly enough to not influence our determined excess fluxes.

Several indices exist that give an estimate of the activity level, such as S_{MWO} or R'_{HK} , which have been defined in Sec. 2.2. Of these two, S_{MWO} is much easier to calculate, and we have performed this calculation for every spectrum. The easiest option is therefore to define a threshold value for S_{MWO} to separate our sample into “active” and “inactive”. We need to find a sensible threshold value which is high enough so that a sufficient number of stars are available for comparison, but low enough for those to not show any significant levels of activity. Our first test used a threshold value of $S_{\text{MWO}} = 0.17$, which is roughly the activity level of the Sun. But this turned out to include too few comparison objects, so that we slightly increased it to $S_{\text{MWO}} = 0.18$. This allowed us to perform the comparison and determination of F_{Exc} . However, S_{MWO} shows a strong dependence on $B - V$ or equivalently T_{eff} (as we will later see in Fig. 8.9). This is not the case for R'_{HK} , as this index aims to remove the photospheric contributions in the Ca II H- & K-lines, and subsequently normalizes the flux by σT_{eff}^4 . As we have mentioned before, this index can be estimated from a measured value of S_{MWO} , and the star’s $B - V$ -value. Henry et al. [1996] defined a threshold of

Table 4.1: **Overview of the data used in this chapter, categorized by spectral type.** This table was originally published in Martin et al. [2017].

Type	# Obj.	# Obs.	SNR	Exp. time [s]
			min/med/max	min/med/max
F	9	265	36.1 / 60.7 / 161.3	120 / 360 / 2578
G	46	1419	20.1 / 59.2 / 114.0	60 / 622 / 4767
K	27	590	20.4 / 64.3 / 114.8	60 / 799 / 4846
Total	82	2274	20.1 / 60.4 / 161.3	60 / 610 / 4846

“active” and “inactive” from this index at $\log R'_{\text{HK}} \geq -4.75$. The switch to this index increases the amount of available comparison objects, especially at higher values for $B - V$, which improves the comparison and determined excess for the later types. The results for found correlations, as well as conversion relations which we attempt to find in a later chapter, do not depend strongly on this criterion.

4.4 Finding a comparison star

When comparing spectra of active stars to the corresponding spectrum of an inactive one, we must ensure that the comparison star features values for F_{phot} and $F_{\text{chrom,basal}}$ that coincide as close as possible with the active star under consideration. As these fluxes depend on the stellar parameters, we therefore must pick the comparison star with the least deviation in stellar parameters and therefore the line profile. As we have mentioned before, the main influences on the line profile for the Ca II IRT are T_{eff} and $[M/H]$, with no large dependence on $\log g$. Since the comparison stars will also determine the flux scale in our method, which depends mainly on T_{eff} , we give that value the highest priority, followed by $[M/H]$. Here we mention again the condition of $v \sin i \leq 5 \text{ km s}^{-1}$, which ensures that the comparison spectrum is not too strongly broadened in the comparison process (see Sect. 3.4). We have tried several different sets of weights for these parameters, and have finally used the values given below. Using different weights here – as long as the change is not dramatic¹ – does not affect the results much. For each inactive star, a score p is calculated by multiplying the absolute deviation in stellar parameters $\Delta(B - V)$, $\Delta[M/H]$, $\Delta \log g$, defining the strength of their influence by setting a power to those parameters. We also add the typical error on these parameters as a minimum value:

$$p = (0.05 + \Delta(B - V))^{2.25} (R'_{\text{HK}}) (0.1 + \Delta[M/H]) \cdot (0.2 + \Delta \log g)^{0.25} (1 + (v \sin i)_{\text{inactive}})^{0.2}. \quad (4.3)$$

We have also tried adding parameters to this score calculation, such as the amount of observations, following the rationale that a low number of spectra increases the chance for faulty spectra, bad SNR or cosmics. However, in practice this did not improve the results, as there are stars available with few observations that show a very high quality in the spectrum. The low influence of $v \sin i$ ensures that this parameter works as “tie-breaker” only, and does not dominate the picking process. The star that features the lowest value for p is then chosen as comparison star.

After this star has been picked, the best spectrum of that star – defined as the spectrum with the highest SNR and R'_{HK} below the threshold – is used as comparison spectrum for all spectra of the star under consideration, after correction of telluric line contamination (Sect. 2.7). Table B.3 in the appendix shows which star was compared to which object. In this way, we obtain a value F_{Exc} for the Ca II IRT-lines, Ca II H- & K-lines and the H α -line, for every observation with $\text{SNR} \geq 20$, for a total of 2274 observations of 82 stars. Table 4.1 gives an overview of the distribution of the objects, and their exposure time.

¹e.g. changing the sign of a weight, or increasing it by orders of magnitude.

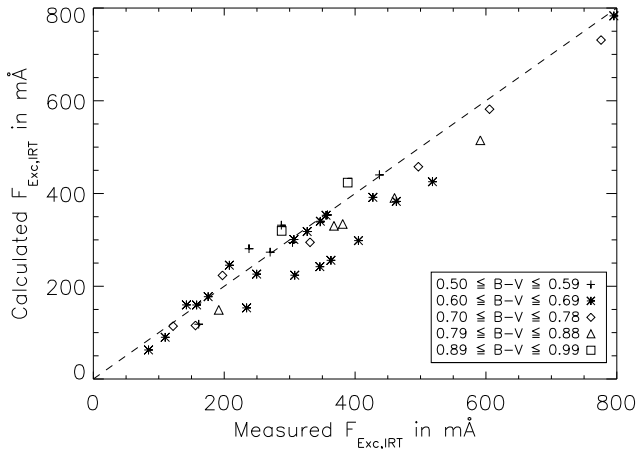


Figure 4.1: **Comparison of the excess flux determined from subtracting the resulting value from a fitting relation from Table 4.2 to the measured line flux (ordinate) to the excess flux in continuum units determined by using the method described in Chapter 3 (abscissa).** Plotted here are the results for the 42 most active stars with observations displaying a level of activity exceeding $\log R'_{\text{HK}} = -4.52$. The dashed line corresponds to the identity relation. This plot originally appeared in Martin et al. [2017].

4.5 Empirical relations for fluxes of stars in inactive state

Instead of performing the steps outlined in Chapter 3, the excess flux can in theory be more easily determined by finding the difference of the integrated flux in the line center for both the active and inactive star spectra. Our set of inactive comparison stars can be used for such an analysis. To do so, we find an empirical relation $F_{\text{center}}(v \sin i)$, describing the flux in the line center for this inactive comparison star, that was artificially rotationally broadened with a value of $v \sin i$. Here, we exemplarily perform this and show the results for the sum of the flux in the three Ca II IRT-lines. In the appendix, we show the corresponding results for the H α -line and the Ca II H- & K-lines.

We define the line center as the 1 Å-wide region in the line center (2 Å for Ca II H- & K-lines, see appendix). Then, for each of our comparison spectra, we perform the normalization according to Sect. 3.2, convert the scale to $\text{ergs}^{-1} \text{cm}^{-2}$, using the relation from Hall [1996] and integrate the resulting flux in the line center, after performing the rotational broadening according to Sect. 3.4 for a variety of selected values of $v \sin i$. We use 0 km s^{-1} (no broadening), 5 km s^{-1} , 15 km s^{-1} , 20 km s^{-1} , 30 km s^{-1} , 40 km s^{-1} and 50 km s^{-1} . This leaves us with seven values of $F_{\text{inact,center}}(v \sin i)$ for this particular inactive star. For each of those, we then fit a second-order polynomial to these values, which describes the shape of the function well.

Busà et al. [2007] introduced a new activity indicator ΔW_{IRT} , which is similar to our excess flux, except that it has not been converted to $\text{ergs}^{-1} \text{cm}^{-2}$, using the continuum flux scale. Therefore this index is given in units of Å. In order to convert to this index, we perform these steps also with the normalized spectrum without converting to the $\text{ergs}^{-1} \text{cm}^{-2} \text{Å}^{-1}$ scale. The results are given in Table 4.2. Using these relations, a value for the excess flux F_{Exc} in the spectrum of a star can now be obtained by integrating the flux in that spectrum to estimate $F_{\text{act,center}}$, and subtracting the calculated value $F_{\text{inact,center}}$. This value can be found from the relation given for a suitable comparison star in Table 4.2, by plugging in the star's rotational velocity. The resulting flux is the excess flux F_{Exc} . If the active star's spectrum was normalized, the relation for ΔW_{IRT} must be used, to obtain a value ΔW_{IRT} . It can then, afterwards, be converted to F_{Exc} using the relations given in Hall [1996]. Finding the excess flux using this intermediate step of first finding ΔW_{IRT} is preferable, as both stars likely feature slightly different values of $B - V$, which is reflected in their scale for the flux. We can compare the results obtained from this approach to the integrated excess flux, as determined by the method described in Chapter 3. The results from this comparison are shown in Fig. 4.1, for the 42 most active stars with $R'_{\text{HK}} \geq 3 \cdot 10^{-5}$. The results agree clearly, but there is an offset of about $\approx 20 \text{ mÅ}$, as determined by the median of the offset. This corresponds to an error of about 5%. It should be noted however that the real measured quantity is not the difference in ΔW_{IRT} , but rather the integrated counts in the normalized spectrum, which is of the order of $\approx 1.5 \text{ Å}$. The 20 mÅ therefore correspond to a relative measurement error of only about 1.3%. The calculated value of ΔW_{IRT} can be improved by subtracting the aforementioned 20 mÅ .

Table 4.2: **Relations to estimate the summed up flux in an 1 Å-window in the center of all three Ca II IRT lines for inactive objects.** v_{rot} must be entered in units of km s^{-1} . Values for $B - V$, $\log g$ and $[\text{Fe}/\text{H}]$ are taken from Soubiran et al. [2010]. This table was originally published in Martin et al. [2017].

Star	$B - V$	$\log g$	$[\text{Fe}/\text{H}]$	$\log R'_{\text{HK}}$	Estimated total flux in 1 Å-bandpasses in all Ca II IRT lines	
					in $10^6 \text{ ergs}^{-1} \text{ cm}^{-2}$	W_{IRT} from normalized spectra in Å
HD 739	0.40	4.27	-0.09	-4.91	$8.645 + 0.026 \cdot v_{\text{rot}} + 6.106 \cdot 10^{-4} v_{\text{rot}}^2$	$1.371 + 0.004 \cdot v_{\text{rot}} + 0.972 \cdot 10^{-4} v_{\text{rot}}^2$
HD 159332	0.45	3.85	-0.23	-4.99	$7.326 + 0.024 \cdot v_{\text{rot}} + 5.770 \cdot 10^{-4} v_{\text{rot}}^2$	$1.250 + 0.004 \cdot v_{\text{rot}} + 0.987 \cdot 10^{-4} v_{\text{rot}}^2$
HD 216385	0.48	3.95	-0.29	-4.98	$7.318 + 0.025 \cdot v_{\text{rot}} + 5.791 \cdot 10^{-4} v_{\text{rot}}^2$	$1.309 + 0.005 \cdot v_{\text{rot}} + 1.039 \cdot 10^{-4} v_{\text{rot}}^2$
HD 45067	0.53	4.01	-0.09	-4.90	$6.323 + 0.025 \cdot v_{\text{rot}} + 4.679 \cdot 10^{-4} v_{\text{rot}}^2$	$1.224 + 0.005 \cdot v_{\text{rot}} + 0.909 \cdot 10^{-4} v_{\text{rot}}^2$
HD 187691	0.56	4.26	+0.10	-4.89	$5.862 + 0.022 \cdot v_{\text{rot}} + 4.432 \cdot 10^{-4} v_{\text{rot}}^2$	$1.190 + 0.004 \cdot v_{\text{rot}} + 0.903 \cdot 10^{-4} v_{\text{rot}}^2$
HD 100180	0.57	4.25	-0.06	-4.76	$6.134 + 0.020 \cdot v_{\text{rot}} + 4.188 \cdot 10^{-4} v_{\text{rot}}^2$	$1.265 + 0.004 \cdot v_{\text{rot}} + 0.866 \cdot 10^{-4} v_{\text{rot}}^2$
HD 124570	0.58	4.05	+0.08	-5.05	$5.504 + 0.023 \cdot v_{\text{rot}} + 4.536 \cdot 10^{-4} v_{\text{rot}}^2$	$1.153 + 0.005 \cdot v_{\text{rot}} + 0.953 \cdot 10^{-4} v_{\text{rot}}^2$
HD 19373	0.59	4.21	+0.08	-4.84	$5.698 + 0.021 \cdot v_{\text{rot}} + 4.367 \cdot 10^{-4} v_{\text{rot}}^2$	$1.213 + 0.004 \cdot v_{\text{rot}} + 0.931 \cdot 10^{-4} v_{\text{rot}}^2$
HD 168009	0.60	4.23	-0.01	-4.77	$5.711 + 0.019 \cdot v_{\text{rot}} + 4.289 \cdot 10^{-4} v_{\text{rot}}^2$	$1.242 + 0.004 \cdot v_{\text{rot}} + 0.935 \cdot 10^{-4} v_{\text{rot}}^2$
HD 10307	0.62	4.32	+0.03	-4.84	$5.635 + 0.019 \cdot v_{\text{rot}} + 3.969 \cdot 10^{-4} v_{\text{rot}}^2$	$1.257 + 0.004 \cdot v_{\text{rot}} + 0.888 \cdot 10^{-4} v_{\text{rot}}^2$
HD 157214	0.62	4.31	-0.40	-4.80	$5.922 + 0.018 \cdot v_{\text{rot}} + 3.963 \cdot 10^{-4} v_{\text{rot}}^2$	$1.321 + 0.004 \cdot v_{\text{rot}} + 0.886 \cdot 10^{-4} v_{\text{rot}}^2$
HD 34411	0.62	4.22	+0.08	-4.85	$5.458 + 0.021 \cdot v_{\text{rot}} + 3.975 \cdot 10^{-4} v_{\text{rot}}^2$	$1.218 + 0.005 \cdot v_{\text{rot}} + 0.890 \cdot 10^{-4} v_{\text{rot}}^2$
HD 95128	0.62	4.30	+0.01	-4.85	$5.888 + 0.018 \cdot v_{\text{rot}} + 4.288 \cdot 10^{-4} v_{\text{rot}}^2$	$1.312 + 0.004 \cdot v_{\text{rot}} + 0.957 \cdot 10^{-4} v_{\text{rot}}^2$
HD 38858	0.64	4.48	-0.22	-4.79	$5.798 + 0.017 \cdot v_{\text{rot}} + 3.754 \cdot 10^{-4} v_{\text{rot}}^2$	$1.335 + 0.004 \cdot v_{\text{rot}} + 0.868 \cdot 10^{-4} v_{\text{rot}}^2$
HD 146233	0.65	4.42	+0.03	-4.75	$5.380 + 0.018 \cdot v_{\text{rot}} + 3.774 \cdot 10^{-4} v_{\text{rot}}^2$	$1.258 + 0.004 \cdot v_{\text{rot}} + 0.885 \cdot 10^{-4} v_{\text{rot}}^2$
HD 186427	0.65	4.32	+0.07	-4.80	$5.166 + 0.019 \cdot v_{\text{rot}} + 3.785 \cdot 10^{-4} v_{\text{rot}}^2$	$1.208 + 0.004 \cdot v_{\text{rot}} + 0.888 \cdot 10^{-4} v_{\text{rot}}^2$
HD 12846	0.66	4.38	-0.26	-4.78	$5.875 + 0.015 \cdot v_{\text{rot}} + 3.984 \cdot 10^{-4} v_{\text{rot}}^2$	$1.391 + 0.004 \cdot v_{\text{rot}} + 0.946 \cdot 10^{-4} v_{\text{rot}}^2$
HD 43587	0.67	4.29	-0.04	-4.80	$5.528 + 0.018 \cdot v_{\text{rot}} + 3.879 \cdot 10^{-4} v_{\text{rot}}^2$	$1.327 + 0.004 \cdot v_{\text{rot}} + 0.933 \cdot 10^{-4} v_{\text{rot}}^2$
HD 115617	0.70	4.39	-0.01	-4.80	$4.934 + 0.017 \cdot v_{\text{rot}} + 3.450 \cdot 10^{-4} v_{\text{rot}}^2$	$1.248 + 0.004 \cdot v_{\text{rot}} + 0.874 \cdot 10^{-4} v_{\text{rot}}^2$
HD 178428	0.70	4.25	+0.14	-4.88	$4.659 + 0.018 \cdot v_{\text{rot}} + 3.663 \cdot 10^{-4} v_{\text{rot}}^2$	$1.178 + 0.005 \cdot v_{\text{rot}} + 0.929 \cdot 10^{-4} v_{\text{rot}}^2$
HD 3795	0.70	3.91	-0.63	-4.83	$5.331 + 0.015 \cdot v_{\text{rot}} + 4.096 \cdot 10^{-4} v_{\text{rot}}^2$	$1.347 + 0.004 \cdot v_{\text{rot}} + 1.037 \cdot 10^{-4} v_{\text{rot}}^2$
HD 117176	0.71	3.97	-0.06	-4.90	$4.584 + 0.018 \cdot v_{\text{rot}} + 3.628 \cdot 10^{-4} v_{\text{rot}}^2$	$1.177 + 0.005 \cdot v_{\text{rot}} + 0.934 \cdot 10^{-4} v_{\text{rot}}^2$
HD 10700	0.72	4.48	-0.50	-4.75	$5.163 + 0.014 \cdot v_{\text{rot}} + 3.325 \cdot 10^{-4} v_{\text{rot}}^2$	$1.347 + 0.004 \cdot v_{\text{rot}} + 0.869 \cdot 10^{-4} v_{\text{rot}}^2$
HD 26965	0.85	4.51	-0.27	-4.89	$3.944 + 0.012 \cdot v_{\text{rot}} + 2.855 \cdot 10^{-4} v_{\text{rot}}^2$	$1.265 + 0.004 \cdot v_{\text{rot}} + 0.919 \cdot 10^{-4} v_{\text{rot}}^2$
HD 75732	0.87	4.41	+0.28	-4.84	$3.372 + 0.014 \cdot v_{\text{rot}} + 2.740 \cdot 10^{-4} v_{\text{rot}}^2$	$1.110 + 0.005 \cdot v_{\text{rot}} + 0.905 \cdot 10^{-4} v_{\text{rot}}^2$
HD 145675	0.90	4.45	+0.41	-4.80	$3.150 + 0.013 \cdot v_{\text{rot}} + 2.729 \cdot 10^{-4} v_{\text{rot}}^2$	$1.087 + 0.005 \cdot v_{\text{rot}} + 0.944 \cdot 10^{-4} v_{\text{rot}}^2$

It follows that this method of finding a value of F_{Exc} or ΔW_{IRT} is a possible alternative to the more complicated and reliable approach chosen here.

Since our criteria for the selection of the comparison star are mainly based on $B - V$ and $[\text{M}/\text{H}]$, we can include those two parameters into a fit. A three-dimensional, second-order polynomial describing the flux in the Ca II IRT-lines in the inactive state now has the form:

$$\begin{aligned} F_{\text{inact}}(B - V, [\text{M}/\text{H}], v \sin i) = & a_{000} + a_{100}(B - V) + a_{010}[\text{M}/\text{H}] + & (4.4) \\ & a_{001}v \sin i + \\ & a_{200}(B - V)^2 + a_{020}[\text{M}/\text{H}]^2 + a_{002}v \sin i^2 + \\ & a_{110}(B - V)[\text{M}/\text{H}] + a_{101}(B - V)v \sin i + \\ & a_{011}[\text{M}/\text{H}]v \sin i, \end{aligned}$$

with ten coefficients a_{ijk} . Fitting all the values of F_{inact} we have measured at once using MPFit [Markwardt, 2009] yields:

$$\begin{aligned} F_{\text{inact}}(B - V, [\text{M}/\text{H}], v \sin i) = & 14.983 - & (4.5) \\ & 21.253(B - V) - 2.237[\text{M}/\text{H}] + \\ & 0.061v \sin i + 9.746(B - V)^2 - \\ & 0.841[\text{M}/\text{H}]^2 + 4.08 \cdot 10^{-5}v \sin i^2 + \\ & 1.379(B - V)[\text{M}/\text{H}] - 0.065(B - V)v \sin i + \\ & 3.43 \cdot 10^{-3}[\text{M}/\text{H}]v \sin i, \end{aligned}$$

with the resulting F_{inact} in $10^6 \text{erg s}^{-1} \text{cm}^{-2}$. The values for $v \sin i$ must be entered in km s^{-1} . Performing such a fit, but neglecting the conversion to $\text{erg s}^{-1} \text{cm}^{-2} \text{\AA}^{-1}$ via the continuum relations yields:

$$\begin{aligned} W_{\text{inact,IRT}}(B - V, [\text{M}/\text{H}], v \sin i) = & 1.248 + & (4.6) \\ & 0.046(B - V) - 0.417[\text{M}/\text{H}] + \\ & 5.02 \cdot 10^{-3}v \sin i - 0.084(B - V)^2 - \\ & 0.197[\text{M}/\text{H}]^2 + 9.249 \cdot 10^{-5}v \sin i^2 + \\ & 0.158(B - V)[\text{M}/\text{H}] - 0.001(B - V)v \sin i + \\ & 7.44 \cdot 10^{-4}[\text{M}/\text{H}]v \sin i, \end{aligned}$$

with the result in \AA . Similar relations for the Ca II H- & K-lines and the H α -line are given in the appendix.

Equations (4.6) and (4.7) fit the measured values of F_{inact} very well. Especially if no single star in Table 4.2 is a particular good fit, these relations are a good choice to calculate the necessary inactive line flux to compare to.

4.6 Outliers and objects not suitable for our method

Not all stars that have observations available can be used for our method. A number of observations had to be removed because either the automatic approach described in Chapter 3 failed, due to an error in the stellar parameters, or because of an incorrect assumption. For example, we had to remove observations from HD 114378, as this object has been found to be a binary star [Malkov et al., 2012]. Although it is in principle possible to perform this method for a binary star², we have not done this here. We have therefore removed binary stars from the sample, except those for which

²To do so, we must compare the binary star's spectra to a binary, inactive template, which has been created specifically for the binary star at the observation time. Due to the orbit of the two stars, the shifts in the two component's individual spectral contributions depend on time, strongly affecting the spectrum. We will go into detail on how this can be achieved and show examples in Chapter 11 (Sect. 11.2.1).

the effects from the secondary star are not significantly affecting the spectrum. Such a spectrum without the contribution of a secondary component would only show a time-dependent wavelength shift, which is automatically corrected by the algorithm via cross-correlation, as described previously in Chapter 3, Sect. 3.3.

The determined excess fluxes from HD 6920 do not follow the correlations between the excess fluxes clearly outlined by the rest of the sample (see e.g. Fig. 4.5). A possible reason for this is that our assumption of this object as a main-sequence F8 star is incorrect. Several authors have classified this star as a subgiant [Abt, 1986, Fuhrmann, 1998, Gray et al., 2001, Anderson and Francis, 2012]. Here, again, we would require a different template star to compare the spectra to. Our result of this star not following expected main-sequence star behavior strongly suggests that the subgiant-classification is correct. This star has been removed from the sample as well.

Visual inspection of the spectra of other stars, that do not fall in line with the correlation shown by the large majority of the sample, shows that the SNR in the line center is simply too low. As we have described in Sect. 2.6.3, the SNR given can be an inaccurate description of the spectrum’s quality in the region we are interested in. This is especially troublesome if combined with a large rotational velocity, as this smears out the already small excess flux over a large amount of highly noisy data points. At this point, no reliable determination of the excess flux distribution can be performed. There is no general, physical reason for these stars that suggests that their excess flux could not be determined from this method, but spectra with higher SNR are required. For this work, we remove these stars from the sample.

4.7 Resulting excess fluxes and their correlations

We have now obtained integrated excess fluxes from 2274 spectra of 82 stars. Notably, in some cases, the determined excess flux is negative, of which we show an example in Fig. 4.2. This happens only for the least active stars included in the sample, that barely pass the “active” threshold. In those cases, the actual excess can be so low that due to noise, a negative value is obtained. Additionally, this large noise level also affects the normalization, the normalization correction, and the photospheric correction described in Chapter 3. Obtaining a negative excess is usually only encountered for faster rotators, as their excess flux is spread out across a larger region. Therefore, some flux is “shifted” out of the bandpass we use for integrating. However, most stars that are fast rotators are somewhat active, so this occurs only for very few stars.

The excess distribution of some of the most active stars is not entirely covered by the 1 Å-wide window chosen for the Ca II IRT-lines, e.g. for HD 152391. This unfortunately leads to an underestimation of the value, though only by a few percent, comparable to the errors on these spectra. In this chapter, we have chosen not to automatically determine the integration region the excess falls in, instead choosing a constant value. We have done so as tests have shown that due to the high noise level on some of the spectra, and a subsequent noisy excess, a poor region was chosen in those cases. Similarly, picking a larger region to integrate in increases the noise on the total sample, as for the majority of objects, only noise is left outside the line center after subtraction of the comparison spectrum.

As a first step, we compare the Ca II IRT-lines and the H α -line to the Ca II H- & K-lines. The latter have been well-established as an activity indicator, so a good correlation between the excess fluxes suggests that the line compared to the Ca II H- & K-lines is a good activity indicator as well. We show the Spearman correlation coefficient ρ here, rather than the Pearson-correlation coefficient ρ_{Pearson} ³. ρ_{Pearson} of two sets x and y is calculated as the covariance of x and y , divided by the product of their standard deviation [Pearson, 1895]:

$$\rho_{\text{Pearson}}(x, y) = \frac{\frac{1}{n} \sum (x_i - \bar{x})(y_i - \bar{y})}{\sigma_x \sigma_y}. \quad (4.7)$$

³In some sources, the Pearson-correlation coefficient is given as p or r .

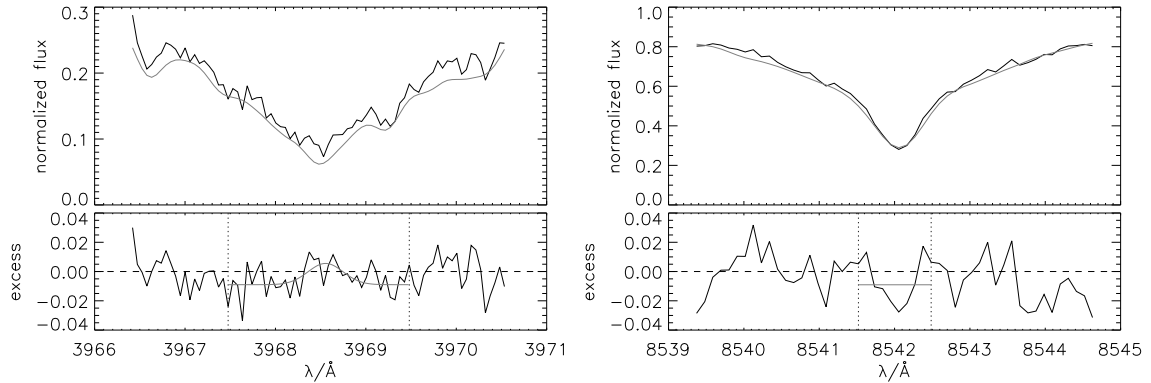


Figure 4.2: **Example of a negative excess flux obtained for Ca II H (left) and one of the Ca II IRT-lines (right).** This plot shows the obtained excess distribution for HD 32147, as it was observed by TIGRE on February 20th, 2016. The top plot shows the observed spectrum (black) compared to the template spectrum (gray), that was broadened to the rotational velocity of HD 32147. The dotted vertical lines in the bottom plot show the bandpass used for integrating, the gray line shows the best fit to the excess, which is also not reliable in this case.

The covariance (nominator) becomes large if large deviation from the average values occur for x and y simultaneously (for the same value of i), and the sign of this deviation matches. If the direction of the deviations is always inverted, the absolute value of ρ_{Pearson} will be large, but the sign will be negative. By nature of how ρ_{Pearson} is defined, it estimates how well two parameters are *linearly* correlated. Consider the example of $y = x^3$, with $x \in [-1, 1]$. Then, $\bar{x} = \bar{y} = 0$, and data points with x close to 0 will deviate less strongly from the average than those with $|x| \approx 1$, contributing less to the covariance (the nominator in Eq. (4.7)). As these deviations are normalized by the standard deviation, the overall value for ρ_{Pearson} is then lowered. In our example, $\rho_{\text{Pearson}} \approx 0.9$, even though the values are perfectly correlated in the sense that a higher value of x implies a higher value of y ! However, we are interested whether or not two parameters are well correlated, regardless of the underlying functional relation between the two. That is, we want to know if the two parameters have a monotonic relation or not. This is why we use the Spearman correlation coefficient ρ . When calculating ρ , the data points are first reordered into a new set x_R and y_R according to their rank in both dimensions x and y (here, x and y represent the integrated excess flux in a certain line). The rank is the index the data point would occupy in an ordered list. Then, $\rho(x, y) = \rho_{\text{Pearson}}(x_R, y_R)$. Due to the reordering, the actual appearance of the relation between x and y is disregarded, and any monotonic relation shows a linear relation in the ranks. To determine an error on the value of ρ , we perform 10 000 Monte-Carlo iterations, vary the obtained excess flux values within their errors, obtain the value for ρ for this iteration, and then determine ρ and σ_ρ from the resulting distribution, just like we have described for the error determination of the fitted parameters in Sect. 3.7.

We show the correlations between all individual lines, as well as the sum of the Ca II IRT-lines and Ca II H- & K-lines in Table 4.3. Generally, the correlations are very high, with the calcium lines showing values of $\rho \geq 0.9$, and the other lines close behind. Our results therefore support the conclusion that these lines can be used as activity indicators, at least for F, G and K main-sequence stars. We will see in a later chapter (Chapter 10) that the lines are however not always perfectly correlated, due to differences in the location or process of the chromospheric excess formation. Still, it is apparent that either line can be used to estimate the flux in another. Relations to do so will be given in a later chapter (Chapter 8).

As mentioned earlier, the correlation between the calcium lines is very high. This is expected, and mirrors results of previous studies (e.g. Andretta et al. [2005], Chmielewski [2000], Martínez-Arnáiz et al. [2011a]). The largest correlation is found, as expected, between the two Ca II H- & K-lines (Fig. 4.3). Since they show a strong excess that is much larger than the noise level even at comparatively

Table 4.3: **Correlation between the integrated excess flux of different lines.** This table shows the result from obtaining the excess flux by comparing spectra of active stars to spectra of inactive stars. “Sum” refers to the summed up flux in either both Ca II H- & K-lines, or in all three Ca II IRT-lines.

		— Ca II H & K —			— Ca II IRT —				
		$\lambda 3968$	$\lambda 3934$	Sum	$\lambda 8498$	$\lambda 8542$	$\lambda 8662$	Sum	H α
Ca II H & K	$\lambda 3968$	—	0.95	0.98	0.90	0.90	0.88	0.90	0.83
	$\lambda 3934$	0.95	—	0.99	0.90	0.91	0.89	0.91	0.81
	Sum	0.98	0.99	—	0.90	0.91	0.89	0.91	0.82
Ca II IRT	$\lambda 8498$	0.90	0.90	0.90	—	0.97	0.96	0.99	0.86
	$\lambda 8542$	0.90	0.91	0.91	0.97	—	0.97	0.99	0.84
	$\lambda 8662$	0.88	0.89	0.89	0.96	0.97	—	0.98	0.85
	Sum	0.90	0.91	0.91	0.99	0.99	0.98	—	0.85
H α		0.83	0.81	0.82	0.86	0.84	0.85	0.85	—

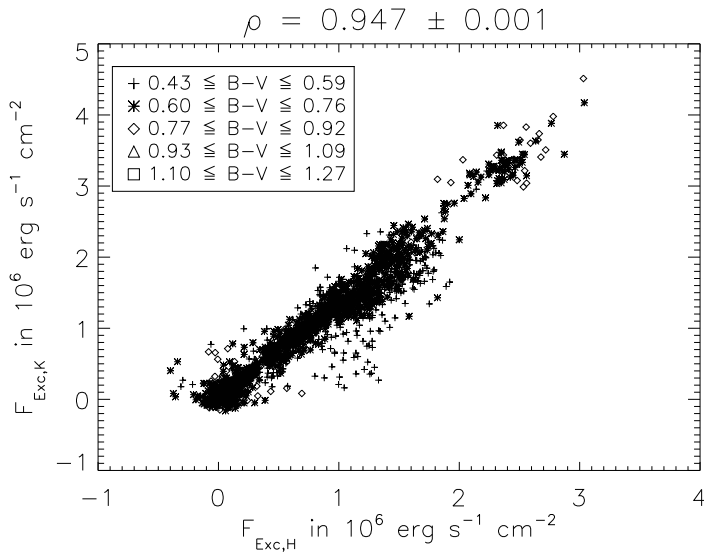


Figure 4.3: **Correlation of the determined excess flux in the Ca II H and Ca II K-lines.** This plot includes data from 2274 observations of 82 stars.

small activity levels, they manage to beat the still very strong correlation of the Ca II IRT-lines (Fig. 4.4). More interesting is the strong correlation between the two sets of calcium lines, as evidenced in Fig. 4.5. The combined fluxes from the Ca II IRT-lines and Ca II H- & K-lines show a very strong correlation of 0.91. Therefore, the Ca II IRT-lines should prove to be an excellent indicator for stellar activity. The H α -line is also well correlated, but with a lower value of $\rho \approx 0.8$ (Fig. 4.6). The relation between the H α -line and the other lines appears to be slightly “curved”. However, the noise level of the obtained excess flux is too large to conclude this, as the few data points at the highest levels of activity, which influence the visual appearance of whether or not the structure is curved the most, are not reliable enough. This might only appear by chance from the large band due to the scattering from statistical distribution of the noise. We also note that we have found almost no variation in the excess flux in the H α -line for some stars. The likely reasons are the aforementioned difficulties in obtaining the excess flux in this line.

Until now, we have always presented the integrated excess flux in $\text{erg s}^{-1} \text{cm}^{-2}$. But as we have mentioned, Busà et al. [2007] have introduced a parameter ΔW_{IRT} that is calculated similarly. They give values of ΔW_{IRT} for two stars that are featured in our sample: HD 25998 and HD 82443. For

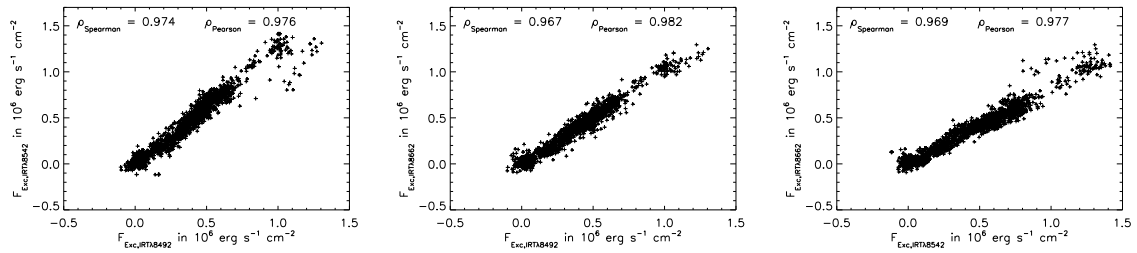


Figure 4.4: Correlation between the excess fluxes in the individual Ca II IRT-lines, obtained by comparing to inactive template star spectra. The correlation coefficients are given in the plots.

both of these objects, and all three Ca II IRT-lines, the values of ΔW_{IRT} they give are larger than ours, however, they all agree within 1σ . The difference is likely due to the fact that Busà et al. [2007] compare with models – thus, the remainder ΔW_{IRT} still includes a basal flux contribution. Additionally, we only integrate within a 1 \AA -wide bandpass, whereas Busà et al. [2007] do not give details on their integration range. Details are given in Table 4.4.

Table 4.4: Comparison of the range of our obtained values for ΔW_{IRT} as defined by Busà et al. [2007] to their values.

	ΔW_{IRT} in \AA		
	$\lambda 8498$	$\lambda 8542$	$\lambda 8662$
HD 25998			
Busà et al. [2007]	104.6 ± 18.3	133.0 ± 22.6	111.9 ± 25.2
Range found in this work	39.9 ± 13.5 — 105.1 ± 10.7	80.6 ± 9.2 — 142.9 ± 6.9	63.2 ± 10.0 — 109.5 ± 9.7
HD 82443			
Busà et al. [2007]	273.6 ± 76.1	416.3 ± 128.1	367.3 ± 151.7
Range found in this work	193.4 ± 7.7 — 241.4 ± 5.6	281.5 ± 5.8 — 342.8 ± 5.2	226.1 ± 5.3 — 273.0 ± 7.1

4.8 Fitted parameters

As mentioned in Chapter 3, we also fit Gaussians to the obtained excess distribution. We call the Amplitude of the fit A_f , the positional offset from the line center $(\Delta\lambda)_f$, and the width σ_f . To improve the fit for very noisy spectra, we perform a smoothing operation on the found excess distribution, using the IDL-procedure `GAUSS_SMOOTH`. This process folds the spectra with a Gaussian kernel, equivalently smoothing the data by replacing each data point with a weighted average of the points in the vicinity. The disadvantage is that the resulting structure will be slightly broadened, and thus less high. We try to minimize these effects by choosing the Gaussian kernel width carefully, and set it to only about 1.2 data points.

With this correction, the obtained amplitude correlates very well. Here, we show the amplitude in fraction of the continuum in the left plot of Fig. 4.7 (that is, the amplitude of the excess distribution obtained from subtracting two normalized spectra), which can be converted to $\text{erg s}^{-1} \text{cm}^{-2} \text{\AA}^{-1}$, e.g. using the relations from Hall [1996] (right plot in Fig. 4.7). Neglecting to perform this step results in a strong $B - V$ dependency, as the continuum ratio in the red and blue regions of the Ca II H- & K-lines and Ca II IRT-lines varies.

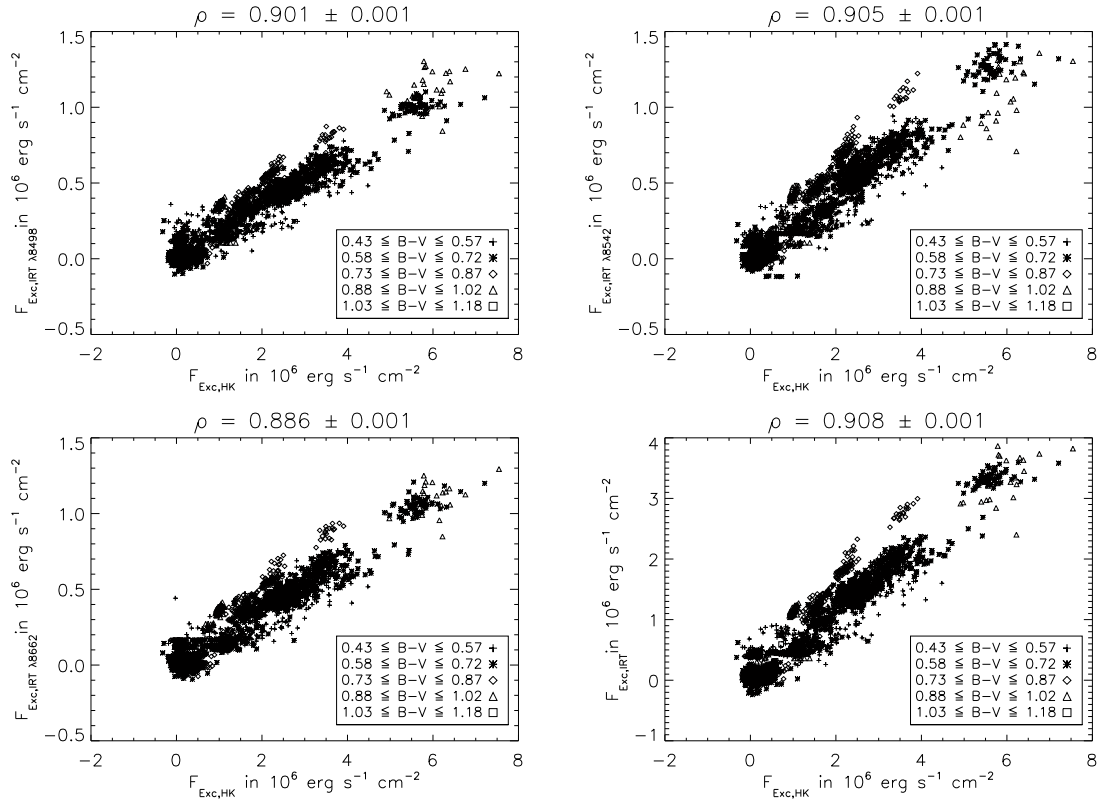


Figure 4.5: Measured chromospheric excess flux in the Ca II H- & K-lines compared with the excess flux in the individual Ca II IRT-lines, as well as the sum of all Ca II IRT-lines (bottom right). This plot includes data from 2274 observations of 82 stars, and appeared originally in Martin et al. [2017].

We have also experimented with fitting functions other than Gaussians, namely Lorentzian- or Moffat-profiles [Moffat, 1969]. However, the results are not any better or worse, likely because the resolution of TIGRE is simply not high enough to fully resolve these profiles, turning them into Gaussian profiles. All in all, A_f appears to be slightly worse as an activity indicator compared to the integrated flux, with ρ “only” reaching up to ~ 0.88 . We give the resulting correlations for A_f in Table 4.5. While the correlation becomes slightly worse between the calcium lines, it does increase between the calcium lines and the H α -line. The width shows a smaller correlation of about $\rho \approx 0.75$, but there is much stronger scatter involved. This parameter shows a small correlation of $\rho \approx 0.4$ to the star’s rotational velocity. This implies that the width fitted here is not only determined by rotational broadening, but might be affected by the actual formation of the chromospheric excess. Of course, due to the varying resolution of TIGRE spectra, some scatter is introduced that is not physical in nature. Therefore, we do not analyze this parameter any further.

The excess fitted position within the line $(\Delta\lambda)_f$ is another parameter that suffers highly from noise. However, this parameter shows a positive correlation between the Ca II H- & K-lines and Ca II IRT-lines for stars rotating faster than 20 km s^{-1} , which may imply where these excess fluxes are formed. If the values for $(\Delta\lambda)_f$, converted to km s^{-1} were identical, this would strongly suggest that these excesses were formed in the same region. However, this is not the case, as the value $(\Delta\lambda)_f$ tends to be higher for the Ca II IRT-lines. While this could occur due to a constant offset in latitude for the regions the lines are formed in, a more likely explanation is that this offset is introduced from a systematic error in the shift of the comparison stars. As the noise level on this parameter and the amount of stars rotating fast enough for this kind of analysis is rather low, we do not further

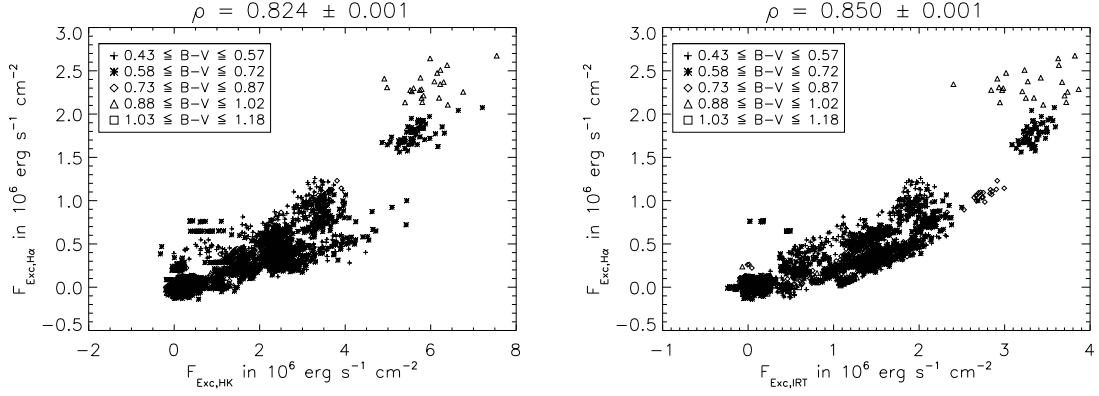


Figure 4.6: Comparison of the measured chromospheric excess flux in the H α -line to the chromospheric excess flux of the Ca II H- & K-lines (left) and the Ca II IRT-lines (right). This plot includes data from 2274 observations of 82 stars.

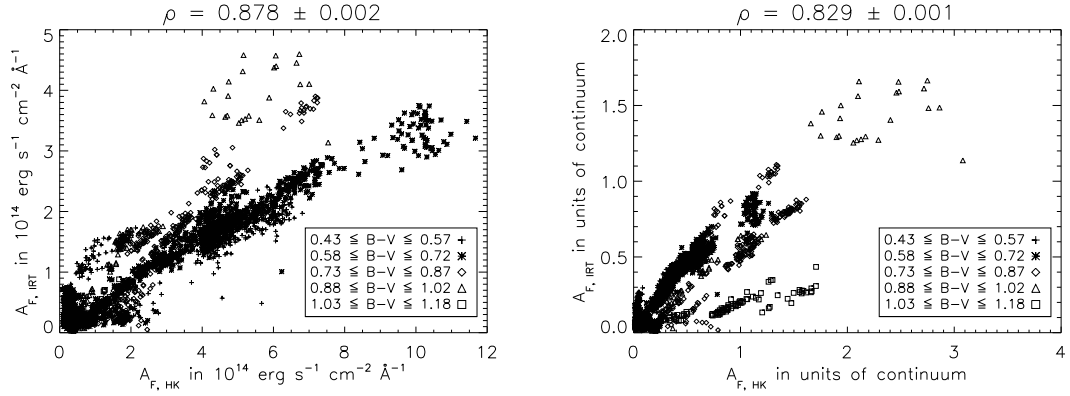


Figure 4.7: Comparison of the sum of the amplitudes of Gaussians fitted in the Ca II H- & K-lines (abscissa) and Ca II IRT-lines (ordinate), after conversion to $\text{erg s}^{-1} \text{cm}^{-2} \text{\AA}^{-1}$ (left) and before conversion in continuum units (right). This plot includes data from 2274 observations of 82 stars. The triangles that appear to not fit the otherwise linear relation belong to HD 22468.

investigate here, however, we will get back to this parameter in Sect. 11.2.2.

We can also estimate the excess flux from the fitted parameters:

$$F_{\text{Gauss,Exc}} = A_f \sigma_f \sqrt{2\pi}. \quad (4.8)$$

Due to the limits on the parameters forced during the fit, the resulting flux can never be negative, or exceed a certain threshold value. While the overall flux distribution is very well behaved, as shown in the figures, we have measured a negative excess for some low-activity stars (Fig. 4.2). In these cases, the error on the obtained value is higher than the (absolute value of the) excess flux. Unfortunately, the noise in the line center was simply too large compared to the very low excess flux. Since such a value cannot be found from the flux of the fit, it is more useful for these stars. Generally speaking, however, it makes little difference which value is used, as they show an extremely strong correlation of $\rho \approx 0.95$. We show the correlation for the case of the Ca II H- & K-lines and the Ca II IRT-lines in Fig. 4.8. For the high-activity stars, the value calculated from the fitted parameters is somewhat higher than the directly integrated one. This is due to the flux contribution that falls outside the integrating bandpass. Therefore, this plot also shows that the loss of flux from the choice in bandpass has been insignificant for all but the highest-activity stars. In case of the

Table 4.5: **Correlation between the amplitude of the Gaussians fitted to the excess flux of different lines, converted to $\text{erg s}^{-1} \text{cm}^{-2} \text{\AA}^{-1}$.** This table shows the result from obtaining the excess flux by comparing spectra of active stars to spectra of inactive stars.

		— Ca II H & K —			— Ca II IRT —				
		$\lambda 3968$	$\lambda 3934$	Sum	$\lambda 8498$	$\lambda 8542$	$\lambda 8662$	Sum	$H\alpha$
Ca II H & K	$\lambda 3968$	—	0.96	0.99	0.88	0.89	0.87	0.89	0.87
	$\lambda 3934$	0.96	—	0.99	0.87	0.88	0.86	0.88	0.87
	Sum	0.99	0.99	—	0.87	0.88	0.87	0.88	0.87
Ca II IRT	$\lambda 8498$	0.88	0.87	0.87	—	0.94	0.93	0.98	0.86
	$\lambda 8542$	0.89	0.88	0.88	0.94	—	0.94	0.98	0.88
	$\lambda 8662$	0.87	0.86	0.87	0.93	0.94	—	0.97	0.86
	Sum	0.89	0.88	0.88	0.98	0.98	0.97	—	0.88
	$H\alpha$	0.87	0.87	0.87	0.86	0.88	0.86	0.88	—

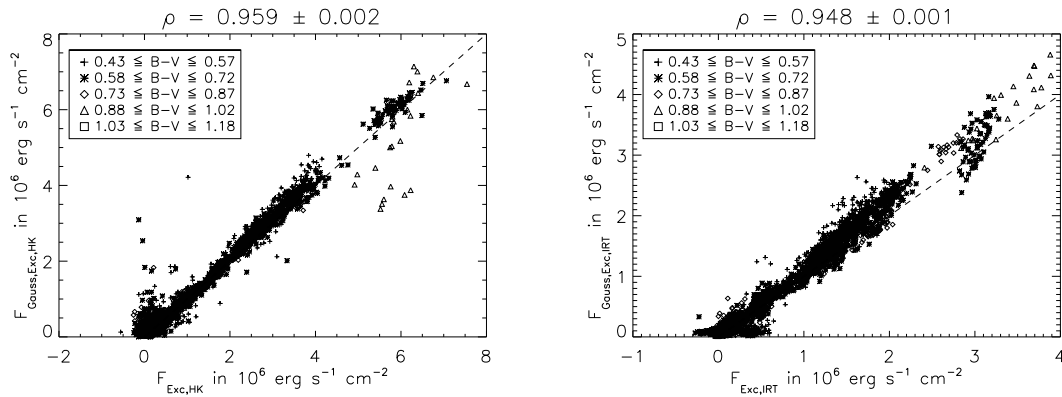


Figure 4.8: **Comparing the measured excess flux (abscissa) to the one calculated from the fitted Gaussian parameters (ordinate), for the Ca II H- & K-lines (left) and the Ca II IRT-lines (right).** The dashed line corresponds to the identity.

Ca II H- & K-lines, the wider bandpass chosen weakens this effect, to where it is no longer relevant compared to the scatter.

Some outliers can also be seen in Fig. 4.8. These correspond to spectra with higher levels of noise. In these cases, the fitting routine favors large widths and offsets, effectively fitting the far out wings of the Gaussian, which is the closest match to the erratic noise distribution of the excess. Figure 4.9 shows an example of this behavior. While it would be possible to limit the fit width and position to stricter limits as we have used, we can also use this behavior to filter out spectra where the noise fully dominates the determined excess. In further sections where we use this value, we perform this filtering step.

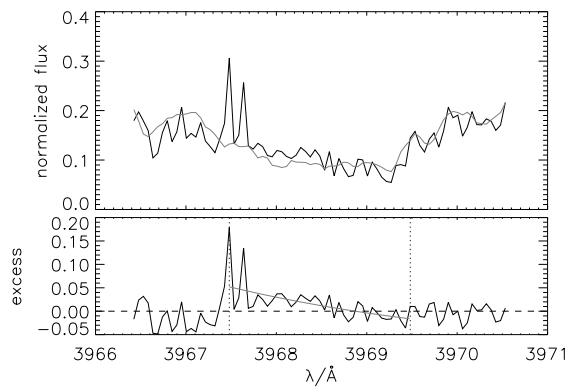


Figure 4.9: **Problematic excess Gaussian fit for highly noisy spectra.** *Top:* To obtain the excess, we compare a spectrum of HD 75732 (black) to a spectrum of its comparison star (HD 145675) (gray). *Bottom:* We fit a Gaussian (gray) to the obtained excess (black) inside the 2 Å-wide bandpass (marked by dashed vertical lines). Due to the large levels of noise, the resulting structure is far from Gaussian in shape. The fit is therefore dominated by the noise, which in turn results in a very large area under the fitted Gaussian.

Chapter 5

Modeling stellar spectra with PHOENIX

This chapter focuses on a new approach in interpolating and extrapolating synthetic spectra generated by PHOENIX. This approach has been used to allow reliable interpolation even without available model spectra sampled in a regular grid. We describe the algorithm, and show examples that illustrate its performance.

5.1 Introduction and rationale

Previously, we have compared the observed spectra of active stars to those of inactive stars with similar parameters. Assuming that the inherent differences between the two spectra are mostly caused by activity, this is a valid approach. However, as both the sample of available, inactive comparison stars, as well as the knowledge of the stars' stellar parameters is limited, further errors are introduced: No two stars show a completely similar spectrum, and if both stars have different effective temperatures or metallicities, the resulting line profile will differ, which we would previously mistaken as a contribution to the excess flux. While we estimated this effect to be not significant, for the stars at the lower end of activity, this difference might reach a similar order than the actual excess flux from activity. This may also be the reason why we have determined a negative excess value in some cases.

Another aspect of interest is the chromospheric basal flux [Pérez Martínez et al., 2014a]. Even for “quiet” stars that show very little signs of activity, there is still some residual level of chromospheric emission (compare Fig. 2.4). This is called the chromospheric basal flux. The spectrum of an inactive comparison star will also include this contribution, and therefore the determined excess in the previous chapter has not included this level. It is of interest though to determine a value for this residual flux level, and to determine its dependence on stellar parameters such as effective temperature (or $B - V$). To find this flux, one needs to know the spectrum of a hypothetical star without a chromosphere. Stellar models may provide such spectra. Here, we use PHOENIX [Hauschildt et al., 1999], a modern and reliable stellar atmosphere code¹. During the calculation of the stellar atmosphere, PHOENIX only calculates the photospheric structure, and does not feature the temperature minimum that defines the beginning of the chromosphere. The spectrum derived from the atmosphere will therefore include no chromospheric contributions. It should be mentioned that it is possible to include the chromospheric structure into the PHOENIX-calculations [Fuhrmeister et al., 2005, Aquino, 2016], however, this is not standard behavior.

Hypothetically, using models calculated with exactly the stellar parameters of the star of interest would be ideal. However, stellar parameters are rarely known with sufficient precision, not to mention that different atmosphere codes would yield differing spectra for the same parameters. Put in

¹More information about PHOENIX is available on the official website of the Hamburger Sternwarte: http://www.hs.uni-hamburg.de/index.php?option=com_content&view=article&id=14&Itemid=294&lang=en

other words, if fitting a model to the spectrum to determine e.g. T_{eff} , one would find different values depending on the atmosphere code used. Since we want to compare our spectra to PHOENIX model spectra, we must find the correct PHOENIX model for the star.

5.2 Short overview of PHOENIX

To quote the official website, “PHOENIX is a general-purpose state-of-the-art stellar and planetary atmosphere code”². We use it to generate spectra of main sequence stars of spectral type F, G and K, though it can also be used to generate model atmospheres and spectra of giants and even novae (e.g. Petz et al. [2005]) and supernovae (e.g. Jack et al. [2015a]). Additionally, PHOENIX can perform the calculations both in one dimension, or use a three-dimensional mode (see for example Aquino [2016]). For our purposes, 1D-models are sufficient. Model atmosphere generation in PHOENIX is started from an input file that defines the type of star that should be calculated. Here, we pass effective temperature T_{eff} , $\log g$, metallicity and stellar mass (estimated from homology relations). Additionally, PHOENIX can use an existing atmosphere model as a starting point to reach convergence faster (though this is not required, and a gray atmosphere can be used as a starting point), for which we have used the corresponding one from Husser et al. [2013]. PHOENIX then calculates hydrostatic, rate and radiative transfer equations in subsequent iterations, until the model has converged or the maximum amount of iterations has been reached. If this is not the case, PHOENIX performs a temperature correction [Hauschildt et al., 2003] with the intention of establishing radiative equilibrium, and proceeds with another iteration. PHOENIX can work under the assumption of local thermodynamic equilibrium (LTE), where every point individually is in thermodynamic equilibrium (though not the star as a whole), which allows to simplify the calculation and allows to define a temperature T for each point. Level populations are then given by the Saha-Boltzmann distribution [Rutten, 2003]:

$$\frac{n_c}{n_i} = \frac{1}{n_e} \frac{2g_c}{g_i} \left(\frac{2\pi m_e kT}{h^2} \right)^{3/2} \exp\left(-\frac{\chi_{ci}}{kT}\right), \quad (5.1)$$

with n_x the number of ions in the ionization level x , n_e as electron density, g_x the statistical weight for the level x , m_e the electron mass, and χ_{ci} as the ionization energy from level i to level c . The source function is then a Planck function. The process for the calculation of an LTE atmosphere is shown in Fig. 5.1.

It is possible to forfeit the assumption of LTE for individual elements. This case is called Non-LTE (NLTE for short). The population may now differ from Eq. (5.1). To solve this, PHOENIX calculates the rate equations [Hauschildt and Baron, 1999]:

$$\sum_{j<i} n_j (R_{ji} + C_{ji}) - n_i \left[\sum_{j<i} \left(\frac{n_j^*}{n_i^*} \right) (R_{ij} + C_{ji}) + \sum_{j>i} (R_{ij} + C_{ij}) \right] + \sum_{j>i} n_j \left(\frac{n_i^*}{n_j^*} \right) (R_{ji} + C_{ij}) = 0 \quad (5.2)$$

with R_{ab} and C_{ab} as the radiative and collisional transition rate coefficients between the levels a and b and n_i^* as the LTE population density of level i , which is given by:

$$n_x^* = \frac{g_i}{g_j} n_k \frac{2h^3 n_e}{(2\pi m_e kT)^{3/2}} \exp\left(-\frac{E_i - E_k}{kT}\right), \quad (5.3)$$

where n_k is the non-LTE, population density of the ground state of the next higher ionization state of the same element, and E_i is the excitation energy of level i , whereas E_k is the ionization energy from the ground state to the corresponding ground state of the next higher ionization state (i.e. the same one n_k is referring to). In PHOENIX, these equations are solved by operator splitting [Hauschildt and Baron, 1999].

²http://www.hs.uni-hamburg.de/index.php?option=com_content&view=article&id=14&Itemid=294&lang=de

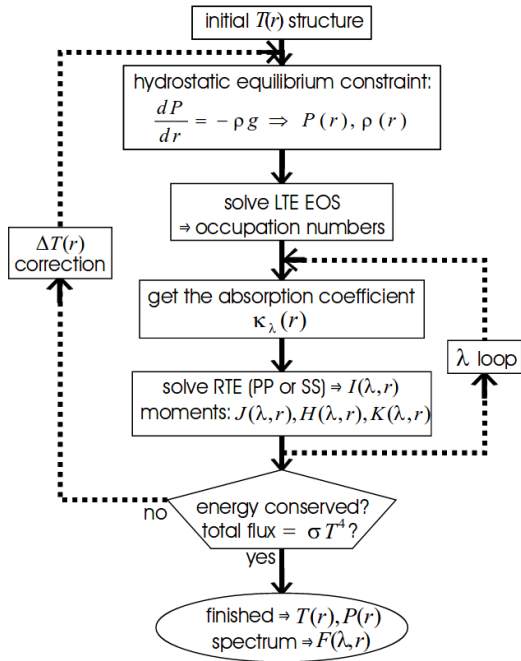


Figure 5.1: **How PHOENIX calculates an LTE atmosphere.** This flowchart shows the process by which the stellar atmosphere is modeled and calculated. “EOS” refers to the Equation of State, “RTE” stands for the Radiative Transfer Equation, “PP” and “SS” are short for “plane-parallel” and “spherical symmetry”, two possible modes for the assumption of the geometry to simplify calculations. Some steps are performed for each wavelength point, indicated by the “ λ loop”. This figure is originally from Wawrzyn [2009].

5.3 Interpolating on irregular grids

The easiest way to perform an interpolation of model spectra is to calculate models (and the spectra resulting from them) in a regular grid, covering the entire region of interest in equidistant steps. For example, Husser et al. [2013] calculated model spectra in a grid ranging from an effective temperature of 2300 to 7000 K in 100 K-steps, $\log g$ of 0.0 to 6.0 with a step size of 0.5, and a value of $[M/H]$ from -2.0 to 1.0 with a step size of 0.5 (in fact, their grid is extended beyond these ranges, but with larger step sizes). This approach allows for easy interpolation of a spectrum from the eight model spectra that form the vertices of the cube around the triplet $(T_{\text{eff}}, \log g, [M/H])$ of stellar parameters for the desired spectrum. The disadvantage of this approach is the large amount of computation time needed to calculate all models required. With the example values above, almost 3400 model atmospheres alone need to be calculated. This is a daunting task even on modern hardware, and requires the use of large computer clusters (the use of which PHOENIX is optimized for).

Precalculated grids of this kind are available, such as the aforementioned set. However, we do require a few elements to be calculated without the assumption of local thermodynamic equilibrium. In most cases, only a fraction of elements have been calculated in NLTE. Among other elements, we require iron to be calculated in NLTE, as this affects the determined continuum, which will in turn set our flux scale. The determined excess flux will be in true physical units only if the continuum was calculated correctly, as its used to define the physical scale. Of course, calcium must also be calculated in NLTE, in the most important ionization states. Additionally, to optimize the shape of the Ca II IRT-lines, we use a profile function, which was provided by Homeier [2015]. Therefore, to use model spectra fulfilling all these conditions, we need to calculate our own models that require those conditions. Table 5.1 shows which elements and which ionization states were calculated in NLTE.

Calculating the large amount of models required to cover the entire range of stellar parameters in our sample is impractical. Removing models from such a regular grid creates an irregular grid. Going one step further, if removing the requirement of an equidistant step size, we can optimize the sample of models to calculate, by sampling the region of interest in stellar parameters finely, while we sample coarsely further out. As a proof-of-concept, we have decided to proceed with such an approach, to find out if this is feasible. Additionally, this allows us to automatically and reliably

Table 5.1: **List of atomic species calculated in NLTE.** For the calcium lines, line profile functions were used for the Ca II IRT-lines, as well as the lines at $\lambda = 4226 \text{ \AA}$, and the red Ca I triplet at $\lambda = 6103 \text{ \AA}$, $\lambda = 6122 \text{ \AA}$ and $\lambda = 6162 \text{ \AA}$.

Element name	Species calculated in NLTE	Comment
Hydrogen	HI	
Helium	He I, He II	
Calcium	Ca I, Ca II, Ca III	Profile functions in use
Sodium	Na I, Na II	
Magnesium	Mg I, Mg II, Mg III	
Carbon	Ca I, Ca II	
Nitrogen	N I, N II	
Oxygen	O I, O II	
Iron	Fe I, Fe II	Strong influence on continuum

determine the stellar parameters from TIGRE observations. We have adapted the algorithm given by McLain [1976] to the three-dimensional scenario of this problem. The main issue for an interpolation method on an irregularly sampled grid is that it is not immediately evident which points to use for interpolating. In this algorithm, this problem is solved by first segmenting the available data points by grouping them into tetrahedra. To do so, we consider the triplet of $(T_{\text{eff}}, \log g, [M/H])$ of each model spectrum available as a point in the three dimensional space made up by a T_{eff} -, $\log g$ - and $[M/H]$ -axis. To find a spectrum corresponding to any point in that space, we then need to select the tetrahedron this point falls into, and use those four points for interpolation. We will describe this process in more detail below.

5.3.1 Determining the grid

The goal of this exercise is to analyze the differences in the results from the model comparisons to the results obtained earlier by comparing to inactive objects. For this reason, the same sample was chosen. Therefore, our models need to cover a part of the main sequence, from earlier F to K stars. To avoid calculating unnecessary models, only combinations of T_{eff} and $\log g$ were chosen that are relevant to our sample. Table 5.2 shows which models were chosen for our irregular grid. Each of these combinations were calculated five times, with $[M/H]$ varying from -0.5 to 0.5 in steps of 0.25. This is a finer step size than the one of 0.5 chosen for existing PHOENIX grids, for instance in Husser et al. [2013] or Hauschildt et al. [1999]. The same step size of 0.5 was chosen by Castelli and Kurucz [2004] (on the website³ there is an additional step at $[M/H] = +0.2$). We chose a smaller step size as Andretta et al. [2005] found that the Ca II IRT-line wings are very sensitive to changes in metallicity. To test if this is true for the PHOENIX models as well, we plot the three Ca II IRT-lines for different sets of T_{eff} , $\log g$ and metallicity, only varying one parameter at a time. Figure 5.2 shows the results. We find the same behavior: A change in gravity (second column in Fig. 5.2) affects the line profile only weakly, whereas metallicity results in a much stronger effect. The changes are most pronounced in the first Ca II IRT-line. Effective temperature, as expected, also changes the line profile, however, the step size shown in Fig. 5.2 between two spectra is three times larger as the typical grid spacing of 100 K, whereas the extreme cases plotted in the third column differ in metallicity by the typical step size of 0.5! However, T_{eff} is the main parameter in determining the actual flux scale, and therefore must also be selected carefully.

Every model spectrum calculated was degraded to the resolution given for TIGRE. As is evident from the table, our grid is almost regular, and thus, the simpler linear interpolation method could feasibly be chosen if one adds the missing 55 models to the grid (or potentially only the five for

³<http://wwwuser.oats.inaf.it/castelli/grids.html>, in the version from January 6th, 2016

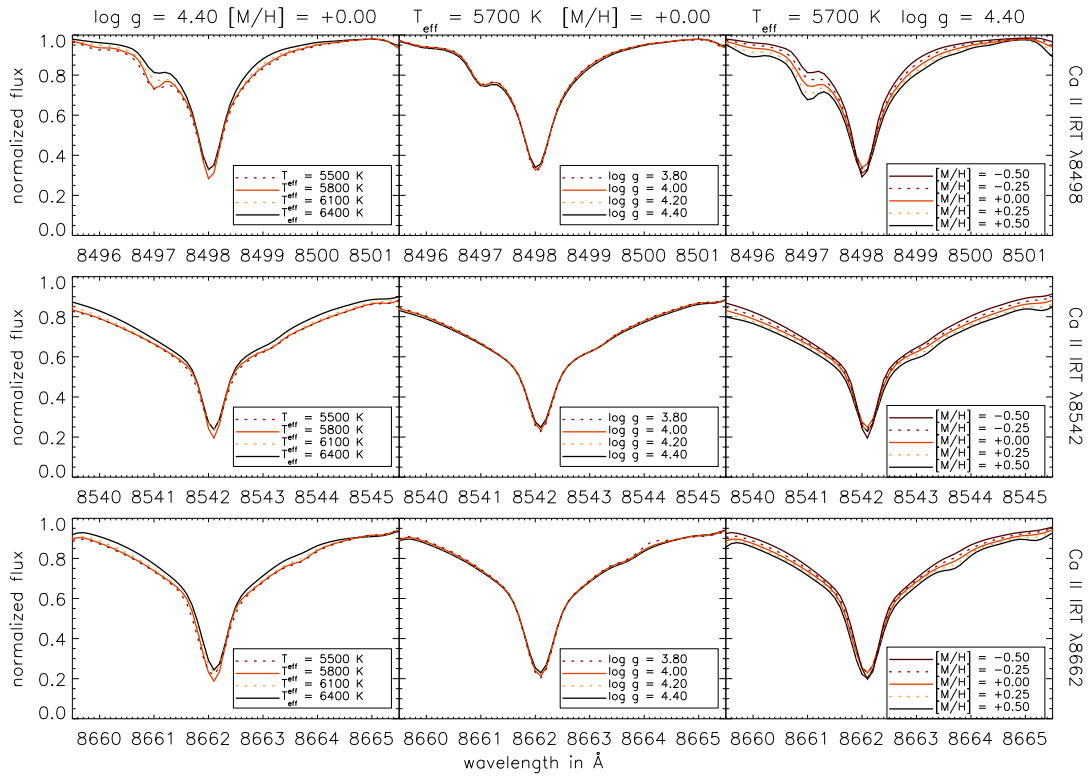


Figure 5.2: **Line profile changes for the Ca II IRT-lines from varying stellar parameters.** Each row corresponds to one Ca II IRTline, whereas each column fixes two parameters. In the first column, the effective temperature was changed, while keeping $\log g$ and metallicity constant. In the second and third column, $\log g$ and $[M/H]$ were changed respectively, while keeping the other parameters constant.

Table 5.2: **Overview of the calculated PHOENIX-models.** Fields marked with X have been computed for metallicity values of -0.5 to 0.5 in steps of 0.25.

T_{eff}	log g				
	3.8	4.0	4.2	4.4	4.6
5500 K		X	X	X	X
5600 K		X	X	X	X
5700 K		X	X	X	X
5800 K		X	X	X	X
5900 K		X	X	X	X
6000 K		X	X	X	X
6100 K		X	X	X	X
6200 K		X	X	X	X
6300 K		X	X	X	X
6400 K		X	X	X	X
6500 K	X	X	X	X	

$T_{\text{eff}} = 6500$, $\log g = 4.6$ and ignores the models with $\log g = 3.8$). The approach chosen requires some calculations to be done beforehand. Most notably, segmenting the grid into tetrahedra, and calculating a number of polynomial coefficients. While this is a slow process, predetermining these values allows very fast calculation of the actual spectra, in turn resulting in a very fast fitting of the large number of TIGRE spectra.

5.3.2 Partitioning the grid

Here, we look at a three-dimensional problem, with T_{eff} , $\log g$ and $[M/H]$ as our axes. We convert to a problem without any units, by defining:

$$\begin{aligned} x &= T_{\text{eff}}/\Delta T_{\text{eff}} \\ y &= \log g/\Delta \log g \\ z &= [M/H]/\Delta[M/H]. \end{aligned} \tag{5.4}$$

In this work, we have set the values of the steps to:

$$\begin{aligned} \Delta T_{\text{eff}} &= 100 \text{ K} \\ \Delta \log g &= 0.2 \text{ dex} \\ \Delta[M/H] &= 0.25 \text{ dex} \end{aligned} \tag{5.5}$$

This normalizes the problem and defines the scale: each step size is seen as the same distance in the three-dimensional problem. This definition of scale must be taken with care, as this can define which existing model spectra are considered “closest”, and thus given the strongest weight in calculating and interpolating a spectrum.

In partitioning the grid, we define which models should be used to interpolate between for any arbitrary set of points T_{eff} , $\log g$ and $[M/H]$. While this is trivial in the case of a regular grid, it is not for an arbitrary selection of data points. The algorithm described in McLain [1976] connects the points to triangles, as it concerns the two-dimensional case. In our three-dimensional adaptation, we create a connected structure out of individual tetrahedra. Their vertices are the points (x_i, y_i, z_i) from each calculated model. Ideally, the partitioning ensures that any point lies at least as close to one of the tetrahedron’s vertices it is surrounded by as to any other model data point.

We begin by finding a boundary surface of the tetrahedra structure. This is done by taking the point furthest from the center, then combining it with all combinations of two other points. We choose as the first surface the combination that forms a triangle surface (i.e. the points are not on

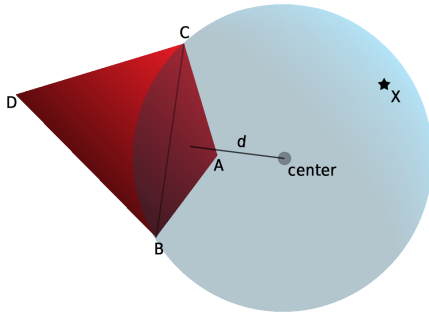


Figure 5.3: **Performing the iteration and finding the next tetrahedron.** Starting with the surface A, B, C of a tetrahedron A, B, C, D , we iterate through all points X (star) opposite the surface from D . The sphere with the points A, B, C and X on its surface, and its center (circle) is found. The score assigned to the possible tetrahedron A, B, C, X is the distance d of the surface center to the sphere center, and considered negative if the sphere center is on the same side of the surface as D .

a line) and where all other points are on the same side of this triangle. This check is performed by ensuring the sign of the dot-product of surface normal and directional vector towards any other point is constant for all points. If there are several such triangles, the one with the smallest area is chosen. This triangle is used as the starting surface for finding the first tetrahedron. We then cycle through all remaining points, to find the one that creates a tetrahedron (i.e. is not in the surface) with the smallest volume. The main iteration starts with this first tetrahedron.

In the three-dimensional case, we start with a surface made up of three vertices A, B and C that make up a tetrahedron, together with a fourth vertex D , see Fig. 5.3. Now, we iterate through all other points. For each of those points X (star in Fig. 5.3) on the side opposite to D , we find the center of the sphere with the points A, B, C, X on its surface using the method described in Hollasch [1993]. We assign this potential tetrahedron A, B, C, X a score according to the distance d of the sphere's center to the plane. Like in the two-dimensional case described in McLain [1976], this score is taken to be negative if the center point lies on the same side as vertex D . After iteration through all such surfaces A, B, C and suitable points X , the tetrahedron with the lowest score is added to the current group of tetrahedra, and this procedure is continued until all tetrahedron surfaces are either shared between two tetrahedra, or do not have any points on the outward side of the surface. Any added tetrahedron always shares a side with an existing tetrahedron. For each tetrahedron, the normal of all four surfaces is precalculated now, so that it always points outward (e.g. the normal of the surface A, B, C of the tetrahedron A, B, C, D points away from D , looking from the surface center).

This procedure guarantees a convex shape, which is necessary to avoid unnecessary extrapolation. We describe the reason for this, as well as a method to add to a concave structure until it is convex in the appendix.

5.3.3 Filling holes

While not common, in certain edge cases, this way of partitioning can result in holes (Volumes in the space that are not covered by the tetrahedra) in the structure. To fix these problems, an additional pass can be performed in which any tetrahedron's side that is not shared with another tetrahedron is checked if it is part of the external surface (If the surface is made up of points A, B, C of the tetrahedron A, B, C, D , then it is a boundary surface if all other points are on the same side as D). The filling of the structure is performed by merging four points on non-boundary surfaces into a new tetrahedron, if it does not intersect any existing tetrahedron. If several of such tetrahedra exist, the one with the smallest volume is chosen, and the iteration continues until no more holes exist.

This brute-force algorithm can take a long time if started with a structure featuring many holes, as each tetrahedron added adds more surfaces to check. It is therefore recommended to only use this in cases where it can be guaranteed that the holes are filled rather quickly.

After this process, all tetrahedra surfaces at the boundary of the structure are marked as such and stored in its own array for fast access to this list.

5.3.4 Problematic partitions

Unlike the case in two dimensions, this implementation of the algorithm can return a structure in which tetrahedra intersect or where the partitioning was not ideal in every case. A statistical analysis of 100 000 points has shown that no point lies in two tetrahedra. This check was performed as a sanity check only, as this result was expected from construction, since any newly placed tetrahedron was checked to ensure it does not intersect existing tetrahedra. More problematic is the fact that about $\sim 11\%$ of all random positions checked lie in tetrahedra that does not include the point closest to X – instead, the closest vertex to X is the next closest grid point. This tends to happen when points lie very close to the shared surface of two tetrahedra. This is not a large problem in practice, however: Given the spacing of our models, and subset of stellar parameters chosen, interpolating from the “second-best” choice of models still results in a well-behaved spectrum, as the changes in the spectra are relatively smooth (compare with Fig. 5.2). To test this, we used the complete partitioned grid to calculate spectra as described below for the troublesome points and compare them by eye to the neighboring spectra and the closest point. Figure 5.4 shows such an example. The interpolation worked fine, and no large artifacts or errors were introduced. This follows expectations: Given the spacing of our models and subset of stellar parameters chosen, the change in the spectra is rather smooth and not too large from one point to the next.

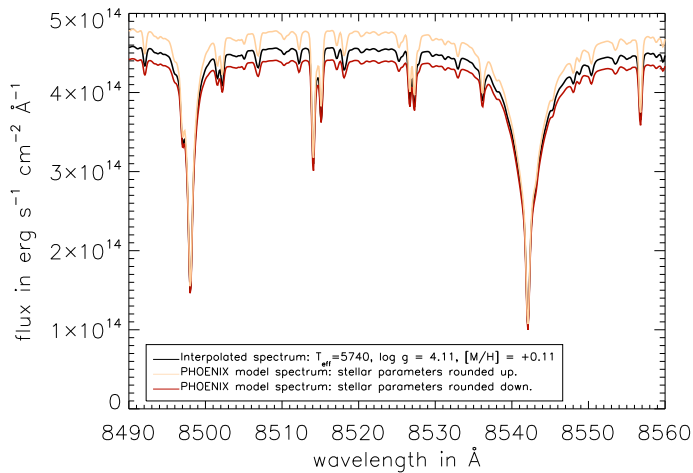


Figure 5.4: **Interpolating spectra for points that do not fulfill the ideal partitioning condition.** The final partition is not completely ideal. This test of the spectra resulting from the entire interpolation process shows that the interpolated spectra are sensible and “well-behaved”, suggesting that this problem is not severe.

5.3.5 Determining polynomial coefficients

With the partitioning done, the simplest way to do the interpolation to find a spectrum at a point $(T_{\text{eff}}, \log g, [M/H])$ would be to find the tetrahedron that encloses this point, and then interpolating their spectra, weighting them by the distance to the point in the $(T_{\text{eff}}, \log g, [M/H])$ -space. However, this results in sharp edges at the surfaces of the tetrahedra, and is not ideal. Instead, McLain [1976] suggests to do the interpolation by assigning each point A the coefficients a_{ij} of a second-order polynomial:

$$f_{\text{datapoint}}(x, y) = a_{00} + a_{10}x + a_{01}y + a_{20}x^2 + a_{11}xy + a_{02}y^2, \quad (5.6)$$

These coefficients can be determined numerically exactly by fitting this polynomial using the known values at A and the five nearest points. McLain [1976], however, suggests to fit these parameters using all the data of all points available, weighting them by their distance to A . In our three-dimensional case, we find one such polynomial for each wavelength point λ , and Eq. (5.6) becomes:

$$\begin{aligned} f_{\text{datapoint}}(x, y, z, \lambda) = & a_{000,\lambda} + a_{100,\lambda}x + a_{010,\lambda}y + a_{001,\lambda}z + \\ & a_{200,\lambda}x^2 + a_{020,\lambda}y^2 + a_{002,\lambda}z^2 + \\ & a_{110,\lambda}xy + a_{101,\lambda}xz + a_{011,\lambda}yz, \end{aligned} \quad (5.7)$$

with 10 coefficients $a_{ijk,\lambda}$ for every wavelength point λ . Assuming 25 000 wavelength points and 220 models included in the grid, as well as using the `double` variable type (64 bits), this results in roughly 440 MB of data. This is a justifiable amount of memory to use for such a purpose, as keeping this data in memory is the key to interpolating the spectra very fast. The fit is done using the Levenberg-Marquardt method [Moré, 1978, Moré and Wright, 1993] using the IDL implementation by Markwardt [2009]. The distance-weighting when calculating the coefficients of point A is done by assigning each data point B an error of the form:

$$\begin{aligned}\sigma_{AB} &= \exp \frac{d_{AB}^2}{25} \cdot (0.2 + d_{AB}^2), \\ \text{with } d_{AB}^2 &= ((x_A - x_B)^2 + (y_A - y_B)^2 + (z_A - z_B)^2)\end{aligned}\quad (5.8)$$

This is based on the distance-weighting used in McLain [1974], with the constants tweaked for the best performance in our case. The relative difference in this weighting-factor of two neighboring points (for which the distance is defined to be 1) is 6.2. This results in a very strong preference of the fit to return the actual value of the data point and close neighboring points, as desired.

5.3.6 Interpolating and extrapolating from model spectra

We have partitioned the grid and found a second-order polynomial for each point in the grid. We are now ready to calculate a spectrum for any arbitrary point $P = (T_{\text{eff}}, \log g, [\text{M}/\text{H}])$, or the equivalent point in the normalized space $\vec{p} = (T_{\text{eff}}/\Delta T_{\text{eff}}, \log g/\Delta \log g, [\text{M}/\text{H}]/\Delta[\text{M}/\text{H}])$. First, we cycle through all tetrahedra to find the one enclosing P : If the directional vector from any surface center to P points in the same direction as its normal, the point is not inside that tetrahedron. Let the vertices of the tetrahedron that includes P be called A_1, A_2, A_3 and A_4 , each with their own polynomial Eq. (5.8). For each vertex A_i , a distance d_i is now calculated. This, however, is *not* the euclidean distance from the vertex to P , but rather the distance from the surface opposite to the vertex A_i , divided by the distance of A_i to that surface (this normalizes the scale). Therefore, this distance value d_i is never less than zero, and never more than one, which it is only if P coincides with A_i (it is lower the further away it is from A_i).

The calculation of this normalized distance from the surface can be expressed as:

$$\begin{aligned}d &= (\vec{p} - \vec{s}_c) \cdot \vec{n} \cdot f \\ &= (\vec{p} \cdot \vec{n} - \vec{s}_c \cdot \vec{n}) \cdot f,\end{aligned}\quad (5.9)$$

where \vec{s}_c is any point on the surface (we take the surface center), and f is the factor ensuring the correct normalization. We can define

$$\vec{n}_0 = \vec{n} \cdot f \quad (5.10)$$

And then express Eq. (5.10) by using a four-dimensional scalar product:

$$d = \begin{pmatrix} p_x \\ p_y \\ p_z \\ 1 \end{pmatrix} \cdot \begin{pmatrix} n_{0,x} \\ n_{0,y} \\ n_{0,z} \\ -\vec{s}_c \cdot \vec{n}_0 \end{pmatrix} \quad (5.11)$$

The four parameters $n_{0,x}, n_{0,y}, n_{0,z}$ and $\vec{s}_c \cdot \vec{n}_0$ are precalculated and stored for each tetrahedron surface.

As recommended in McLain [1976], the four thus calculated distances d_i are then cubed for our three-dimensional case, and used as weights for the results of the four polynomials, which are evaluated at the position of P . The so determined value is considered the final interpolated value, and one such value is calculated for each wavelength point. This creates the interpolated spectrum at point P :

$$F_P(\lambda) = \frac{1}{\sum_{i=1}^4 d_i^3} \sum_{i=1}^4 d_i^3 f_{A_i}(\vec{p}, \lambda). \quad (5.12)$$

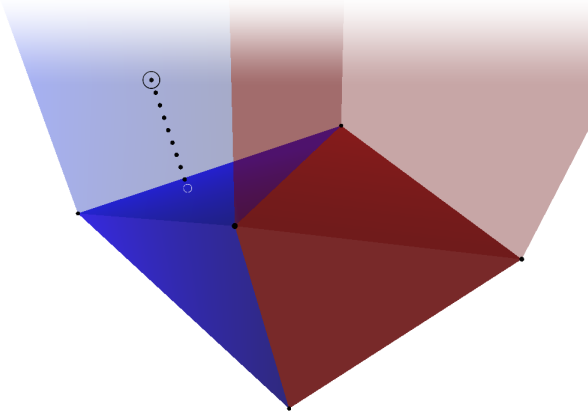


Figure 5.5: **Extrapolating if a point falls outside the tetrahedra.** If the point P (black ring, upper left) falls outside the tetrahedra structure, it is necessary to extrapolate, instead of interpolating. Since the structure is always convex, the point P always falls in one of the extruded boundary surface volumes (transparent blue and red) of one of the outside tetrahedra (blue and red, below). In this case, P falls in the blue extruded surface structure. Therefore, the polynomials of the vertices (black dots) of the outward blue tetrahedron surface should be used for estimating the value at point P .

It is possible that the point P is not inside any tetrahedron, this is the case if the chosen stellar parameters are outside the parameter range of the models in our sample, because we have guaranteed for the partitioning structure to be convex. Therefore, there is exactly one defined tetrahedron surface at the boundary that would include P if extruded along its normal to infinity (Fig. 5.5). Now, the polynomials of the three vertices A_1, A_2, A_3 making up that surface are calculated, and weighted according to $w_i = d_i^3$, with d_i here as the euclidean distance from A_i to P . We interpolate the values of the three polynomials evaluated at P , weighted by w_i . This value is considered to be the final extrapolated value:

$$F_P(\lambda) = \frac{1}{\sum_{i=1}^3 w_i} \sum_{i=1}^3 w_i f_{A_i}(\vec{p}, \lambda). \quad (5.13)$$

Note that the actual extrapolation is thus done in the second-order polynomial. Far out extrapolation cannot be reliably done in this fashion, as such a polynomial cannot reliably predict the changes in the model.

5.3.7 Sanity check: comparing the results

As a sanity check, we can now compare the spectra calculated with the approach described to the model spectra calculated by PHOENIX. Figure 5.6 shows the simplest case: Here, we compare a model that was “interpolated” at a vertex of one of the tetrahedra in the partitions. In other words, that particular model spectrum, calculated with PHOENIX, was available during the interpolation. Naturally, we expect no large deviations. In fact, the median deviation is actually just 0.03%, and the maximum deviation is about 5%. Unfortunately, the strongest deviation occurs in the line centers. However, those are mostly contained within one or two wavelength points, which means that this deviation will not affect the results obtained from integrating within the entire line much. It is also worth mentioning that since the flux is lowest in the line centers, the relative deviation will be largest there. Now, we compare the behavior outside of tetrahedra vertices. We pick two calculated PHOENIX models, and calculate fifteen models with stellar parameters linearly in between those of the models. We show the results for the case of varying all parameters in Fig. 5.7. In Fig. 5.8, we vary either one or two parameters: In each row, we show the case of only varying one parameter (left), or of varying all others and keeping that parameter constant (right). We find that the interpolated models are changing smoothly from one PHOENIX model to the next, as expected. As we see no sudden, strong changes, we are confident that this way of interpolating works well and is, in fact, a good choice for our use case.

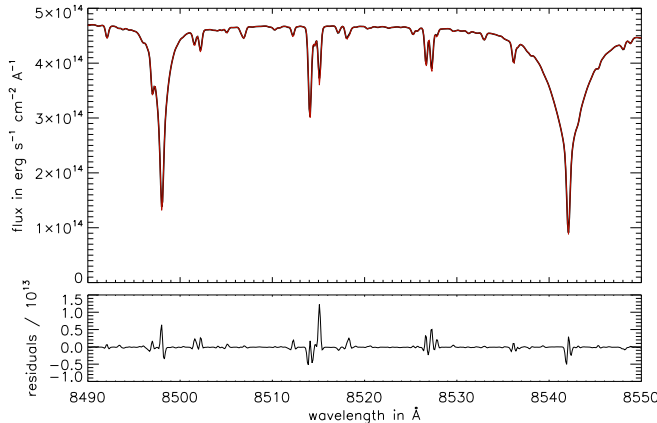


Figure 5.6: **Checking the interpolation results for the simple case.** Here, we compare the spectrum calculated from the partitioned grid at $T_{\text{eff}}=5800$, $\log g=4.4$, $[M/H]=0$ (red) with the (degraded) PHOENIX spectrum (black). It is hard to make out differences by eye. The lower plot shows the residuals: The maximum deviation here is 3.6%. The flux is given in $\text{erg s}^{-1} \text{cm}^{-2} \text{\AA}^{-1}$.

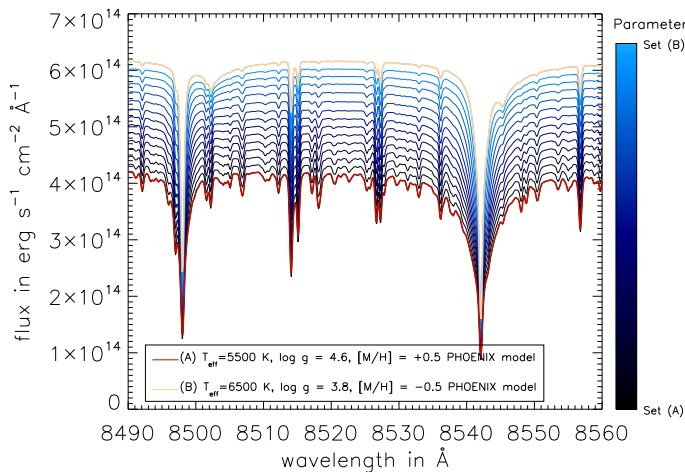


Figure 5.7: **Checking the interpolation: Varying all parameters.** These plots show the interpolated spectra on a color scale from black to blue. Their parameters are interpolated linearly from the starting PHOENIX model (red) to the final value (orange).

5.4 Summary

In this chapter, we have described our implementation of an adaption of the interpolation algorithm described by McLain [1976], for our three-dimensional case for interpolating PHOENIX model spectra. This allows to calculate an inter- or extrapolated spectrum as a function of T_{eff} , $\log g$ and $[M/H]$. The strength of this algorithm is its great performance on irregular grids, and its high speed in generating the actual interpolated spectrum. While the grid we are using is close to being regular, the intention of this algorithm is to allow easy addition to the model grid. By calling this procedure, the TIGRE pipeline may be able to automatically determine stellar parameters for all kind of stars. The range of stars for which this is suitable can simply be increased by adding spectra of stars of various luminosity classes and spectral types to the irregular grid. This addition can be optimized for high coverage in the region of interest, without being limited by the grid step size, and without obligation of filling in “unphysical” parts of the grid.

To perform such a determination of stellar parameters, an observed spectrum is fitted by a model spectra. This process is not trivial, despite the idea being simple in principle. We have performed such fits to determine the stellar parameter. The next chapter describes this process.

We give a detailed overview on how to use the code in the appendix, Sect. A.2.

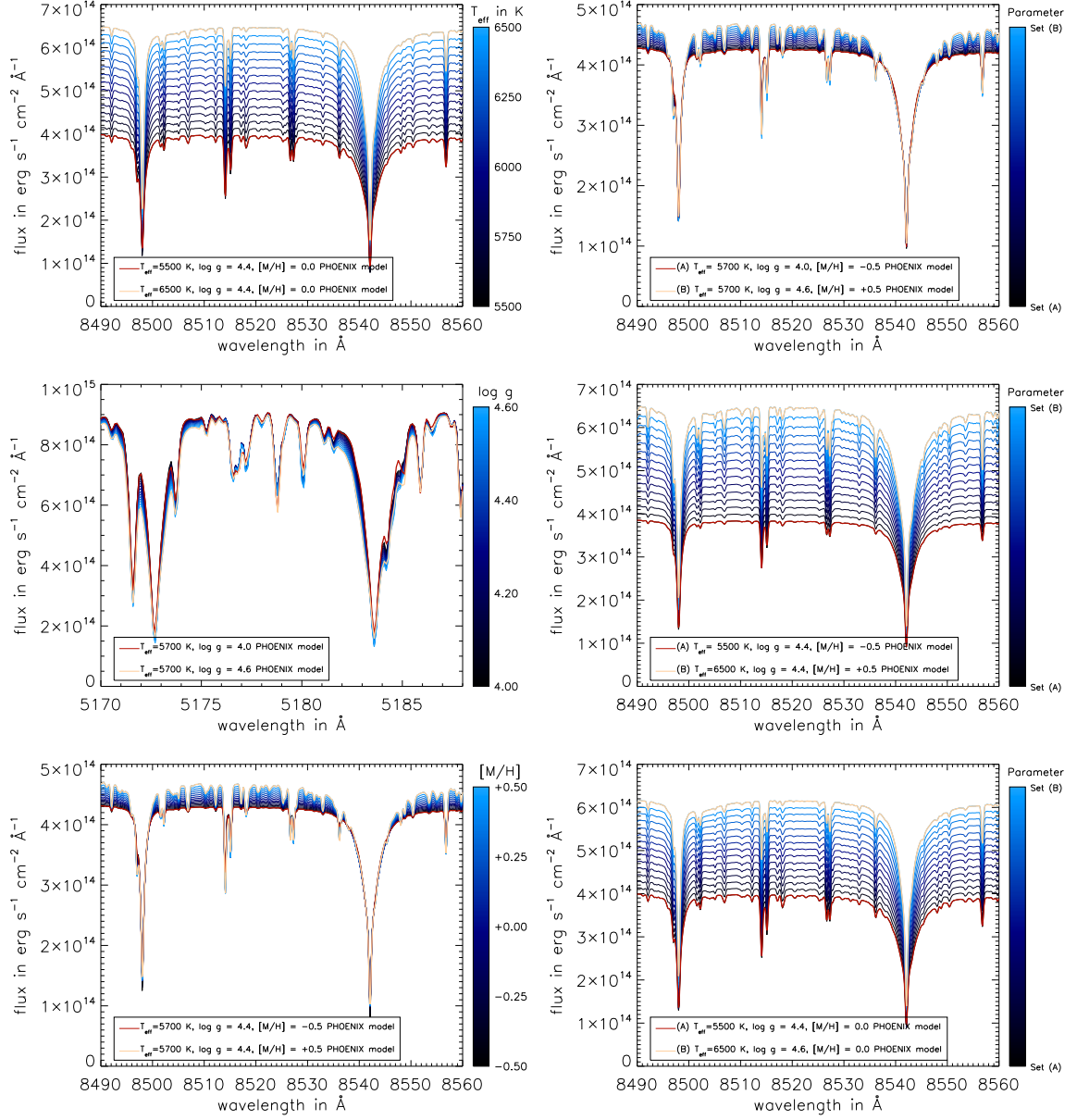


Figure 5.8: **Checking the interpolation: Varying one or two parameters.** These plots show the interpolated spectra on a color scale from black to blue. Their parameters are interpolated linearly from the starting PHOENIX model (red) to the final value (orange). *Left column:* From top to bottom, T_{eff} , $\log g$ and $[M/H]$ are changed, while the other parameters are kept constant. *Right column:* From top to bottom, T_{eff} , $\log g$ and $[M/H]$ are kept constant, while the other parameters are changed.

Chapter 6

Fitting TIGRE spectra with PHOENIX models

Our goal is to use PHOENIX models to determine the excess flux in the active lines, most notably the Ca II IRT-lines. However, as we have seen, even relatively small deviations in stellar parameters can influence the line profile (Fig. 5.2). For this reason, we must carefully choose the right model to perform the comparison with.

One might think that the easiest way to do so would be to take literature values into consideration. The problem here is that for many stars, these are not determined to sufficient accuracy. Especially the metallicity, which shows a strong effect in the Ca II IRT-lines, is often only poorly known. For example, the star HD 106516 has 41 separate entries listed in the SIMBAD database [Wenger et al., 2000]¹ for the stellar parameters. There, T_{eff} ranges from 5478 K [Wallerstein, 1962] to 6316 K [Gray et al., 2003] – that is almost the entire range of our grid! The other parameters show a similar range: $\log g$ is given as low as 3.8 [Peterson, 1980], but as high as 4.6 [Gratton et al., 1996], and [M/H] covers values from -0.98 [Hartmann and Gehren, 1988] to 0.05 [Wallerstein, 1962]. Such deviations can be systematic, and stem from different approaches in determining these values. Even different model atmosphere codes will return different spectra, depending on a variety of conditions, one of which is the line list used. While most stars do not show such large effects, several hundred K difference in T_{eff} is not uncommon. For our particular case, we require a good fit of the PHOENIX model spectrum to the observed spectrum. To ensure this, we determine the respective stellar parameters ourselves by fitting the model spectra to our dataset.

6.1 Method of the fit

To reliably determine the stellar parameters from our TIGRE observation data, we first merge all available spectra from each object, and weigh them according to their SNR. This is done to increase the SNR in the resulting spectrum, but it has the fortunate side effect of removing (or at least drastically reducing) any peculiar effects that a single spectrum may show, such as cosmics (see Fig. 2.13). When merging spectra together, we must ensure that any potential shifts are taken care of. Shifts in the spectra can occur due to many reasons, such as errors in the wavelength calibration, an incorrect value for the barycentric velocity, but also due to a red- or blueshift induced from the physical movement of the star. While constant red- or blueshifts from the radial velocity have been filtered and are usually well-known, binaries have an additional, time-dependent red- or blueshift that is not filtered in this fashion. No matter the case, however, such a shift must be corrected before merging the spectra. A constant, global shift in the spectrum would not be a large problem and easily taken care of by allowing a wavelength shift in the fit, but a relative shift from one spectrum to the next will appear as an effective reduction of resolution. Therefore, we perform a

¹Database visited on February 16th, 2017.

Table 6.1: **Regions the fit is performed in.** The fit is not performed across the entire spectral region of TIGRE, but instead across a selection of carefully picked regions. These are normalized individually. Additionally, some points in these regions are ignored in the fit, these are given in Table 6.2.

Region	Comment
5 100 — 5 200	
6 099 — 6 200	
6 520 — 6 580	Center of H α -line ignored via mask
7 740 — 7 840	
8 480 — 8 520	To ensure agreement in the Ca II IRT-line wings
8 550 — 8 650	

cross-correlation on the individual spectra to correct any relative wavelength shift between them. This spectrum is then compared to a PHOENIX model spectrum. Here, we use the interpolation system described in Chapter 5, which allows the very fast calculation of a model spectrum for any set of stellar parameters. We now give more details on this process.

6.1.1 Regions to perform the fit in, and those to ignore

It is impossible to bring our PHOENIX spectra to a complete agreement with observed spectra, even disregarding the noise of the latter. Some lines in the spectra do not match, even when using the correct stellar parameters for the model, due to errors in the model spectrum calculation, e.g. due to an error in the line list in use. Therefore, we must accept the fact that some regions in the spectra are simply not suitable to determine the stellar parameters. We combine parts of the regions given in Ryabchikova et al. [2016] with three more regions around the Ca II IRT-lines. Note that we do not use all regions given in Ryabchikova et al. [2016], even some that were in TIGRE’s spectral range. The sections used were selected from comparing a PHOENIX spectrum using the Sun’s stellar parameters and a TIGRE spectrum of the Moon (the Sun’s reflection spectrum). Even in those sections, some line profiles do not match. We need to ignore these in the fit. For this reason, there is a mask in use. During the fit, wavelength points covered by the mask are automatically set to the corresponding value of the observed spectrum: In this way, they will not influence the fit, as their contribution to the χ^2 -value will be zero. However, this does affect the number of degrees of freedom (and thus the value for the reduced χ^2_{ν}).

Regions are normalized individually during the fit. To find those regions, we compare the co-added TIGRE spectra of the Moon with the corresponding PHOENIX model spectrum. In a first pass, an automatic detection of poorly matching points is performed, where a point is considered to match poorly if the residuals are too large compared to the deviation to the normalized continuum flux. This means that there is a larger effective tolerance for deeper lines. This automatically determined mask is then adapted and changed by hand.

We give the regions in use in Table 6.1, while Table 6.2 gives the first few entries in the mask used, whereas the full mask is listed in the appendix in Table B.6. Figure 6.1 shows a 15 Å-section of the regions and masks given in Tables 6.1 and 6.2, respectively. In this figure, the PHOENIX model is compared to co-added TIGRE spectra of the Moon, as well as the high-resolution spectrum given in Neckel and Labs [1984], degraded to TIGRE’s resolution. Regions that are part of the mask are marked as well.

6.1.2 Fitting normalized spectra

TIGRE spectra are given in arbitrary units, and have not been converted to the physical flux units PHOENIX model spectra are given in. Additionally, the spectra tend to not follow the same general structure as the model spectra do. We show this for the case of HD 140538 in Fig. 6.2. This means

Table 6.2: **Mask in use to ignore certain regions in the fit.** This table is only the first part of the complete table given in the appendix in Table B.6.

Mask region		
5117.16 – 5117.56	5117.89 – 5118.02	5120.94 – 5121.14
5123.39 – 5124.32	5124.52 – 5124.85	5125.44 – 5125.77
5126.17 – 5127.81	5130.24 – 5130.65	5132.60 – 5132.81
5135.85 – 5136.20	5140.68 – 5140.89	5142.06 – 5142.26
5142.88 – 5143.23	5146.04 – 5146.24	5150.68 – 5151.29
5151.70 – 5152.04	5152.31 – 5152.51	5153.53 – 5153.67
⋮		

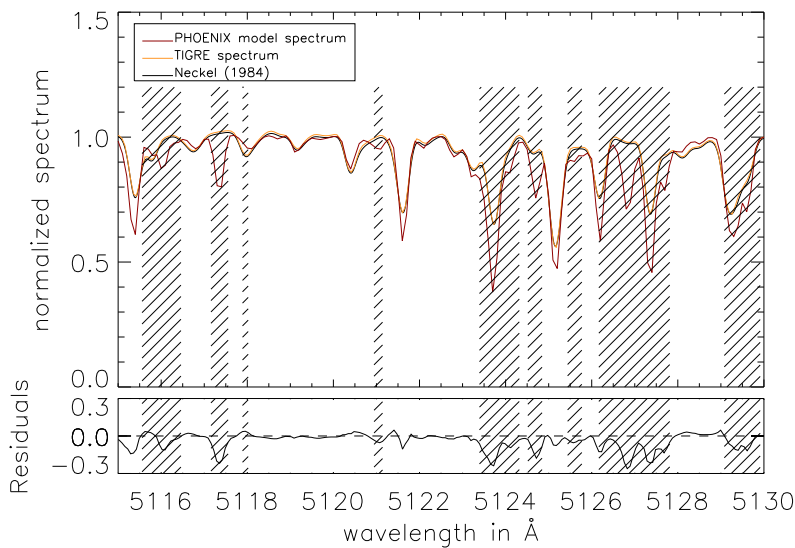


Figure 6.1: **Determining the Masks for the Fit.** Comparison of the PHOENIX model spectrum created from stellar parameters (red) with observed spectra from both TIGRE (orange) and Neckel and Labs [1984] (black). The masks given in Table 6.2 are marked as regions with diagonal lines.

that we cannot rely on the overall spectrum’s shape to constrain T_{eff} . However, as T_{eff} , affects line profiles as well (Fig. 5.2), it is possible to fit normalized spectra instead.

Normalizing both TIGRE spectrum as well as the interpolated model spectrum is performed in the same way as described in Sect. 3.2. The merged TIGRE spectra show some noise, which affects the normalization to a small degree. This can add up to a small offset across the entire spectral region. A fit would then seek to correct this offset by adapting stellar parameters. This is not the desired behavior, so we allow to separately fit two parameters for each region as a linear correction of this offset. These parameters can vary from 0.5-1.5, but they are usually very close to one.

6.1.3 Finding the spectral resolution

As we have mentioned in Sec. 2.6.2, TIGRE spectra do not have a constant resolution R (Eq. (2.13)). In fact, it does vary quite strongly even across small wavelength ranges (Fig. 2.12). If the TIGRE spectrum has a lower resolution than we assumed when degrading the model spectra, lines will be comparatively broader, which a fit would seek to correct by varying the stellar parameters. To avoid this problem, we fit the resolution and allow it to vary to a value lower than the $\sim 21\,000$ that the model spectra were degraded to. In this fashion, every region has been assigned an individual value for the resolution. Figure 6.3 illustrates the difference in the results obtained from a fit with an adaptive resolution to the results of a fit without resolution as a free parameter. It shows that the problem described does indeed happen, and wrong stellar parameters are recovered. An even worse

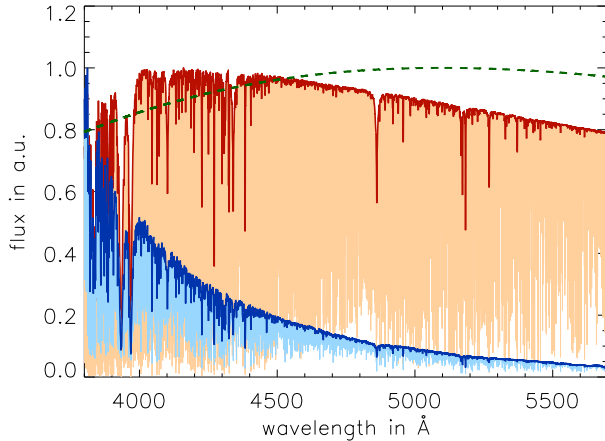


Figure 6.2: **Comparing the trend of a TIGRE spectrum (blue) for HD 140538 to the trend of a PHOENIX model spectrum (red).** Spectra taken by TIGRE do not follow the same trend as PHOENIX model spectra do, which are closer to the approximation of a blackbody (green dashed line). Thick lines are upper envelopes to see the overall trends more easily.

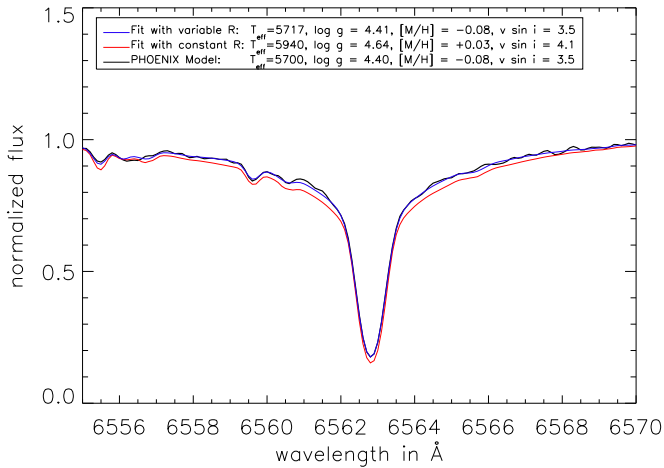


Figure 6.3: **Checking the necessity of fitting the resolution.** This plot shows the resulting best fit of a resolution-degraded PHOENIX model with noise added to it for the two cases of allowing the resolution to be fitted as well (blue line) and the case of keeping the resolution fixed (red line).

problem for our case is a poor fit in the line center and wings, as this results in us determining an incorrect excess distribution, as well as an incorrect value for the integrated excess flux.

6.2 Performing the fit of PHOENIX model spectra to TIGRE observations

In this section, we will describe the actual process of fitting TIGRE spectra with PHOENIX model spectra. Using the process described in Chapter 5, we can quickly generate normalized spectra for any set of stellar parameters, and subsequently degrade them, too. In an iterative process, constantly adapting these parameters to optimize the match of calculated to measured spectrum in the regions given in Table 6.1 allows us to find the best set of such parameters, which we interpret as the “real” set. The complete set of parameters to fit, including the normalization corrections and resolution values, is given in Table 6.3. There are several algorithms available for performing such a fit, each with their own advantages and disadvantages. We have used the Levenberg-Marquardt-algorithm, as well as a Markov Chain Monte Carlo. In this section, we show the results and compare the two.

Table 6.3: **Parameters to fit.** Optionally, the routines can fit a wavelength shift, a normalization correction and the spectrum’s resolution. The normalization correction is done by dividing the interpolated model spectrum by a linear fit through the levels N_0 and N_1 at the beginning and the end of the region, respectively.

	Parameter	Constraints	Comment
	T_{eff}	5.3 - 8.0	In units of 10^3 K
	$\log g$	3.8 - 4.9	
	[M/H]	-1.5 - 1.5	
	$v \sin i$	1 - 500	In units of km s^{-1}
	$\Delta\lambda$	-0.5 - 0.5	Wavelength shift in \AA
For each Region	N_0	0.5 - 1.5	Start continuum level of norm. spectrum
	N_1	0.5 - 1.5	End continuum level of norm. spectrum
	R	16 000 - 20 738	Resolution in this region. Interpolated spectra have $R_0 = 20\,738$, unless further degraded to this.

6.2.1 Fitting the spectrum with the Levenberg-Marquardt algorithm

To perform a fit using the Levenberg-Marquardt algorithm, we use again the MPFIT-package [Markwardt, 2009]. We attempted to fit the stellar parameters to the merged TIGRE-spectra three times, each time varying the starting parameters: First, by using the literature values from Chapter 4 as starting parameters, second, by always using the Sun’s stellar parameters as starting parameters, and finally by testing a set of possible starting parameters, and then choosing the best one.

The results show that in many cases, this fitting algorithm tends to stay too close to the starting values, especially for [M/H] and $v \sin i$. We have experimented by varying the step size, used for the calculation of the partial derivatives, but the improvements were marginal at best. It appears that the fitting algorithm quickly finds a local minimum, and stops there. This is expected behavior for this algorithm [Markwardt, 2009], which may be worsened by the fact that parameters are highly correlated. For this reason, the algorithm requires a solid set of starting parameters. Therefore, using completely static starting values does not give great results. In order to obtain those with just the prior assumption of the star’s stellar parameters being covered by our grid, we first try the models of a variety of stellar parameters and use the best one of this set as starting parameters, leaving the actual fit to optimize these parameters. The “best” set is the one that results in the lowest χ^2 values, and a small grid is used for this check. However, this approach suffers from a high time requirement. The MPFIT fitting algorithm is very fast and highly optimized, but the necessary test of the sets for the starting parameters requires a large amount of calculations, namely the degradation and normalization, that slows down the entire fitting process. It should be noted that MPFIT often stops as the relative deviations of the input parameters become too low (the optional output variable STATUS is set to 2), which suggests that the actual fit cannot be brought to total agreement, as this would result in a real convergence of the spectrum output. We now describe the results of the three approaches in detail.

In Fig. 6.4, we compare the result of the first fit to the literature values stemming mostly from the PASTEL-catalog [Soubiran et al., 2010]. In this first fit, we have used these literature values as starting values. The dashed line shows the identity, and the dotted lines correspond to given “typical step sizes” used in many grids of $\Delta T_{\text{eff}} = 100$ K, $\Delta \log g = 0.5$ dex and $\Delta[\text{M}/\text{H}] = 0.5$ dex, since these values can be considered the “common wisdom” as to a small value deviation with a small effect on the spectrum. Since we are comparing to the starting parameters here, no change in the parameters from the fit would result in the best agreement in this plot, but this fit can give us an idea of the tendency of the offset between the ideal-fit values of our fitted parameters to the literature values. It is clear that the deviation between the found values and the literature values is very small for the

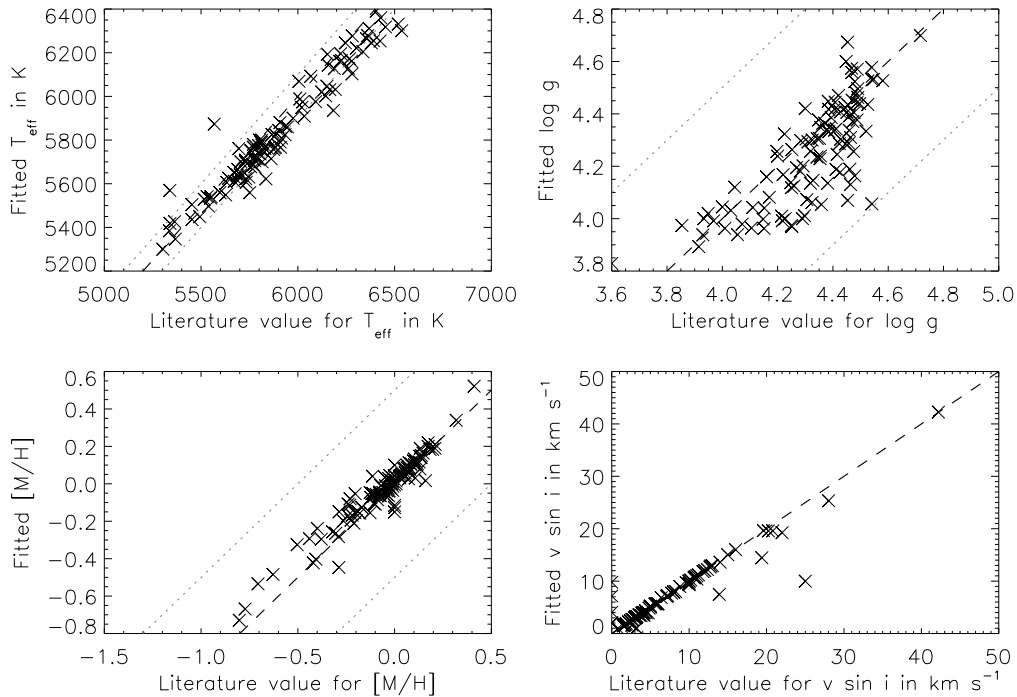


Figure 6.4: **Comparing fitted stellar parameters to literature values, for the case of using literature values as starting parameters.** This plot shows the fit results of 105 stars. The dashed line shows the identity, whereas the dotted lines show the offset corresponding to commonly chosen step sizes of grids with $\Delta T_{\text{eff}} = 100$ K, $\Delta \log g = 0.5$ dex and $\Delta [M/H] = 0.5$ dex.

vast majority of cases, with a few outliers mostly in the rotational velocity, which is a parameter that is difficult to fit (see below). This proves that the approach of fitting does not introduce any large systematic errors. At the same time, the fit in this case is rather uninteresting, as we use known values for the stellar parameters to begin with. More interesting is the case of “no prior information”, in which the fit of the interpolated model spectra alone will find the correct stellar parameters. It must be mentioned that our set of stars we are analyzing here has been selected to be a main sequence star of spectral type F, G or K (see Sect. 2.5.3), so that we do actually use some prior information, namely that a star’s parameters will fall into the ranges best described by the model grid we have created for this particular purpose.

The simplest way to perform the fit uses a static starting set of parameters. The results when using solar parameters as starting values for the fit of all stars in our sample is shown in Figure 6.5. It becomes apparent that this method tends to stay somewhat close to the starting set of parameters, as evidenced by the tendency of points to cluster around certain values (horizontal lines in Fig. 6.5), rather than being distributed evenly across the entire range. For example, there is a large band of stars forming around $T_{\text{eff}} = 5777$ K, the solar value, as well as a somewhat smaller band around $\log g \approx 4.44$. Rotational velocity has been especially poorly fitted, with most values staying very low and only a few at $\approx 19 \text{ km s}^{-1}$ – a relative increase of $\sim 800\%$ – with almost no points in between. When calculating the partial derivative for $v \sin i$, the algorithm calculates a new model with a rotational velocity of $v \sin i \pm \Delta v \sin i$ (the sign is chosen for optimal efficiency, and to avoid leaving the fitting range). If $v \sin i$ is too low in the current iteration, then the model is deeper in the center, with too narrow wings. If $\Delta v \sin i$ is too large, the algorithm “overshoots”, and the partial derivative is estimated from the χ^2 -value of a spectrum that is now broadened too much, being too shallow in the center, and too wide in the wings (Fig. 6.6). As this spectrum is so broad, it may show a higher χ^2 . In other words, even though the algorithm correctly tested a higher velocity, the

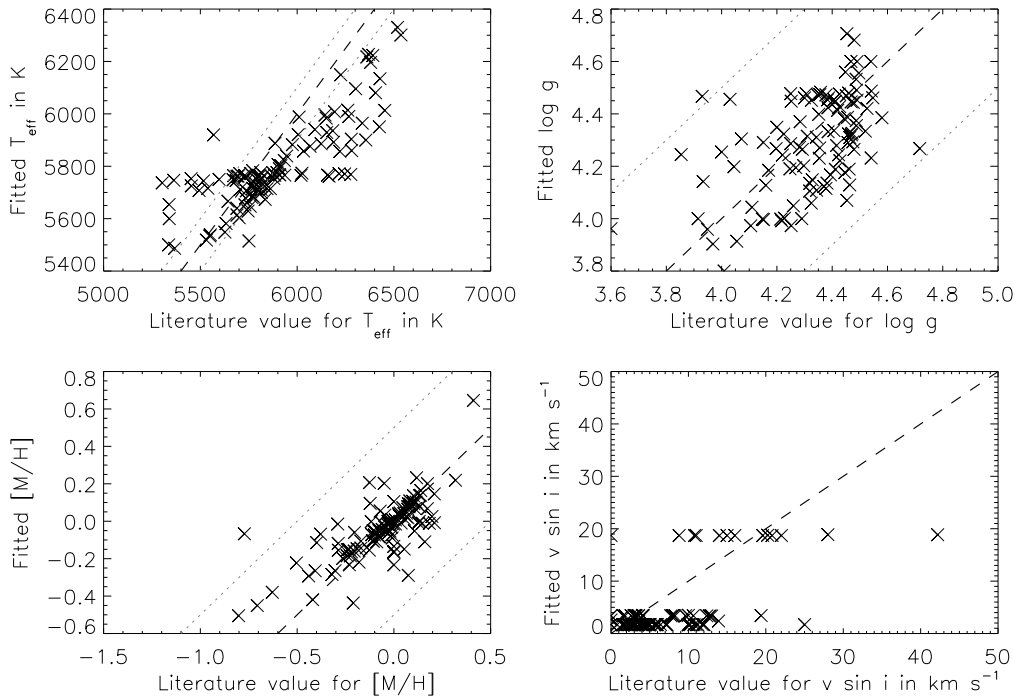


Figure 6.5: **Comparing fitted stellar parameters to literature values, for the case of using solar values as starting parameters.** Same as in Fig. 6.4, with the dashed lines marking the typical grid-step sizes. Here, we used solar values as the starting values for the fit.

algorithm might actually decrease $v \sin i$ for the next iteration in an attempt to improve χ^2 . The same is true if the rotational velocity was set too high in the current iteration. To alleviate this, we set `MPSIDE` to force a two-directional calculation of the partial derivatives (i.e., it is calculated from models with $v \sin i - \Delta v \sin i$ and $v \sin i + \Delta v \sin i$), and experiment with step-widths, both with constant absolute, constant relative, and dynamic ones. However, no satisfactory result could be reached in this fashion. Still, while the overall fit of T_{eff} , $\log g$ and $[M/H]$ is acceptable, there is still room for improvement, especially for $v \sin i$, which is an important parameter in the determination of the excess flux. We therefore conclude that better starting values are required.

Figure 6.7 shows the result of the fit when the starting parameters were found from the search of a suitable set from a grid, corresponding to the case of “least information”. First, we compare the observed spectrum to a set of model spectra corresponding to a particular set of stellar parameters, arranged in a coarse grid. The set of parameters of the model-spectrum that fits best of this set is then used as the starting parameter. Again, we compare the resulting values with the literature values. The found values appear to cluster around the values that have been checked in the coarse starting parameter grid. While their steps are small compared to the model step sizes, it is still suggesting that the steps in searching the starting values are too large compared to the changes the MPFIT algorithm performs. However, as this search for the starting parameter is already the bottleneck of this method, we decided to go with a Monte-Carlo approach instead. In all cases, the uncertainties of the stellar parameters returned by the Levenberg-Marquardt-algorithm are very low. The statistical uncertainties are much smaller than the grid-spacing, which as systematic errors define our lower limit for the errors: We are only estimating the change in spectra in between those actually calculated by PHOENIX. It is possible that the spectrum changes in a fashion not described by our polynomial ansatz, for instance, in reality there might be a sharp change in spectrum at a particular value, e.g. for T_{eff} , but our interpolation approach assumes a smooth change. We must conservatively assume the error to be at least as high as half a grid spacing.

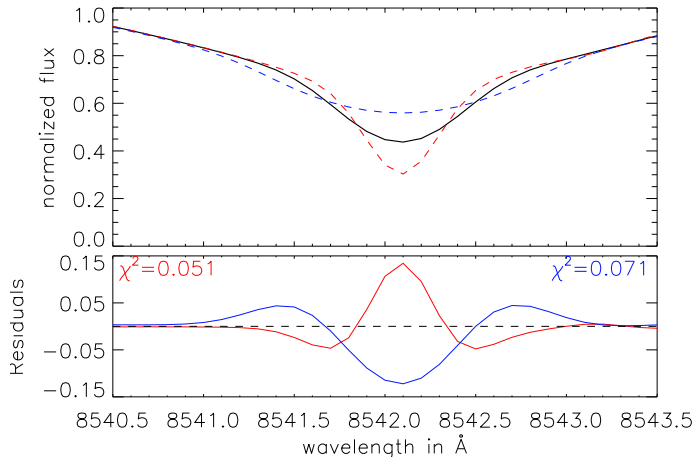


Figure 6.6: **Illustrating the problem of fitting rotational velocity.**

We try to fit the black spectrum from the current iteration (top plot, red dashed line), where the value for $v \sin i$ is too low. When calculating the partial derivative of χ^2 in regards to $v \sin i$, $v \sin i$ is adapted and increased, resulting in a spectrum that is too shallow (top plot, blue dashed line). The residual structure (bottom plot, same colors) has reversed and the value for χ^2 increased. Therefore, the algorithm will now pick a lower $v \sin i$ for the next iteration.

6.2.2 Fitting the spectrum with a Markov Chain Monte Carlo

Another option of finding the correct stellar parameters is by using a Markov Chain Monte Carlo (MCMC) sampler². In this procedure, the parameters are varied randomly. The new set of parameters of each step is either accepted or rejected, with a random chance based on how much better the new parameters describe the data, which in turn is here determined by the χ^2 -values. Since the algorithm can allow a step even if the proposed new parameters are a worse fit, this is not a simple hill-climbing algorithm. We used solar parameters as the starting values, and the code implementation by Zobitz et al. [2011], which uses the adaptive Metropolis-Hasting Algorithm [Metropolis et al., 1953]. It defines that the next parameter step is chosen from their current values from a normal distribution, with the width of it being changed automatically to ensure that 50% of samples are rejected. This method has the advantage of exploring a larger fraction of the parameter space, but at the cost of a higher runtime, as a large number of iterations are required. Errors can be estimated from a histogram obtained from the stellar parameters sampled during the sampling procedure, which approximates the posterior. The list of all samples is called the trace. If a proposed sample is rejected, the previous one is added to this list. Figure 6.8 shows the final 10 000 samples from the trace of HD 111456 for the four parameters fitted, and their resulting histogram. The found parameter is the maximum of the distribution, whereas the errors are estimated from the width. To ensure that a reasonable value is found even in asymmetric or otherwise unusual cases, we find the range around the best parameter that 68% of samples lie in. However, the errors found in this fashion are extremely small, and not representative, as the grid-spacing defines the true lower limit for our errors, as described above. In Fig. 6.9, we show the results from the MCMC algorithm, where we have used 150 000 iterations for each spectrum and compare them to literature values. We generally note a good match between fitted and literature values. However, this way of determining the stellar parameters is much slower than the Levenberg-Marquardt fit.

6.3 Results and comparison

We show the result of the fitting procedure in Table 6.4 and Table 6.5 for the Levenberg-Marquardt algorithm using the starting parameter set determined from the grid search, or the MCMC approach, respectively. These two approaches correspond to the interesting case of least information, with no prior knowledge of the actual star's parameters, except for the assumption that they can be suitably described by interpolating our model spectra. The statistical uncertainties as determined are unrealistically low, no matter the method. For this reason, they have been set from the grid spacing as described in the previous sections. It is interesting to compare the results of both methods,

²A great introduction to MCMC can be found in Wiecki [2015]

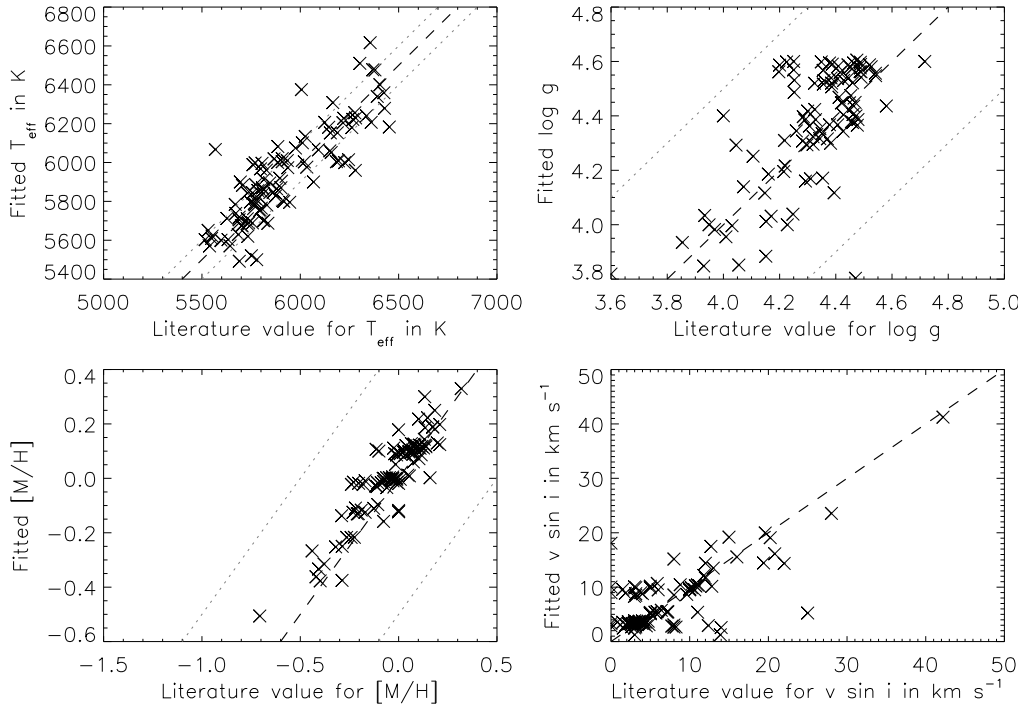


Figure 6.7: **Comparing fitted stellar parameters to literature values, for the case of the best grid search result as starting parameters.** Same as Fig. 6.4, but with starting parameters chosen from a grid search.

which is done in Figure 6.10.

Generally speaking, both methods are in agreement, as the deviations in fitted values are usually rather small compared to the scale given by the usual grid-spacing. However, for T_{eff} , a larger number of objects deviate by more than 100 K. Since the Levenberg-Marquardt algorithm did not often deviate too far from the starting value obtained from sampling a grid, especially in $[M/H]$ and $v \sin i$, it may very well have tried correcting the resulting error by adapting T_{eff} . For the other parameters, the offsets are less strong. We note that the results from the MCMC-approach tend to be higher in $\log g$, though this tendency disappears at $\log g \approx 4.5$, close to the solar value. Metallicity, an important parameter in the description of the Ca II IRT-lines, has been fitted tendentially lower in the MCMC approach, and additionally does not show the strong clustering around the starting set of values that the fitted parameters from the Levenberg-Marquardt method show. This may have been from a poor choice of grid sampling starting values, however.

To find out which of the two methods is the better one, we calculate χ^2 across the regions fitted (ignoring the masked regions), and compare the results. By dividing the values for χ^2 of both approaches, we can easily see which of the two algorithms was a better fit and resulted in stellar parameters that show less deviation from the observed one. This is shown in Fig. 6.11, where each point refers to one object. Plotted is the ratio of the χ^2 -values, so that a value larger than 1 means that the Levenberg-Marquardt results described the spectrum better, whereas a value less than 1 means that the MCMC results describe the spectrum better. To ensure a fair comparison of only the stellar parameters, the other parameters given in Table 6.3 were fitted another time while keeping the stellar parameters constant. Afterwards, the value for χ^2 was calculated and the ratio derived. The results show that the MCMC approach resulted in the “better” parameters in almost all cases, corresponding to the lower value for χ^2 . The median value across all objects for this ratio is 0.91, which implies that one can expect a 10% worse χ^2 when using the Levenberg-Marquardt algorithm. The 11 out of 105 stars for which that algorithm resulted in better fits are

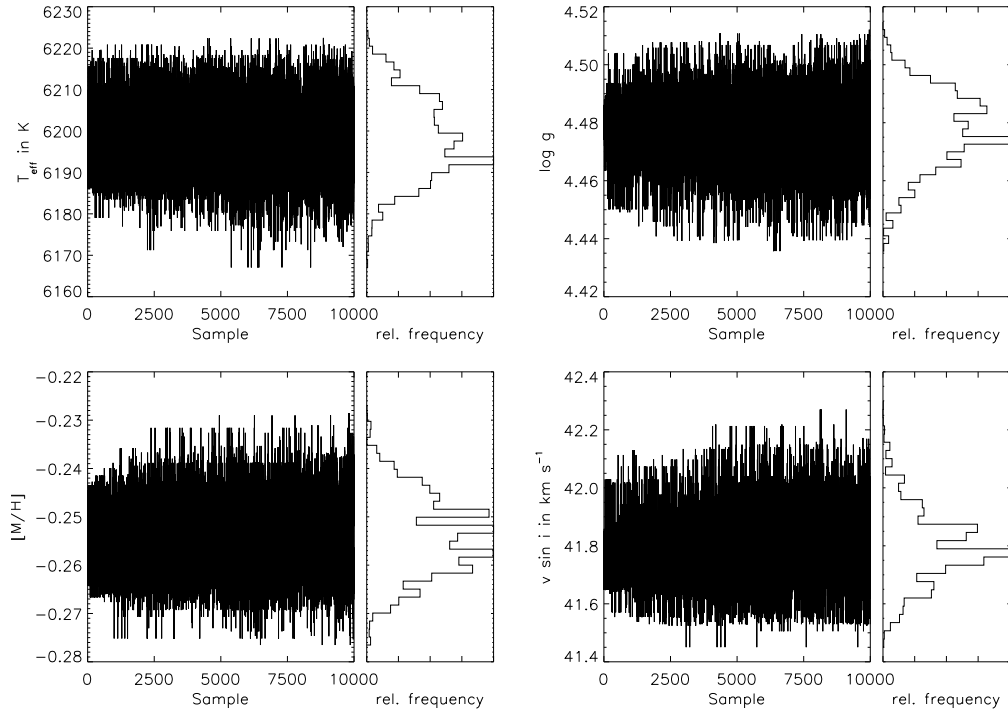


Figure 6.8: **Determining “best-fit” value and errors from the trace.** The left-hand side of these plots show 10 000 elements of the trace, that is the list of accepted points sampled, of HD 111456 for T_{eff} (top left), $\log g$ (top right), $[M/H]$ (bottom left) and $v \sin i$ (bottom right).

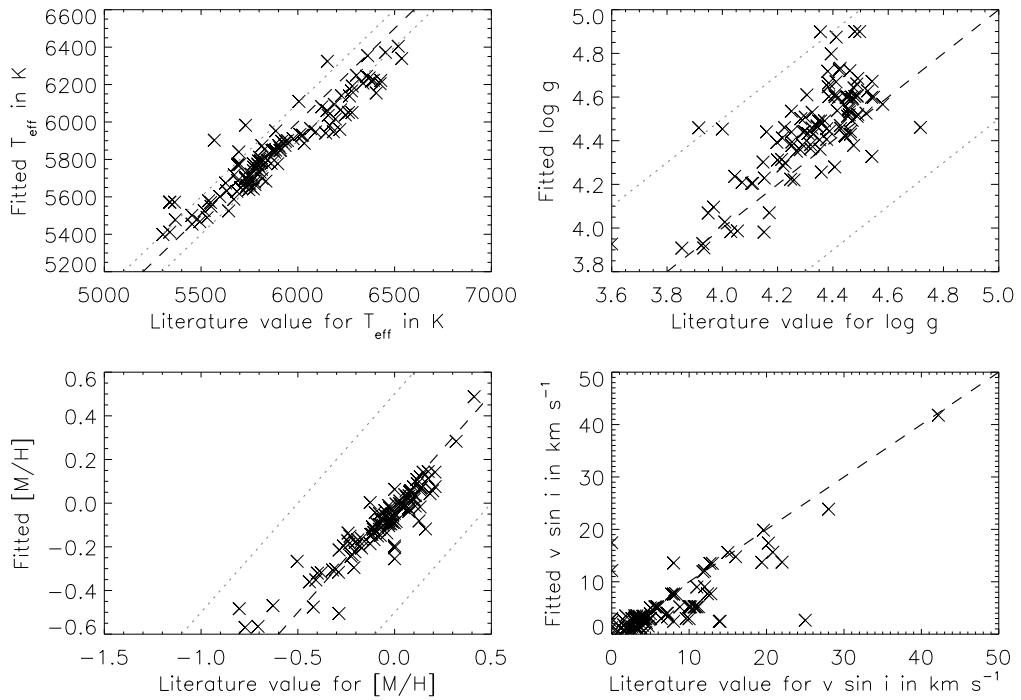


Figure 6.9: **Comparing fitted stellar parameters to literature values, for the MCMC approach.** Same as Fig. 6.4, but this plot shows the result of the MCMC algorithm.

Table 6.4: **Result of the Levenberg-Marquardt-Fit, with starting parameters searched from a grid search.** The fit has been performed as described in the text, with the regions and masked given in Table 6.1 and Table 6.2. Other parameters have been fitted that are not shown here, such as resolution and a wavelength shift, see Table 6.3. The errors are defined by the grid spacing, and are therefore 50 K, 0.10 for $\log g$, and 0.12 for $[M/H]$, and 1 km s^{-1} . This is part of the full table, which can be found in the Appendix in Table B.7

Object	T_{eff}/K	$\log g$	$[M/H]$	$v \sin i/\text{km s}^{-1}$
HD 157214	5491	4.36	-0.38	8.5
HD 168009	5499	4.00	-0.00	3.8
HD 129333	5520	3.80	+0.00	14.4
HD 184385	5570	4.56	+0.12	3.3
HD 178428	5570	4.04	+0.12	3.5
HD 43162	5600	4.54	+0.00	8.7
HD 82885	5602	4.59	+0.33	5.5
HD 111395	5603	4.55	+0.07	3.1
HD 68017	5609	4.41	-0.27	9.6
HD 42807	5620	4.38	-0.01	9.0
HD 115617	5621	4.51	-0.00	3.4
HD 140538	5629	4.45	+0.01	5.4
HD 117176	5650	3.98	-0.03	3.1
HD 20619	5674	4.45	-0.22	3.5
HD 20630	5675	4.54	+0.01	5.5
		⋮		

Table 6.5: **Result of the MCMC-Fit.** See caption of Table 6.5. The errors are defined by the grid spacing, and are therefore 50 K, 0.10 for $\log g$, and 0.12 for $[M/H]$, and 1 km s^{-1} . This is part of the full table, which can be found in the Appendix in Table B.8

Object	T_{eff}/K	$\log g$	$[M/H]$	$v \sin i/\text{km s}^{-1}$
HD 82443	5398	4.60	+0.00	5.2
HD 145675	5411	4.60	+0.49	1.8
HD 152391	5454	4.60	-0.03	3.1
HD 131156A	5467	4.60	-0.14	2.9
HD 3795	5477	4.46	-0.47	0.7
HD 117176	5489	4.10	-0.10	2.8
HD 101501	5501	4.60	-0.08	3.5
HD 178428	5524	4.22	+0.07	0.7
HD 82885	5525	4.61	+0.28	3.3
HD 115617	5549	4.60	-0.06	2.8
HD 68017	5569	4.72	-0.36	0.8
HD 224930	5571	4.87	-0.57	3.1
HD 10700	5571	4.90	-0.27	0.6
HD 6582	5571	4.90	-0.48	3.4
HD 184385	5579	4.69	+0.09	2.9
		⋮		

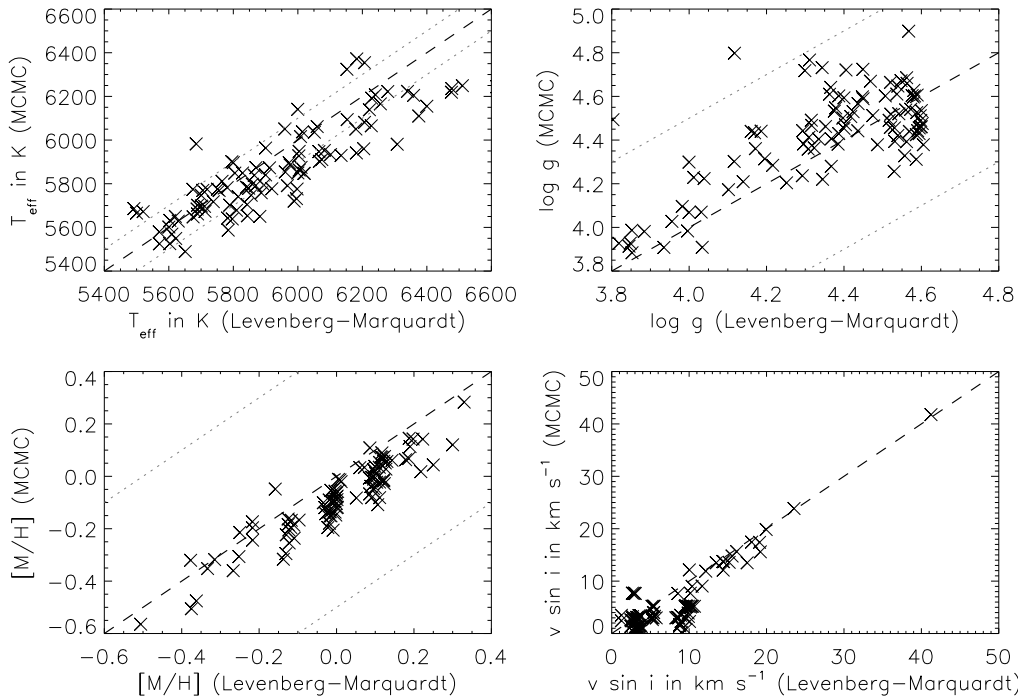


Figure 6.10: **Comparing the fitted stellar parameters from the Levenberg-Marquardt-method combined with a grid search to the results from the MCMC approach.** Same as Fig. 6.4, but this plot compares the results of two different fits.

covering a range in $B - V$, so it appears that there is no clear range in stellar parameters for which Levenberg-Marquardt results in a better fit. The same is true when plotting against T_{eff} , $\log g$ or $[M/H]$. While this strongly implies that MCMC is the better choice, there is an argument to be made for the Levenberg-Marquardt-approach. After all, its runtime is orders of magnitudes shorter, which is very useful for the automatic approach of analyzing a large number of objects. Since the deviations in found values tends to be small compared to the typical grid-spacing (Fig. 6.10), it can be argued that the result from the Levenberg-Marquardt approach is good enough for many cases, if combined with a grid-search to find suitable starting parameters. Rotational velocity may need to be estimated rather reliably beforehand. Still, even then the found parameters often do not deviate much from those grid-aligned starting values, which can be a problem for some applications, or if the starting value search samples the grid more coarsely. In that case, either a tighter grid or a switch to the MCMC approach, both strongly increasing the runtime, can be chosen.

Finally, we note that we can also use the found parameters from the MCMC approach as starting values for a Levenberg-Marquardt fit. Results of this approach are detailed in the appendix.

6.4 Summary

It has become clear that the spectra interpolated are a powerful and useful tool to have. Combined with a fast and efficient interpolation algorithm that works reliably even for a non-regular grid, it is possible to fit TIGRE observations to model spectra. Here, we have described and explained the application of the algorithms described by McLain [1974, 1976] for this purpose, and have demonstrated the implementation that was done as part of this work. We were able to determine stellar parameters with this algorithm from just the prior assumption that the observed spectrum can suitably be described by interpolating our model spectra (i.e. is a main-sequence star of type F, G or K). It is clear from comparing the found parameters to literature values that this approach is feasible

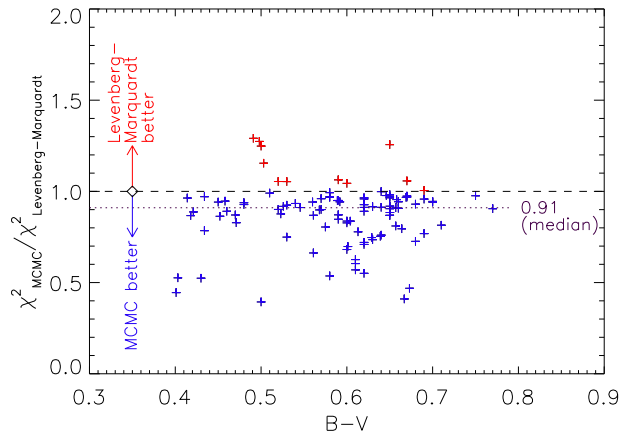


Figure 6.11: **Comparing the χ^2 -values for the fitted parameters for the two approaches discussed: Levenberg-Marquardt and MCMC.** Shown here is the ratio of the χ^2 -values, first derived from the fit using the set of stellar parameters obtained via MCMC, and this value then divided by the χ^2 value from the fit using the set of parameters obtained via Levenberg-Marquardt. Every point corresponds to one of the stars fitted, and the result is then plotted against the star's $B - V$. The ratio is below 1 for 94 out of 105 cases, implying that MCMC resulted in the better fit in almost 90% of cases. The median value of this ratio is 0.91.

and that the obtained parameters can be trusted and used in further science, as we plan on doing for the excess flux determination in the next chapter. Finally, we have compared the approach using the Levenberg-Marquardt and MCMC algorithms, and have discussed their differences in detail. It has become apparent that MCMC resulted in better fits, but both algorithms yielded satisfactory results. We will continue using the stellar parameters from the MCMC algorithm.

Chapter 7

Comparing TIGRE Observations to PHOENIX models

In this chapter, we apply the method described in Chapter 3 to compare TIGRE spectra of stars with $B - V$ of 0.4 to 0.8 to PHOENIX model spectra. This allows us to find the chromospheric flux of these stars, including the basal component, which we attempt to isolate and define in a later chapter. We compare the observed spectra with the PHOENIX models interpolated to the best-fit values obtained for the observed star in the previous chapter.

In this chapter, we analyze the results of 3630 observations of 109 stars. Unlike before, we also analyze the inactive stars, increasing the sample size despite the lower range in $B - V$. We then give a quick comparison of the results of Chapter 4.

7.1 Introduction and goals

Here, we compare TIGRE spectra to PHOENIX model spectra for an individual star according to the procedure described in Chapter 3. Unlike before, however, the PHOENIX models we are using do not include a chromospheric component. This means that the excess after the subtraction of the PHOENIX model spectrum is:

$$F_{\text{Exc}} = F_{\text{chrom,basal}} + F_{\text{chrom,act}}, \quad (7.1)$$

a combination of the chromospheric basal flux $F_{\text{chrom,basal}}$ [Schrijver, 1987] and the purely activity-related flux $F_{\text{chrom,act}}$. The basal flux has not been included in the previous comparison, as it was also included in the comparison spectrum, and therefore also subtracted. The results of this chapter will allow us to estimate F_{basal} , the residual flux component the chromosphere always contributes, regardless of activity. In Chapter 9, this will be performed by analyzing the values for F_{Exc} we obtain in this chapter, using various different methods.

In this approach, the search for a comparison star has been replaced by fitting PHOENIX model spectra to the star, which we have described in Chapter 6. In this chapter, we use the results of the MCMC-approach (Sect. 6.2.2), as they have been found to be the most reliable. The actual comparison is similar to that in Chapter 4, with a few differences we describe in the next section. Previously, we divided our sample into “active” and “inactive” stars, based on the classification of $\log R'_{\text{HK}} \geq -4.75$, as given in Henry et al. [1996]. Such separation is now no longer necessary. All stars will be handled in the same way in this approach, as even the inactive stars are expected to show $F_{\text{Exc}} > 0$, due to the non-vanishing component of the basal flux.

7.2 Differences in the method to Chapter 4

As we are now comparing to a PHOENIX model spectrum, some changes were made for the excess flux determination. Some of these were necessary in order to obtain the real value, while others have

been made possible due to the lower overall noise. This section lists the major differences between the procedure performed in this chapter to the one from Chapter 4.

7.2.1 Fit of the resolution

We are now comparing a TIGRE spectrum to a PHOENIX model spectrum. The latter is originally given in a much higher resolution of $R \approx 500\,000$. We therefore are required to degrade the resolution to the TIGRE resolution of $R \approx 20\,000$. To first order, we can simply degrade all PHOENIX spectra to this resolution before we begin. We have performed this step, and all model spectra we are interpolating already have $R = 21\,000$. However, as we have seen in Sect. 2.6.2, the actual resolution of TIGRE spectra varies strongly, and has been given as low as $R \approx 16\,000$ in some cases. Neglecting this effect results in finding a negative excess value, as the additional broadening from the lower resolution results in shallower lines. However, the exact value of the resolution is unknown, and depends on the wavelength, and so must be determined individually for each line beforehand. To do so, we perform a fit using MPFit [Markwardt, 2009], with varying step sizes, to find the correct value of R . The rotational broadening must, of course, also be considered. At this point, the value for $v \sin i$ has been determined, and so we can simply add the rotational broadening according to that value of $v \sin i$ in the fitting process. The resulting value of R is then passed to our routine, which performs the degradation and takes the errors into account. This fitting process has not been performed for the Ca II H- & K-lines. This is due to the broad intrinsic shape of these lines, which reduces the effects of lower resolution.

We have performed the entire comparison process without this step as well. The overall results are very similar, but the scatter – especially of the parameters of the Gaussians we fit to the excess distribution – is higher, and the correlations lower. We conclude that we were right in assuming the necessity of fitting the resolution. All further results given have been obtained by including this resolution fit.

7.2.2 Automatic determination of the excess region

Before, we have used TIGRE spectra of inactive stars for comparison. While we have taken great care to pick the best possible spectrum with the highest SNR, there was naturally still some residual noise left. The determined excess then suffers from the noise of the two spectra compared. Now, the comparison spectrum is free of noise (see below), and therefore the resulting excess distribution is less noisy as well. This allows us to automatically determine the region the integration is performed in, as described in Sect. 3.6. As a result, we lose less excess flux of the high-activity stars, and suffer from less noise for the lower-activity stars.

7.2.3 Noise of the comparison spectrum

The comparison spectra are free of noise, since they are PHOENIX model spectra. However, we have not determined the stellar parameters with infinite precision. An error on T_{eff} , for example, must therefore propagate into an error on the model. We have thus chosen a conservative approach and estimate the errors on the model spectra from the expected deviation in the spectrum from varying the stellar parameters within their errors. As the change in the model spectra is monotonous in this small range of the three stellar parameters T_{eff} , $\log g$ and $[M/H]$ (compare Fig. 5.8), it is enough to test the $2^3 = 8$ limiting cases. Therefore, we calculate the spectra with the following stellar parameters, and set the error to half the deviation of the largest and smallest flux derived for each wavelength point:

$$\begin{array}{ll} (T_{\text{eff}} + \Delta T_{\text{eff}}, \log g + \Delta \log g, [M/H] + \Delta[M/H]) & (T_{\text{eff}} - \Delta T_{\text{eff}}, \log g + \Delta \log g, [M/H] + \Delta[M/H]) \\ (T_{\text{eff}} + \Delta T_{\text{eff}}, \log g - \Delta \log g, [M/H] + \Delta[M/H]) & (T_{\text{eff}} - \Delta T_{\text{eff}}, \log g - \Delta \log g, [M/H] + \Delta[M/H]) \\ (T_{\text{eff}} + \Delta T_{\text{eff}}, \log g + \Delta \log g, [M/H] - \Delta[M/H]) & (T_{\text{eff}} - \Delta T_{\text{eff}}, \log g + \Delta \log g, [M/H] - \Delta[M/H]) \\ (T_{\text{eff}} + \Delta T_{\text{eff}}, \log g - \Delta \log g, [M/H] - \Delta[M/H]) & (T_{\text{eff}} - \Delta T_{\text{eff}}, \log g - \Delta \log g, [M/H] - \Delta[M/H]) \end{array}$$

We set the minimum error on the stellar parameters to $\Delta T_{\text{eff}} = 50\text{ K}$, $\Delta \log g = 0.125$ and for metallicity $\Delta[M/H] = 0.125$. In Fig. 7.1, we show an example for the case of a solar-like star

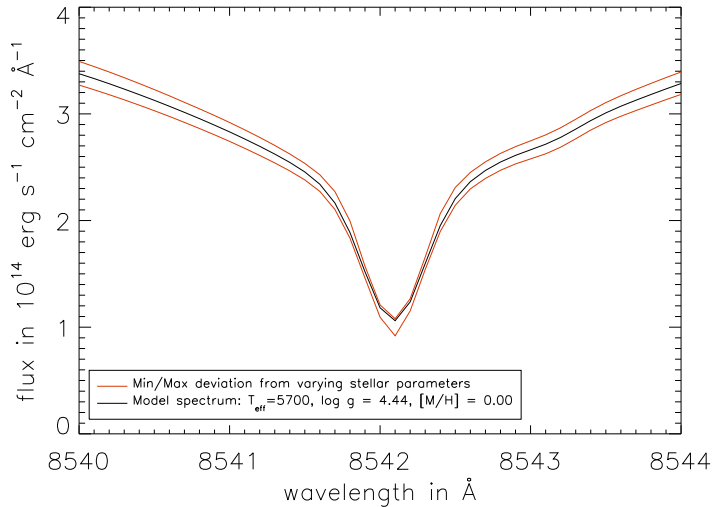


Figure 7.1: **Determining an error on the PHOENIX model spectra from the error on the stellar parameters.** The errors on the stellar parameters propagate to an error on the model spectrum. Varying the stellar parameters yield the upper and lower deviation (red lines) from the spectrum (black line).

(black line). Calculating the eight spectra yields a higher and lower value for each wavelength point (red line). Half this deviation is then taken to be the error at this wavelength point. The relative error is about a 5% relative error. This error is not statistical, but systematic in nature: If the stellar parameters actually were wrong, the effect would be a somewhat different shape of the model spectrum. This error is now used as if it were statistical in nature and independent for each wavelength point. This is especially noteworthy, as the formerly mentioned systematic error could, depending on its severity, be corrected by further steps performed during the comparison (e.g. by the shift to find an agreement in the wings). Therefore, interpreting this error as the error on the model is a conservative estimate, and may lead to an overestimation of the final error.

7.2.4 Limitations of the sample

When comparing to inactive stars as we have done in Chapter 4, we finally used a sample of 2274 observations of 82 stars, with $B - V$ values ranging from 0.4 to 1.2. Unfortunately, our model grid does not fully cover this region. While it is possible to extrapolate spectra from the available dataset (Sect. 5.3.6), the results are lackluster when extrapolating too far out of the covered range. This effect is magnified when the covered range is exceeded for several stellar parameters at once (e.g. T_{eff} and $\log g$). For this reason, it would be desirable to add further models to the model grid in the future. Because of the poor extrapolation, we now only cover the spectral range of $B - V = 0.4 \dots 0.8$. This includes the majority of stars from our previous sample (see also Fig. 2.10), and is the reason why this range was chosen for the model grid. Nevertheless, some stars that have been included in the previous sample are no longer included in this chapter. This is slightly made up for by the fact that no further division into two sets of “active” and “inactive” is necessary. Therefore, stars that did not fulfill the $\log R'_{\text{HK}} \geq -4.75$ criteria [Henry et al., 1996] are included in this sample, but not in the previous one. These stars are rather inactive, and their determined low excess flux features a high relative error.

7.3 Outliers and objects not suitable for this analysis

For some spectra, the procedure failed and no adequate excess could be determined. In Table 7.1, we give a list of the stars that were removed from this particular sample, as well as the reason for it. $B - V$ values given are literature values, mostly from the PASTEL-catalog [Soubiran et al., 2010], see Sect. 4.2. We have removed a lower number of stars than when we were comparing to inactive stars (Chapter 4). The reason for this is that some of the stars removed previously fall outside the

Table 7.1: **Stars that were removed from the sample.** This table gives the stars that were removed from the sample, as no adequate excess could be determined for them, for the reason given below.

Star	$B - V$	Reason
HD 111456	0.43	Low SNR in the line center and high $v \sin i$
HD 106516	0.46	Binary star
HD 88737	0.53	Low SNR in the line center
HD 100563	0.53	Low SNR in the line center
HD 6920	0.56	Possible subgiant (see Sect. 4.6)
HD 197027	0.65	Low SNR in the line center
HD 133640A	0.65	Binary star

$B - V$ -range considered here, as we had to decrease it due to the limitations of our model grid. For some stars, the lower levels of noise introduced by the PHOENIX model spectra allows us to use their results now. For those, it was previously impossible, as the additional noise introduced from the comparison spectrum pushed the noise of the excess distribution just above the threshold. This effect is made stronger, as the automatic approach in finding the excess bandpass the integration is performed in removes regions with no excess flux in them. We give more details on the remaining sample under consideration here in Table 7.2. The amount of F-stars has dramatically increased. However, due to the grid sampling, the amount of K-stars is down to only four objects, though with still more than a hundred observations. All in all, despite the lower $B - V$ -validity range, we could still perform this procedure with more stars and observations overall, with 109 stars and 3630 spectra analyzed.

For some correlations, we will disregard the “inactive” stars with $\log R'_{\text{HK}} < -4.75$. The reason for this is that their low excess level (close to the basal level), compared to their rather high noise, only adds scatter to the obtained relations. They should not be used to define the level of correlation of the activity-related excess flux. An overview over this smaller sample with this enforced condition is given in Table 7.3. Reintroducing this criterion reduces the sample to 81 stars with 2148 observations.

Table 7.2: **Overview of the data used in this chapter, categorized by spectral type.**

Type	# Obj.	# Obs.	SNR min/med/max	Exp. time [s] min/med/max
F	33	1113	21.0 / 58.3 / 161.3	60 / 300 / 3550
G	72	2416	20.9 / 60.8 / 136.8	60 / 660 / 4767
K	4	101	35.7 / 63.6 / 83.6	180 / 752 / 4051
Total	109	3630	20.9 / 60.1 / 161.3	60 / 524 / 4767

Table 7.3: **Overview of the data sample used in this chapter, categorized by spectral type, if the criterion $\log R'_{\text{HK}} > -4.75$ is reintroduced.**

Type	# Obj.	# Obs.	SNR min/med/max	Exp. time [s] min/med/max
F	22	559	25.4 / 59.6 / 161.3	60 / 360 / 3215
G	57	1515	20.9 / 60.6 / 114.0	60 / 793 / 4767
K	2	74	35.7 / 65.5 / 83.6	180 / 692 / 4051
Total	81	2148	20.9 / 60.3 / 161.3	60 / 608 / 4767

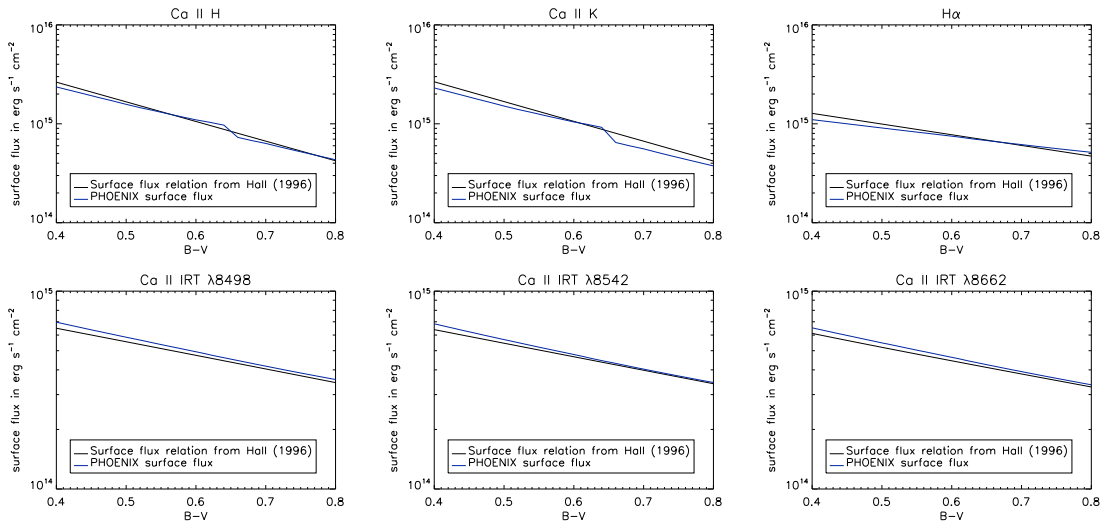


Figure 7.2: Comparing the surface flux relations from Hall [1996] (black) to those obtained by integrating the continuum derived from PHOENIX model spectra (blue) at the different lines. Overall, both relations match, but there is an offset that depends on $B - V$. The jump, especially noticeable for the Ca II H- & K-lines, appears at $B - V \approx 0.65$, corresponding to a jump in the used tabulated $\log g$ -values.

7.4 Difference in flux scale to Chapter 4

We are interested in excess flux values, in units of $\text{erg s}^{-1} \text{cm}^{-2}$. As TIGRE spectra are not flux-calibrated, we need to convert that arbitrary scale to the real units. This step has made use of the relation $F_{\text{cont,Hall}}(B - V)$ by Hall [1996] in Chapter 4, but we now use the flux scale as given by the PHOENIX model spectra. This alone may produce a systematic difference in the obtained values. To find this difference, we take the average of the continuum (see Sect. 3.2) of PHOENIX models with different $B - V$ at the different line positions in a 1 \AA -wide bandpass. Since we require T_{eff} and $\log g$ to interpolate the model spectra correctly, but $B - V$ for the relations given by Hall [1996], we convert the $B - V$ scale to a T_{eff} -scale via the relation of Gray [2005]:

$$\log T_{\text{eff}} = 3.981 - 0.4728 \cdot (B - V) + 0.2434 \cdot (B - V)^2 - 0.0620 \cdot (B - V)^3. \quad (7.2)$$

To find a realistic main-sequence star value for $\log g$, we interpolate the given typical values of $\log g$ in Gray [2005] (their Table A.2) to the required $B - V$ value. In the end, we obtain a value $F_{\text{cont,model}}(B - V)$ in this fashion, which we can now compare to $F_{\text{cont,Hall}}$. Figure 7.2 shows the result in the range of $B - V$ from 0.4 to 0.8 for the six lines we are considering here. The relations are notably similar. For the Ca II IRT-lines, the deviation is always less than 6%, and about 4% on average. Here, the surface flux derived from the PHOENIX model spectra (blue line) is always higher. Contrary to that, it is always lower for the Ca II H- & K-lines, where the average deviation is also 6% higher for Ca II H and 10% for Ca II K. The maximum deviation is 10% for Ca II H and 24% for Ca II K. For the $H\alpha$ -line, the deviation is varying – the derived surface flux from using the relations given by Hall [1996] spectra is higher for the lower $B - V$ values and vice versa. The deviation is about 5% on average. The PHOENIX surface flux for the Ca II H- & K-lines shows an irregular jump, unlike the smooth analytical relation from Hall [1996]. This jump occurs at $B - V \approx 0.65$. This corresponds to a jump in $\log g$ from the tabulated values, however, this is likely by chance, as the position of this jump shifts, depending on the metallicity of the PHOENIX model. Performing the same procedure to determine the surface fluxes, yet this time using a linear fit $\log g(B - V)$ to the tabulated values reduces the height of the jump, but does not make it disappear. It is likely that some lines change so strongly that the continuum determination is affected, especially

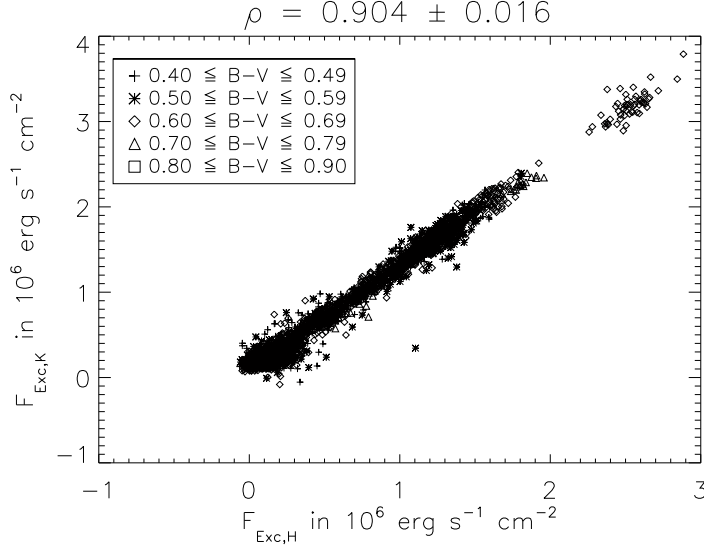


Figure 7.3: **Correlation of the determined excess flux in the Ca II H and Ca II K-lines.** This plot includes data from 3630 observations of 109 stars.

in the complicated region surrounding the Ca II H- & K-lines. However, the effect is not too strong: This jump is covering a very narrow region in $B - V$, and therefore not too many stars will be affected. Additionally, the deviation found is not so large overall, so that this should only increase the scatter somewhat. Assuming that the relations should be smooth in $B - V$, we can perform a linear fit to the surface flux ratio. These can be used to correct the effects of using the different surface flux deviations. The relations are:

$$\begin{aligned}
 F_{\text{cont,H,Hall}}/F_{\text{cont,H,PHOENIX}} &= 1.173 - 0.219 \cdot (B - V) & (7.3) \\
 F_{\text{cont,K,Hall}}/F_{\text{cont,K,PHOENIX}} &= 1.054 + 0.125 \cdot (B - V) \\
 F_{\text{cont,H}\alpha,\text{Hall}}/F_{\text{cont,H}\alpha,\text{PHOENIX}} &= 1.391 - 0.589 \cdot (B - V) \\
 F_{\text{cont,IRT}\lambda 8498,\text{Hall}}/F_{\text{cont,IRT}\lambda 8498,\text{PHOENIX}} &= 0.903 + 0.090 \cdot (B - V) \\
 F_{\text{cont,IRT}\lambda 8542,\text{Hall}}/F_{\text{cont,IRT}\lambda 8542,\text{PHOENIX}} &= 0.889 + 0.136 \cdot (B - V) \\
 F_{\text{cont,IRT}\lambda 8662,\text{Hall}}/F_{\text{cont,IRT}\lambda 8662,\text{PHOENIX}} &= 0.897 + 0.105 \cdot (B - V)
 \end{aligned}$$

This offset in surface flux is especially important when we are comparing the obtained excess fluxes from comparing to model spectra to those obtained from comparing to inactive stars, as the difference between the two can be used to estimate the basal flux. As it tends to be small, this $\sim 10\%$ difference must be corrected to not under- or overestimate the basal flux level.

7.5 Resulting flux and correlations

We have obtained the excess fluxes as described, and now show the results from 3630 observations of 109 stars. First, we consider the correlation between the Ca II H and Ca II K line, shown in Fig. 7.3. We expect a very large correlation between the two, and in fact we observed exactly that in Chapter 4, where we found $\rho \approx 0.95$. Here, we have a nominally lower Spearman correlation coefficient of $\rho = 0.90$. However, the distribution is much smaller, with lower scatter, which is reflected in a higher Pearson correlation coefficient. It is $\rho_{\text{Pearson}} = 0.991$ here for our comparison to models, but “only” $\rho_{\text{Pearson}} = 0.965$ for the comparison to inactive stars. This mirrors the visual impression of the tighter linear fit. Since a clear linear relation between the excess fluxes of the two lines is expected, the higher Pearson correlation coefficient indicates an improvement in the procedure from the changes discussed in Sect. 7.2. To perform this same comparison for the Ca II IRT-lines, we need to perform the filtering and only consider stars with $\log R'_{\text{HK}} > -4.75$. The reason for this is that the stars not fulfilling this condition have a very low level of residual

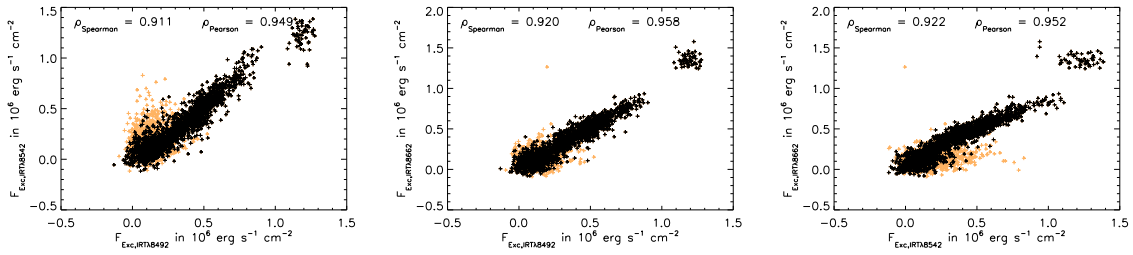


Figure 7.4: **Checking the correlation between the excess fluxes in the individual Ca II IRT-lines, obtained by comparing to PHOENIX model spectra.** The correlation coefficients are given in the plots, but only the data points of active stars fulfilling $\log R'_{\text{HK}} > -4.75$ (black) are taken into account for that calculation. The inactive stars that do not fulfill this condition are plotted in bright orange.

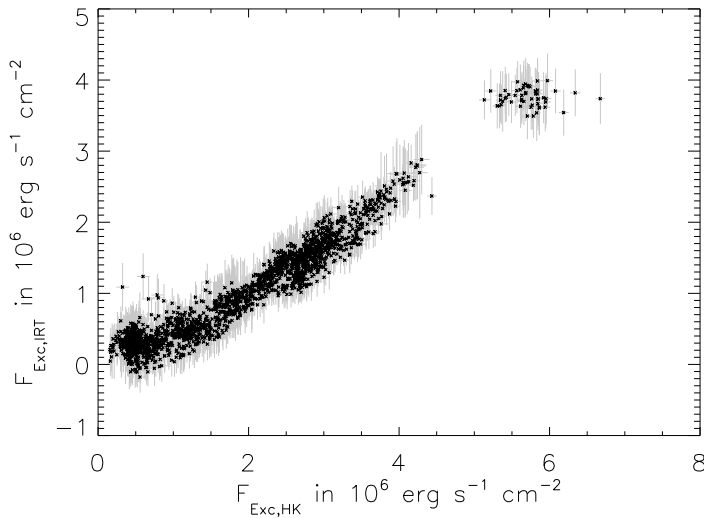


Figure 7.5: **Comparing the error on the determined excess fluxes to the correlation distribution.** The gray lines indicate the errors on the determined excess fluxes (black crosses). They appear larger than the scatter inherent in the distribution, suggesting that they may be overestimated.

flux, which cannot reliably be disentangled from the noise on these spectra. The data points of their determined excess flux therefore appears as a scattered cloud close to the zero-level. This was less of a problem in the Ca II H- & K-lines, as the flux is about three times larger there. We show the correlations of the individual Ca II IRT-lines in Fig. 7.4, where the bright orange points are those of stars that do not fulfill $\log R'_{\text{HK}} > -4.75$, and have not been taken into account when determining the correlation. Comparing the Pearson correlation values here to the corresponding ones from Chapter 4, which are $\rho_{\text{Pearson}} = 0.976$, $\rho_{\text{Pearson}} = 0.982$ and $\rho_{\text{Pearson}} = 0.977$, respectively, we find that the previous comparison yielded the better values, in the sense of a stronger linear correlation. This might be due to the difficulties from the variable resolution fitted, which is less significant for the broader Ca II H- & K-lines, or a general error on the line profile from the PHOENIX model spectra in the Ca II IRT-lines. It is therefore clear that this approach is not universally better, however, it is also not worse, depending on the lines we are interested in. Finally, we note that the correlations are very high across all lines considered, and we are comparing at a very high quality level. Due to the large amount of error-prone parameters that go into the determination of the excesses, the obtained excess fluxes have rather large errors. Comparing the error bars to the correlation (Fig. 7.5) suggests that we may have overestimated the errors for the Ca II IRT lines and the H α -line, due to the conservative approach taken. As a result, the correlation coefficient itself has a rather large error, as determined from Monte-Carlo sampling. To give a fair value for the correlation, we filter out the stars with $\log R'_{\text{HK}} < -4.75$ in the calculation of the correlation. We give the resulting

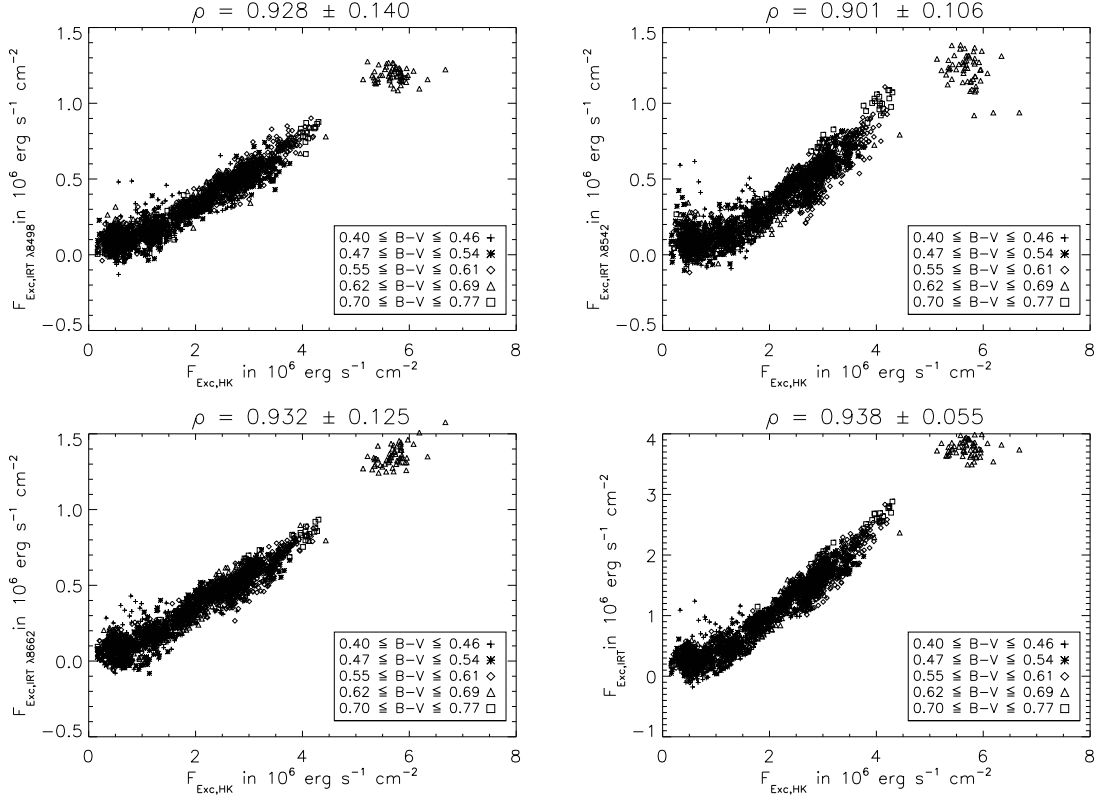


Figure 7.6: Measured chromospheric excess flux, obtained by comparing TIGRE spectra to PHOENIX model spectra, in the Ca II H- & K-lines compared with the excess flux in the individual Ca II IRT-lines, as well as the sum of all Ca II IRT-lines (bottom right). This plot includes data from 2148 observations of 81 stars.

values of the individual correlations in Table 7.4, and show the correlations between the $\text{H}\alpha$ -line, the Ca II IRT-lines and the Ca II H- & K-lines in Fig. 7.6 and Fig. 7.7. In general, we find a very strong correlation between the calcium lines, both on an individual level, but also when grouped together. While the correlation tends to be lower than before, likely related to the previously discussed higher scatter in the Ca II IRT excess fluxes, the correlation coefficients are still very large. However, the correlation coefficients between the calcium lines and the $\text{H}\alpha$ -line have decreased dramatically. While $\rho \approx 0.7$ still indicates a correlation, this value is lower than our previous result (when comparing to inactive stars, we found $\rho \approx 0.82$). This might be due to difficulties in accurately modeling the $\text{H}\alpha$ -line profile. It is also apparent that the correlation between the $\text{H}\alpha$ -line and the calcium lines is not linear, mirroring the result from Chapter 4. We will come back to this when converting the excess fluxes into one another (Chapter 8).

For all the lines shown, excess fluxes below zero have been determined, however, only for a few spectra from a small selection of stars. For those, the noise level found is of the order of the chromospheric flux. Therefore, the noise on the spectrum, as well as the errors on the stellar parameters, can be enough to dominate the residuals, hiding the excess flux. An example is shown in Fig. 7.8. The number of points below zero is lower when compared to the results of Chapter 4, despite the similar number of points total. The likely explanation for this is the additional chromospheric basal flux that is included in the excess determined here.

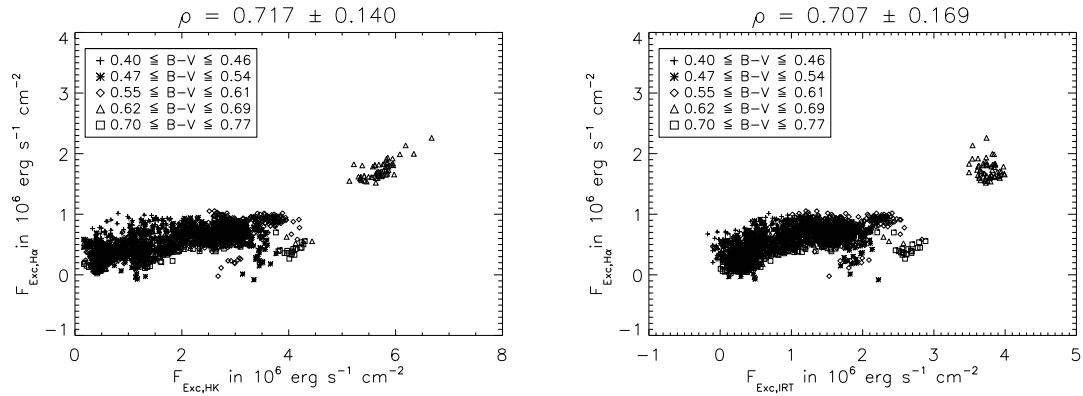


Figure 7.7: Comparing the measured chromospheric excess flux in the $H\alpha$ -line with the excess flux in the Ca II H- & K-lines (left) and Ca II IRT-lines (right). This plot includes data from 2148 observations of 81 stars.

Table 7.4: Obtained Spearman correlation coefficients between the integrated excess fluxes in the different lines. The excess was determined by comparing the TIGRE spectra of stars fulfilling $\log R'_{HK} > -4.75$ to PHOENIX model spectra.

		— Ca II H & K —			— Ca II IRT —				
		$\lambda 3968$	$\lambda 3934$	Sum	$\lambda 8498$	$\lambda 8542$	$\lambda 8662$	Sum	$H\alpha$
Ca II H & K	$\lambda 3968$	—	0.98	0.99	0.93	0.90	0.93	0.94	0.71
	$\lambda 3934$	0.98	—	1.00	0.92	0.90	0.93	0.93	0.72
	Sum	0.99	1.00	—	0.93	0.90	0.93	0.94	0.72
Ca II IRT	$\lambda 8498$	0.93	0.92	0.93	—	0.91	0.92	0.97	0.69
	$\lambda 8542$	0.90	0.90	0.90	0.91	—	0.92	0.97	0.68
	$\lambda 8662$	0.93	0.93	0.93	0.92	0.92	—	0.97	0.70
	Sum	0.94	0.93	0.94	0.97	0.97	0.97	—	0.71
	$H\alpha$	0.71	0.72	0.72	0.69	0.68	0.70	0.71	—

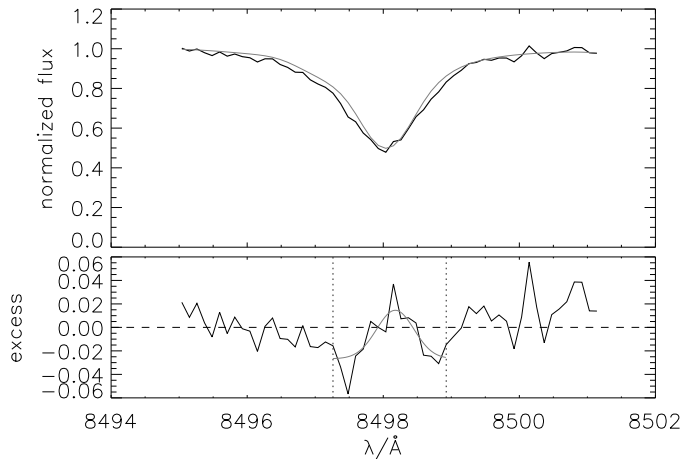


Figure 7.8: Determining a negative excess flux for HD 18256. *Top*: Finding the excess by comparing the spectrum (black line in top plot), taken on January 4th, 2014, to the corresponding PHOENIX model spectrum (gray line). *Bottom*: The residuals correspond to the excess, which is shown in black. The overall distribution is so noisy that the integrated excess flux would here be determined to be negative. The fitted Gaussian (gray line) is found to be positive, due to an introduced offset of it.

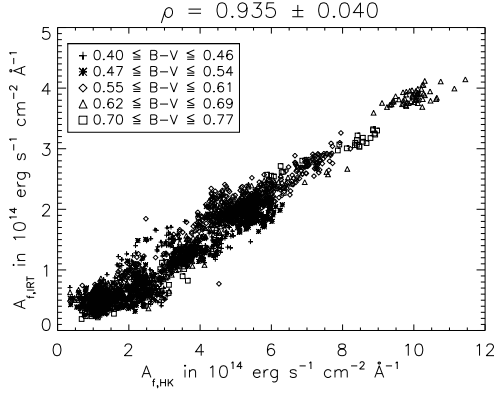


Figure 7.9: **Correlation between the sum of the amplitudes A_f of the Gaussians fitted to the excess distribution of the Ca II H- & K-lines (abscissa) and the Ca II IRT-lines (ordinate).** This plot only includes data of spectra fulfilling $\log R'_{\text{HK}} > -4.75$: 2148 spectra of 81 stars.

Table 7.5: **Obtained Spearman correlation coefficients between the Gaussian amplitude A_f fitted to the excess distribution in the different lines.** The excess was determined by comparing the TIGRE spectra of stars fulfilling $\log R'_{\text{HK}} > -4.75$ to PHOENIX model spectra.

		— Ca II H & K —			— Ca II IRT —				
		$\lambda 3968$	$\lambda 3934$	Sum	$\lambda 8498$	$\lambda 8542$	$\lambda 8662$	Sum	H α
Ca II H & K	$\lambda 3968$	—	0.97	0.99	0.91	0.93	0.91	0.93	0.66
	$\lambda 3934$	0.97	—	0.99	0.91	0.93	0.90	0.93	0.66
	Sum	0.99	0.99	—	0.92	0.93	0.91	0.94	0.66
Ca II IRT	$\lambda 8498$	0.91	0.91	0.92	—	0.94	0.91	0.98	0.69
	$\lambda 8542$	0.93	0.93	0.93	0.94	—	0.93	0.98	0.68
	$\lambda 8662$	0.91	0.90	0.91	0.91	0.93	—	0.96	0.68
	Sum	0.93	0.93	0.94	0.98	0.98	0.96	—	0.70
H α		0.66	0.66	0.66	0.69	0.68	0.68	0.70	—

7.6 Fitted parameters

Like before, we also obtain the parameters A_f , σ_f and $(\Delta\lambda)_f$ from fitting a Gaussian to the smoothed excess (see Sect. 3.6). We show the results of the correlation coefficients of the fitted amplitudes, converted to $\text{erg s}^{-1} \text{cm}^{-2} \text{\AA}^{-1}$, for all stars fulfilling $\log R'_{\text{HK}} > -4.75$ in Table 7.5 and Fig. 7.9. The conversion is necessary to remove the $B - V$ dependency, which we have already seen in Fig. 4.7, though it is less strong here, on account of the smaller range in $B - V$ covered. We again see large correlations with $\rho > 0.9$ between the calcium lines, and lower values for the correlations between those and the H α -line.

The width σ_f is very often close to the lower limit set for the fit, which is given by the TIGRE resolution. Disregarding the many points that lie at this lower limit, we find a correlation for the width between the Ca II IRT-lines of $\rho \approx 0.8$, but this correlation does not extend to the Ca II H- & K-lines ($\rho \approx 0.13$), and neither does it extend to the H α -line. It is likely then, that this is an effect of the resolution being approximately constant across the Ca II IRT region. This effect is not observed for the correlation of the individual Ca II H- & K-lines, as there the correlation for σ_f is $\rho \approx 0.24$. This suggests that the width we have obtained here is not a useful activity indicator, at least not when determined from spectra with TIGRE's resolution.

The position of the excess in the line $(\Delta\lambda)_f$ does not show a significant correlation this time, with $\rho \approx 0.25$ between the (summed) shifts in the Ca II IRT-lines and the Ca II H- & K-lines, if only the stars with $v \sin i > 20 \text{ km s}^{-1}$ are taken into account. This rather low value is only a weak indicator of a real existing correlation. As we have concluded in Chapter 4, the resolution of TIGRE, and the average SNR in the line centers, is simply too low for this kind of analysis.

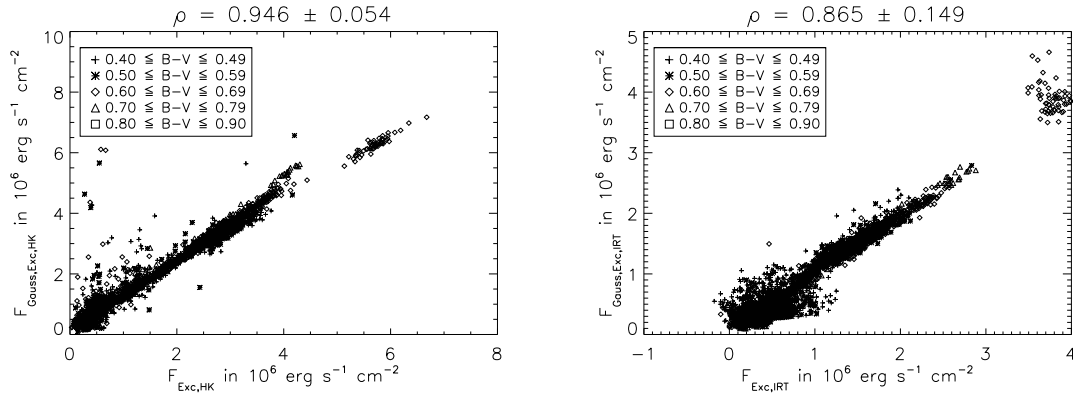


Figure 7.10: Comparison of the measured excess flux (abscissa) to the one calculated from the fitted Gaussian parameters (ordinate), for the Ca II H- & K-lines (left) and the Ca II IRT-lines (right).

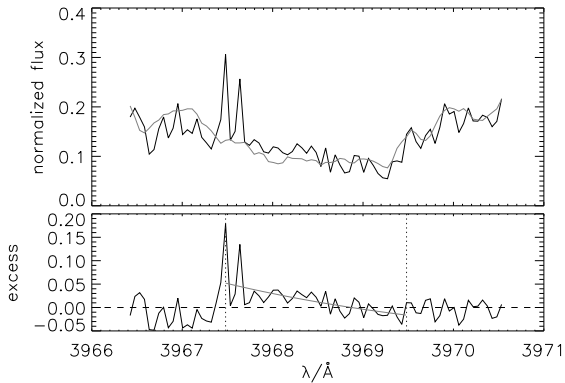


Figure 7.11: Problematic excess Gaussian fit of the excess distribution on highly noisy spectra. *Top*: Comparison of a spectrum of HD 75732 (black) to a spectrum of its comparison star (HD 145675) (gray). *Bottom*: Gaussian fit (gray) to the obtained excess distribution (black) inside the 2 Å-wide bandpass (marked by dashed vertical lines).

We can estimate the excess flux from the fitted Gaussians $F_{\text{Gauss,Exc}}$, using Eq. (4.8), and compare that value to the measured one, which we show in Fig. 7.10. Since we were able to limit the excess fit parameters to realistic values (i.e. forcing the excess to be positive and within the line), the resulting values are also limited to realistic values. The difference between the measured flux and the one calculated is very small, as is evidenced by the high degree of correlation of $\rho = 0.95$ for the Ca II H- & K-lines and $\rho = 0.87$ for the Ca II IRT-lines. Note that this includes *all* stars, even those that do not fulfill $\log R'_{\text{HK}} > -4.75$. If that condition is enforced, just like it was in Chapter 4, the correlation coefficients rise to $\rho = 0.98$ and $\rho = 0.95$, higher for the Ca II H- & K-lines, where we have already noticed lower scatter (Fig. 7.3 compared to Fig. 4.3), and about the same level of scatter for the Ca II IRT-lines. We can also see some outliers in the plot. These can be explained by a faulty Gaussian fit, where a very low activity level, combined with a relatively high noise level in the spectrum, results in an excess distribution that is effectively just noise, as shown in Fig. 7.11. Integrating the Gaussian fitted here results in an incorrect, large value.

We conclude that the fit parameters can also be used as an activity indicator. As we have explained, the additional limitations on the fit make this value more robust for the very low-activity stars, in the sense that no negative excess flux is found. Outliers, such as the one seen in Fig. 7.11, could be handled by either stricter requirements for the SNR, or by imposing additional limitations on the fitted parameters (most notably the position) for the Gaussian fit. For this reason, we choose to use the excess flux estimated from this fit in Chapter 9.

7.7 Comparison to results from Chapter 4

We have seen a strong correlation between the determined excess fluxes and fitted amplitudes in both this chapter and Chapter 4. As we have seen in Eq. (7.1), the determined excess distributions in this chapter always include a chromospheric basal flux contribution, which makes up the difference between the excess fluxes determined here and those found in Chapter 4. Therefore, we expect the excess fluxes determined in this chapter to be generally higher, though not by much, as the basal flux is generally low, close to the level of noise inherent in our spectra, and a more in-depth comparison is necessary to accurately compare the two.

Generally, we find a slightly lower noise level, due to the fact that the comparison spectrum is free of noise, and the excess region to integrate in can be determined automatically depending on the excess distribution. Combined with the fit described in Chapter 6, this method has the additional advantage that no prior information (aside from the star being a main-sequence star, covered by our grid) is necessary to acquire the excess flux, whereas the excess fluxes shown in Chapter 4 include information from outside sources (required for the selection of the comparison star). In principle, a comparison star could have been chosen using the results from the model fit, which would also require no prior information. Regardless, in both these cases, assumptions have been made in the line formation in the creation of the model spectra. Both methods work very well and do not yield very different excess fluxes. We make use of this to obtain a way to convert the excess fluxes, and activity indices, into one another, and to find a relation for the basal flux level.

Chapter 8

Converting Activity Indices into one another

We have already seen that there is a correlation between the excess fluxes determined in the various lines (Chapter 4, Chapter 7). Since this correlation is so strong, we can use the determined excess flux in one line to estimate the corresponding excess flux in another. By the same logic, data from the Ca II IRT-lines or the H α -line could be used to estimate a value for established activity indices, such as S_{MWO} or R'_{HK} . Finding such conversion relations is the goal of this chapter. From our sample, we will use two different methods to obtain empirical relations to find a value of one activity indicator from the value of another. We give such equations from a direct linear regression, followed by those found using a somewhat more complex method.

Parts of this chapter were previously published in Martin et al. [2017]. Some of the relations given have changed very slightly: The exact selection of stars in the sample is different, which is the main reason for this change. Additionally, there is a small degree of randomness in the second method we are using (see below).

8.1 Rationale

For many stars, archival data for S_{MWO} , or other indicators based on Ca II H- & K-lines, is available. This large amount of data allows determination of rotational periods and differential rotation [Baliunas et al., 1995, Hempelmann et al., 2016]. Furthermore, it made it possible to focus on long-term cycles in stars other than the Sun [Baliunas and Soon, 1995]. With the launch of GAIA [Prusti, 2012], a large number of Ca II IRT-spectra are expected. These spectra do not cover the Ca II H- & K-lines, therefore we may determine excess fluxes for the Ca II IRT, but not for the activity indicators based on Ca II H- & K-lines. With the strong correlation between these lines, it should be possible to convert the former into the latter, or vice versa. This allows the combination of datasets focusing on different lines, increasing the temporal baseline for these studies dramatically. Our large data sample of simultaneous observations of the various lines allows us to find such relations. We first find them using linear regression and follow up with another approach where the dataset is divided into smaller groups first. We describe and compare these two methods in the next section. With the two methods explained, we will use them to find a conversion between the various excess fluxes we obtained, as well as S_{MWO} , R'_{HK} and R^+_{HK} . We will focus on the excess fluxes from Chapter 4 and Chapter 7 separately, and describe the results in Section 8.3 and Section 8.2.3. We will start by giving the conversion relation of the various excess fluxes ($F_{\text{Exc,HK}}$, $F_{\text{Exc,IRT}}$, $F_{\text{Exc,H}\alpha}$) into the activity indices S_{MWO} , R'_{HK} and R^+_{HK} . This is then followed by the conversion relations of excess fluxes into the estimated excess flux in another line. Since we have noted that the amplitude of the Gaussian fitted to the excess distributions is well-suited as an activity index, we also give conversion relations to convert the amplitudes A_f of the Gaussian fitted to the excess distribution in one line into the corresponding value A_f for another line.

8.2 Methods for finding conversion relations

8.2.1 Linear regression

The first method we use to find such a conversion relation is by linear regression. Here, we will describe the procedure. For the moment, let y be the activity index we want (e.g., $F_{\text{Exc, HK}}$) to estimate from a known activity index x (e.g., $F_{\text{Exc, IRT}}$), so that we look for a relation $y(x)$ (e.g., a relation $F_{\text{Exc, HK}}(F_{\text{Exc, IRT}})$). From the figures in Chapter 4 and Chapter 7, we see that the relation is linear for a constant value of $B - V$. Therefore, we use the ansatz:

$$y(x) = m(B - V)x + b(B - V), \quad (8.1)$$

with m as the slope and b the intercept, and both of those parameters depending on $B - V$. If we consider the errors on x to be of similar order across the sample so that all values can be weighted equally, we then find that the deviation χ^2 to minimize is¹:

$$\chi^2 = \sum_i^N (y_i - y(x_i))^2, \quad (8.2)$$

where x_i and y_i are the i -th of N total measured values, and $y(x)$ is our relation from Eq. (8.1). From construction, it is apparent that χ^2 can only feature a minimum. Therefore, it is sufficient to require:

$$\frac{\partial \chi^2}{\partial m_i} = \frac{\partial \chi^2}{\partial b_j} = 0, \forall i, j. \quad (8.3)$$

We assume that $m(B - V)$ and $b(B - V)$ can be described by polynomials of order n :

$$\begin{aligned} m(B - V) &= \sum_{j=0}^n m_j (B - V)^j \\ b(B - V) &= \sum_{j=0}^n b_j (B - V)^j \end{aligned} \quad (8.4)$$

Inserting Eq. (8.4) into Eq. (8.1), and the result into the first part of Eq. (8.3) yields the following n equations (one for each k), where $(B - V)_i$ is the $B - V$ value of the star the i -th measurement was taken of:

$$\begin{aligned} \frac{\partial \chi^2}{\partial m_k} &= -2 \sum_{i=1}^N (B - V)_i^k x_i y_i \\ &\quad + 2 \sum_{j=0}^n m_j \sum_{i=1}^N x_i^2 (B - V)_i^{j+k} \\ &\quad + 2 \sum_{j=0}^n b_j \sum_{i=1}^N x_i (B - V)_i^{j+k} \stackrel{!}{=} 0 \\ \Leftrightarrow \sum_{i=1}^N (B - V)_i^k x_i y_i &= \sum_{j=0}^n m_j \sum_{i=1}^N x_i^2 (B - V)_i^{j+k} + \\ &\quad \sum_{j=0}^n b_j \sum_{i=1}^N x_i (B - V)_i^{j+k} \end{aligned} \quad (8.6)$$

¹This definition is equivalent to the standard definition of a χ^2 -value if all errors are set to 1.

Likewise, from the second part of Eq. (8.3):

$$\sum_{i=1}^N (B - V)_i^k y_i = \sum_{j=0}^n m_j \sum_{i=1}^N x_i (B - V)_i^{j+k} + \sum_{j=0}^n b_j \sum_{i=1}^N (B - V)_i^{j+k}. \quad (8.7)$$

Together, Eq. (8.7) and Eq. (8.8) form a system of $2n$ equations linear in m_j and b_j . We solve this using LU decomposition (Gaussian elimination) via the IDL procedure `LA_LINEAR_EQUATION`.

The obtained values m_i , b_j describe, due to their construction, the polynomial that is the best approximation of $m(B - V)$ and $b(B - V)$. These polynomials can then be used to convert a parameter x from our sample into the parameter y .

8.2.2 Subdividing sample into groups with similar $B - V$

The previous approach is highly optimized for the stars in our sample. However, the stars in our sample are not evenly distributed across the $B - V$ -range, as evidenced from e.g. Fig. 2.10. For this reason, a relation found by the previous method is optimized to fit well near the regions in $B - V$ with many stars in our sample, at around $B - V \approx 0.65$, at the cost of the less populated regions. To fix this problem, we use a second approach to find the relation. We still assume a linear relation $y(x) = m(B - V)x + b(B - V)$, with polynomial functions $m(B - V)$, $b(B - V)$ (Eq. (8.4)). We divide the $B - V$ range into k segments. For each of these segments, a fit is performed to find the parameters m and b for stars only with $B - V$ in that segment. In this way, we find k values of m and b for each value of $B - V$ of every segment. To take the errors into account, we use a Monte-Carlo approach, and perform this fit a thousand times, varying the parameters x and y within their errors each time.

The resulting k values are then fitted by a polynomial of n -th order. This gives every $B - V$ -segment the same weight for the fit, solving the problem of the dominance of the segment with $B - V \approx 0.65$. Due to this different approach, the resulting fit will however appear to show *higher* residuals than the one before, since the sample we use for testing is the same we use for determining this relation, and therefore features the very same $B - V$ imbalance². We have tested various segmentation of the $B - V$ -range, and have not noticed this to strongly affect the results. We are using a rather fine segmentation, with steps of $\Delta B - V \approx 0.05$ for the lower end of the $B - V$ -range to $\Delta B - V \approx 0.1$ for the higher $B - V$ values. This was chosen so that no bin holds too many stars. To avoid that the higher amount of bins near the $B - V$ value of most stars reintroduces the sampling bias, the weighting of the points in the fit can be adjusted.

In principle, it is possible to fit the entire data sample for every $B - V$ segment, instead of only fitting data from stars that fall into that $B - V$ segment. One such option is to use a different set of weights for the available data that depends on the segment under consideration. For example, when considering the segment with $(B - V) = (B - V)_{\text{seg}}$, an option for the weights w_i for data points of a star with $(B - V) = (B - V)_{\text{star}}$ could be:

$$w_i \propto \exp\left(-\frac{((B - V)_{\text{seg}} - (B - V)_{\text{star}})^2}{2\sigma^2}\right), \quad (8.8)$$

with some width σ chosen from the segment width. We have tried several of these weighting functions, and have not noticed a strong effect on the resulting conversion relations. Therefore, we use the simple approach of ignoring observations with $B - V$ outside the currently considered segment, which is equivalent to a boxcar weighting function. We have also experimented with automatically determining and ignoring outliers. However, even after experimenting with different criteria for the outlier recognition, no significant influence on the results was found. We therefore have not

²This problem can be fixed by determining the residuals from an randomly picked subsample of data points that are evenly distributed in $B - V$.

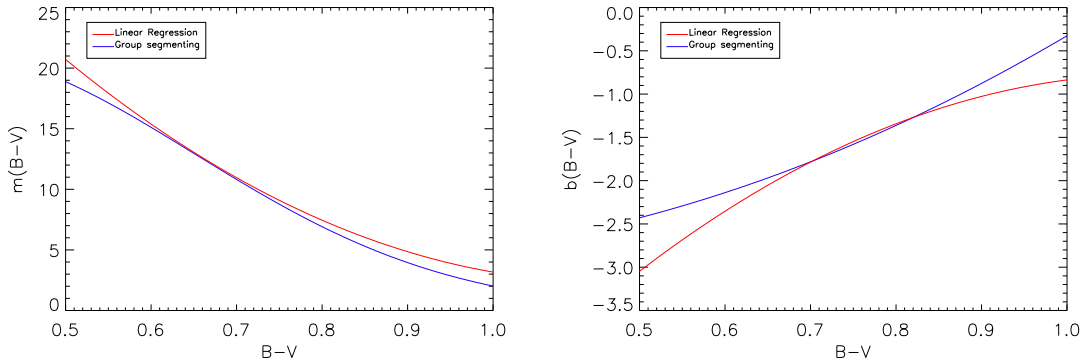


Figure 8.1: **Comparing the relations for $m(B - V)$ (left) and $b(B - V)$ (right) for $F_{\text{Exc,HK}}(S_{\text{MWO}}, B - V)$ from the LR (red) and GS (blue) approach.** The slope m is rather similar, with the largest deviations in $b(B - V)$ occurring at the limit of the $B - V$ range considered here.

performed this step in the determination of the relations given below.

This approach can be extended to higher-order polynomials. In most cases, this has not been necessary, but we have performed such a conversion in order to transform the excess flux from the H α -line. We give more details below.

In this approach, we have sometimes opted to fit $\log m$ as a polynomial of $B - V$, instead of m directly. Using the logarithm for this parameter is commonly done in the literature, for example by Rutten [1984]. This is especially necessary for relations that yield a flux value from an activity indicator, as the relation for the continuum flux follow an exponential function [Hall, 1996].

8.2.3 Comparison of the two methods

Both methods yield similar relations, as expected. We recommend using the results from the latter approach, as it does not feature the bias introduced from the uneven sample, despite the fact that the results from the linear regression will show lower residuals, due to the testing sample showing the same sampling bias.

To show how similar the results are, we compare the results of two relations $F_{\text{Exc,HK}}(S_{\text{MWO}})$ obtained with the two methods of linear regression (hereafter abbreviated “LR”) and the group-segmenting approach (“GS”). Figure 8.1 shows the obtained relations for $m(B - V)$ and $b(B - V)$ from the two approaches for the conversion of S_{MWO} to $F_{\text{Exc,HK}}$. The slope m (the more important parameter of the two) is very similar with only very little deviation (left plot in Fig. 8.1). b , on the other hand, deviates further towards the higher and lower values of $B - V$. This is likely because the LR approach yields relations optimized for the $B - V$ region with many stars in our sample, at $B - V \approx 0.65$ (see Fig. 2.10), where the two relations are very similar. However, since this deviation in b results in an absolute offset, the effect of this is rather limited, with less than $0.5 \cdot 10^6 \text{ erg s}^{-1} \text{ cm}^{-2}$ on average.

In Fig. 8.2, we plot the deviation of the two relations in the absolute (left) and relative scale (right). The deviation is not exceeding 15% for almost the entire region shown, which corresponds to the error of the relations, and is therefore expected. Only at the edge of the validity range of the relation – at high and low values for $B - V$ – do the deviations exceed this, reaching 35% for very small values of S_{MWO} and high values of $B - V$. For $B - V$ higher than 0.95 and low values for S_{MWO} , the relative deviation becomes rather large, as the absolute values are very small. We have cut the plot at $B - V = 0.9$ for this reason, as this structure would dominate the plot otherwise. This structure is not visible in the plot of the absolute deviation. The dark band (low deviation) corresponds to the points where both polynomials are congruent. We can conclude that in most practical settings, it does not matter whether the relation resulting from the GS- or LR-approach is picked, as their difference is likely small compared to the errors on the measured quantities, or

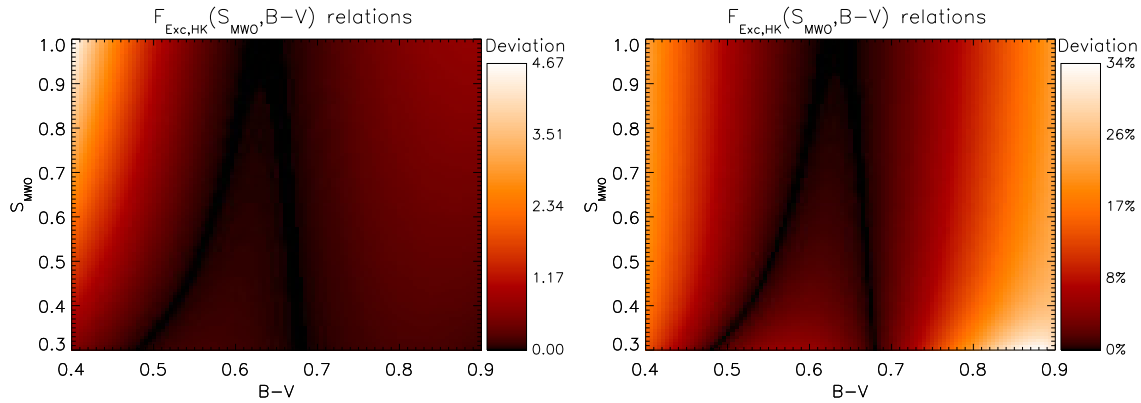


Figure 8.2: **Comparing the relations for $F_{\text{Exc,HK}}(S_{\text{MWO}}, B - V)$ from the LR and GS approach, in the absolute (left) and relative scale (right).** The deviation does not exceed the 15% level which we give as an error (Sect. 8.3), except for the edges of the validity range (borders). At the lower $B - V$ values, and the lower S_{MWO} -levels, the relative deviation is strongly increased, due to the low value for $F_{\text{Exc,HK}}$ at these points.

the resulting converted values. We give both for completeness' sake, but stress again that only the relations from the GS approach are free of sampling bias, and should therefore be picked. (despite the nominally higher residuals). To give an indicator on the quality of the conversion, we also determine the linear Pearson correlation (see Sect. 4.7) between converted and measured values, as we can now expect a linear correlation (actually the identity). In the following, this value is always very high, indicating that also the resulting distribution of the conversion is valid. For conversion from the $H\alpha$ -line excess flux, the correlation is lower at $r \approx 0.85$, which is not surprising as there was a lower degree of correlation between it and the calcium lines to begin with.

8.3 Conversion relations from the result of Chapter 4

In this section, we show the results for the conversion relations from both approaches. To determine the quality of the conversions, we give the absolute residual value at which 68% of points lie below, roughly corresponding to 1σ . The errors are not truly 1σ -error values, however, as the distribution is not a Gaussian. The residuals are always given in the unit of the converted value, i.e. in $\text{erg s}^{-1} \text{cm}^{-2}$ for fluxes and in units of 1 for indices. Below, we then give the average, relative deviation across the entire sample. To obtain these relations, HD 22468 was removed from the sample: This star is very active, and will therefore strongly affect the linear fits performed. As there is a lot of noise in the obtained values from its spectra, this is not desirable. The found relations are valid for $0.5 \lesssim B - V \lesssim 1.0$, and they can easily be inverted.

8.3.1 Activity indices and excess fluxes

First, we will give relations to estimate excess fluxes from known activity indices.

Estimating $F_{\text{Exc,HK}}$ from S_{MWO}

Here, we have started the segmenting for the GS approach only at $B - V \geq 0.5$, as we found the remaining stars to not follow a reliable linear fit, with coefficients falling within the expected ranges: The data points scatter too much.

This relation converts a known value of S_{MWO} , together with the $B - V$ from the star (necessary for conversion into flux units), into the value of the excess flux in the Ca II H- & K-lines. As we have described before, we have fitted $\log m$ with a polynomial for the GS approach. In the LR approach,

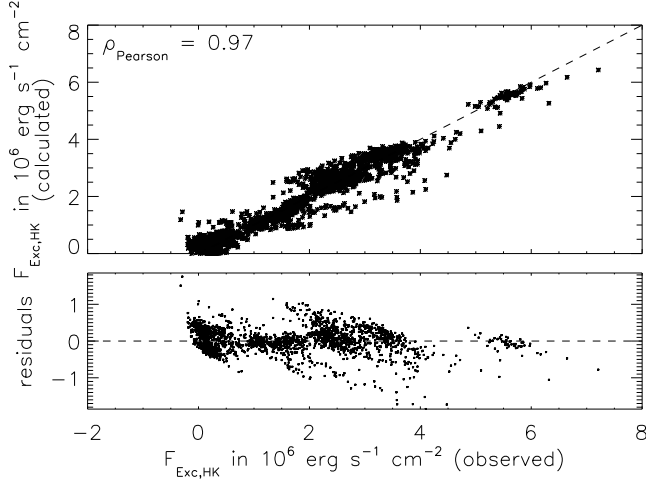


Figure 8.3: **Comparing the converted value $F_{\text{Exc,HK}}(S_{\text{MWO}}, B - V)$ to the measured value, from the GS-approach.** This plot shows the results from 2137 observations of 79 stars, and originally appeared in Martin et al. [2017].

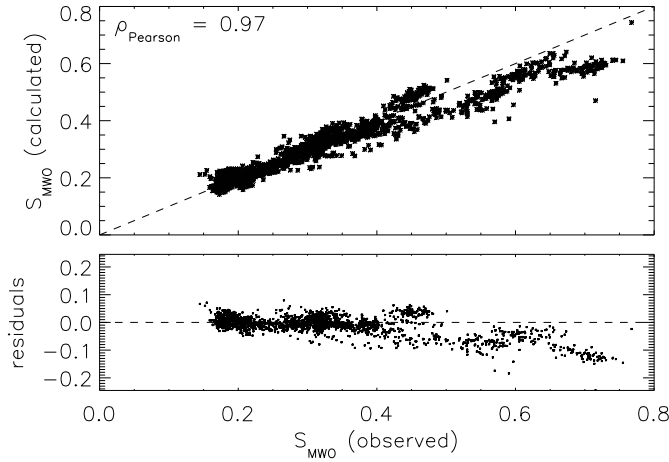


Figure 8.4: **Comparing the converted value $S_{\text{MWO}}(F_{\text{Exc,IRT}}, B - V)$ to the measured value, from the GS-approach.** This plot shows the results from 2076 observations of 76 stars, and originally appeared in Martin et al. [2017].

this is not an option (as the resulting set of equations would no longer be linear in m_i).

	$F_{\text{Exc,HK}} = (m \cdot S_{\text{MWO}} + b) \cdot 10^6 \text{ erg s}^{-1} \text{ cm}^{-2}$	Residuals
GS	$\log m = 1.027 + 1.718 \cdot (B - V) - 2.440 \cdot (B - V)^2$	$3 \cdot 10^5$
	$b = -2.908 - 0.667 \cdot (B - V) + 3.249 \cdot (B - V)^2$	($\sim 11\%$)
LR	$m = 61.070 - 103.516 \cdot (B - V) + 45.614 \cdot (B - V)^2$	$2.3 \cdot 10^5$
	$b = -8.399 + 13.846 \cdot (B - V) - 6.284 \cdot (B - V)^2$	($\sim 11\%$)

The relations for $m(B - V)$ and $b(B - V)$ were shown already in Sect. 8.2.3, where we have also compared them in detail. The results of this conversion are compared to the measured values in Fig. 8.3.

Converting $F_{\text{Exc,IRT}}$ into activity indices

We now give various relations to convert the summed-up excess flux in all three Ca II IRT-lines $F_{\text{Exc,IRT}}$ into S_{MWO} , R'_{HK} and R_{HK}^+ . If not all of the Ca II IRT-lines have been measured, the missing excess fluxes can be estimated, we give relations to do so later. Some spectra in the sample have a large quality difference in the red- and blue-channel. These have been removed to not affect the results.

The result from the conversion below is shown in Fig. 8.4:

		$S_{\text{MWO}} = m \cdot F_{\text{Exc,IRT}} / (\text{erg s}^{-1} \text{cm}^{-2}) + b$	Residuals
GS	$\log m =$	$-6.501 - 2.165 \cdot (B - V) + 2.264 \cdot (B - V)^2$	$3 \cdot 10^{-2}$
	$b =$	$0.045 + 0.199 \cdot (B - V) - 0.012 \cdot (B - V)^2$	($\sim 6\%$)
LR	$m \cdot 10^7 =$	$0.102 - 1.492 \cdot (B - V) + 4.910 \cdot (B - V)^2$	$3 \cdot 10^{-2}$
	$b =$	$0.718 - 1.635 \cdot (B - V) + 1.203 \cdot (B - V)^2$	($\sim 5\%$)

To convert into R'_{HK} :

		$R'_{\text{HK}} = m \cdot F_{\text{Exc,IRT}} / (\text{erg s}^{-1} \text{cm}^{-2}) + b$	Residuals
GS	$\log m =$	$-10.223 - 1.229 \cdot (B - V) + 1.136 \cdot (B - V)^2$	$6 \cdot 10^{-6}$
	$b \cdot 10^5 =$	$-0.154 - 3.639 \cdot (B - V) - 1.516 \cdot (B - V)^2$	($\sim 10\%$)
LR	$m \cdot 10^{11} =$	$1.899 - 1.360 \cdot (B - V) + 4.477 \cdot (B - V)^2$	$6 \cdot 10^{-6}$
	$b \cdot 10^5 =$	$4.460 - 8.090 \cdot (B - V) + 5.739 \cdot (B - V)^2$	($\sim 9\%$)

And to convert into $R'_{\text{HK}}+$:

		$R'_{\text{HK}}+ = m \cdot F_{\text{Exc,IRT}} / (\text{erg s}^{-1} \text{cm}^{-2}) + b$	Residuals
GS	$\log m =$	$-10.252 - 1.141 \cdot (B - V) + 1.042 \cdot (B - V)^2$	$5.5 \cdot 10^{-6}$
	$b \cdot 10^5 =$	$-4.61 + 13.34 \cdot (B - V) - 7.53 \cdot (B - V)^2$	($\sim 11\%$)
LR	$m \cdot 10^{11} =$	$4.940 - 9.559 \cdot (B - V) + 9.774 \cdot (B - V)^2$	$5.0 \cdot 10^{-6}$
	$b \cdot 10^5 =$	$-2.019 + 6.933 \cdot (B - V) - 3.708 \cdot (B - V)^2$	($\sim 9\%$)

As expected, the relations for $m(B - V)$ look very similar for the conversion to R'_{HK} and $R'_{\text{HK}}+$, as these indicators only differ in the additional correction of the small basal flux contribution. This is also true for the relation derived using LR: Inserting numbers reveals that along the $B - V$ -validity interval, the relations $m(B - V)$ are very similar. The results from these conversions are compared in Fig. 8.5.

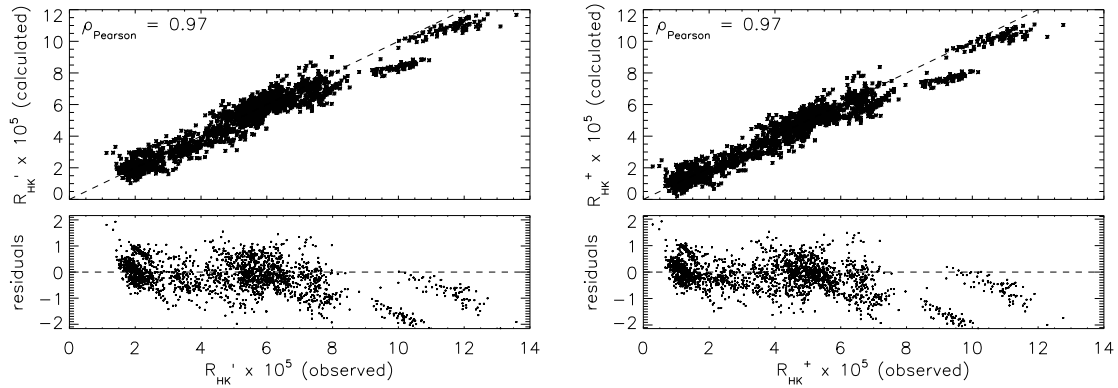


Figure 8.5: Comparing the converted values of R'_{HK} (left) and $R'_{\text{HK}}+$ (right), as a function of $F_{\text{Exc,IRT}}$ and $B - V$ to the measured value, from the GS-approach. These plots show the results from 2076 observations of 76 stars, and originally appeared in Martin et al. [2017].

Converting $F_{\text{Exc,H}\alpha}$ into activity indices

The relations to convert the excess flux in the $\text{H}\alpha$ -line into S_{MWO} , R'_{HK} and $R'_{\text{HK}}+$ were obtained in the same way, with the same segmenting in the GS approach as before:

		$S_{\text{MWO}} = m \cdot F_{\text{Exc,H}\alpha} / (10^6 \text{erg s}^{-1} \text{cm}^{-2}) + b$	Residuals
GS	$\log m =$	$-4.651 + 9.166 \cdot (B - V) - 4.536 \cdot (B - V)^2$	$5 \cdot 10^{-2}$
	$b =$	$0.447 - 0.839 \cdot (B - V) + 0.711 \cdot (B - V)^2$	($\sim 14\%$)
LR	$m =$	$1.017 - 4.038 \cdot (B - V) + 4.340 \cdot (B - V)^2$	$5 \cdot 10^{-2}$
	$b =$	$0.458 - 8.000 \cdot (B - V) + 6.616 \cdot (B - V)^2$	($\sim 13\%$)

		$R'_{\text{HK}} = m \cdot F_{\text{Exc,H}\alpha} / (10^6 \text{erg s}^{-1} \text{cm}^{-2}) + b$	Residuals
GS	$\log m =$	$-8.267 + 9.942 \cdot (B - V) - 5.672 \cdot (B - V)^2$	$1.5 \cdot 10^{-5}$
	$b \cdot 10^5 =$	$2.032 + 1.469 \cdot (B - V) - 0.599 \cdot (B - V)^2$	($\sim 23\%$)
LR	$m \cdot 10^4 =$	$1.194 - 4.113 \cdot (B - V) + 4.789 \cdot (B - V)^2$	$1.2 \cdot 10^{-5}$
	$b \cdot 10^5 =$	$1.164 + 5.040 \cdot (B - V) - 3.442 \cdot (B - V)^2$	($\sim 19\%$)

		$R_{\text{HK}}^+ = m \cdot F_{\text{Exc,H}\alpha} / (10^6 \text{erg s}^{-1} \text{cm}^{-2}) + b$	Residuals
GS	$\log m =$	$-10.606 + 17.009 \cdot (B - V) - 10.786 \cdot (B - V)^2$	$1.5 \cdot 10^{-5}$
	$b \cdot 10^5 =$	$0.121 + 4.500 \cdot (B - V) - 2.602 \cdot (B - V)^2$	($\sim 30\%$)
LR	$m \cdot 10^4 =$	$1.527 - 4.991 \cdot (B - V) + 5.342 \cdot (B - V)^2$	$1.2 \cdot 10^{-5}$
	$b \cdot 10^5 =$	$-3.176 + 1.454 \cdot (B - V) - 9.634 \cdot (B - V)^2$	($\sim 23\%$)

8.3.2 Converting excess fluxes in one line to the excess flux in another line

Since the excess fluxes in the different lines are strongly correlated, we can convert them into one another. This is the focus of this section.

Estimating the excess flux in groups of lines from an individual line

The Ca II H- & K-lines are very well correlated. The K-line shows higher levels of flux, and we have found its flux to be about 33% higher than the one in the H-line. This value is very close to the value of 27% observed by Wilson [1968]. Since they are so close to each other, we find no $B - V$ -dependency, so the GS-approach is not appropriate. The result is then:

$$F_{\text{Exc,K}} = 1.332 \cdot F_{\text{Exc,H}}.$$

We present the relations to convert the Ca II IRT-lines into each other in Table 8.1. Here, too, the relations are independent of $B - V$.

Conversion of excess fluxes in various lines into one another

We find that there is no need for an intercept b for the conversions from $F_{\text{Exc,IRT}}$ to $F_{\text{Exc,HK}}$. The relation we find is:

$$F_{\text{Exc,HK}} = 10^{0.606 - 0.612 \cdot (B - V)} \cdot F_{\text{Exc,IRT}}, \quad (8.9)$$

with residuals of about $3.7 \cdot 10^5 \text{erg s}^{-1} \text{cm}^{-2}$, a relative error of about 20%. The converted values are compared to the observed excess fluxes in Fig. 8.6. For completeness' sake, this same relation in continuum units is:

$$F_{\text{Exc,HK}} = (-0.085 + 1.402 \cdot (B - V)) \cdot F_{\text{Exc,IRT}}, \quad (8.10)$$

Table 8.1: **Relations to estimate the excess flux in one Ca II IRT-line from measurements of another.** The errors of such a conversion are about $30\,000 \text{erg s}^{-1} \text{cm}^{-2}$. This is a differently formatted version of a table that originally appeared in Martin et al. [2017]. These are the conversions obtained by using the results from comparing spectra to those of inactive stars (Chapter 4).

Source line	Target Flux		
	$F_{\text{Exc,IRT } \lambda 8498} =$	$F_{\text{Exc,IRT } \lambda 8542} =$	$F_{\text{Exc,IRT } \lambda 8662} =$
Ca II IRT $\lambda 8498$		$1.232 \cdot F_{\text{Exc,IRT } \lambda 8498}$	$1.006 \cdot F_{\text{Exc,IRT } \lambda 8498}$
Ca II IRT $\lambda 8542$	$0.801 \cdot F_{\text{Exc,IRT } \lambda 8542}$		$0.808 \cdot F_{\text{Exc,IRT } \lambda 8542}$
Ca II IRT $\lambda 8662$	$0.976 \cdot F_{\text{Exc,IRT } \lambda 8662}$	$1.210 \cdot F_{\text{Exc,IRT } \lambda 8662}$	

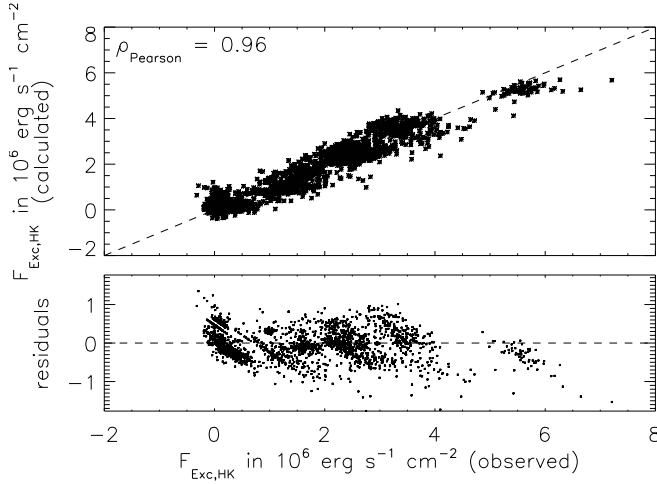


Figure 8.6: **Comparison of the values for $F_{\text{Exc,HK}}$, converted from $F_{\text{Exc,IRT}}$, to the measured ones.**

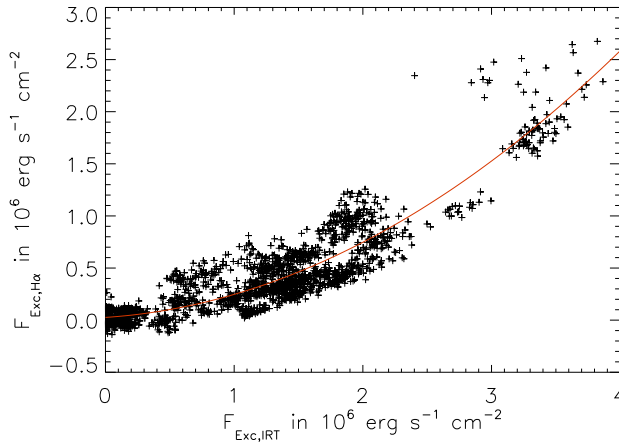


Figure 8.7: **The best quadratic fit (red line) to the obtained excess fluxes of the $H\alpha$ -line and the sum of the Ca II IRT-lines.** Unlike the other relations, this one appears to be quadratic rather than linear. The best fit is given in Eq. (8.12).

with residuals of about $60 \text{ m}\text{\AA}$.

We have removed an additional ten stars from the sample to obtain the conversions with the $H\alpha$ -line involved, as for these ten stars, the excess flux in the $H\alpha$ -line found showed no variation, indicating that the comparison could not have been done reliably. We have already noted that the relation between the $H\alpha$ -line and the calcium lines does not appear to follow a linear relation. In our tests, a second-order polynomial fits the relation better than the typical linear one (with coefficients dependent on $B - V$), as is evident in Fig. 8.7, where we exemplarily show the best quadratic fit to one dataset. These best fits are:

$$\begin{aligned}
 F_{\text{Exc,H}\alpha} &= 0.010 \cdot 10^6 \text{erg s}^{-1} \text{cm}^{-2} + 0.092 \cdot F_{\text{Exc,HK}} + \\
 &\quad 0.038 \cdot F_{\text{Exc,HK}}^2 / (10^6 \text{erg s}^{-1} \text{cm}^{-2}) \\
 F_{\text{Exc,HK}} &= 0.483 \cdot 10^6 \text{erg s}^{-1} \text{cm}^{-2} + 4.178 \cdot F_{\text{Exc,H}\alpha} - \\
 &\quad 0.806 \cdot F_{\text{Exc,H}\alpha}^2 / (10^6 \text{erg s}^{-1} \text{cm}^{-2}),
 \end{aligned} \tag{8.11}$$

for the conversion between the $H\alpha$ -line and Ca II H- & K-lines, and

$$\begin{aligned}
 F_{\text{Exc,H}\alpha} &= 0.026 \cdot 10^6 \text{erg s}^{-1} \text{cm}^{-2} + 0.081 \cdot F_{\text{Exc,IRT}} + \\
 &\quad 0.140 \cdot F_{\text{Exc,IRT}}^2 / (10^6 \text{erg s}^{-1} \text{cm}^{-2}) \\
 F_{\text{Exc,IRT}} &= 0.257 \cdot 10^6 \text{erg s}^{-1} \text{cm}^{-2} + 2.672 \cdot F_{\text{Exc,H}\alpha} - \\
 &\quad 0.590 \cdot F_{\text{Exc,H}\alpha}^2 / (10^6 \text{erg s}^{-1} \text{cm}^{-2}).
 \end{aligned} \tag{8.12}$$

The residuals of these conversions are about $0.56 \cdot 10^6 \text{ erg s}^{-1} \text{ cm}^{-2}$ for converting to $F_{\text{Exc,HK}}$ from the H α -line, and $0.14 \cdot 10^6 \text{ erg s}^{-1} \text{ cm}^{-2}$ when converting to $F_{\text{Exc,H}\alpha}$ from the Ca II H- & K-lines. For the relations given in Eq. 8.12, the respective residuals are about $0.15 \cdot 10^6 \text{ erg s}^{-1} \text{ cm}^{-2}$ for converting to $F_{\text{Exc,H}\alpha}$ from the Ca II IRT-lines, and $0.40 \cdot 10^6 \text{ erg s}^{-1} \text{ cm}^{-2}$ for converting to $F_{\text{Exc,IRT}}$. The ratio of these errors roughly correspond to the ratio of the excess flux in the lines.

We have also performed a GS approach for such a quadratic polynomial, i.e. finding the coefficients c_i in a relation of the form

$$y = c_0(B - V) + c_1(B - V) \cdot x + c_2(B - V) \cdot x^2, \quad (8.13)$$

with x and y for the respective excess fluxes. This slightly improves the relation, however, the large scatter makes it difficult to reliably determine $c_i(B - V)$. The best result from this approach shows residuals of about $0.13 \cdot 10^6 \text{ erg s}^{-1} \text{ cm}^{-2}$ for the conversion $F_{\text{Exc,H}\alpha}(F_{\text{Exc,IRT}}, B - V)$, and is given in Table 8.2. As an example, we compare the conversion from $F_{\text{Exc,H}\alpha}$ to $F_{\text{Exc,IRT}}$ from this approach (right) and the simple parabola fit to the entire sample according to Eq. (8.12) (left) in Fig. 8.8. The linear Pearson correlation coefficient is now 0.94, an improvement to the value of 0.92 obtained from the simple relations in Eq. (8.12), indicating that the conversion was improved as it is now closer to the ideal linear relation and shows less spread, but at the cost of higher residuals at lower values. For the conversion to Ca II H- & K-lines, the Pearson correlation coefficient is lower than before, namely $r \approx 0.88$. The resulting relations for the excess fluxes of the other lines are also given in Table 8.2.

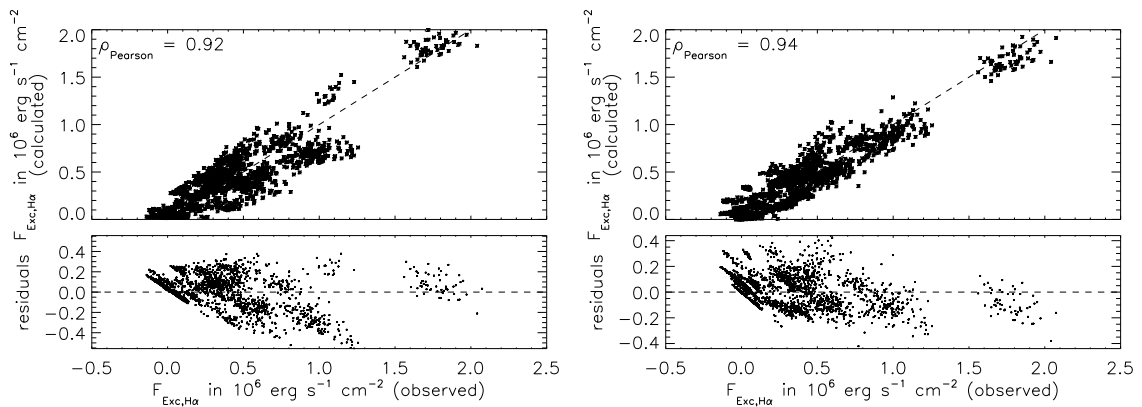


Figure 8.8: **Comparing the converted values of $F_{\text{Exc,H}\alpha}$ from $F_{\text{Exc,IRT}}$ to the observed value, converted from Eq. (8.12) (left) and the advanced GS-approach (right).** The advanced GS approach yields slightly better results overall, but the simpler approach gives better results at low values. Shown is the data of 2076 observations from 76 stars.

8.3.3 Conversion of the amplitude of Gaussians fitted to the excess distribution

We now give relations for the amplitude A_f of the Gaussian that we fitted to the excess distribution (see Sect. 3.6). Here, we only give the relations for the fitted amplitude in $\text{erg s}^{-1} \text{ cm}^{-2} \text{ \AA}^{-1}$. The parameter A_f is originally determined in units of the continuum, but later converted to these units using the relations from Hall [1996]. As we have now established that there is no major difference between the relations from the two approaches LR and GS (Sect. 8.2.3), we only show the results of the latter in this Section. Again, we find no intercept b necessary. The relations we find are:

$$A_{f,\text{HK}} = 10^{0.708+0.218 \cdot (B-V)} A_{f,\text{H}\alpha}, \quad (8.14)$$

with residuals of $8 \cdot 10^{13}$ ($\sim 24\%$). To convert from the Ca II IRT-line data:

$$A_{f,\text{HK}} = 10^{0.754-0.576 \cdot (B-V)} A_{f,\text{IRT}}, \quad (8.15)$$

Table 8.2: **Relations to convert the excess flux in the H α -line to the value in the Ca II H- & K-lines and Ca II IRT-lines, and vice-versa.** These relations have been determined using the GS-approach. Residuals and fluxes are given in $\text{erg s}^{-1} \text{cm}^{-2}$, and must be entered in these units as well.

$F_{\text{Exc,H}\alpha} = c_0(B - V) + c_1(B - V) \cdot F_{\text{Exc,HK}} + c_2(B - V) \cdot F_{\text{Exc,HK}}^2$		Residuals
$c_0 =$	$1.942 \cdot 10^6 - 5.035 \cdot 10^6(B - V) + 3.141 \cdot 10^6(B - V)^2$	$1.6 \cdot 10^5$
$c_1 =$	$-6.996 \cdot 10^{-1} + 2.166(B - V) - 1.413(B - V)^2$	($\sim 26\%$)
$c_2 =$	$2.338 \cdot 10^{-7} - 5.785 \cdot 10^{-7}(B - V) + 4.024 \cdot 10^{-7}(B - V)^2$	
$F_{\text{Exc,HK}} = c_0(B - V) + c_1(B - V) \cdot F_{\text{Exc,H}\alpha} + c_2(B - V) \cdot F_{\text{Exc,H}\alpha}^2$		Residuals
$c_0 =$	$-1.304 \cdot 10^6 + 5.892 \cdot 10^6(B - V) - 4.420 \cdot 10^6(B - V)^2$	$5.9 \cdot 10^5$
$c_1 =$	$1.606 \cdot 10^{-1} + 1.010 \cdot 10^1(B - V) - 5.637(B - V)^2$	($\sim 23\%$)
$c_2 =$	$7.179 \cdot 10^{-7} - 4.698 \cdot 10^{-6}(B - V) + 3.109 \cdot 10^{-6}(B - V)^2$	
$F_{\text{Exc,H}\alpha} = c_0(B - V) + c_1(B - V) \cdot F_{\text{Exc,IRT}} + c_2(B - V) \cdot F_{\text{Exc,IRT}}^2$		Residuals
$c_0 =$	$1.848 \cdot 10^5 - 4.452 \cdot 10^5(B - V) + 3.134 \cdot 10^5(B - V)^2$	$1.2 \cdot 10^5$
$c_1 =$	$1.484 - 3.065(B - V) + 1.414(B - V)^2$	($\sim 25\%$)
$c_2 =$	$-2.572 \cdot 10^{-7} + 7.619 \cdot 10^{-7}(B - V) - 2.658 \cdot 10^{-7}(B - V)^2$	
$F_{\text{Exc,IRT}} = c_0(B - V) + c_1(B - V) \cdot F_{\text{Exc,H}\alpha} + c_2(B - V) \cdot F_{\text{Exc,H}\alpha}^2$		Residuals
$c_0 =$	$2.354 \cdot 10^6 - 4.915 \cdot 10^6(B - V) + 2.684 \cdot 10^6(B - V)^2$	$3.5 \cdot 10^5$
$c_1 =$	$-7.207 + 2.321 \cdot 10^1(B - V) - 1.196 \cdot 10^1(B - V)^2$	($\sim 19\%$)
$c_2 =$	$3.601 \cdot 10^{-6} - 9.944 \cdot 10^{-6}(B - V) + 5.203 \cdot 10^{-6}(B - V)^2$	

with residuals of $6 \cdot 10^{13}$ ($\sim 20\%$). The last relation is:

$$A_{f,\text{H}\alpha} = 10^{0.098 - 0.887 \cdot (B - V)} A_{f,\text{IRT}}, \quad (8.16)$$

with residuals of $1.2 \cdot 10^{13}$ ($\sim 26\%$).

For all of these, the linear Pearson correlation coefficient is larger than 0.9, indicating a good conversion.

8.4 Conversion relations from result of Chapter 7

We can now obtain the conversion relations in the same fashion, using the LR and GS method, but with the data sample obtained in Chapter 7. The major differences are that the excess fluxes determined in Chapter 7 include a basal flux, and that the flux scale is defined by PHOENIX model spectra. Since the stars analyzed in that chapter cover a smaller range in $B - V$, some segments for the GS-approach previously used are not in use here. For the same reason, these relations are only valid for $0.5 \lesssim B - V \lesssim 0.8$.

8.4.1 Activity indices and excess fluxes

As we have done before, we can estimate the excess flux from activity indices, and vice versa. We give relations to do so here.

Estimating $F_{\text{Exc,HK}}$ from S_{MWO}

For the GS approach, we are using the same $B - V$ segments that we have used previously described in Section 8.2.2. The resulting relation for $F_{\text{Exc,HK}}(S_{\text{MWO}}, B - V)$ is very similar, as expected, and shows a Pearson linear correlation coefficient of 0.99 between converted and measured values. The higher value of ρ_{Pearson} is most likely due to the smaller range covered in $B - V$, as well as the overall

lower noise in the data. The relations that we find are given by:

	$F_{\text{Exc,HK}} = (m \cdot S_{\text{MWO}} + b) \cdot 10^6 \text{ erg s}^{-1} \text{ cm}^{-2}$	Residuals
GS	$\log m = 1.047 + 1.505 \cdot (B - V) - 2.191 \cdot (B - V)^2$ $b = -0.790 - 8.641 \cdot (B - V) + 11.085 \cdot (B - V)^2$	$2 \cdot 10^5$ ($\sim 14\%$)
LR	$m = 16.360 + 21.637 \cdot (B - V) - 42.042 \cdot (B - V)^2$ $b = -2.655 - 1.283 \cdot (B - V) + 4.216 \cdot (B - V)^2$	$2 \cdot 10^5$ ($\sim 13\%$)

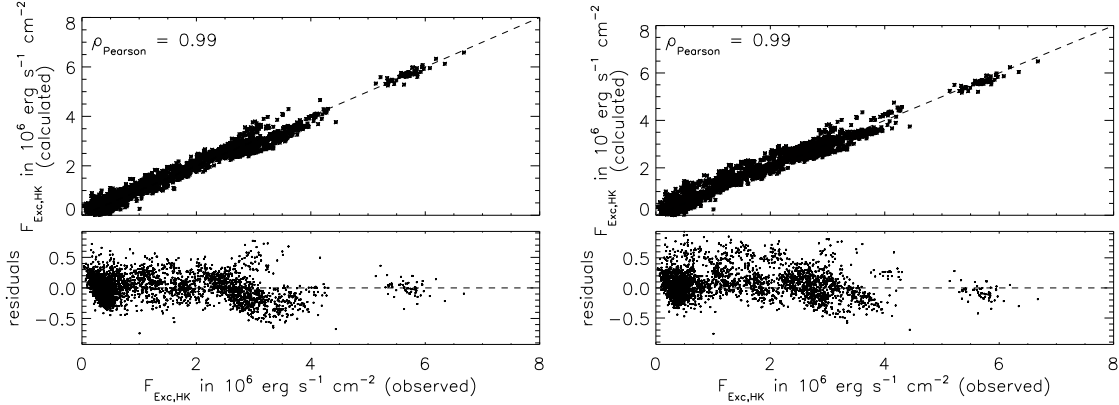


Figure 8.9: Comparing the converted values of $F_{\text{Exc,HK}}$ from S_{MWO} to the observed value, converted from the LR approach (left) and the advanced GS-approach (right). The excess values used are from Chapter 7, and therefore also include the chromospheric basal flux. Both methods yield very similar conversion results.

In Fig. 8.9, the results of these conversions are compared to the measured values. Independent of the approach used, the congruence of converted to measured values is very good, as expected from the high value of ρ_{Pearson} . There is a somewhat higher spread in the conversion from the GS approach, but not by much. This is evidenced in the almost identical relative deviation (14% vs. 13%), which is expected to be higher for the GS approach anyway, due to it optimizing without taking the bias from the irregular sampling in $B - V$ into consideration.

Conversion of $F_{\text{Exc,IRT}}$ into activity indices

Just like before, we can use the data to obtain relations to convert the combined excess flux in the Ca II IRT-lines to activity indicators. The values for $F_{\text{Exc,IRT}}$ also include the chromospheric basal flux here. We disregard the data points from spectra that are classified as “inactive” according to the criterion from Henry et al. [1996], as their low excess level compared to the noise introduce a lot of scatter. Since they also fall into the extreme lower end of the fitting range, they have a comparatively high weight on the linear fits, which is not desirable due to their scatter. The flux is expected to be entered in units of $\text{erg s}^{-1} \text{ cm}^{-2}$ in these relations. The relations to find a value for S_{MWO} are given by:

	$S_{\text{MWO}} = m \cdot F_{\text{Exc,IRT}} / (\text{erg s}^{-1} \text{ cm}^{-2}) + b$	Residuals
GS	$\log m = -8.380 + 3.422 \cdot (B - V) - 1.894 \cdot (B - V)^2$ $b = 0.602 - 1.461 \cdot (B - V) + 1.234 \cdot (B - V)^2$	$2 \cdot 10^{-2}$ ($\sim 6\%$)
LR	$m \cdot 10^7 = 1.721 - 5.216 \cdot (B - V) + 6.753 \cdot (B - V)^2$ $b = 0.409 - 7.836 \cdot (B - V) + 6.234 \cdot (B - V)^2$	$2 \cdot 10^{-2}$ ($\sim 6\%$)

The coefficients appear to differ strongly from the ones for the same conversion when using the values from Chapter 4, however, the resulting values for m and b , if a value $B - V$ in the validity

range is inserted, do not differ much. The remaining difference can be traced back to the different flux scale and basal flux. The relations we find to convert the excess flux into R'_{HK} are given by:

	$R'_{\text{HK}} = m \cdot F_{\text{Exc,IRT}} / (\text{erg s}^{-1} \text{cm}^{-2}) + b$		Residuals
GS	$m \cdot 10^{11} =$	$1.158 + 2.080 \cdot (B - V)$	$7 \cdot 10^{-6}$
	$b \cdot 10^5 =$	$2.317 - 0.320 \cdot (B - V)$	($\sim 9\%$)
LR	$m \cdot 10^{11} =$	$3.587 - 5.577 \cdot (B - V) + 6.803 \cdot (B - V)^2$	$6 \cdot 10^{-6}$
	$b \cdot 10^5 =$	$8.673 - 21.165 \cdot (B - V) + 15.751 \cdot (B - V)^2$	($\sim 9\%$)

We have fitted m here in the GS approach, rather than $\log m$ like we did earlier. This resulted in a better fit to the data, though the deviations between converted and measured values are of a similar order if m is we fit a relation to $m(B - V)$ instead. Finally, the conversion to R_{HK}^+ is given by:

	$R_{\text{HK}}^+ = m \cdot F_{\text{Exc,IRT}} / (\text{erg s}^{-1} \text{cm}^{-2}) + b$		Residuals
GS	$\log m =$	$-10.860 + 0.396 \cdot (B - V)$	$7 \cdot 10^{-6}$
	$b \cdot 10^5 =$	$1.317 - 5.083 \cdot (B - V)$	($\sim 12\%$)
LR	$m \cdot 10^{11} =$	$3.597 - 5.612 \cdot (B - V) + 6.831 \cdot (B - V)^2$	$6 \cdot 10^{-6}$
	$b \cdot 10^5 =$	$7.698 - 20.977 \cdot (B - V) + 15.816 \cdot (B - V)^2$	($\sim 12\%$)

The relations are rather similar again. However, due to the additional correction for the basal flux from the R_{HK}^+ relation by Mittag et al. [2013], which is a logarithmic function of $B - V$, we now find a better fit for $\log m$. The converted values according to these relations are compared to the measured values in Fig. 8.10.

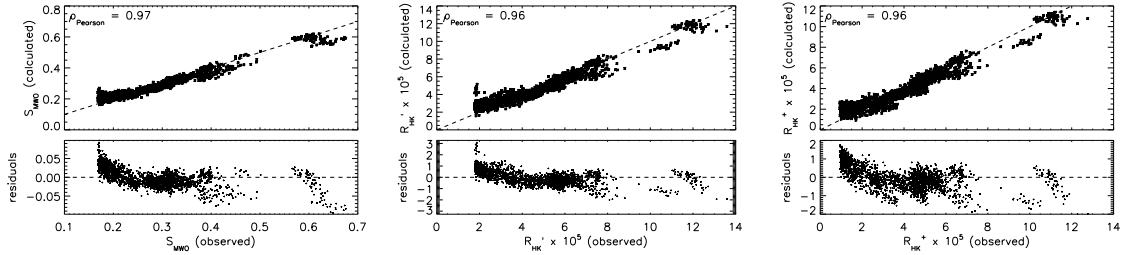


Figure 8.10: Comparing the measured values for the activity indices S_{MWO} (left), R'_{HK} (middle) and R_{HK}^+ (right) to the one converted from $F_{\text{Exc,IRT}}$ (obtained by comparing to PHOENIX model spectra). The conversion relations used were obtained using the GS approach.

Conversion of $F_{\text{Exc,H}\alpha}$ into activity indices

The $\text{H}\alpha$ -line and the calcium lines show a comparatively lower correlation. We can still find relations to convert their excess fluxes into one another. The correlation between the $\text{H}\alpha$ -line excess flux and S_{MWO} is also comparatively low, with $\rho \approx 0.612$, even after disregarding stars with low activity. For this reason, and due to the rather high relative errors (relative errors in excess of 40% and even higher are not uncommon), the resulting conversion is rather poor, with a median relative deviation of converted to measured values of almost 20%. Because the relative errors are so high (an effect exaggerated due to our conservative estimates) we have used fewer segments, so that more data points are included in each segment. We have additionally opted to not use the Monte Carlo approach for these conversions, and to not vary the found data points within their errors. We are underestimating the resulting error on the coefficients by not using this approach, but since we estimate the error on the conversion from the residuals, this problem is not severe. The GS-approach further limits its sampling for each step in $B - V$, so the large amount of data does not fully alleviate this issue. The LR algorithm is less sensitive to the high level of noise in the data. The overall rather poor quality of this conversion is still evident, e.g. from the fact that $m(B - V)$ may become negative for

$B - V \lesssim 0.45$, which is highly unphysical. The result is then given by:

	$S'_{\text{MWO}} = m \cdot F_{\text{Exc,H}\alpha} / (\text{erg s}^{-1} \text{cm}^{-2}) + b$	Residuals
GS	$m \cdot 10^6 = -0.803 + 2.943 \cdot (B - V) - 2.008 \cdot (B - V)^2$	$5 \cdot 10^{-2}$
	$b = 0.654 - 1.644 \cdot (B - V) + 1.293 \cdot (B - V)^2$	($\sim 12\%$)
LR	$m \cdot 10^6 = -1.799 + 6.016 \cdot (B - V) - 4.324 \cdot (B - V)^2$	$4 \cdot 10^{-2}$
	$b = 1.491 - 4.519 \cdot (B - V) + 3.721 \cdot (B - V)^2$	($\sim 11\%$)

While typical residuals (in the sense of 68% of points falling below this value) are about 0.04, about $\sim 4\%$ of points show large errors in excess of 0.1. The results of the conversion are compared to the measured values for both approaches in Fig. 8.11.

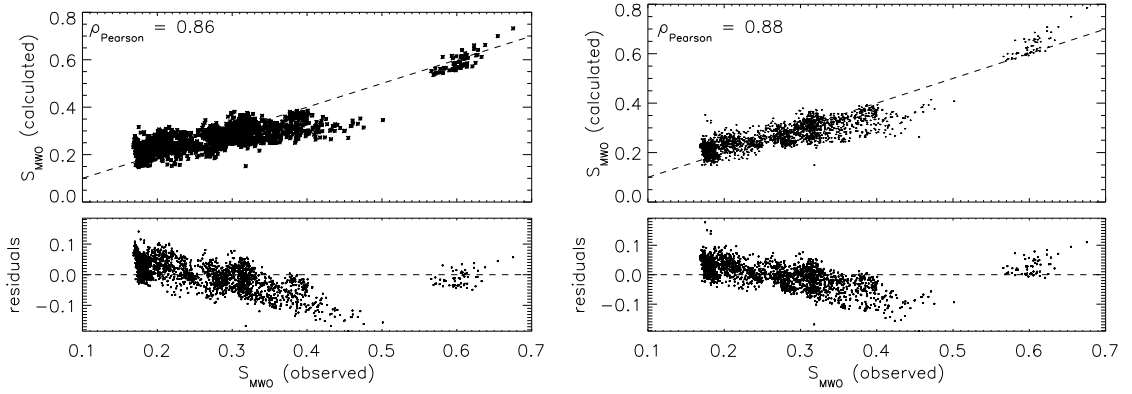


Figure 8.11: Comparing the measured values for S_{MWO} to the one converted from $F_{\text{Exc,H}\alpha}$ (obtained by comparing to PHOENIX model spectra), with the conversion relations from the LR approach (left) and the GS approach (right). This conversion is of overall lower quality than e.g. those shown in Fig. 8.10, due to the high relative errors on the determined excess fluxes on the H α -line.

We obtain the following relations for converting to R'_{HK} and R^+_{HK} by performing the same steps as above:

	$R'_{\text{HK}} = m \cdot F_{\text{Exc,H}\alpha} / (\text{erg s}^{-1} \text{cm}^{-2}) + b$	Residuals
GS	$m \cdot 10^{10} = -1.852 + 7.052 \cdot (B - V) - 4.939 \cdot (B - V)^2$	$1.2 \cdot 10^{-5}$
	$b \cdot 10^4 = 1.474 - 4.221 \cdot (B - V) + 3.200 \cdot (B - V)^2$	($\sim 19\%$)
LR	$m \cdot 10^{10} = -5.389 + 1.883 \cdot (B - V) - 1.460 \cdot (B - V)^2$	$1.2 \cdot 10^{-5}$
	$b \cdot 10^4 = 3.501 - 11.187 \cdot (B - V) + 9.088 \cdot (B - V)^2$	($\sim 18\%$)
	$R^+_{\text{HK}} = m \cdot F_{\text{Exc,H}\alpha} / (\text{erg s}^{-1} \text{cm}^{-2}) + b$	Residuals
GS	$m \cdot 10^{10} = -1.848 + 7.043 \cdot (B - V) - 4.935 \cdot (B - V)^2$	$1.2 \cdot 10^{-5}$
	$b \cdot 10^4 = 1.372 - 4.179 \cdot (B - V) + 3.180 \cdot (B - V)^2$	($\sim 24\%$)
LR	$m \cdot 10^{10} = -5.392 + 1.884 \cdot (B - V) - 1.461 \cdot (B - V)^2$	$1.2 \cdot 10^{-5}$
	$b \cdot 10^4 = 3.406 - 1.117 \cdot (B - V) + 9.099 \cdot (B - V)^2$	($\sim 23\%$)

8.4.2 Estimation of excess fluxes from other excess fluxes

Estimating the excess flux in groups of lines from an individual line

Just like with the results using the determined excess fluxes from Chapter 4, we find that the K-line shows about 33% more flux, just like before, again with no $B - V$ dependency:

$$F_{\text{Exc,K}} = 1.332 \cdot F_{\text{Exc,H}}.$$

Table 8.3: **Relations to estimate the excess flux in one Ca II IRT-line from measurements of another.** The errors of such a conversion are about $30\,000\text{ erg s}^{-1}\text{ cm}^{-2}$. Given here are the conversions obtained using the results from the comparison of spectra to PHOENIX model spectra (Chapter 7).

Source line	Target Flux		
	$F_{\text{Exc,IRT } \lambda 8498} =$	$F_{\text{Exc,IRT } \lambda 8542} =$	$F_{\text{Exc,IRT } \lambda 8662} =$
Ca II IRT $\lambda 8498$		$1.021 \cdot F_{\text{Exc}, \lambda 8498}$	$1.051 \cdot F_{\text{Exc}, \lambda 8498}$
Ca II IRT $\lambda 8542$	$0.943 \cdot F_{\text{Exc}, \lambda 8542}$		$1.007 \cdot F_{\text{Exc}, \lambda 8542}$
Ca II IRT $\lambda 8662$	$0.926 \cdot F_{\text{Exc}, \lambda 8662}$	$0.959 \cdot F_{\text{Exc}, \lambda 8662}$	

We present the relations to convert the Ca II IRT-lines into each other in Table 8.3. The relations are again independent of $B - V$. Some of them have changed notably from earlier (Table 8.1). These changes all incorporate the second Ca II IRT-line. This line shows the lowest degree of correlation to the other two lines (Table 7.4), suggesting that this line may suffer from systematic errors, for example from errors on the PHOENIX line profile.

Conversion of excess fluxes in various lines into one another

Previously, we set no intercept b for the conversion between the excess fluxes of the Ca II H- & K-lines and the Ca II IRT-lines, which we argued was unnecessary from the definition of the excess flux. However, the excess fluxes considered in this section include a basal flux contribution, which acts like a $B - V$ -dependent offset. Therefore, we require an intercept b here. Due to their high noise level, we additionally ignore excess fluxes from HD 2454. We obtain the following relations:

		$F_{\text{Exc,HK}} = m \cdot F_{\text{Exc,IRT}} + b$	Residuals
GS	$\log m =$	$-0.539 + 2.650 \cdot (B - V) - 2.333 \cdot (B - V)^2$	$3 \cdot 10^5$
	$b \cdot 10^{-6} =$	$5.833 - 18.122 \cdot (B - V) + 14.602 \cdot (B - V)^2$	($\sim 11\%$)
LR	$m =$	$0.215 + 5.440 \cdot (B - V) - 5.222 \cdot (B - V)^2$	$3 \cdot 10^{-2}$
	$b \cdot 10^{-6} =$	$3.964 - 1.213 \cdot (B - V) + 9.852 \cdot (B - V)^2$	($\sim 11\%$)

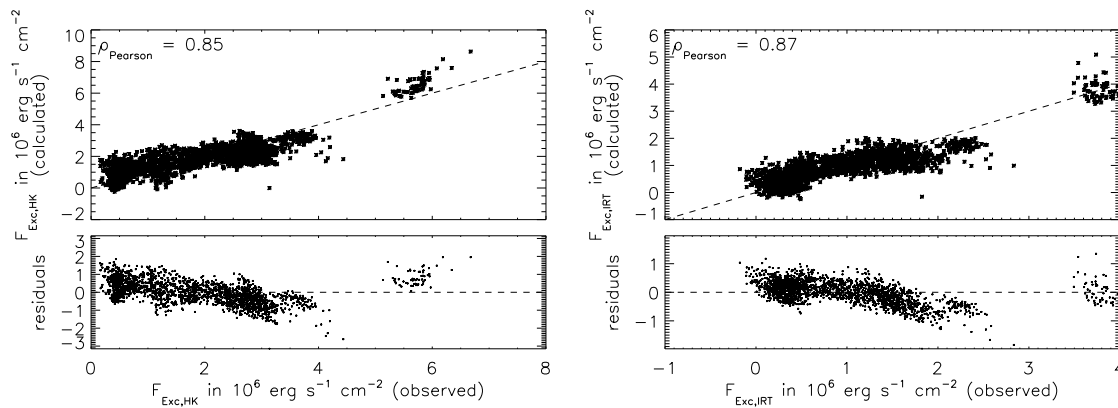


Figure 8.12: **The results of the conversion of the excess flux in the H α -line into the corresponding summed-up excess fluxes of the Ca II H- & K-lines and Ca II IRT-lines.** The conversion relations used are summarized in Table 8.4.

For the H α -line, there are now only a few stars available with significantly higher levels of excess flux. Therefore, using a quadratic fit in the GS approach that we introduced in Sect. 8.3.2 does not significantly improve the results. Its result shows very similar (yet slightly better) residuals. However, since the overall dependency appears closer to quadratic than linear, we model the relation

Table 8.4: **Relations to convert the excess flux in the H α -line to the value in the Ca II H- & K-lines and Ca II IRT-lines, and vice-versa.** These relations were obtained with the GS-approach. Residuals and fluxes are given in $\text{erg s}^{-1} \text{cm}^{-2}$, and must be entered in these units as well.

$F_{\text{Exc,H}\alpha} = c_0(B - V) + c_1(B - V) \cdot F_{\text{Exc,HK}} + c_2(B - V) \cdot F_{\text{Exc,HK}}^2$		Residuals
$c_0 =$	$-3.711 \cdot 10^4 + 1.461 \cdot 10^6 * (B - V) - 1.533 \cdot 10^6 * (B - V)^2$	$1.3 \cdot 10^5$
$c_1 =$	$1.043 - 2.582 \cdot (B - V) + 1.750 \cdot (B - V)^2$	($\sim 15\%$)
$c_2 =$	$-3.021 \cdot 10^{-7} + 8.430 \cdot 10^{-7} * (B - V) - 5.309 \cdot 10^{-7} * (B - V)^2$	
$F_{\text{Exc,HK}} = c_0(B - V) + c_1(B - V) \cdot F_{\text{Exc,H}\alpha} + c_2(B - V) \cdot F_{\text{Exc,H}\alpha}^2$		Residuals
$c_0 =$	$5.179 \cdot 10^6 - 1.632 \cdot 10^7(B - V) + 1.203 \cdot 10^7(B - V)^2$	$6.4 \cdot 10^5$
$c_1 =$	$-1.478 + 1.191 \cdot 10^{+1}(B - V) - 5.514(B - V)^2$	($\sim 26\%$)
$c_2 =$	$-8.993 \cdot 10^{-6} + 2.955 \cdot 10^{-5}(B - V) - 2.413 \cdot 10^{-5}(B - V)^2$	
$F_{\text{Exc,H}\alpha} = c_0(B - V) + c_1(B - V) \cdot F_{\text{Exc,IRT}} + c_2(B - V) \cdot F_{\text{Exc,IRT}}^2$		Residuals
$c_0 =$	$1.708 \cdot 10^5 + 7.637 \cdot 10^5(B - V) - 9.607 \cdot 10^5(B - V)^2$	$1.3 \cdot 10^5$
$c_1 =$	$1.927 - 4.231(B - V) + 2.603(B - V)^2$	($\sim 15\%$)
$c_2 =$	$-1.087 \cdot 10^{-6} + 2.787 \cdot 10^{-6}(B - V) - 1.690 \cdot 10^{-6}(B - V)^2$	
$F_{\text{Exc,IRT}} = c_0(B - V) + c_1(B - V) \cdot F_{\text{Exc,H}\alpha} + c_2(B - V) \cdot F_{\text{Exc,H}\alpha}^2$		Residuals
$c_0 =$	$1.122 \cdot 10^6 - 4.216 \cdot 10^6(B - V) + 3.309 \cdot 10^6(B - V)^2$	$3.7 \cdot 10^5$
$c_1 =$	$-1.803 + 9.789(B - V) - 5.669(B - V)^2$	($\sim 31\%$)
$c_2 =$	$-1.052 \cdot 10^{-6} + 4.184 \cdot 10^{-6}(B - V) - 3.765 \cdot 10^{-6}(B - V)^2$	

in that way. The relations we find are summarized in Table 8.4. We give two examples of the conversion results in Fig. 8.12.

Converting fitted amplitudes

We end this section by giving relations for the amplitudes A_f of the Gaussians fitted to the excess. Like before, we only give the relations for the amplitudes in units of $\text{erg s}^{-1} \text{cm}^{-2} \text{\AA}^{-1}$.

$$\begin{aligned}
 A_{f,\text{HK}} &= m(B - V) \cdot A_{f,\text{H}\alpha} + b(B - V), \text{ with} & (8.17) \\
 \log m &= -2.256 + 8.419 \cdot (B - V) - 5.826 \cdot (B - V)^2 \\
 b \cdot 10^{-15} &= 1.536 - 5.097 \cdot (B - V) + 3.831 \cdot (B - V)^2.
 \end{aligned}$$

This conversion yields residuals of $1 \cdot 10^{14}$ ($\sim 26\%$). This high value is due to the rather poor correlation between the amplitudes of the fitted Gaussians in the two lines. To convert from the Ca II IRT-line data:

$$\begin{aligned}
 A_{f,\text{HK}} &= m(B - V) \cdot A_{f,\text{IRT}} + b(B - V), \text{ with} & (8.18) \\
 \log m &= -0.477 + 3.079 \cdot (B - V) - 2.645 \cdot (B - V)^2 \\
 b \cdot 10^{-15} &= 1.263 - 4.299 \cdot (B - V) + 3.604 \cdot (B - V)^2.
 \end{aligned}$$

The residuals for this conversion are $4.8 \cdot 10^{13}$ ($\sim 11\%$). Finally, we have:

$$\begin{aligned}
 A_{f,\text{H}\alpha} &= m(B - V) \cdot A_{f,\text{IRT}} + b(B - V), \text{ with} & (8.19) \\
 \log m &= -0.099 - 1.508 \cdot (B - V) + 1.409 \cdot (B - V)^2 \\
 b \cdot 10^{-14} &= 1.678 - 1.996 \cdot (B - V) + 26.01 \cdot (B - V)^2.
 \end{aligned}$$

Here, the residuals are $1.7 \cdot 10^{13}$ ($\sim 11\%$).

The linear Pearson correlation coefficient is always larger than 0.85, which is lower than before, but still high enough to argue that the converted values can be used as estimate for the real one.

8.5 Summary and choice of conversion relations

We have made use of the good correlation between the various activity indices and excess fluxes to find relations to convert them into one another. To eliminate sampling bias, we have introduced the “Group segmenting” (GS) approach, which do not alter the results significantly (as our tests suggest), but by construction should eliminate some of the sampling bias. This is important, as it is rather significant otherwise. The relations found are valid for $0.5 \lesssim B - V \lesssim 1.0$ for Sect. 8.3, but only up to $B - V \approx 0.8$ for the relations from Sect. 8.4. The reason for this is the incomplete coverage of the PHOENIX model grid used for the excess determination.

This leaves the question which relation one should use to convert activity indices. First, this depends on which value should be converted. If they obtained their excess flux by comparing to an inactive star, then no basal flux is included, and the relations given first, in Sect. 8.3 should be used. On the other hand, if the excess still includes a basal flux component, then the relations from Sect. 8.4 are the better choice. The relations marked “LR” are suffering from sampling bias, as no effort was made to correct the fact that most stars are close to $B - V \approx 0.65$, while there are only comparatively few with higher $B - V$. This suggests that these relations yield more accurate results when converting values of a star with $B - V \approx 0.65$ region. Therefore, if values of stars with $B - V$ very similar to $B - V \approx 0.65$ should be converted, then these relations are the better choice. On the contrary, if a larger sample is considered, then the relations marked “GS” should be used, as the underlying procedure fixes this bias. However, the difference between the two relations is rarely significantly higher than the errors on the excess fluxes we used.

Note that the relations from Sect. 8.3 and Sect. 8.4 use different flux scales. While the difference is only $\sim 5\text{-}10\%$, as shown in Sect. 7.4, an error from this can easily be avoided, and even corrected, using the relations we gave in the same section.

For activity studies, an excess flux that does not include the basal flux is more desirable. Therefore, if none of the previously mentioned arguments are of importance, then this final argument suggests to use the relations from Sect. 8.3.

A short overview on how to use the code written for obtaining these conversions is given in the appendix, Sect. A.3

Chapter 9

Obtaining the Chromospheric Basal Flux

So far, we were most interested in the chromospheric excess flux as a possible indicator for stellar activity. However, not all of the chromospheric contributions are related to magnetic activity. In Schrijver [1987], the concept of a chromospheric basal flux was introduced: Even the most inactive stars show a residual flux level that stems from the chromosphere.

We have acquired a large sample of excess flux values, some of which include a chromospheric basal flux contribution. By analyzing this sample in detail, or by comparing to the set without the basal flux contribution, we can estimate the basal flux in the lines we have analyzed. In this chapter, we perform this determination using our dataset with a variety of different methods, after performing a simple check and determination with a comparison of literature values. We will also compare the relations we have found to a number of relations given in the literature.

9.1 Basal flux relations given in the literature

There are some basal flux relations available in the literature. In most cases, these relations are obtained by finding a relation that fits the lower envelope of the measured flux in the lines of a large sample of stars. The most inactive stars will make up the lower envelope, as they show only photospheric and chromospheric basal flux, but no additional flux component stemming from magnetic activity. If the photospheric flux in the line is known, this component can be subtracted, leaving only chromospheric contributions. The lower envelope of this sample is then just the basal flux. This method was used for example by Mittag et al. [2013], where the authors used PHOENIX model spectra to determine a relation for the photospheric flux, and subtracted that value from an estimated total line flux in the Ca II H- & K-lines. Combining their photospheric relation with the lower envelope of the total line flux given by Rutten [1984] or Rutten et al. [1991] similarly yields such a relation. Other authors used a different approach we will use as well: By subtracting model spectra directly from observed spectra, only the chromospheric contributions remain. The lower envelope then estimates the basal flux contribution. This was done e.g. in Pérez Martínez et al. [2014b], and yields a simple relation for $\log F_{\text{Ca II H\&K}}$ as a function of $\log T_{\text{eff}}$. Unlike our model spectra (Chapter 5), their models are strictly LTE, which affects the absolute flux scale in use, or the region in which the Ca II H- & K-lines lie. Additionally, only 25 stars are used to make up their lower envelope, distributed among all luminosity classes, leaving only a small fraction of that sample of main sequence stars. While their data quality is higher (they use UVES data) in the sense of higher SNR than most of the TIGRE spectra we are using, our larger data sample, as well as better model spectra suggest that we can improve on their relation.

Finally, Fawzy [2015] used another approach: They try to model the basal flux theoretically. They find a simple linear relation $\log F_{\text{Ca II H\&K}}(\log T_{\text{eff}})$, by modeling the energy deposited by acoustic waves into the chromosphere.

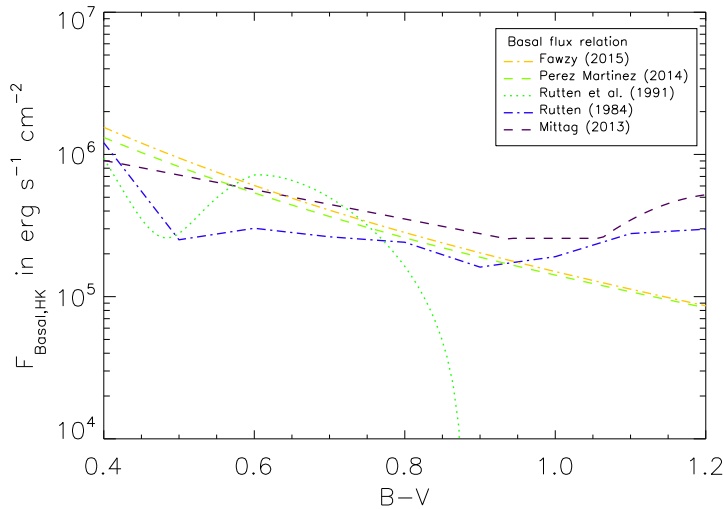


Figure 9.1: Comparing various relations for the basal flux $F_{\text{Basal,HK}}$ from the literature. The relation by Rutten et al. [1991] has been interpolated from its low original resolution for better visualization.

The general shape of these relations is similar, but there are still some deviations between them. These are especially noteworthy, as we work on a logarithmic flux scale here. Figure 9.1 shows all the relations in the $B - V$ -region that we consider here. Especially the early lower envelopes used by Rutten [1984] and Rutten et al. [1991] show a clear rise towards higher temperatures (lower $B - V$), for $B - V \lesssim 0.4$. In the paper by Rutten et al. [1991], only one data point is given for this region. In their other paper, there is no such step visible, unless the photospheric contribution is removed. The other, more modern relations do not show this trend, and all agree well with each other. Note that all these relations are only for the basal flux in both Ca II H- & K-lines. We will also attempt to find relations for the other lines we have considered in this work, including each of the Ca II H- & K-lines individually. This process is difficult, however, as the low values of the basal flux within them, combined with the high noise in many of the determined excess flux values will result in large errors. In that sense, the relations we will find can definitely be improved upon by using spectra with higher SNR.

9.2 Finding the basal flux by comparison of our results to literature values

Parts of this section were previously published in Martin et al. [2017].

The excess flux determined in Chapter 4 does not include a basal flux contribution, so one might assume that it is impossible to obtain a value for the basal flux contribution just from this dataset. While it is true that the excess flux from Chapter 7 is better suited for this purpose, we can make use of relations from the literature to obtain a rough estimate. The flux in the line is made up of the three components of a photospheric flux F_{phot} , the chromospheric basal flux $F_{\text{chrom,basal}}$ and finally, the activity-related flux $F_{\text{chrom,act}}$, so that we can write:

$$F_{\text{Line}} = F_{\text{phot}} + F_{\text{chrom,basal}} + F_{\text{chrom,act}}. \quad (9.1)$$

There are several relations available in the literature to estimate this value from a known value for S_{MWO} and the star's $B - V$. The excess flux from Chapter 4 was determined from subtracting the value of F_{Line} of an inactive star to the value for an active star. If we assume that the inactive star is fully inactive, then it has $F_{\text{chrom,act}} = 0$. Since the comparison star was chosen to be as similar as possible to the active target star, it should have the same photospheric F_{phot} and chromospheric basal flux $F_{\text{chrom,basal}}$. Therefore, the remaining excess flux determined is simply $F_{\text{chrom,act}}$. We can now perform the steps in opposite order: We can calculate F_{Line} using a literature relation

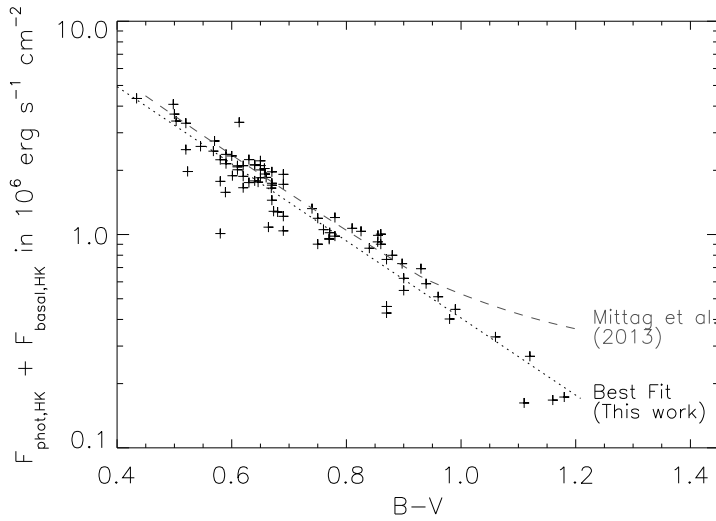


Figure 9.2: **Photospheric and basal flux, determined from a comparison of the excess flux, obtained by comparing to inactive stars, to the entire line flux calculated according to Rutten [1984].** We compare the resulting best fit (dotted line) to the relation from Mittag et al. [2013] (dashed line). This plot shows the average measured values for 82 stars. This plot was previously published in Martin et al. [2017].

by inserting that spectrum's S_{MWO} , and then subtract the determined excess flux, which is just $F_{\text{chrom.act}}$. The remainder will then be the photospheric and chromospheric basal flux contribution. Performing this operation using the relations from Rutten [1984] for the total line flux according to Eq. (9.1), we end up with the result shown in Fig. 9.2, where we also compare this to the relation from Mittag et al. [2013]. The two relations are rather similar, with only a slight offset between the two for most of the $B - V$ -region covered. The two relations start to differ more significantly only at about $B - V \approx 1.0$. The relation from Mittag et al. [2013] is defined in steps, with one such step occurring at $B - V = 0.94$. From our data, it appears that the continued linear fit is a better match. However, we do not have many data points beyond this point, so we cannot make any definite statement, considering that in Mittag et al. [2013], such datasets were available. Regardless, the best fit to the data is found to be

$$\log(F_{\text{phot,HK}} + F_{\text{basal,HK}}) = 7.42 - 1.81 \cdot (B - V). \quad (9.2)$$

This also includes the photospheric contribution, which we expect to be larger than the chromospheric basal flux. However, we can go one step further by using a relation for only the photospheric flux. One such relation is given in Mittag et al. [2013] as:

$$\log F_{\text{phot,HK}} = 7.49 - 2.06 \cdot (B - V). \quad (9.3)$$

Subtracting Eq. (9.3) from Eq. (9.2), we find the relation for just the basal flux contribution:

$$F_{\text{basal,HK}} = 10^{7.42-1.81 \cdot (B-V)} - 10^{7.49-2.06 \cdot (B-V)} \quad (9.4)$$

$$\Rightarrow \log F_{\text{basal,HK}} \approx 6.26 - 1.094 \cdot (B - V) \quad (9.5)$$

We have performed a Taylor series around $B - V = 0.8$ (close to the center of the range covered) in the last step. We show both relations in Fig. 9.3, from where it is apparent that the relation in Eq. (9.4) is well described by the Taylor approximation given in Eq. 9.5. The relation Eq. (9.4) shows somewhat unexpected behavior as it falls towards *lower* basal fluxes when $B - V$ goes below 0.5. The other relations found do not show this behavior. Therefore, it is likely an artifact from the fit in Eq. (9.2) being less reliable at the lower end of our $B - V$ range. The overall match of this relation to the ones from the literature is pretty good, and it falls between the simple relations linear in $\log T_{\text{eff}}$ [Fawzy, 2015, Pérez Martínez et al., 2014b] and the point-wise defined one by [Rutten, 1984, Rutten et al., 1991].

This method relies heavily on relations from other sources. However, those may introduce systematic errors, as the fluxes estimated from external relations may use differently determined flux scales.

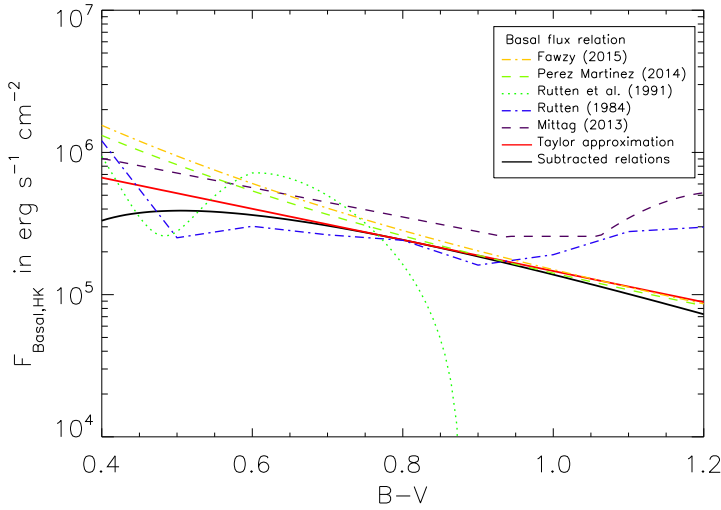


Figure 9.3: Comparing the relation for the basal flux in the Ca II H- & K-lines given in Eq. 9.4 (black line) and its Taylor approximation to first order Eq. (9.5) (red line) to the various literature relations given in Sect. 9.1.

Such errors may very well be of the order of the basal flux level. These results may therefore be less reliable.

We can only perform this method for the summed up basal flux in both of the Ca II H- & K-lines, as there are no other relations available for the lines individually, or the other lines considered here.

9.3 Finding the basal flux from the lower envelope of the chromospheric flux

The “classical” approach used to obtain the relations in Rutten [1984], Rutten et al. [1991], Mittag et al. [2013] is to determine the line flux for a large sample of stars. Then, the photospheric contribution can be estimated from models or scaling relations. Subtracting this contribution from the total line flux then leaves a sample of just the chromospheric contribution for a variety of $B - V$ -values. The lower envelope of the distribution is then made up by the inactive stars, which now only show the basal flux.

We find a relation from our determined chromospheric flux in the same way. Because these chromospheric flux values are required to still contain the basal flux, we must use the values determined in Chapter 7. Our goal is a relation for the basal flux in each spectral line analyzed here as a function of $B - V$, in the range of $0.4 < B - V < 0.8$, limited from the incomplete model grid we have used. In a first filtering step, we ignore the highest values – the values that make up the highest fraction are certainly not the ones to determine the lower envelope, which we verify by visual inspection. The value for this fraction used for the different lines is given in Table 9.1.

The excess fluxes we have determined include uncertainties, which in many cases are close, or even larger than the level of the excess flux. Therefore, the “real” lower envelope is unlikely to be the one obtained from simply connecting the lowest points of the relation $F_{\text{Exc}}(B - V)$. With such large errors, some points are likely to lie below the real lower envelope. Note that this effect will be visually enhanced by us using a logarithmic scale in the plot. In this sense, this problem is similar to obtaining the continuum from a noisy spectrum with absorption lines, described in Sect. 3.2. Performing our method for obtaining the continuum on the inverted excess fluxes yields what can ultimately be considered the envelope on the data, despite the noise on the data. The exact settings for the filter of this method used have been tweaked until a good visual match with the data was achieved. It is necessary to use different filter settings, as the distribution of excess fluxes varies: A steeper fall-off, as is the case for the H α -line, means that the fraction of the highest data points that we can safely ignore must be lower than for other lines. Similarly, the threshold in use for the

envelope determination is mostly affected by the error levels: The higher the relative error is, the lower this value needs to be. We tweaked the actual threshold parameters according to two criteria: First, that less than 32% of points fall below the envelope at the 1σ level. Second, that even when disregarding the errors, not more than roughly 25% of points fall below the envelope. However, because the errors are so large – likely too large, as we have taken a conservative approach to error estimation (Sect. 3.6, Sect. 7.2.3) – the second condition was always the limiting factor. We give the exact filtering thresholds used in Table 9.1.

Table 9.1: **Threshold values used for determining the lower envelope for the basal flux determination.** The first row gives the fraction of values ignored for the entire determination. The lower envelope of the remaining data points was found using the method described in Sect. 3.2, which continues the procedure until a fraction of points lie below the fit. This fraction is given in the second row.

Threshold	Ca II H	Ca II K	— Ca II IRT —			H α
			$\lambda 8498$	$\lambda 8542$	$\lambda 8662$	
Upper fraction ignored	0.336	0.336	0.252	0.252	0.252	0.210
Filter for envelope	0.550	0.550	0.525	0.519	0.519	0.519

9.3.1 Basal flux for individual lines

In this way, we obtain the lower envelope of the six lines considered here, which we show in Fig. 9.4. The line represents the determined lower envelope, which we consider as the basal flux level. The relations are generally similar, with the basal flux decreasing with higher $B - V$ for all lines. The Ca II K line shows only a small dependence on $B - V$. This is surprising, as we expected the same dependency as for the Ca II H line, which mirrors the behavior of the literature relations much better. Since its flux is largest of all lines considered, it will have a stronger effect in the relation for the sum of both lines, lowering the slope to only ≈ -0.5 (see next section), notably lower than the literature relations. We would have expected this line to be the most “well-behaved”, due to the largest flux and subsequently lowest relative noise levels.

While this basal flux varies by about 20%, and is largest for the earlier-type stars, the total flux σT_{eff}^4 is halved over this $B - V$ -region! The *relative* amount of chromospheric flux is therefore greatly increased for the late-type stars, which mirrors the common knowledge of later types being more active.

The relations we find, and which have been plotted in Fig. 9.4, are given in Table 9.2. In the plots, we also show the fraction of data points that fall below the envelope with and without taking the error into account (see previous section). Only for display reasons we have added a small, random offset added to the $B - V$ -values of each data point in the plots, to more accurately portray the density of these points.

Table 9.2: **Coefficients for calculating the basal flux inside the lines from the lower envelope determination.** Plugging these coefficients into $\log F_{\text{Basal}} = a + b \cdot (B - V)$ yields an estimate of the basal flux. Due to the limiting coverage of our PHOENIX model spectra, these relations are valid for $0.4 < B - V < 0.8$. These relations are plotted in Fig. 9.4.

— $\log F_{\text{Basal}} / (\text{erg s}^{-1} \text{cm}^{-2}) = a + b \cdot (B - V)$ —						
Coefficient	Ca II H	Ca II K	— Ca II IRT —			H α
			$\lambda 8498$	$\lambda 8542$	$\lambda 8662$	
a	5.70	5.55	5.46	5.43	5.48	6.67
b	-0.61	-0.18	-0.96	-0.90	-0.74	-1.72

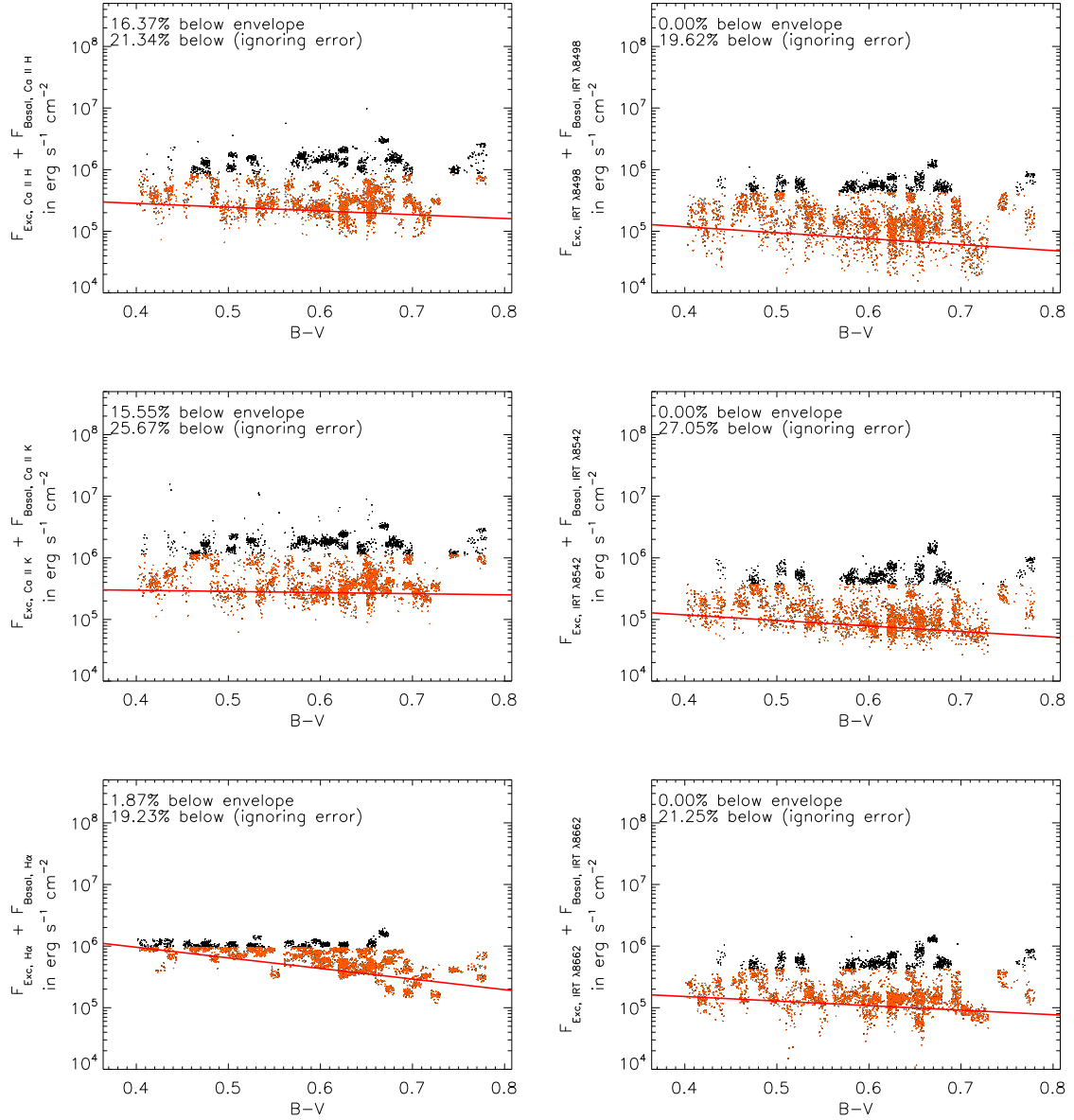


Figure 9.4: **Basal flux of the lower fraction of fluxes (orange points) as the lower envelope of the chromospheric contribution (red line) for the six lines under consideration. Left column, Top to bottom: Ca II H, Ca II K, H α . Right column shows the Ca II IRT.** In this method, the lower envelope is obtained from only a fraction of points. Due to the high errors on the data points (not shown), a fraction of the points lie below this threshold: This fraction is given in the top left of each plot, both when taking the error into account (first number), and without (second number). Just for the plot, the points have been randomly moved across the $B - V$ -axis by no more than 0.01, to more accurately show the density of the points. The resulting relations are given in Table 9.2.

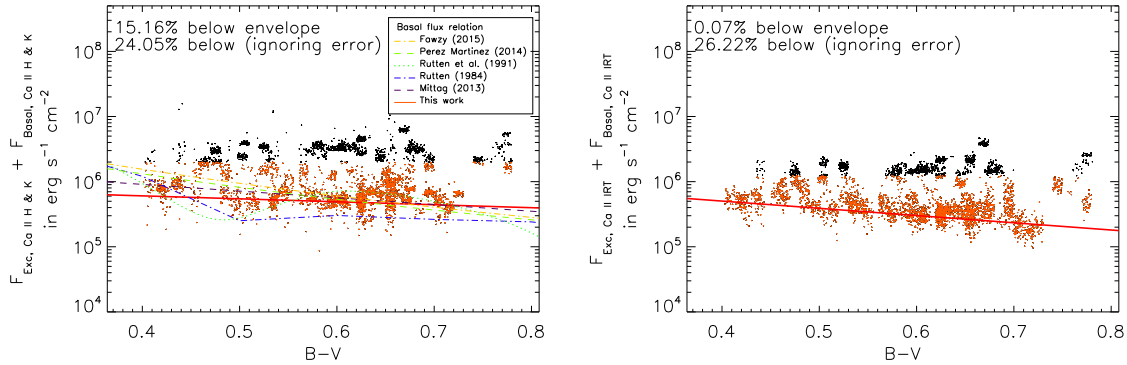


Figure 9.5: **Obtaining the basal flux (red line) as the lower envelope of the excess fluxes (black and red dots) determined from Chapter 7 for the summed up basal flux in the Ca II H- & K-lines (left) and the Ca II IRT-lines (right).** Same as Fig. 9.4, but for the summed-up values for the Ca II H- & K-lines and Ca II IRT-lines.

9.3.2 Combined basal flux in groups of lines

To find the basal flux in groups of lines – such as the summed up value for the Ca II H- & K-lines, as we have done in the previous section – we could in principle simply form the sum of the individual relations. However, it is better to *first* combine the determined excess fluxes, and to find the lower envelope on this sum, to lower the relative noise on each individual data point, and more accurately define their lower envelope. The relations we find are then:

$$\log F_{\text{Basal, Ca II H \& K}} / (\text{erg s}^{-1} \text{cm}^{-2}) = 5.96 - 0.45 \cdot (B - V), \quad (9.6)$$

for the Ca II H- & K-lines, and

$$\log F_{\text{Basal, Ca II IRT}} / (\text{erg s}^{-1} \text{cm}^{-2}) = 6.15 - 1.11 \cdot (B - V), \quad (9.7)$$

for the Ca II IRT-lines. We show the relations in Fig. 9.5, where we also compare Eq. (9.6) to the various literature relations. Our relation for the basal flux in the Ca II H- & K-lines fits about as well as the relation from the previous section, and again falls between the literature relations, though below the “modern” ones. The slope of the relation is lower, however, due to the strong influence of the almost flat relation from the Ca II K line (Table 9.2). Still, the deviation of our relation to the modern literature ones of Pérez Martínez et al. [2014b] and Fawzy [2015], especially at higher $B - V$ is low, considering the large error level on the excess fluxes. This error is even larger on the excess fluxes from the Ca II IRT-lines, as evidenced by the extremely low fraction of data points falling below the envelope at the 1σ -level (0.07%). This makes it hard to accurately define a basal flux relation for the Ca II IRT-lines, though the one we have chosen appears to fit well. We will see in the next Section that similar relations are obtained by other methods. For a typical main sequence star of $B - V \approx 0.8$, Eq. (9.6) corresponds to $3.98 \cdot 10^5 \text{ erg s}^{-1} \text{cm}^{-2}$ for the Ca II H- & K-lines, and Eq. (9.7) to $1.83 \cdot 10^5 \text{ erg s}^{-1} \text{cm}^{-2}$ for the Ca II IRT-lines, respectively. We compare the two relations in Fig. 9.6. The Ca II IRT-lines always show a lower basal flux level, ranging from roughly 85% of the basal flux of the Ca II H- & K-lines at the lowest $B - V$, where the relation may be least trustworthy, to about half of its flux level. Interestingly, this basal flux fraction relation goes opposite to the fraction of measured *excess* fluxes. This may hint at a different physical source for the chromospheric basal flux, instead of a low residual activity as has been suggested by some authors [Fawzy et al., 2002].

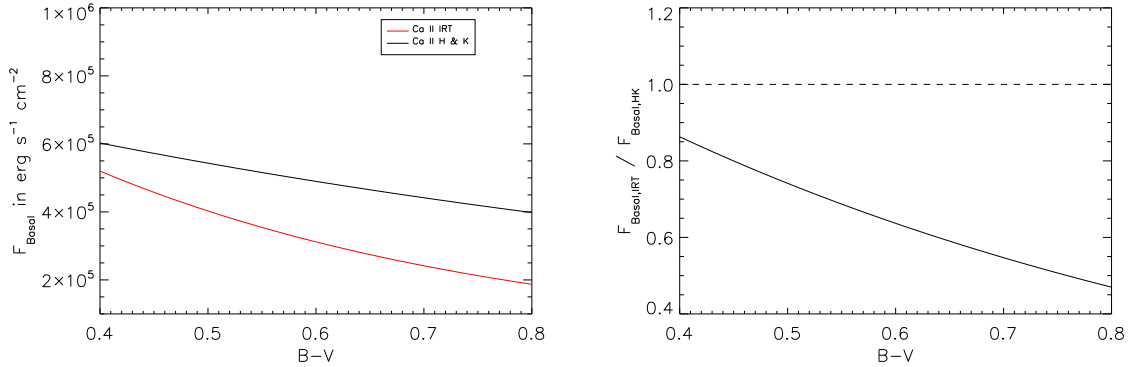


Figure 9.6: **Comparing basal flux relations for the Ca II H- & K-lines and the Ca II IRT-lines (left), as well as their fraction (right), from the lower envelope method.** The dashed line on the right corresponds to identical basal flux levels in the Ca II H- & K-lines and Ca II IRT-lines. The combined basal flux in the Ca II IRT-lines is only about 65% of the basal flux in the Ca II H- & K-lines across this region in $B - V$.

9.4 Finding the basal flux by comparison of our results from different comparison sources

In the previous section, we performed the basal flux determination by defining the lower envelope of the $F_{\text{Exc}}(B - V)$ relation. A disadvantage of this procedure is that only a fraction of all data points are of interest then, namely the ones that make up the lower envelope. The large number of excess fluxes for active stars are of no interest in this case. However, we have access to two types of excess fluxes for each observation. The one obtained from comparing to inactive stars $F_{\text{Exc,inact}} = F_{\text{chrom,act}}$ and the one from comparison to model spectra $F_{\text{Exc,model}} = F_{\text{chrom,basal}} + F_{\text{chrom,act}}$. The difference of the two is therefore just the basal flux level. In principle, every observation of a star, compared to its specific comparison star, would result in the same basal flux level from this procedure. This is because subtracting the defined excess fluxes in this fashion is just removing the contribution of the active star:

$$\begin{aligned}
 F_{\text{Exc,model}} - F_{\text{Exc,inact}} &= (F_{\text{phot}} + F_{\text{chrom,Basal}} + F_{\text{chrom,act}} - F_{\text{phot}}) - & (9.8) \\
 & (F_{\text{phot}} + F_{\text{chrom,Basal}} + F_{\text{chrom,act}} - (F_{\text{phot}} + F_{\text{chrom,Basal}})) \\
 &= F_{\text{chrom,Basal}}.
 \end{aligned}$$

Technically, one could therefore simply compare the inactive stars used as comparison from Table 4.2, or a relation such as Eq. (4.6) and compare the result to PHOENIX model spectra. We however make use of the large data sample and use all determined excess fluxes individually. The reason for the preference to this approach is that in the process of the excess flux determination, certain errors, e.g. an incorrect or different normalization, were handled already by the comparison method (see Chapter 3). Additionally, over the large sample of data points, the error is more likely to just result in scatter around the real value, with the average value still being correct. When using only the very small amount of comparison stars, this is no longer necessarily true.

9.4.1 Comparing the measured values directly

To perform the comparison, we first need to cross-check which observations were actually in both excess flux samples. Since we found different outliers, and used a different range in $B - V$ for the object selection, not all stars and observations were analyzed in both Chapter 4 and Chapter 7. We must correct for the different flux scales in use. We have already seen that the difference is only of

Table 9.3: **Coefficients for calculating the basal flux inside the lines from comparing the obtained excess fluxes from Chapter 4 and Chapter 7.** Inserting these coefficients into $\log F_{\text{Basal}} = a + b \cdot (B - V)$ yields an estimate of the basal flux. Due to the limiting coverage of our PHOENIX model spectra, these relations are valid for $0.4 < B - V < 0.8$. These relations are plotted in Fig. 9.7.

— $\log F_{\text{Basal}} / (\text{erg s}^{-1} \text{cm}^{-2}) = a + b \cdot (B - V)$ —						
Coefficient	— Ca II IRT —			H α		
	Ca II H	Ca II K	$\lambda 8498$	$\lambda 8542$	$\lambda 8662$	
a	5.57	5.65	5.49	5.14	5.60	6.60
b	-0.59	-0.48	-1.02	-0.49	-1.01	-1.65

the order of a few percent, rising to about 10% in the worst case. For each data point, we have calculated the fraction of the surface flux according to PHOENIX model spectra (used in the excess fluxes determined in Chapter 7) to the surface flux according to Hall [1996] (used in the excess fluxes determined in Chapter 4). After correcting the parameters for this value, we can subtract the determined excess fluxes directly to obtain $\Delta F_{\text{Exc}} = F_{\text{chrom,basal}}$, which are then given in the PHOENIX flux scale. Looking at the previous results, we can tell that the basal flux will be roughly at the level of a few $10^5 \text{ erg s}^{-1} \text{ cm}^{-2}$. Unfortunately, this is right at the noise level of the TIGRE spectra. For this reason, we often find negative values for the difference between the excess fluxes. To account for this problem, we disregard all values that are unrealistic according to the relations we have found so far, those below $10^5 \text{ erg s}^{-1} \text{ cm}^{-2}$ and those higher than $10^7 \text{ erg s}^{-1} \text{ cm}^{-2}$. Another result of the high noise level is that the actual tendency of the basal flux relation, which we obtain by a linear fit, varies depending on these selection criteria, and on factors such as whether we use the average value of each star instead of the individual ones from each spectrum. We found better agreement, as determined by visual inspection, as well as a better match to the previously given relations, when fitting all data points at once, rather than the average for each star. Considering Fig. 9.1, we try to optimize for a relatively flat $B - V$ dependency. The overall value should be correct, but the trend we find might be determined incorrectly, due to the scatter we expect from the data points.

We use the directly integrated excess flux, as opposed to the one estimated from the Gaussian fit in the next part. We fit a linear relation to the data points. When doing so, we take their errors into account, and disregard outliers¹. The obtained coefficients are given in Table 9.3. The results of the fit for the individual lines are shown in Fig. 9.7.

The fits we find are very sensitive to our selection criteria. Neglecting certain stars can have a strong influence on the results if they feature a large number of data points. While this could in theory be improved by simply taking the average value for each star and carefully choosing a weight of each averaged value, we found no clear improvement from this step. The main reasons for the high sensitivity of the result on the exact set of stars used are likely the large errors in the data points, and the difficulty in estimating the systematic contribution to them (e.g. from an incorrectly chosen comparison spectrum in Chapter 4), which affects all observations of one star in the same fashion. The nominal residuals of each of these are therefore of the order of 30-50%. Using higher SNR spectra, and selecting the comparison values from a fit (similar to how we have done it in Chapter 7, a step that is also affected by the SNR quality of the star's spectra) would be one way to improve on this.

9.4.2 Combined lines

We will now use the flux estimated from the fitted Gaussian, as we have mentioned before, instead of the directly measured one. This value is slightly less prone to errors and does not become negative, due to the limitations set upon it in the fit. In turn, we have assumed that a Gaussian is a good description of the excess distribution, however, visual inspection has revealed that this is generally a

¹We employ the IDL routine `ROBUST_POLY_FIT` for this purpose

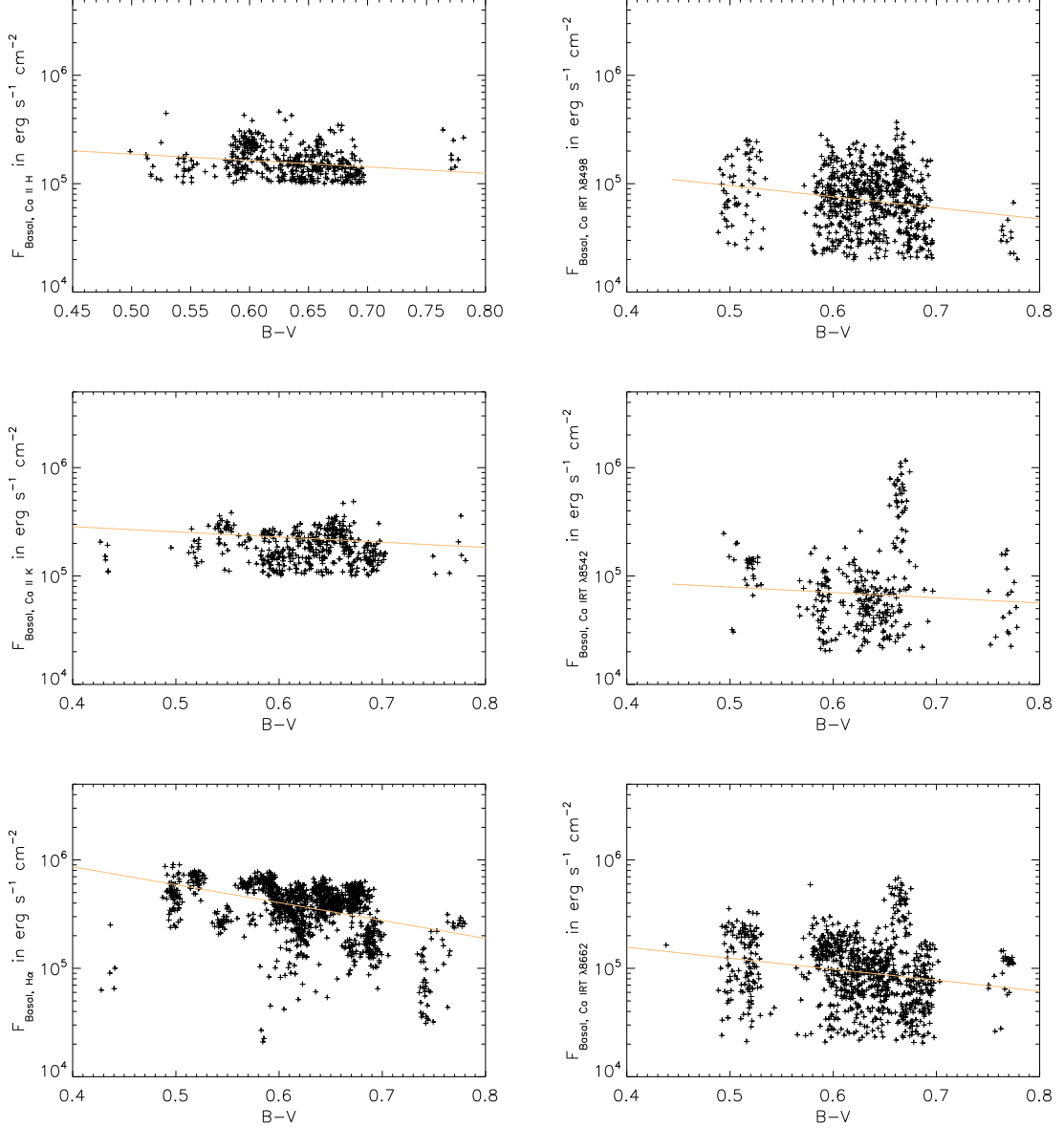


Figure 9.7: Basal flux, determined by fitting the value of $\Delta F_{\text{Exc}} = F_{\text{Basal}}$, which is the difference of the two excess fluxes determined in Chapter 4 and Chapter 7. Left column, top to bottom: Ca II H, Ca II, $H\alpha$. Right column shows the Ca II IRT-lines. After careful filtering to remove clearly incorrect data points, we perform a fit disregarding outliers to the sets of measured basal flux values. This process is rather delicate as the resulting flux is highly contaminated by noise. For plotting purposes, the points have again been randomly moved across the $B - V$ -axis by no more than 0.01, to more accurately show the density of the points. The resulting relations are given in Table 9.3.

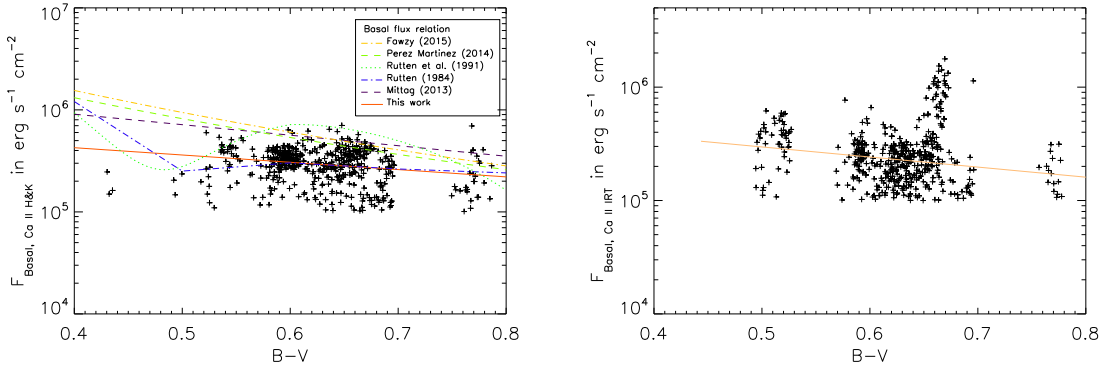


Figure 9.8: **Plotting the basal flux relations from comparing the results from Chapter 4 and Chapter 7 for the Ca II H- & K-lines (left), which we also compare to literature values, and the Ca II IRT-lines (right).** The data points are slightly shifted in $B - V$ to better show their density.

good assumption (see Fig. 3.7). Just like before, we do not simply add together the relations found for the individual lines, but rather combine the excess fluxes *first*, and then fit the resulting values. This lowers the noise on each individual data point, resulting in a slightly more accurate fit. We find for the Ca II H- & K-lines:

$$\log F_{\text{Basal, CaII H \& K}} / (\text{erg s}^{-1} \text{cm}^{-2}) = 5.92 - 0.72 \cdot (B - V), \quad (9.9)$$

and for the Ca II IRT-lines, we find:

$$\log F_{\text{Basal, CaII IRT}} / (\text{erg s}^{-1} \text{cm}^{-2}) = 5.96 - 0.97 \cdot (B - V). \quad (9.10)$$

These two relations are shown in Fig. 9.8.

9.5 Results

We were able to obtain relations for the chromospheric basal flux from a variety of methods, all of which yielded results that agree well with each other. The relations we have found are somewhat similar in their tendency to show decreasing absolute excess fluxes towards higher $B - V$. The first relation, Eq. (9.5) features the most assumptions and relations from other authors. Since its result is similar to the other ones, we focus now on our new relations that have been found fully from our data and methods. All relations for $F_{\text{Basal, CaII H \& K}}$ fall in between the literature relations, further solidifying the approach we have taken. If we only consider the more modern literature relations, and disregard the ones from Rutten [1984] and Rutten et al. [1991], then all our relations fall below the literature relations, and so do the determined basal fluxes. However, while the determined *relative* difference is rather large, we are analyzing fluxes at the very edge of the capabilities of our dataset, given their noise levels. The actual measured values are much higher, by roughly a factor of ten, so that the relative error is strongly increased when considering only this small fraction. Because of this, we can be satisfied with the relations we found, as their deviation from the found literature values is comparable to the average error on the excess flux points. None of the approaches given is inherently better than the others. They all make use of an unique method to determine the basal flux level. Therefore, we can average the relations we found to obtain our final relation:

$$\log F_{\text{Basal, CaII H \& K}} / (\text{erg s}^{-1} \text{cm}^{-2}) = 5.94 - 0.59 \cdot (B - V) \quad (9.11)$$

We compare this relation to other literature relations in the left plot of Fig. 9.9. The right plot shows the corresponding average for the Ca II IRT-lines, given as:

$$\log F_{\text{Basal, CaII IRT}} / (\text{erg s}^{-1} \text{cm}^{-2}) = 6.05 - 1.04 \cdot (B - V). \quad (9.12)$$

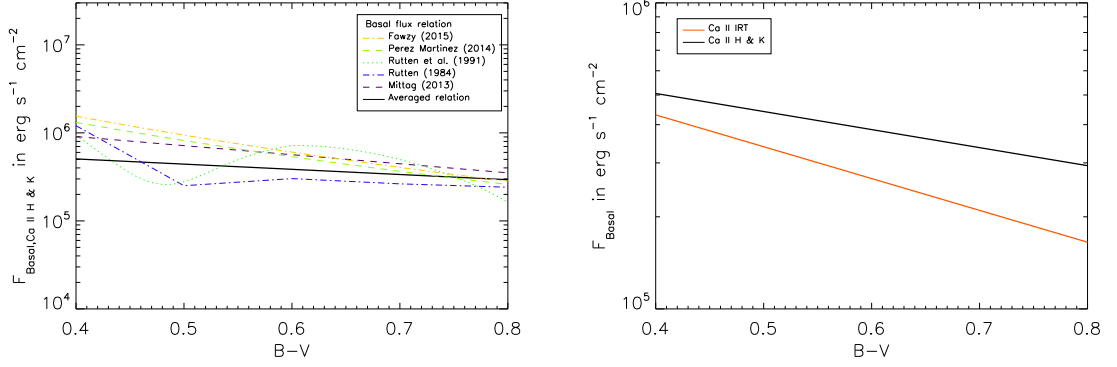


Figure 9.9: **Plotting the average flux relations from the basal flux relations we have found.** We compare the relation for the Ca II H- & K-lines in the left plot, and the two relations Eq. (9.11) and Eq. (9.12) in the right plot.

These relations are valid in the range covered by our PHOENIX model spectra grid ($0.4 < B - V < 0.8$). The slope of the relation Eq. (9.11) is much flatter than of the literature values, but overall, the magnitude of the basal flux level is similar. While we find a good match for the late-type stars, for lower $B - V$ -values our relation is too low. Indeed, the sampling in that region is not very good, as many spectra could not have been taken into account, or the difference of their determined excess fluxes became negative, suggesting a systematic error towards the lower $B - V$ values. The sharp bend observed in the relation by Rutten [1984] and Rutten et al. [1991] is not reproduced in our sample, but neither is it in the other literature relations.

The quality of the dataset is limited and does not allow a more specific analysis, as we have found the relations to be very sensitive to the exact selection of stars to use, corresponding to the filter threshold values given in Table 9.1. Interestingly, for the Ca II IRT-lines, the basal flux absolute slope is roughly twice as large compared to the Ca II H- & K-lines, and overall, they show roughly 20-30% less basal flux across the $B - V$ validity range, as seen in the right plot of Fig. 9.9. These values can be compared to the $\log gf$ values of the lines, a measure of the transition probability that influences a line's strength. They are given in Kramida et al. [2015] as -0.18 and 0.135 for the Ca II H- & K-lines, respectively, and -1.318, -0.36 and -0.622 for the Ca II IRT-lines. The ratio of these summed-up gf values is 0.35, which is quite different from the ratio of the basal fluxes. This may be an indicator of a different formation process for the basal flux.

Chapter 10

Correlations for Individual Stars and Finding Periods

We have seen that the excess fluxes determined from the individual lines correlate very well across the entire sample. In this chapter, we consider the measured excess values of individual stars separately. Differences in the formation process or region of the excess fluxes in the different lines may introduce a slightly different behavior in the excess fluxes, which may lower, or in extreme cases even invert the correlation between them. But even without these effects, we must expect a lower correlation generally, as the variation observed in the excess fluxes will be much lower compared to the noise level.

Meunier and Delfosse [2009] used high-resolution ($R \approx 500\,000$) solar spectra, obtained at Kitt Peak Observatory, to analyze the normalized line core intensity in the Ca II H- & K-lines and the H α -line. They found that there is no perfect, permanent correlation, but rather that the degree of it varies strongly from -1 to 1, and in case of the Sun depends on the cycle phase. Furthermore, they interpret this behavior as a result of different behavior of these two lines for plage and filaments: The emission in the Ca II H- & K-lines becomes larger when plages are present, with no strong effect from filaments. For the H α -line, however, filaments increase the absorption in the line, and plages contribute to its emission. Then, different degrees of correlations could be explained from different degrees contrast in the H α -line.

Here, we analyze stars with at least five measurements with errors significantly smaller than the variation in the excess fluxes. We determine the degree of correlation between these fluxes, and compare these values to stellar parameters. If the Ca II IRT-lines were to show the same correlations than the H α -line, than this could be an indicator for a similar behavior regarding the effects of plages and filaments.

The variation of the S_{MWO} index has been used to determine periods in a variety of stars. In fact, the majority of spectra analyzed in this work have originally been taken to determine rotational periods [Hempelmann et al., 2016]. With the excess fluxes determined in this thesis, we will analyze the temporal behavior of a few select stars with a variety of methods.

10.1 Correlations for individual stars

In this section, we will perform a statistical analysis of the correlations of the different excess fluxes obtained, only considering the data for one individual star at a time. Unlike before, the vastly lower amount of data points, combined with a much lower range for these few values (especially compared to the errors) means that we must reconsider what we recognize as “well correlated”. We therefore consider the relative difference of the determined correlations, and the histogram distributions here, rather than their absolute value. As we have seen in Chapter 8, the relations between two excess fluxes, or the fitted amplitudes, is linear for a set value of $B - V$, except for the H α -line. Therefore, we use the Pearson correlation coefficient for all lines, except the H α -line, where we use the Spearman

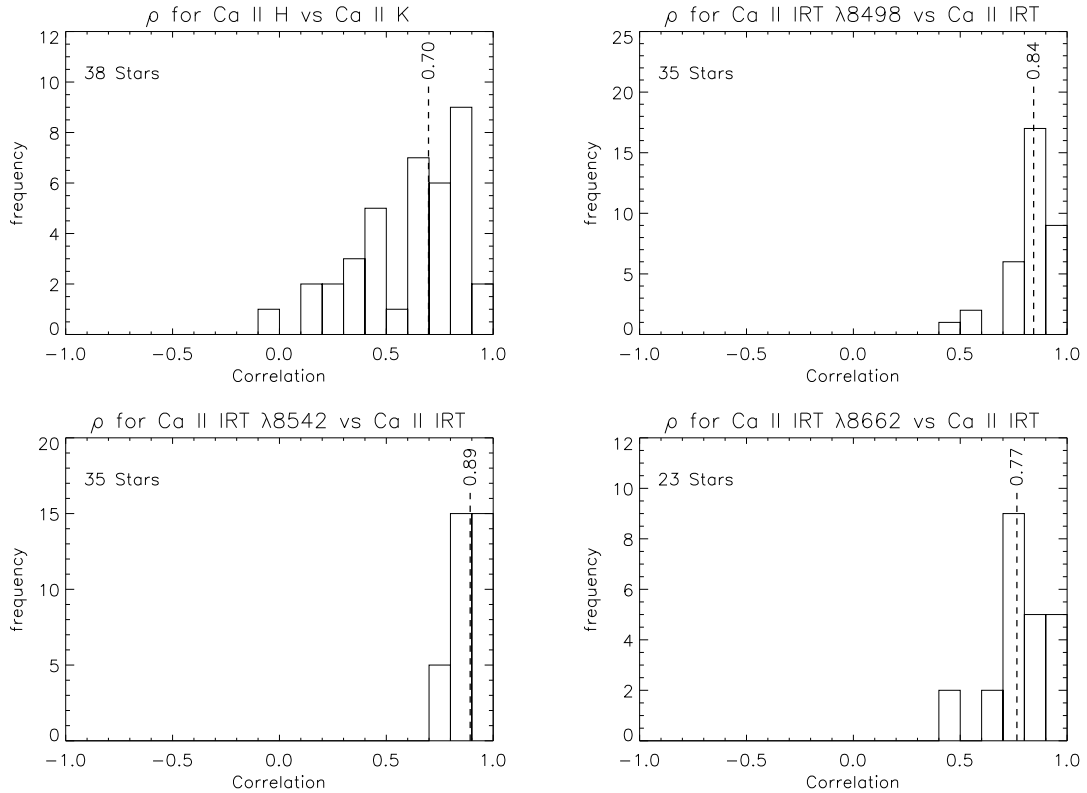


Figure 10.1: **Histogram of determined correlation coefficients for the determined excess flux of all stars fulfilling the selection criteria (the amount of stars that fulfill them is given in the top left of each plot), for the Ca II H- & K-lines (top left) and the Ca II IRT-lines.** We compare the Ca II H- & K-lines with each other (top left), but the Ca II IRT-lines are compared to their sum, see text. The dashed line shows the median correlation.

correlation coefficient, because of the non-linearity we saw in the correlation plots (See for example Fig. 8.7). The difference between these indices and the resulting histogram distributions for the H α -line is not very significant, with the median value shifting by about 0.08.

For each star and line, we go through our results of Chapter 4 and Chapter 7, and take the larger set of determined values. In case there is the same amount of values from both chapters, we give priority to the results from the comparison to model spectra. We disregard stars that are either not active, as defined by the $\log R'_{\text{HK}} > -4.75$ criterion, have less than five data points, or where the entire range covered by these values is less than two times of a conservative estimate of the typical uncertainty on the excess fluxes determined for that star. This estimate is defined as the lowest value that is higher than 70% of all uncertainty values found for that star. This value is used to handle strongly-varying uncertainties in a robust way.

The histogram of determined correlations in single stars for the entire sample is given in Fig. 10.1 for the Ca II H- & K-lines individually, and each Ca II IRT-line excess flux compared to their sum. The reason for this is as follows: As the excess flux is lower for the Ca II IRT-lines, the selection criteria are only fulfilled by a few stars. For this kind of comparison, it must be fulfilled for two lines at the same time, however, reducing the amount of stars for the histogram even further. If we compare with the summed-up excess flux in all three Ca II IRT-lines instead, we can compare a higher number of stars. For Ca II H- & K-lines, the filtering is less severe, due to the higher levels of excess flux, and therefore such a step is not necessary. Generally speaking, the correlation is rather good for all lines. It is positive in almost all cases, with just one single star showing a very weak negative correlation between the Ca II H- & K-lines. The lower correlation level for the individual

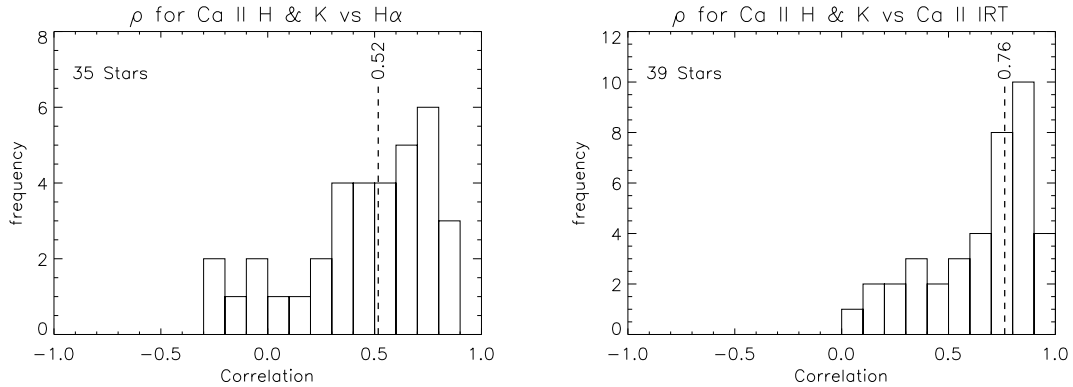


Figure 10.2: Same as Fig. 10.1, but for the correlation between the excess fluxes in the Ca II H- & K-lines and the H α -line (left) and for Ca II H- & K-lines and the Ca II IRT-lines (right).

Ca II H- & K-lines is explained well by the fact that the single Ca II IRT-lines are compared to the summed-up excess flux in all three Ca II IRT-lines, which includes the component of the single line. The median correlation for the Ca II H line to the sum of the excess fluxes in the Ca II H- & K-lines is 0.89, and for Ca II K it is 0.93. Both of these values are higher than the corresponding values for the Ca II IRT-lines. This is as expected from the higher excess flux levels of the Ca II H- & K-lines. We will now check how the H α -line compares. As mentioned before, it has been found that while there is an overall correlation between the H α -line and the Ca II H- & K-lines, in individual cases, negative correlations have been observed. In fact, even with our strict selection criteria employed here, we find five out of thirty-five (14%) stars show such a negative correlation¹. The histogram distribution for this correlation, as well as the one between the calcium line groups is given in Fig. 10.2. It is immediately apparent that while the correlation tends to be positive in most cases, it is significantly stronger for the Ca II IRT-lines compared to the H α -line. This is mirrored both in the median correlation found (0.52 compared to 0.76), but also in the distribution, which is less broad and more defined for the Ca II IRT-line comparison. This is not surprising, given that the Ca II IRT-lines are also Ca II lines.

We can now go one step further and try to find if there is a particular group of stars, or a stellar parameter, which determines the quality of correlation between the Ca II H- & K-lines and the H α -line. We will use the correlation between the two calcium line groups as our comparison each time. As we are unfortunately suffering from a rather low number of stars in the sample after the rigorous selection process, we can only show qualitative tendencies here.

10.1.1 The effect of stellar parameters on the correlations

In Gomes da Silva et al. [2014], the authors analyzed the correlation across their sample depending on stellar parameters. One of their results was that stars with higher metallicity were more likely to show a negative correlation coefficient. In Fig. 10.3, we show the histogram distributions, which do not reproduce this effect. However, our sample is much smaller, and with only about eleven stars showing a negative correlation coefficient, all of which have $\rho > -0.5$, this does not negate their result, which focuses on stars with $|\rho| > 0.5$. For both cases, H α and Ca II IRT, no strong shift in the distribution can be seen. We can now perform this same step with T_{eff} , or $B - V$, which we have used so far. In Gomes da Silva et al. [2014], they find that cooler stars show more positive correlation than hotter stars. Figure 10.4 shows the same tendency in our data: Cooler stars (higher $B - V$) show higher correlation, and form the right end of the histogram distribution. However,

¹We find different, higher values here compared to those given in Martin et al. [2017], because of a larger sample of stars considered, stricter selection criteria, and the usage of the results from model spectra comparison.

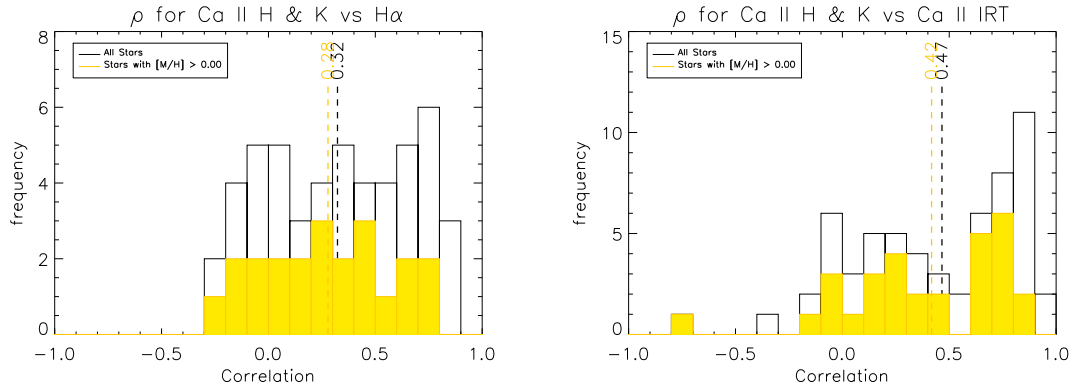


Figure 10.3: **Histogram of determined correlation coefficients for all stars (black), as well as the subsample of stars that exceed a certain metallicity threshold (yellow).** The dashed line and number shows the median value for the correlation coefficient. The histogram distribution does not change significantly.

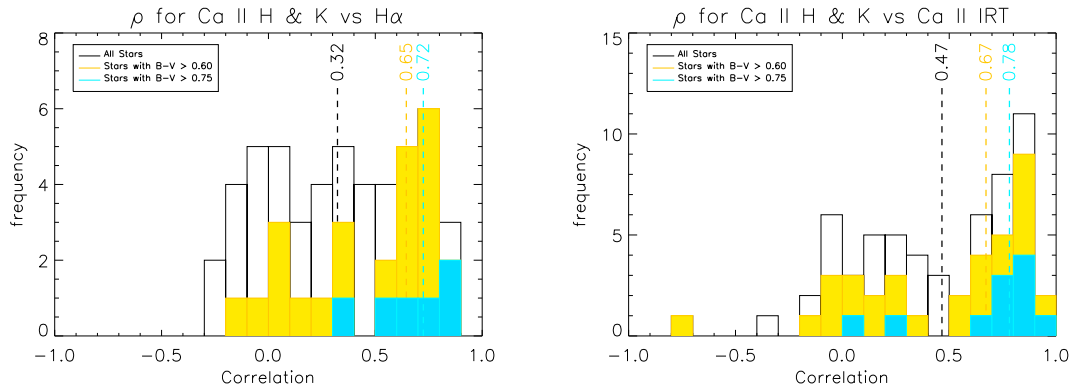


Figure 10.4: **Histogram of determined correlation coefficients for all stars (black), as well as the subsample of stars that exceed a certain $B - V$ threshold (yellow, blue).** The dashed line and number shows the median value for the correlation coefficient. Stars with higher $B - V$ tend to show stronger correlation.

as mentioned by Gomes da Silva et al. [2014], this might be an effect from the effective correlation between higher activity and cooler stars. If this is true, then we would expect to see a strong effect of the individual levels of correlation and that star's activity level, which is the next step in our analysis.

The value of $\log g$ does not appear to affect the correlation at all: The histogram distributions do not change shape when we filter out low or high gravity values.

10.1.2 Correlation for different levels of activity

Similarly, Gomes da Silva et al. [2014] analyzed their sample in regards to whether a higher level of activity suggests a stronger correlation. In fact, they found that the correlation between activity indices from the Ca II H- & K-lines and the H α -line is always positive if $\log R'_{\text{HK}} > -4.7$. In Fig. 10.5, we analyze the sample, and subsets of the sample of more active stars, in regards to the average value of R'_{HK} . We can see that the higher the activity, the stronger the correlation, for both cases, which mirrors the earlier result. The explanation from Meunier and Delfosse [2009] for the H α -line case is that at the higher activity levels, the absorption contribution in the filaments saturates, and

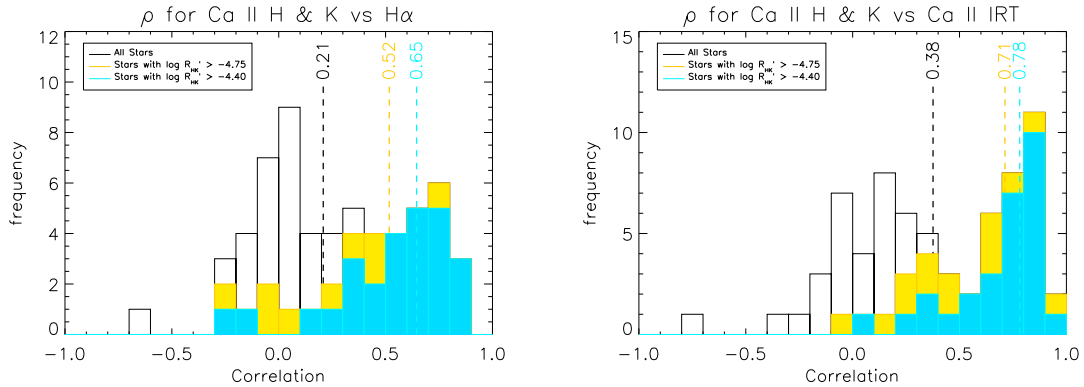


Figure 10.5: **Histogram of determined correlation coefficients for all stars (black), as well as the subsample of stars that exceed a certain activity threshold (yellow, blue).** The dashed line and number shows the median value for the correlation coefficient. It is apparent that the correlation becomes stronger for higher activity.

only the contribution of the plages remain. It stands to reason how much of this effect stems from the simple fact that the determined excess fluxes of more active stars are relatively less affected by noise. It is unlikely that this is the sole effect, as we require the range of the data to exceed the noise. Many stars with $\log R'_{\text{HK}} > -4.75$ show low correlation. These stars show very little chromospheric flux, other than their basal flux. Even before, in Fig. 7.6, we saw that these stars did not fall in line with the overall linear trend, but rather showed a horizontal branch, dominated by noise. This supports our observation that we don't see a strong correlation for these stars. The effect of activity on the strength of the correlation appears to be different for the case of the correlation between Ca II H- & K-lines and the Ca II IRT-lines, compared to the correlation between Ca II H- & K-lines and the $H\alpha$ -line. In the former case, the improvement in correlation for the group of highest activity stars (blue in Fig 10.5) to all active stars (orange) is only about half (about 0.07) than it is in the latter case (where it is 0.14). However, the total improvement in correlation from the entire sample to the most active stars is similar, and about 0.4 in both cases. For the $H\alpha$ -line, there is overall much higher scattering in the data, so that we cannot see such a clear division into two parts in the correlation. We can still see a clear improvement in the correlation when disregarding the inactive stars, with further improvements for higher activity thresholds. However, we are suffering from small-number statistics at this point, so that we unfortunately cannot reach a clear conclusion.

10.1.3 Summary

We have seen that after filtering out stars unsuitable for such an analysis, the stars of our sample show correlation between the measured excess fluxes in the lines on an individual level, though the strength of this effect varies by some degree. It is strong between the calcium lines, and less so for the $H\alpha$ -line. This degree of correlation is stronger for cooler, more active stars, and less so for the hotter stars. Unlike Gomes da Silva et al. [2014], we could not reproduce the effect of metallicity on the individual level of correlation. However, not many stars in our sample fulfilled the selection criteria, and none of those featured a strong negative correlation, where the metallicity effect is most pronounced.

The level of correlation between the individual lines is important for our confidence in the conversion relations found in Chapter 8. If there were no strong correlation for the data set of an individual star, adding converted activity indices to an existing time series would introduce strong, systematic errors, up to the possible removal of actual existing periods in the data. While such a systematic offset possibly exists, especially for some stars that show weaker correlation overall, the more active and cooler ones do not seem to suffer significantly from such an effect.

10.2 Measuring periods

As we have mentioned, a large part of the sample investigated in this work was originally taken to search for rotational periods [Hempelmann et al., 2016]. While a star with a stellar spot on its surface rotates, the spot moves into view, across the surface, and finally moves out of view, until the star has finished another half rotation, at which point the spot moves back into view. This appearance and disappearance of the spot forms a periodic signal. Since such a spot correlates with chromospheric emission, our data points for the excess flux can be used to find such signals. Other periodical signals stem from the usually much longer stellar activity cycles, for which we usually do not have enough data point coverage here, so that we focus on rotational periods.

While such spot-induced signals are not completely sinusoidal in nature, a Lomb-Scargle periodogram has historically yielded great results in finding their periods. Even from pure rotation, we may expect to find more than one signal. Due to differential rotation, spots on different latitudes move at different speeds, and therefore show different periods. The focus of this work is not the determination of periods. However, as an example of an application of the dataset we have obtained, we analyze the temporal behavior of the determined activity-related indices and fluxes of a few select stars. We perform this by analyzing the behavior on the determined excess fluxes $F_{\text{Exc,HK}}$, $F_{\text{Exc,IRT}}$, their sum $F_{\text{Exc,Ca II}}$ and $F_{\text{Exc,H}\alpha}$, as well as the S_{MWO} -index.

As our data is not regularly sampled, we cannot make use of many available methods for finding periods, for example a Fast Fourier Transform. Therefore, we will explore other options in the following.

10.2.1 Lomb-Scargle periodograms

The first method we are using is a Lomb-Scargle Periodogram [Lomb, 1976, Scargle, 1982] (using the IDL implementation `scargle`), which has also been used to determine the results in Hempelmann et al. [2016]. The Lomb-Scargle Periodogram compares the dataset (t_i, y_i) under consideration with sine and cosine waves sampled at the same times t_i , similar to obtaining a cross correlation of sampled data, and subsequently normalizes the result [Scargle, 1982]:

$$P_{LS}(\omega) = \frac{1}{2} \left[\frac{\left(\sum_j y_j \cos \omega(t_j - \tau) \right)^2}{\cos^2 \omega(t_j - \tau)} + \frac{\left(\sum_j y_j \sin \omega(t_j - \tau) \right)^2}{\sin^2 \omega(t_j - \tau)} \right], \quad (10.1)$$

with the delay τ defined to be:

$$\tan 2\omega\tau = \frac{\sum_j \sin 2\omega t_j}{\sum_j \cos 2\omega t_j}. \quad (10.2)$$

Introducing the delay parameter ensures that the Periodogram is invariant under shifts in time. In Eq. (10.1), the data y_i is assumed to have zero mean. To fix this, often the mean is subtracted, effectively replacing $y_i \rightarrow y_i - \bar{y}$. Another option is to take the mean as an additional fit parameter, this is then called a generalized Lomb-Scargle periodogram. This procedure is widely used in astrophysics, and is known to yield reliable results. However, one needs to be aware of effects that can arise from the irregular sampling, such as alias frequencies. The resulting value is often referred to as ‘‘Scargle Power’’. To give this number context, one calculates the False-Alarm Probability (FAP). By calculating many of these Lomb-Scargle Periodograms for white-noise, one can define the Lomb-Scargle Power reached by a certain fraction of these simulations. In this way, we can define the point that 95% of simulated white-noise periodograms do not reach. If the periodogram of our real dataset reaches this point, then we can say that the probability of this being a ‘‘false alarm’’ is 5%. Here, we consider periods that reach that level as significant. We estimate the error on the period following Eq. (3) in Baliunas et al. [1995], where this error is calculated from the variance after removal of the found best period.

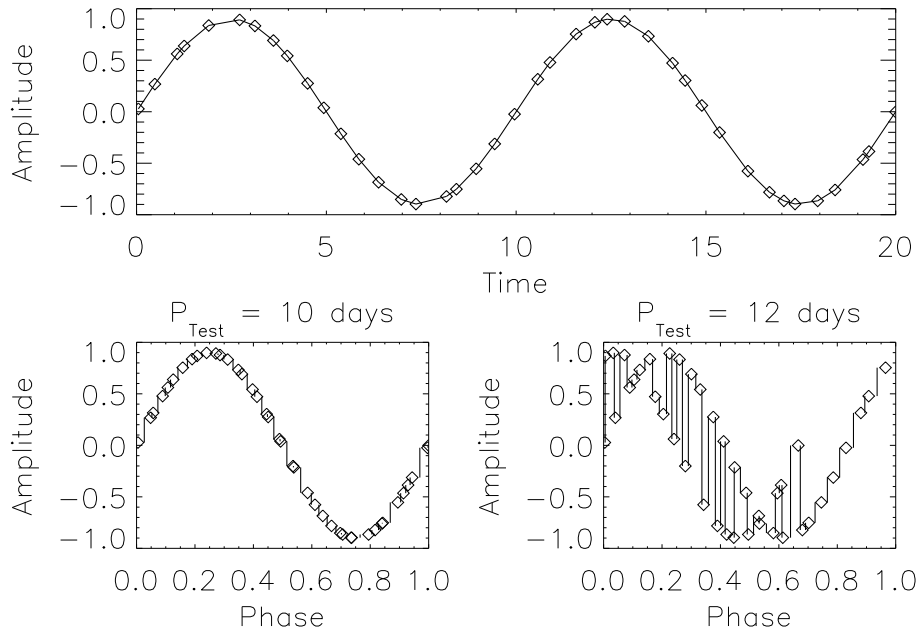


Figure 10.6: **Illustrating the idea behind the String Length procedure.** In this procedure, the original data (top) is folded with a test period P_{Test} . If the correct period is chosen (bottom left), the data points align and neighboring points are close together, and the sum of their vertical distance (black lines) is small. Even with just a small deviation in period (bottom right), neighboring points sometimes fall far apart, resulting in a large sum for the vertical distance.

10.2.2 String length

Our second method is the String Length method [Dworetzky, 1983]. It makes no assumption of the shape of the periodic function, unlike the Lomb-Scargle Periodogram, which assumes sinusoidal relations. As we have mentioned, a single spot does not result in such a relation. In essence, this method tries several periods, reorders the data points according to their phase in this trial period, and measures the distance on the ordinate of neighboring points. This process is illustrated in Fig. 10.6. If there is a period, then the summed-up vertical difference of points reaches a minimum, if the data points were reordered according to that period. The reason for this is that if the data points are correctly sorted, they form the shape of their periodical signal. Since we can assume it to be continuous, neighboring data points will be close together, and the overall difference of neighboring points will be small. If an incorrect trial period is chosen, however, then reordering the data points will jumble them, destroying the continuity of the function. As a result, at least some of the now neighboring points will show a large vertical difference. This method is problematic with datasets that feature more than one period in their signal, as rearranging according to just one of their periods will not necessarily result in a minimum, depending on the relative strength of the periods. We use this method to further analyze stars that we found to show one significant peak when using the Lomb-Scargle Periodogram.

10.2.3 Wavelets

The previously mentioned methods are good at finding periods across the entire range of the data. However, it is possible that only segments of the data show a period, or that the period varies in time, for example due to differential rotation and spots at different latitudes. One way to account for this is to use one of the previous methods for only selected segments of the entire data. However, we will use another option, and perform a wavelet analysis. An example of analyzing the Sun's

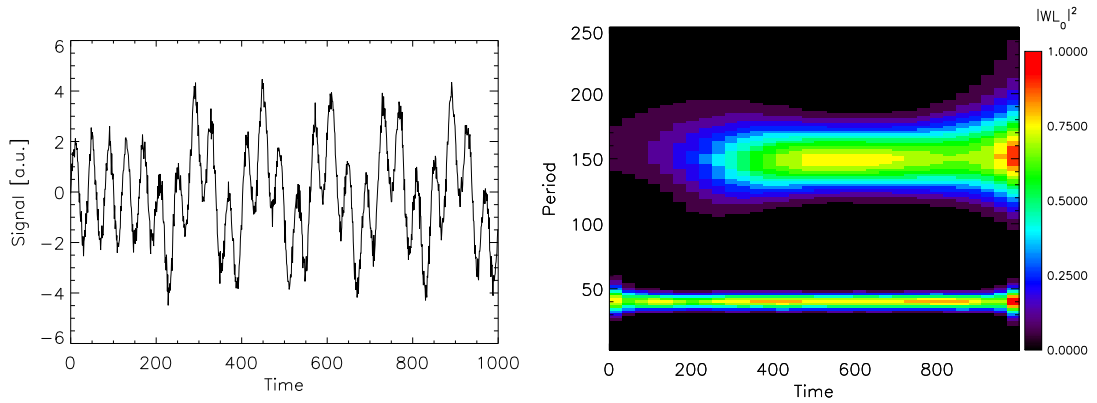


Figure 10.7: **Example for the Wavelet procedure.** For this simple example of a signal featuring a small period of 40 days, and a larger one of 150 days from 200 days forward, plus some synthetic noise (left), we perform a wavelet analysis (right). The resulting values have been normalized, and mapped to the color scale shown on the right. We can clearly see the two periods, as well as the lower resolution towards the higher periods.

activity in order to determine its differential rotation from wavelets is given by Hempelmann and Donahue [1997]. Similar to the Lomb Scargle Method, this method works by comparing the dataset to a function indicating the period, sampled at the same points. This function is called the wavelet function. This check is performed for a series of such wavelets, which are all derived from a “mother wavelet”. Here, we use the Morlet wavelet [Grossmann and Morlet, 1984], also called Gabor wavelet, in the complex variant. This wavelet is defined as:

$$\Phi_{\sigma}(t) = \left(1 + \exp(-\sigma^2) - 2 \exp(-\frac{3}{4}\sigma^2)\right)^{-\frac{1}{2}} \pi^{-\frac{1}{4}} \exp(-\frac{t^2}{2}) \left(\exp(i\sigma t) - \exp(-\frac{1}{2}\sigma^2)\right), \quad (10.3)$$

with a parameter σ , effectively determining the strength of the exponential falloff. It can therefore be used to determine the length a periodic signal is required to have in the dataset before it is found, increasing the confidence in the found period. At the same time, we are losing temporal resolution. This parameter is therefore a way to select between temporal and frequency resolution. We use $\sigma = 35$ here, after careful consideration on our data sample, as well as the periods we are expecting. The actual wavelet analysis is then performed by comparing Eq. (10.3) to the dataset, and yields a value $P_{\text{WL}}(T, P)$ for each time delay T and period P :

$$P_{\text{WL}}(T, P) = \frac{1}{\sqrt{P}} \sum_j y_j \bar{\Phi}_{\sigma}\left(\frac{t_j - T}{P}\right), \quad (10.4)$$

which shows that the mother wavelet is shifted by the time delay T and scaled by the period P . Generally, to find a complete set of orthogonal base wavelets, one chooses a subset of periods P and time delays T in a certain combination, which allows reconstruction of the original signal from the resulting wavelet. There is then a higher resolution towards the lower periods, just like for the Lomb-Scargle periodograms. For plotting purposes, we have not chosen to only select such a subset, and have therefore overdetermined the actual resulting 2D plot. We note that the irregular sampling adds noise structures to the wavelet plot.

An example of a wavelet analysis for a test case is shown in Fig. 10.7. We use this method to further analyze stars that have shown significant peaks in the Lomb-Scargle Periodogram, to find out where this signal is coming from. For clarity, we sometimes remove a linear trend beforehand. We do not make any attempt to determine a significance from the wavelet results.

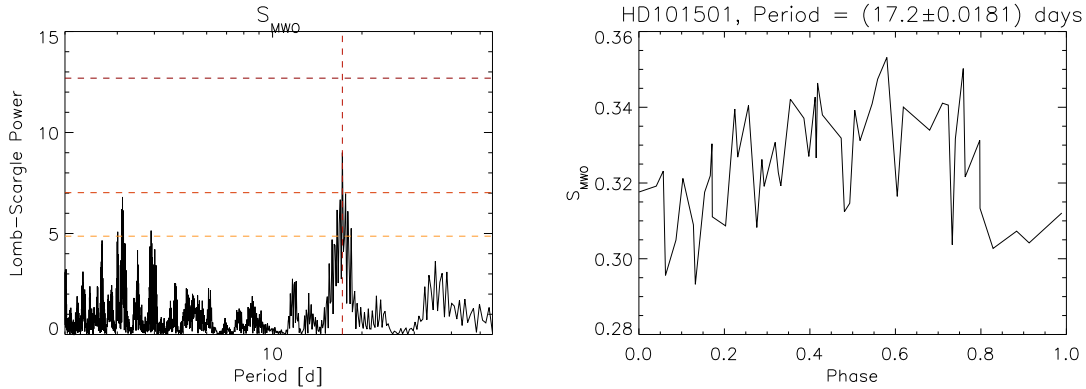


Figure 10.8: **Lomb-Scargle Periodogram (left) and folded light curve (right) for S_{MWO} of HD 101501.** Horizontal dashed lines mark the 1σ , 2σ and 3σ -level, the vertical dashed line shows the most significant period.

10.2.4 Determining periods of stars from TIGRE observations

We are analyzing the periods found in the different excess fluxes for some of the stars for which Hempelmann et al. [2016] have found periods on at least a 1σ -level. Not all of those stars are in our sample, so we cannot perform this analysis for all of these stars. We have selected only those that are relatively well sampled in time, and that showed promising periods of less than 40 days. In their work, Hempelmann et al. [2016] have removed long-term trends by means of subtracting a best-fit polynomial. We do not perform this step, as it affects the determined significances for the periods found. We take the same dataset, using the finely sampled data from the same time period, neglecting other available data, as its less regular, and coarser sampling is not as appropriate to search for periods. In this way, this work performs a check of the results given by Hempelmann et al. [2016]. We will now discuss the results of a few select stars in detail. They have been chosen to show the clearest results in their wavelet plots, so that we can discuss their periods and when they appear.

HD 101501

HD 101501 is a G8V main sequence star [Keenan and McNeil, 1989] with a $B - V$ value of 0.74 [Soubiran et al., 2010]. This star is rather active, and therefore a good candidate to search periods for. Hempelmann et al. [2016] found a period of 17.04 ± 0.09 days on a 3σ -level in the S_{MWO} -index, without any trend removal. We determine a period of 17.178 ± 0.018 days as well analyzing the entire dataset, however, we only find it at a 2σ -level there, as shown in Fig. 10.8. We recover this period (or periods very close to it, with less than a day difference) not only in the S_{MWO} , but also in the total excess flux in the Ca II lines used here, as well as $F_{Exc,H\alpha}$. These periods just barely fall outside each other's 1σ range, but are still so close that we would consider the period confirmed. We also show the folded light curve in Fig. 10.8, which illustrates that the overall dataset suffers from a noise level that is rather close to the amplitude of the assumed sine wave. Since this star is also very active, this period may not be of rotational origin, as the high activity level suggests a level of intrinsic variability that may drown out the rotational period. There are also peaks significant at a 1σ -level at about 3 days (for the excess flux in the Ca II H- & K-lines) and at 4.7 days (for the excess flux in the Ca II IRT-lines). The String-length procedure has recovered a period of 17.6 days, which is in good agreement to the earlier period found. In Fig. 10.9, we show the wavelet for the excess flux in the Ca II H- & K-lines and Ca II IRT-lines, for only the data used by Hempelmann et al. [2016]. The maximum occurs very close to the found period of ~ 17 days, and seems to be most strongly recovered at about 120 days of that signal. While it appears that there is less signal towards the earlier and later time, this is likely related to the much more coarsely sampled data

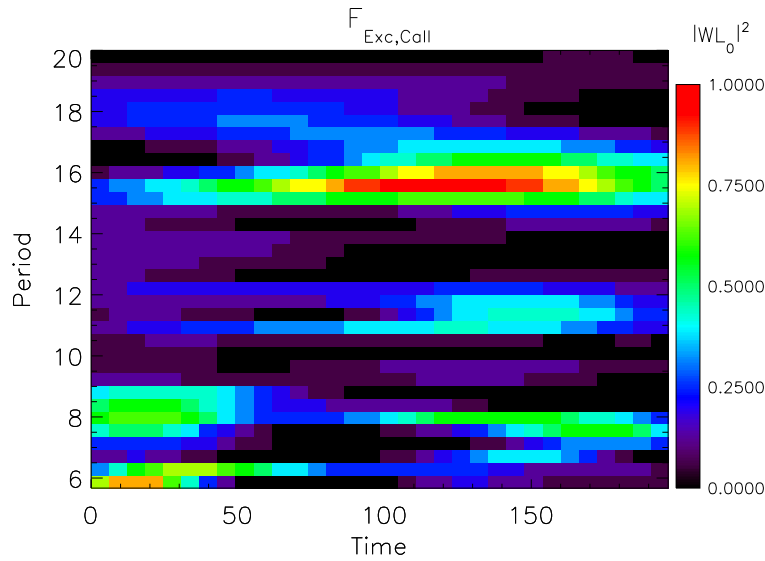


Figure 10.9: **Result of the wavelet procedure for HD 101501 for the summed-up excess fluxes in the Ca II H- & K-lines and Ca II IRT-lines.** Both Time and Period are given in days. The strongest signal is recovered close to the found period of about 17 days.

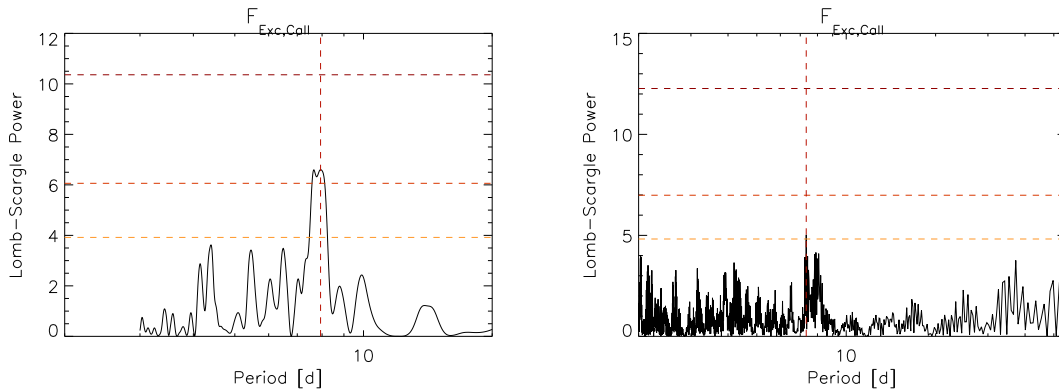


Figure 10.10: **Lomb-Scargle Periodogram for the excess flux in the Ca II H- & K-lines and Ca II IRT-lines for the data sample analyzed by Hempelmann et al. [2016] (left) and the entire data analyzed in this work (right) for HD 97334.** Horizontal dashed lines mark the 1σ , 2σ and 3σ -level, the vertical dashed line shows the most significant period.

there.

All in all, this example shows that we were able to recover the expected period using the excess flux in all lines, further confirming that the Ca II IRT-lines are well suited for activity studies.

HD 97334

For this G0V star, Hempelmann et al. [2016] found a period of 7.93 ± 0.05 days, on a 2σ -level. We do recover the same period, at the same error level, when performing the period search for the summed excess fluxes in the Ca II H- & K-lines and Ca II IRT-lines. We also recover a period of 7.69 ± 0.08 – well in agreement with the previous one – in the excess flux for the H α -line, again at a 2σ -level. However, when the analysis is performed for all data points available, and not just the set analyzed by Hempelmann et al. [2016], the Lomb-Scargle power of that period falls below the 2σ -level, barely reaching 1σ , is defined less clearly, and no longer appears stronger compared to other less significant peaks. This is mostly due to the Ca II H- & K-lines, as the Ca II IRT-lines show a more pronounced peak at that period. Figure 10.10 compares these two Lomb-Scargle periodograms of the excess fluxes in the Ca II H- & K-lines and Ca II IRT-lines. The string-length procedure finds tendentially

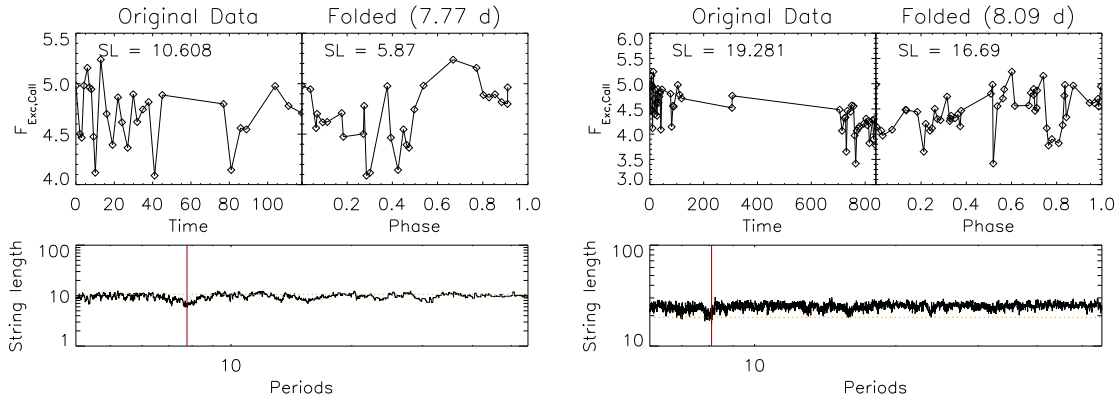


Figure 10.11: **String-Length procedure for the excess flux in the Ca II H- & K-lines and Ca II IRT-lines for the data sample analyzed by Hempelmann et al. [2016] (left) and the entire data analyzed in this work (right) for HD 97334.** The dashed horizontal line in the lower plots mark the string length of the unfolded data, the vertical line the best period found.

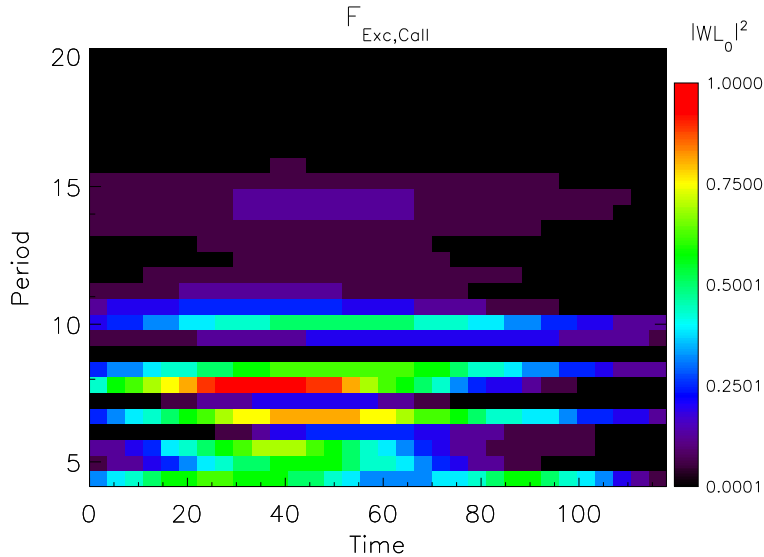


Figure 10.12: **Result of the wavelet procedure for HD 97334 for the summed-up flux excess fluxes in the Ca II H- & K-lines and Ca II IRT-lines.** Both Time and Period are given in days. The found period of about 8 days appears clearly in the plot for earlier time frames, and disappears towards the later ones.

lower periods of 7.7 days and 8.1 days for the restricted and entire dataset, respectively. In the first case, the reduction in string length is significantly higher than in the second, as we show in Fig. 10.11. However, in both cases, the folded light curve (top right plots in Fig. 10.11) does not appear sinusoidal in nature, and features many spikes, likely from noise. The wavelet for this star, shown in Fig. 10.12 unsurprisingly features a lot of noise structures, but the period found can be made out clearly for the earlier times, before it weakens later. This is likely due to the much sparser sampling at days past ~ 45 days. This example shows clearly that irregular sampling strongly complicates the search for periods.

HD 37394

Hempelmann et al. [2016] found a period of 10.74 ± 0.03 days at the 3σ level. For the same set of spectra, we find a very similar period from the calcium lines (10.6 ± 0.08 days), at a 3σ -level, but not for the excess flux in the $H\alpha$ -line, where we only recover a peak at about half with $P = 5$ days, though only at a 1σ -level (Fig. 10.13). This period is also seen in the calcium lines, albeit at a lower significance. When analyzing the entire dataset, the entire periodogram becomes more noisy,

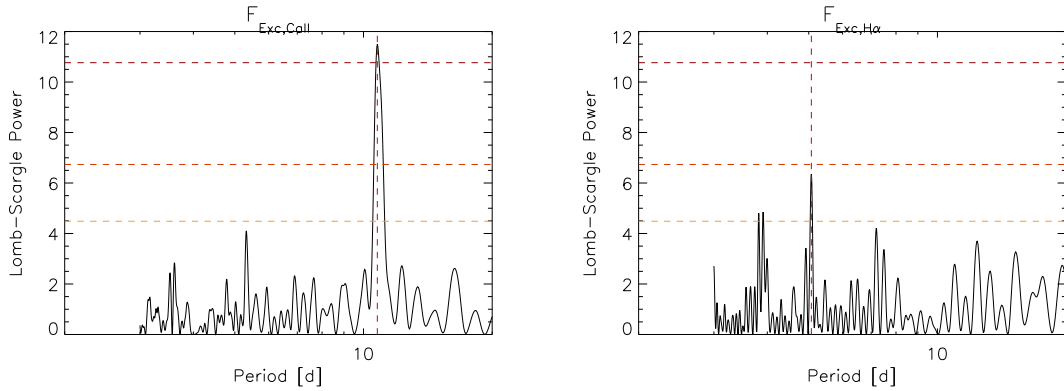


Figure 10.13: **Lomb-Scargle periodogram for the excess flux in the Ca II H- & K-lines and Ca II IRT-lines (left) and for the excess flux in the H α -line (right), for the data sample analyzed by Hempelmann et al. [2016], for HD 37394.** The horizontal lines correspond to the 1σ , 2σ and 3σ -level respectively, the vertical line marks the most significant period found.

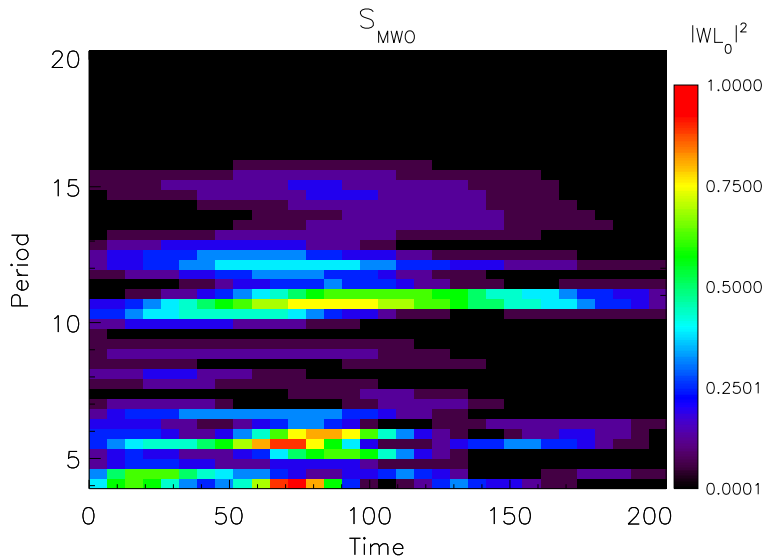


Figure 10.14: **Result of the wavelet procedure for HD 37394, for the S_{MWO} .** Both Time and Period are given in days.

and the significance of the peak lowers to 2σ , yet it is clearly the strongest peak still, with a lower error of now only 0.02 days. The wavelet for this star is shown in Fig. 10.14. Despite the very clearly recovered period in the periodogram, the respective wavelet is less well-defined. However, at around 75 days, a short period of five days dominates the wavelet structure. This corresponds to the respective periods of that length we have found and already discussed. Outside this region in time, the sampling becomes worse, and so this period weakens again. We show the folded S_{MWO} curve in Fig. 10.15. While there is still some noise, the overall shape of the curve appears rather well-defined, especially in the first half, despite some peak structures.

10.2.5 Periods recovered

In Table 10.1, we list the stars we have analyzed here, and the strongest peak for each line. In all cases, the period given by Hempelmann et al. [2016] was also recovered by us in the Ca II H- & K-lines, confirming their result. However, we recover lower levels of significance, which is likely due to the trend removal performed in their work. In only two cases, we were unable to recover the same period in the Ca II IRT-lines, and in one more case, a period close to double the one

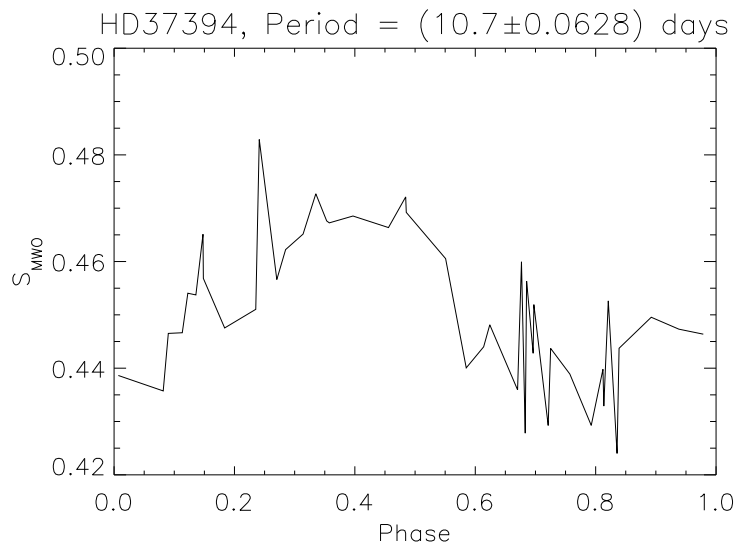


Figure 10.15: **Curve of the S_{MWO} index for HD 37394, folded by the best found period of 10.7 days.**

in the Ca II H- & K-lines was found. In the Ca II IRT, the significance is usually lower, which is unsurprising given the lower levels of the excess flux in these lines. While we have recovered the period in the excess flux of the H α -line in some cases, the overall impression is that the results from that line are less trustworthy and significant, with no significant period at all recovered for five out of eleven stars, one case where twice the period from the Ca II H- & K-lines was recovered, and one with an offset of about a day and a half to the period from the Ca II H- & K-lines for one star.

10.3 Summary

In this chapter, we have analyzed the excess fluxes (or related activity indices) individually, and compared the results. We have seen that generally speaking, there is a clear, strong correlation between the excess fluxes in the different lines. While not perfect, this confirms that they are correlated well enough that a conversion relation like those given in Chapter 8 can in fact be used to analyze data from one particular spectral line in the scale of another. We also saw no dependence of the degree of correlation on stellar parameters, however, stars with higher activity tend to show a stronger correlation. Since $B - V$ is correlated with activity, it follows that there is a correlation between the degree of correlation and $B - V$, or equivalently T_{eff} , mirroring the results from Gomes da Silva et al. [2014].

We have recovered the periods given in Hempelmann et al. [2016] from the same dataset in the other lines for the small subset of stars we have analyzed here. We were able to confirm their results for these stars, albeit at a lower confidence level. For most of the stars, we also found the same period they give in the Ca II IRT-lines, though often at lower significance, likely due to the lower levels of the excess flux in those lines. Finally, the H α -line not only shows the lowest correlation to the Ca II H- & K-lines, but we were able to recover their period from the excess flux in this line only for about half the cases.

Table 10.1: **Periods recovered for a small sample of stars in the various lines.** The values given in the “Literature” column are by Hempelmann et al. [2016].

Star	Literature	— From F_{Exc} in —		
		Ca II H- & K	Ca II IRT	H α
HD 17925	7.15 (2σ)	7.5 (1σ)	13.0 (1σ)	—
HD 35296	3.50 (3σ)	3.5 (1σ)	3.6 (1σ) ¹	—
HD 37394	10.74 (3σ)	10.74 (3σ)	10.8 (1σ)	5.1 (1σ)
HD 39587	5.14 (3σ)	5.16 (2σ)	5.3 (1σ)	— ⁽²⁾
HD 42807	11.77 (2σ)	11.9 (1σ)	11.8 (1σ), 3 (1σ) ⁽³⁾	—
HD 43162	7.08 (3σ)	7.06 (2σ)	5.82 (1σ)	—
HD 72905	5.22 (2σ)	5.2 (2σ)	—	5.2 (2σ)
HD 97334	7.93 (2σ)	7.9 (2σ)	7.6 (2σ)	7.7 (2σ)
HD 101501	17.04 (3σ)	17.0 (2σ)	15.9 (1σ)	17.3 (2σ)
HD 115043	5.86 (2σ)	5.9 (2σ)	5.88 (2σ)	4.3 (1σ)
HD 118972	9.41 (3σ)	9.4 (2σ)	—	9.4 (1σ)

Footnotes: (1) Very close to 2σ ; (2) Period at about 5.2 was almost recovered at 1σ ; (3) The peak at three days is stronger, but the eleven day peak was also recovered in this line group

Chapter 11

Summary and Outlook

We have made use of the large sample of TIGRE spectra available to us, and have carefully compared the spectra of active stars to those of inactive stars similar in stellar parameters, as well as PHOENIX model spectra. To do the latter, a new method to interpolate PHOENIX model spectra from an incomplete, irregularly sampled set was developed, which we have also used to find and determine stellar parameters of the stars in our sample. Our comparison yielded the excess flux, emitted from the star's chromosphere. Detailed analysis has been performed to check the degree of correlation of these fluxes from different lines, both on a general and an individual level.

In this final chapter, we summarize the major results we have found. We will go through the chapters about our own work one by one and give a summary of the results found. In the second part, we will give an outlook into some possible extensions of this work that we have begun work on.

11.1 Summary

For each chapter past the introductory ones, we will give a short summary, both of the method employed, as well as their results. The most important parts have been set in bold.

Chapter 3 – Obtaining chromospheric excess fluxes

This chapter outlined the method we have used to determine the chromospheric excess flux. The idea is simple: A spectrum of an active star differs from the one of a fictitious inactive one with the same stellar parameters by a chromospheric contribution that becomes stronger the more active the star under consideration is. To find just this contribution therefore requires this fictitious inactive comparison spectrum. Regardless of the source of it, whether it is the spectrum of a similar, but inactive star, or a model spectrum, an automated approach for the analysis is necessary, due to the sheer number of spectra we investigate in this work. With the two spectra, subtracting the comparison spectrum from the potentially active star's spectrum then yields the activity-related residuals, which we call the excess flux F_{Exc} . This automated approach must take great care in how it handles the two spectra: They will differ from other reasons as well, and these differences must be corrected first.

We have developed a robust, automatic procedure that performs automatic normalization, degradation, rotational broadening and more, to eliminate as many non-activity related differences as possible. It also takes into account the error on both spectra, as well as the stellar parameters used, by performing several Monte Carlo iterations. As a result, **it returns both the integrated excess flux, as well as the parameters of a Gaussian fitted to the excess distribution**. The method takes the comparison spectrum's physical unit scale to convert the result into $\text{erg s}^{-1} \text{cm}^{-2}$. The procedure has been tested extensively, and used for all stars in this work. Only for one star, HD 22468 (HR 1099) did the shift in the procedure fail, as the extreme and very unusually high level of activity on that star lets the two spectra differ too strongly, so that automatic wavelength-shift determination via cross-correlation no longer works.

Chapter 4 – Determining the excess flux by comparing to inactive stars’ spectra

In this chapter, we have used the method from Chapter 3 to compare the spectra of active stars to inactive stars with similar stellar parameters. To perform such a comparison, we first need to find a suitable comparison star for each active star in our sample. We used literature values – most from Soubiran et al. [2010] – and developed a score for each pair of one active and one inactive star, that indicates the quality of their match, weighting the different stellar parameters by their effects according to the literature. We find the excess fluxes in six lines: the Ca II H- & K-lines, the three Ca II IRT-lines, as well as the H α -line. Since it is known that the Ca II H- & K-lines are an excellent gauge for stellar activity, finding a correlation between the excess fluxes of one of the previously mentioned lines to the excess fluxes of the Ca II H- & K-lines is a good indicator for the suitability of this line as an activity indicator. **We find excellent correlation between the excess fluxes of all six lines investigated here.** Especially the two groups of Ca II lines are very well correlated, with a Spearman correlation coefficient of $\rho \approx 0.9$. While there is some scatter in the distribution, the overall correlation is very clear. **The correlation is good for both the integrated fluxes, as well as the amplitude of the Gaussian fitted to the excess distribution,** though the latter requires smoothing the excess beforehand to avoid noise-spikes dominating the fit. The correlation between the H α -line and the Ca II lines is less strong, but still noteworthy ($\rho \approx 0.8$). When using the widely-adopted S_{MWO} -index, a clear $B - V$ dependence appears, which agrees with previous studies.

Chapter 5 – A new way of interpolating model spectra

Our next goal was to optimize and compare the previous analysis by using PHOENIX model spectra as comparison spectrum. However, we cannot make use of available literature grids, as they do not feature the required species in NLTE, or do not use a necessary profile function for the Ca II IRT-lines. With the intended goal of making this a part of the automatic TIGRE pipeline (see below), we set out to develop a new procedure to interpolate on an irregular grid. Covering the entire range of stellar parameters with suitable step size, especially if those parameters are actually dependent on each other, is a time-consuming process. **The newly implemented approach allows clever selection of a much smaller subset of models,** drastically reducing the amount of models required to perform the interpolation. The algorithm is an applied case for the three-dimensional adaptation of the algorithm described by McLain [1976] for each wavelength point individually. **The resulting interpolation works well, is stable, and fast,** making it very suitable for fitting spectra.

Chapter 6 – Fitting PHOENIX model spectra to TIGRE observations

The interpolated PHOENIX model spectra can be generated very fast. This is ideal for fitting, and allows quick determination of a star’s stellar parameter. Finding the best-fit spectrum is necessary for finding the correct comparison spectrum. We cannot simply use literature values, as the different methods to find the stellar parameters employed by different authors will yield significant, systematic offsets. **For each star, we fitted interpolated PHOENIX model spectra to the TIGRE spectrum with the highest SNR available for that star.** We have analyzed in detail the difference in results from using either a Levenberg-Marquardt approach, or a MCMC approach, and determined that **the MCMC approach is best suited for this fitting process,** despite the much slower process. For various reasons, most notably the resolution varying across the spectrum, performing this fit requires finding regions in the spectrum that show good agreement. To find those regions, we compared TIGRE reflection spectra of the Sun with respective PHOENIX model spectra. We found regions where these two spectra do not agree well, likely due to errors in the line profile functions in the model spectrum generation. We have defined a mask so that these parts of otherwise well-fitting regions are omitted from the fit. For a fit, these regions are normalized individually, and degraded, with the resolution of each region being a parameter of the fit. **The stellar parameter**

we find agree well with literature values, showing deviations that in almost all cases are noncritical (less than a typical step size for grids). It is still useful to perform this determination ourselves, rather than using those literature values, so that those stars where we found significant deviations are also compared to suitable spectra. With the parameters we have found, we could perform the comparison to the correct PHOENIX model spectra to find the excess flux.

Chapter 7 – Determining the excess flux by comparing to PHOENIX model spectra

Now that we know the stellar parameters as determined from fitting PHOENIX model spectra to an active star’s spectrum, we can use the model spectrum to find the excess flux. Unlike before, the comparison spectrum does not include any basal flux contribution, which means we expect to find larger excess fluxes, and to find the strongest correlation only past a certain point in the $F_{\text{Exc}}-F_{\text{Exc}}$ -relation. The results confirm these expectations. **We find strong correlation between all lines again**, with overall lower values for the correlation coefficient ρ due to the contribution of the inactive stars that have formerly been discarded. **The results are very similar to the ones from Chapter 4**, with the largest correlation between the calcium lines. The correlations involving the H α -line are lower, which likely stems from the difficulties in modeling the H α -line.

Chapter 8 – Converting excess fluxes from different lines

While the value for F_{Exc} is useful on its own as an indicator for activity, comparing new measurements of this value to archival data of other indicators requires knowledge of what that values corresponds to in these other indices. Close inspection of the distributions reveals that in most cases, **for a set value of $B - V$, one can find a linear relationship to convert one parameter (excess flux, activity index, ...) into another**, with the excess fluxes in the H α -line as exception. We assume that the resulting relationship of slope $m(B - V)$ and intercept $b(B - V)$ are polynomials. A simple linear regression then yields a linear set of equations, solving these yields the best fit for these relations. However, **to avoid selection bias, we divide the sample into groups, find slope and intercept individually for each group, and fit the result**. These relations have nominally higher residuals, but do not suffer from the bias inherent in the distribution of $B - V$ -values, which is very uneven. In this way, we were able to find conversion relations for the excess fluxes into one another, but also ways to convert excess fluxes into known activity indicators S_{MWO} and R'_{HK} .

Chapter 9 – Obtaining basal flux

Even for inactive stars, there is still some contribution from the chromosphere. This contribution is called the “basal flux”. It is very small compared to the chromospheric excess flux of an active star, which makes it difficult to determine, since most of the excess fluxes we have determined have errors of the order of the basal flux. **We determine the basal flux from the lower envelope of F_{Exc} that include a basal flux** (e.g. from comparing to model spectra) **and from comparing the two sets of F_{Exc} -values we have found**. We compared our results to literature relations for the Ca II H- & K-lines, and found that generally, they agree better for the later types, and we find lower basal fluxes for the earlier types, as Fig. 9.9 shows. The inherent scatter is very large, because of the low values of the basal flux compared to the error on our fluxes. Still, the overall magnitudes of the basal flux relations agree well with the literature.

Chapter 10 – Individual correlations and determining periods

In this chapter, we have analyzed the correlation between the excess fluxes on an individual level for each star. The motivation is that some authors have found that for the H α -line, there is not necessarily a correlation for some stars, or even a negative one! **Careful analysis of our sample shows that we see negative correlation between the excess fluxes in the Ca II H- & K-lines and the H α -line for some stars, but not for the correlation between the excess**

fluxes in the Ca II H- & K-lines and Ca II IRT-lines. On average, the correlation in the first case is $\rho \approx 0.52$, compared to a much higher $\rho \approx 0.76$ for the second. **We find no dependence of this correlation on metallicity, but we do find one on $B - V$ and activity.** We have also used three different methods to find periods in eleven of the candidates given by Hempelmann et al. [2016]. We were able to confirm their results, but found lower significance levels in most cases. **The excess fluxes in the Ca II IRT-lines were almost as reliable as the S_{MWO} index or the excess flux in the Ca II H- & K-lines for finding periods,** though in one case, we only recovered twice the period, and in two more we did not find any period. This is a better result than for the excess flux in the H α -line, where we found the same period only in about half the cases. This chapter confirms that the Ca II IRT-lines are a well-suited group of lines for activity studies, and likely better and easier to obtain results with than the H α -line is.

11.2 Outlook

We have used the method described in Chapter 3 with great success to obtain the excess fluxes of a large number of spectra. However, the method could be used for further science. Outside of analyzing the correlation between the determined excess fluxes in the lines with other activity indices not investigated in this work (e.g. X-Rays), there are a few additional ways that our method can be used for. We consider them promising science opportunities. We give the rationale and idea behind each of them, as well as a short description on some early work we have performed on them, and finally we mention a few challenges we encountered. Finally, since a large part of the code involved in the creation of this work has been written with the intent to work autonomously, implementing them as steps into the TIGRE pipeline is an option. We give reasons for this inclusion and outline how it may work.

11.2.1 Applying the method to binary systems

So far, we have only investigated single main-sequence stars, opting to even remove binaries from our sample (see Sect. 4.6) if the secondary star affected the spectrum too strongly. This was a necessary step, as the method does not work if the comparison spectrum has such a strong systematic difference to the spectrum investigated. Across the orbit, the two stars' contribution to the spectrum shift and change, requiring an orbit-dependent – and thus time-dependent – comparison spectrum. However, such an analysis would be very interesting, as the interaction between the two stars may affect their individual contributions to the chromospheric emission. Therefore, plotting the excess flux against, e.g. the orbital position may yield some insight on this behavior. Here, we examine how such an analysis may look like.

The first change required is to adapt the comparison spectrum. In fact, it should now be pieced together from two separate spectra, both of which must be shifted according to their velocity component in the observer's direction, broadened according to their rotational velocity, and finally correctly scaled according to their brightness and the fraction of the surface visible. Because one star may block some light of the other, this latter fraction is strongly time-dependent.

Geometrical Blocking

For a first estimate, we neglect limb-darkening, and simplify the procedure by only taking the geometrical blocking of two circular surfaces into consideration. We must then estimate the area A of the stellar disk covered by the other star.

Let R_1, R_2 be the radii of the two stars, with $R_1 > R_2$, and let d be the projected distance between them. For the case of $d > R_1 + R_2$, then obviously both stars do not overlap, and we have $A = 0$.

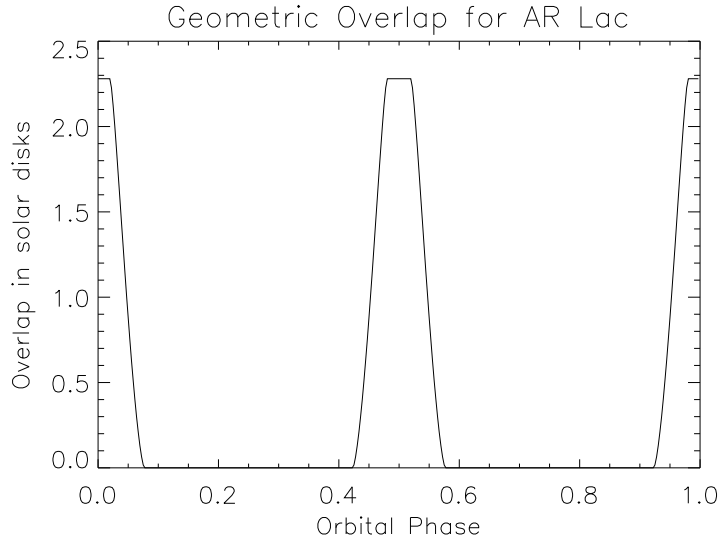


Figure 11.1: **Calculating the geometrical overlap for the AR Lac System according to Eq. (11.2).** For the AR Lac System, the parameters chosen were $R_1 = 2.61R_\odot$, $R_2 = 1.51R_\odot$ and $d = 8.869R_\odot$, and have been taken from Siviero et al. [2006].

Likewise, if $d < R_1 - R_2$, then the smaller star is completely covered, and $A = \pi R_2^2$. This leaves the remaining case, in which the covered area resembles an asymmetric lens, which is given by:

$$\begin{aligned}
 A &= \frac{R_1^2}{2} \cdot (\alpha - \sin \alpha) + \frac{R_2^2}{2} \cdot (\beta - \sin \beta), \text{ with} & (11.1) \\
 \alpha &= 2 \cdot \cos^{-1} \left(\frac{d/2 + (R_1^2 - R_2^2)/(2d)}{R_1} \right) \\
 \beta &= 2 \cdot \cos^{-1} \left(\frac{d/2 + (R_2^2 - R_1^2)/(2d)}{R_2} \right)
 \end{aligned}$$

The function A is plotted as an example in Fig. 11.1. A more accurate procedure would take limb-darkening into account. However, as limb-darkening depends strongly on wavelength, this would ideally require obtaining the necessary behavior directly from calculated model atmospheres.

Adding spectra together

With this factor, we can now create the resulting spectrum from the two components. Taking two comparison spectra relevant to one of the star's components, we can calculate the orbital phase either from an available relation from the literature, or we can consider this a free parameter, and determine it in a fit. Together with an orbital solution¹, we can easily determine the red- and blueshift of the two stars, and shift their spectra accordingly. The orbital solution also determines which of the two stars is currently in front of the other, knowledge of which is required to scale its spectrum according to the blocked surface area using Eq. (11.2).

Fig. 11.2 shows the generated comparison spectra for binary system AR Lac. Its parameters $R_1 = 2.61R_\odot$, $R_2 = 1.51R_\odot$ and $d = 8.869R_\odot$, as well as the other required ones, were taken from Siviero et al. [2006], from where we have also taken the orbital solution. The original spectra for the two subgiants were PHOENIX models for the two components [Fuhrmeister, 2015]. With these comparison spectra, the resulting excess flux can be determined using the method described in Chapter 3. However, it must be passed a value of $v \sin i = 0$, as the rotational broadening has already been performed. Similarly, no further wavelength shift due to radial velocity is required, and the routine will perform a cross-correlation anyhow to correct small discrepancies. However, this routine must be called twice, with adapted values for the actual line center, as this determines where the integration is performed. Here, we require the integration around two line centers, which move

¹With enough available spectra, the parameters of an orbital solution may also be fitted

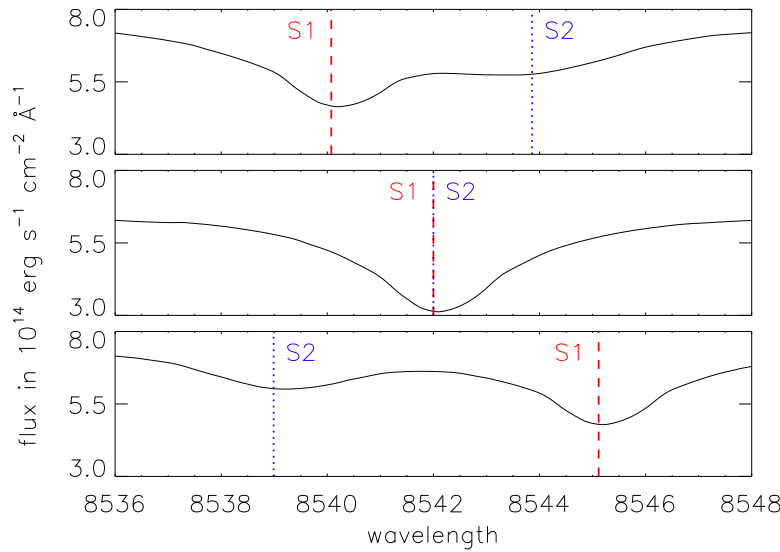


Figure 11.2: **Generating comparison spectra for the binary system AR Lac at different Phases around the second Ca II IRT-line.** The line positions of the first (“S1”) and second star (“S2”), shifted by their orbital-phase dependent radial velocity, are marked in red and blue. After subtracting the observed spectrum by this comparison spectrum, integrating the residuals around these positions yields the excess fluxes.

and change in time. Of course, at some orbital positions, both lines cannot be measured individually anymore, as no flux from this line reaches the observer, or, in case of fast rotators, because the two lines merge into one another.

In this way, excess fluxes could be found for several different orbit phases, analyzing their behavior in more detail.

11.2.2 Applying the method to fast rotators

In this work, we have focused on the level of the excess flux, as determined either by integrating the excess distribution, or by the amplitude of a Gaussian fitted to it. However, the shape of the excess flux may reveal more information. The basic idea here is similar to the one behind Doppler Imaging, which requires that rotational broadening is the dominant broadening process. A spot moving across a star’s surface will affect the resulting spectrum. Since the spot is cooler and therefore darker, the contribution of this surface area is suppressed, resulting in less (continuum) flux emitted from this area. In turn, a spectral line of this normalized flux contribution is less deep [Strassmeier, 1997]. In the spectral line’s profile, this is visible as a clear “bump” with a position within the line corresponding to the radial velocity of this spot. This process is illustrated in Fig. 11.3. Detailed analysis of many spectra of a star taken during its rotation makes it possible to determine an image of the stellar surface. Normally, an additional condition is required to solve this problem fully, since the nonlinearity of the problem does not ensure a unique solution. Often, one solves for maximum entropy, eliminating this problem. There are several results from this method available in the literature. In the same vein, an active region moving across the star would create an excess distribution that, too, moves across the spectral line in the same fashion. Here, we experimentally use part of the dataset obtained by Wolter et al. [2008], and have determined the excess. We then analyzed its position in the line, as well as the amplitude, of the Gaussian fitted to the excess. For example, in Fig. 11.3, fitting a Gaussian to the residual after removal of the undisturbed profile would clearly determine the position of the dip in the line profile. We can then subsequently convert it to a position in the line profile in the Δv -scale. With knowledge of the star’s rotation speed and the observation time, this can in turn be turned into a longitude on the star’s surface.

In a preliminary analysis, we see a clear shift of this excess position across the spectral line. We show this effect – after smoothing the obtained data for better clarification – in Fig. 11.4, where we also compare this result to the one obtained by performing the same step with an iron line not known to show magnetic activity. This line does not show any obvious moving dips.

We can clearly see in the top left plot that the amplitude A_f of a Gaussian fit to the excess distri-

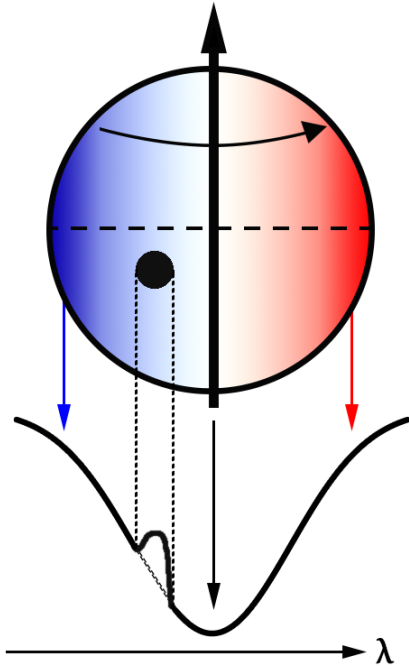


Figure 11.3: **Line profile affected by a stellar spot.** If the broadening of a spectral line is dominated by the star's rotation, then the position of a cooler, stellar spot will result in a visible notch in the line profile, moving across the spectral line.

bution, shows no real structure for a random iron line: The found peaks are distributed randomly, with no visual trend recognizable. For the Ca II IRT-lines, this is very different. All three lines show a clear peak in the beginning, which moves from about -70 km s^{-1} to roughly 70 km s^{-1} , in about a quarter of the phase. The literature value for this star is $v \sin i \approx 134 \text{ km s}^{-1}$, suggesting that this region is not near the equator. This mirrors the result from Wolter et al. [2008], where the authors also found spots close to the poles – a result found often with Doppler Imaging. This also explains the shorter fraction of the phase covered. There is also a black region seen in the Ca II IRT-line related plots in Fig. 11.4, relating to a negative fitted Gaussian. This implies a dip in the line profile, rather than the expected notch. Whether this is ultimately an effect from noise that then dominates the structure of a line that has become flat due to the strong broadening, or if there is some physical nature to this effect, is difficult to say at this point. Further investigation into the cause and behavior of this may be necessary to understand how this was caused.

After the steps performed, we end up with a number of Gaussians, all of which describe one particular peak in the residuals at one particular moment in time. Ideally, the spot moving across the stellar surface will show part of a sinusoidal as it moves across. Since we know this functional shape, we can make use of that and fit the position of Gaussian peaks that are close with their amplitude and width according to a shifted sine wave with an amplitude depending on the latitude of the emitting region. An example for this is shown in Fig. 11.5. In the future, a comparison of this effect observed in different lines, as well as a more accurate analysis of the position of the dips appearing and disappearing, hinting at the spot's latitude, would yield valuable results. In particular, a simple method that assigns a Gaussian contribution $x(\phi, \theta)$ to various points on the stellar surface, which are then used to calculate an excess flux spectrum could be fitted from a series of spectra resolved well in time: This is a simplified variant of the actual Doppler Imaging process.

11.2.3 Implementation as part of TIGRE's pipeline

In this thesis, we have developed a method to determine a star's excess flux, described in Chapter 3, as well as a method to determine a star's stellar parameters (Chapter 6). Both of these methods are highly automated, ideally requiring no human input after the generation of the model tetrahedra structure used for interpolating the model spectra (Chapter 5). Therefore, it is feasible to incorporate

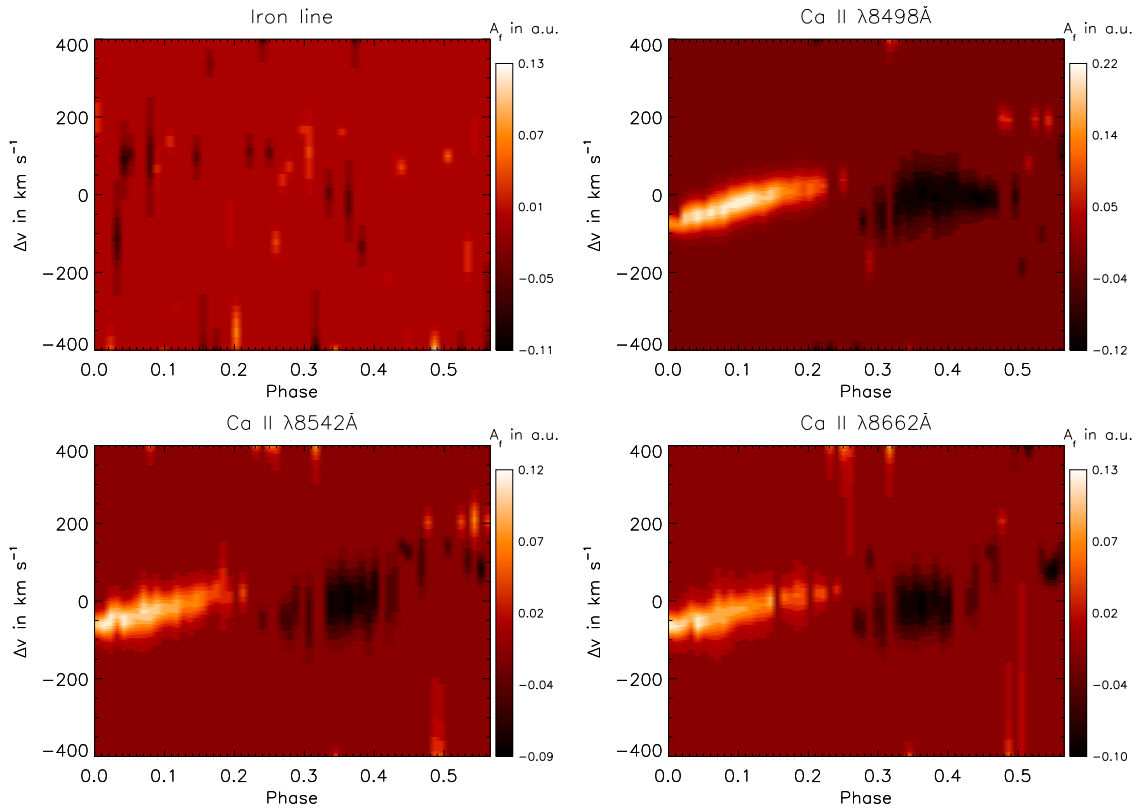


Figure 11.4: **Color plot of the height of the Gaussians fitted to the excess.** After subtracting a comparison spectrum, we fitted Gaussians to the residuals. This plot shows the result of these Gaussians. There is no structure in the comparison line (Top left), but there is in the chromospherically active ones (Ca II IRT-lines, other plots).

these two algorithms into the TIGRE pipeline, and have it automatically determine the stellar parameters of a star, as well as their excess flux. This would generate a large amount of data relevant to the study of activity, and among other things would allow to improve the conversion relations given in Chapter 8, making it valid for a larger range in $B - V$.

To do so, the model tetrahedra structure needs to be extended, because extrapolation results turn unreliable even for spectra close to stellar parameters still covered by the grid. The structure as it has been used here only covers a small part of the main sequence. By adding more models to the grid to cover the entire main sequence, as well spectra of subgiants and giants should turn this procedure into a reliable way to find valuable information about any star observed. As we have described in detail, only model spectra with realistic stellar parameters must be calculated and can then be added to the tetrahedra structure, and no additional model spectra covering the rest of the grid are required. This allows much faster generation of the required data, even if covering a large region in stellar parameters is desired.

After the pipeline has finished reducing the spectrum, it could start our procedure to find the stellar parameters, and use the results obtained in this way to compare the chromospherically active lines directly to the model spectrum just found to be the best fit. The results could then be added to the header, which already stores the TIGRE determined activity indices for the Ca II H- & K-lines and the Ca II IRT-lines. If the model grid is extended suitably, then this process could be used to analyze the excess flux behavior of stars other than F, G and K-type stars. Most notably, the results for M-dwarfs would be of great interest, especially considering that the CARMENES mission will obtain a great number of spectra of such stars. We could not perform such an analysis in this work, as there were unfortunately not enough TIGRE spectra available of M-dwarfs.

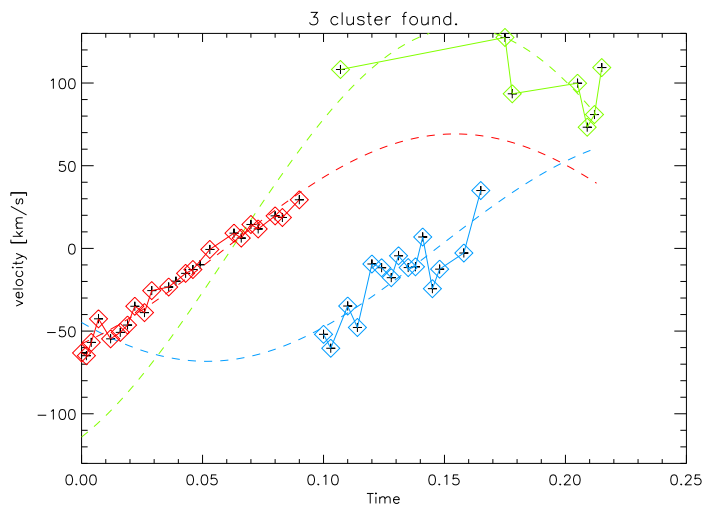


Figure 11.5: **Grouping positions of Gaussians fitted to the residuals together into “Clusters”.** Making use of the known sinusoidal shape these points must lie in, we can group the Gaussians with similar amplitudes and width together, hinting that they may stem from the same emitting region.

11.3 Closing Remarks

This work has clearly shown that the Ca II IRT-lines are very well suited for activity studies. They show a strong correlation to the established activity indicators, and can be converted easily into their scale. We hope that this allows the usage of new data taken by exciting missions such as GAIA to be combined with archival data, to find new results from their temporal behavior, and to better understand the processes governing the creation and behavior of stellar magnetic fields.

This work was possible only thanks to the large amount of data obtained by the automatic observation mode of the TIGRE telescope. While it shows some peculiarities, it is clear that it generates very valuable science data. This is a very powerful tool that, when combined with automatic processes and procedures, can create new science only possible with large datasets. Science like this will only become more valuable in the future, as the amount of data taken increases every day.

Acknowledgements

Writing this thesis has been a big undertaking, and it would not have been possible without the support of many great people.

First, I want to thank my supervisor Prof. Dr. Jürgen Schmitt, for the great opportunity to work on stellar activity in his research group. His feedback and ideas for my work have been invaluable, and I appreciate the trust he has put into me.

I was a member of the Graduiertenkolleg (GrK) 1351 “Extrasolar planets and their host stars” funded by the Deutsche Forschungsgemeinschaft (DFG) for the first two years of my thesis. I was assigned an advisory committee in this time, and I wish to thank its additional members, Dr. Sandra Jeffers and Dr. Birgit Fuhrmeister, for the great advice they have given to me in our regular meetings.

I also want to thank Dr. Birgit Fuhrmeister and Dr. Holger Müller for the many helpful suggestions for my work, and especially my paper and this thesis.

I am grateful to the many friendly colleagues at the Hamburger Sternwarte, who together create a wonderful working atmosphere which I am sure I will miss. Just like the many fun, but also fruitful and interesting discussions with those I shared my office with: Volker Perdelwitz, Dr. Tobias Schmidt, as well as Stefan Dahmke and Dr. Holger Müller.

I am incredibly thankful for the fantastic support my friends and family have shown me during this time, as well as the many relaxing and fun hours that provided a sorely needed reprise from the science work. Finally, to my partner Anna, who has shown me incredible support both in work and life, I want to say thank you. Having you at my side has made every day better.

This research has made use of NASA’s Astrophysics Data System. It has also made heavy use of the SIMBAD-database [Wenger et al., 2000] and VizieR [Ochsenbein et al., 2000]. Finally, I would like to thank *Astronomy & Astrophysics* for the kind permission to reproduce my paper in this work.

Eidesstattliche Versicherung

Hiermit versichere ich an Eides statt, die vorliegende Dissertationsschrift selbst verfasst und keine anderen als die angegebenen Hilfsmittel und Quellen benutzt zu haben.

Die eingereichte schriftliche Fassung entspricht der auf dem elektronischen Speichermedium.

Die Dissertation wurde in der vorgelegten oder einer ähnlichen Form nicht schon einmal in einem früheren Promotionsverfahren angenommen oder als ungenügend beurteilt.

Hamburg, den

Johannes Martin

Bibliography

- H. A. Abt. Spectral classification of weak-lined stars discovered photometrically. *ApJ*, 309:260–264, October 1986. doi: 10.1086/164597.
- M. Ammler-von Eiff and A. Reiners. New measurements of rotation and differential rotation in A-F stars: are there two populations of differentially rotating stars? *A&A*, 542:A116, June 2012. doi: 10.1051/0004-6361/201118724.
- E. Anderson and C. Francis. XHIP: An extended hipparcos compilation. *Astronomy Letters*, 38:331–346, May 2012. doi: 10.1134/S1063773712050015.
- V. Andretta, I. Busà, M. T. Gomez, and L. Terranegra. The Ca II Infrared Triplet as a stellar activity diagnostic. I. Non-LTE photospheric profiles and definition of the R_{IRT} indicator. *A&A*, 430:669–677, February 2005. doi: 10.1051/0004-6361:20041745.
- Ivan De Gennaro Aquino. *3D NLTE Radiative Transfer Modelling of M-dwarf Atmospheres*. PhD thesis, Universität Hamburg, Von-Melle-Park 3, 20146 Hamburg, 2016. URL <http://ediss.sub.uni-hamburg.de/volltexte/2017/8368>.
- H. W. Babcock. The Topology of the Sun’s Magnetic Field and the 22-YEAR Cycle. *ApJ*, 133:572, March 1961. doi: 10.1086/147060.
- S. Baliunas and W. Soon. Are Variations in the Length of the Activity Cycle Related to Changes in Brightness in Solar-Type Stars? *ApJ*, 450:896, September 1995. doi: 10.1086/176193.
- S. L. Baliunas, R. A. Donahue, W. H. Soon, J. H. Horne, J. Frazer, L. Woodard-Eklund, M. Bradford, L. M. Rao, O. C. Wilson, Q. Zhang, W. Bennett, J. Briggs, S. M. Carroll, D. K. Duncan, D. Figueroa, H. H. Lanning, T. Misch, J. Mueller, R. W. Noyes, D. Poppe, A. C. Porter, C. R. Robinson, J. Russell, J. C. Shelton, T. Soyumer, A. H. Vaughan, and J. H. Whitney. Chromospheric variations in main-sequence stars. *ApJ*, 438:269–287, January 1995. doi: 10.1086/175072.
- P. L. Bernacca and M. Perinotto. A catalogue of stellar rotational velocities: I. Main sequence single stars. II. Main sequence spectroscopic binaries and eclipsing systems. *Contributi dell’Osservatorio Astrofisica dell’Universita di Padova in Asiago*, 239, 1970.
- C. Bethge, H. Peter, T. J. Kentischer, C. Halbgewachs, D. F. Elmore, and C. Beck. The Chromospheric Telescope. *A&A*, 534:A105, October 2011. doi: 10.1051/0004-6361/201117456.
- L. Biermann. On the cause of chromospheric turbulence and uv excess of solar radiation. *Z. Astrophys*, 25: 161–177, 1948.
- I. Busà, R. Aznar Cuadrado, L. Terranegra, V. Andretta, and M. T. Gomez. The Ca II infrared triplet as a stellar activity diagnostic. II. Test and calibration with high resolution observations. *A&A*, 466:1089–1098, May 2007. doi: 10.1051/0004-6361:20065588.
- F. Castelli and R. L. Kurucz. New Grids of ATLAS9 Model Atmospheres. *ArXiv Astrophysics e-prints*, May 2004.
- C. Cazorla, T. Morel, Y. Nazé, G. Rauw, T. Semaan, S. Daflon, and M. S. Oey. Chemical abundances of fast-rotating massive stars. I. Description of the methods and individual results. *A&A*, 603:A56, July 2017. doi: 10.1051/0004-6361/201629841.

- Y. Chmielewski. The infrared triplet lines of ionized calcium as a diagnostic tool for F, G, K-type stellar atmospheres. *A&A*, 353:666–690, January 2000.
- C. Cincunegui, R. F. Díaz, and P. J. D. Mauas. $H\alpha$ and the Ca II H and K lines as activity proxies for late-type stars. *A&A*, 469:309–317, July 2007. doi: 10.1051/0004-6361:20066503.
- S. Czesla, S. Schröter, C. P. Schneider, and K. F. Huber. Pyastronomy website. http://www.hs.uni-hamburg.de/DE/Ins/Per/Czesla/PyA/PyA_0_6_0/index.html. Accessed: January 31st, 2017.
- I. De Gennaro Aquino, K.-P. Schröder, M. Mittag, U. Wolter, D. Jack, P. Eenens, J. N. González-Pérez, A. Hempelmann, J. H. M. M. Schmitt, P. H. Hauschildt, and G. Rauw. High spectral resolution monitoring of Nova V339 Delphini with TIGRE. *A&A*, 581:A134, September 2015. doi: 10.1051/0004-6361/201525810.
- D. K. Duncan, A. H. Vaughan, O. C. Wilson, G. W. Preston, J. Frazer, H. Lanning, A. Misch, J. Mueller, D. Soyumer, L. Woodard, S. L. Baliunas, R. W. Noyes, L. W. Hartmann, A. Porter, C. Zwaan, F. Middelkoop, R. G. M. Rutten, and D. Mihalas. CA II H and K measurements made at Mount Wilson Observatory, 1966-1983. *ApJS*, 76:383–430, May 1991. doi: 10.1086/191572.
- MM Dworetzky. A period-finding method for sparse randomly spaced observations or “how long is a piece of string?”. *Monthly Notices of the Royal Astronomical Society*, 203(4):917–924, 1983.
- G. Eberhard and K. Schwarzschild. On the reversal of the calcium lines H and K in stellar spectra. *ApJ*, 38, October 1913. doi: 10.1086/142037.
- J. A. Eddy. The Maunder Minimum. *Science*, 192:1189–1202, June 1976. doi: 10.1126/science.192.4245.1189.
- D. Fawzy, W. Rammacher, P. Ulmschneider, Z. E. Musielak, and K. Stępień. Acoustic and magnetic wave heating in stars . I. Theoretical chromospheric models and emerging radiative fluxes. *A&A*, 386:971–982, May 2002. doi: 10.1051/0004-6361:20020256.
- D. E. Fawzy. Theoretical basal Ca II and Mg II fluxes for late-type stars: results from acoustic wave spectra with time-dependent ionization and multilevel radiation treatments. *MNRAS*, 451:1824–1832, August 2015. doi: 10.1093/mnras/stv1035.
- Eigil Friis-Christensen and Knud Lassen. Length of the solar cycle- an indicator of solar activity closely associated with climate. *Science*, 254(5032):698–700, 1991.
- C. Fröhlich and J. Lean. The Sun’s total irradiance: Cycles, trends and related climate change uncertainties since 1976. *Geophys. Res. Lett.*, 25:4377–4380, December 1998. doi: 10.1029/1998GL900157.
- K. Fuhrmann. Nearby stars of the Galactic disk and halo. *A&A*, 338:161–183, October 1998.
- B. Fuhrmeister, J. H. M. M. Schmitt, and P. H. Hauschildt. Modeling M-dwarf chromospheres with PHOENIX. In F. Favata, G. A. J. Hussain, and B. Battrick, editors, *13th Cambridge Workshop on Cool Stars, Stellar Systems and the Sun*, volume 560 of *ESA Special Publication*, page 559, March 2005.
- Birgit Fuhrmeister. private communication, 2015.
- R. Glebocki and P. Gnacinski. VizieR Online Data Catalog: Catalog of Stellar Rotational Velocities (Glebocki+ 2005). *VizieR Online Data Catalog*, 3244, March 2005.
- J. Gomes da Silva, N. C. Santos, I. Boisse, X. Dumusque, and C. Lovis. On the long-term correlation between the flux in the Ca ii H & K and $H\alpha$ lines for FGK stars. *A&A*, 566:A66, June 2014. doi: 10.1051/0004-6361/201322697.
- R. G. Gratton, E. Carretta, and F. Castelli. Abundances of light elements in metal-poor stars. I. Atmospheric parameters and a new T_{eff} scale. *A&A*, 314:191–203, October 1996.
- David F Gray. *The observation and analysis of stellar photospheres*. Cambridge University Press, 3 edition, 2005.
- R. O. Gray, M. G. Napier, and L. I. Winkler. The Physical Basis of Luminosity Classification in the Late A-, F-, and Early G-Type Stars. I. Precise Spectral Types for 372 Stars. *AJ*, 121:2148–2158, April 2001. doi: 10.1086/319956.

- R. O. Gray, C. J. Corbally, R. F. Garrison, M. T. McFadden, and P. E. Robinson. Contributions to the Nearby Stars (NStars) Project: Spectroscopy of Stars Earlier than M0 within 40 Parsecs: The Northern Sample. I. *AJ*, 126:2048–2059, October 2003. doi: 10.1086/378365.
- Alexander Grossmann and Jean Morlet. Decomposition of hardy functions into square integrable wavelets of constant shape. *SIAM journal on mathematical analysis*, 15(4):723–736, 1984.
- G. E. Hale and S. B. Nicholson. The Law of Sun-Spot Polarity. *ApJ*, 62:270, November 1925. doi: 10.1086/142933.
- J. C. Hall. On the Determination of Empirical Stellar Flux Scales. *Publications of the Astronomical Society of the Pacific*, 108:313, April 1996. doi: 10.1086/133724.
- J. C. Hall. Stellar Chromospheric Activity. *Living Reviews in Solar Physics*, 5(1):2, Mar 2008. doi: 10.12942/lrsp-2008-2. URL <http://www.livingreviews.org/lrsp-2008-2>.
- K. Hartmann and T. Gehren. Metal-poor subdwarfs and early galactic nucleosynthesis. *A&A*, 199:269–290, June 1988.
- P. H. Hauschildt and E. Baron. Numerical solution of the expanding stellar atmosphere problem. *Journal of Computational and Applied Mathematics*, 109:41–63, September 1999.
- P. H. Hauschildt, F. Allard, and E. Baron. The NextGen Model Atmosphere Grid for 3000 μm $T_{\text{eff}}=10,000$ K. *The Astrophysical Journal*, 512:377–385, February 1999. doi: 10.1086/306745.
- P. H. Hauschildt, T. S. Barman, E. Baron, and F. Allard. Temperature Correction Methods. In I. Hubeny, D. Mihalas, and K. Werner, editors, *Stellar Atmosphere Modeling*, volume 288 of *Astronomical Society of the Pacific Conference Series*, page 227, January 2003.
- A. Hempelmann and R. A. Donahue. Wavelet analysis of stellar differential rotation. I. The Sun. *A&A*, 322:835–840, June 1997.
- A. Hempelmann, M. Mittag, J. N. Gonzalez-Perez, J. H. M. M. Schmitt, K. P. Schröder, and G. Rauw. Measuring rotation periods of solar-like stars using TIGRE. A study of periodic CaII H+K S-index variability. *A&A*, 586:A14, February 2016. doi: 10.1051/0004-6361/201526972.
- T. J. Henry, D. R. Soderblom, R. A. Donahue, and S. L. Baliunas. A Survey of Ca II H and K Chromospheric Emission in Southern Solar-Type Stars. *AJ*, 111, January 1996. doi: 10.1086/117796.
- S. Hollasch. Steve’s computer graphics index. <http://steve.hollasch.net/cgindex/geometry/sphere4pts.html>, 1993. Accessed: January 19th, 2017.
- Derek Homeier. private communication, 2015.
- I. Hubeny and D. Mihalas. *Theory of Stellar Atmospheres: An Introduction to Astrophysical Non-equilibrium Quantitative Spectroscopic Analysis*. Princeton Series in Astrophysics. Princeton University Press, 2014. ISBN 9781400852734. URL https://books.google.de/books?id=VA_rAwAAQBAJ.
- K. F. Huber, U. Wolter, S. Czesla, J. H. M. M. Schmitt, M. Esposito, I. Ilyin, and J. N. González-Pérez. Long-term stability of spotted regions and the activity-induced Rossiter-McLaughlin effect on V889 Herculis. A synergy of photometry, radial velocity measurements, and Doppler imaging. *A&A*, 501:715–728, July 2009. doi: 10.1051/0004-6361/200810638.
- T.-O. Husser, S. Wende-von Berg, S. Dreizler, D. Homeier, A. Reiners, T. Barman, and P. H. Hauschildt. A new extensive library of PHOENIX stellar atmospheres and synthetic spectra. *Astronomy & Astrophysics*, 553:A6, May 2013. doi: 10.1051/0004-6361/201219058.
- D. Jack, E. Baron, and P. H. Hauschildt. Identification of the feature that causes the I-band secondary maximum of a Type Ia supernova. *MNRAS*, 449:3581–3586, June 2015a. doi: 10.1093/mnras/stv474.
- D. Jack, M. Mittag, K.-P. Schröder, J. H. M. M. Schmitt, A. Hempelmann, J. N. González-Pérez, M. A. Trinidad, G. Rauw, and J. M. Cabrera Sixto. Time series of high-resolution spectra of SN 2014J observed with the TIGRE telescope. *MNRAS*, 451:4104–4113, August 2015b. doi: 10.1093/mnras/stv1238.

- J. S. Jenkins, F. Murgas, P. Rojo, H. R. A. Jones, A. C. Day-Jones, M. I. Jones, J. R. A. Clarke, M. T. Ruiz, and D. J. Pinfield. Chromospheric activities and kinematics for solar type dwarfs and subgiants: analysis of the activity distribution and the AVR. *A&A*, 531:A8, July 2011. doi: 10.1051/0004-6361/201016333.
- P. G. Judge, M. Carlsson, and R. F. Stein. On the Origin of the Basal Emission from Stellar Atmospheres: Analysis of Solar C II Lines. *ApJ*, 597:1158–1177, November 2003. doi: 10.1086/381222.
- A. Kaufer, H. Mandel, O. Stahl, B. Wolf, and I. Appenzeller. Heros website. <http://www.lsw.uni-heidelberg.de/projects/instrumentation/Heros/>, 2001. Accessed: July 20th, 2017.
- W. Kausch, S. Noll, A. Smette, S. Kimeswenger, M. Barden, C. Szyszka, A. M. Jones, H. Sana, H. Horst, and F. Kerber. Molecfit: A general tool for telluric absorption correction. II. Quantitative evaluation on ESO-VLT/X-Shooterspectra. *A&A*, 576:A78, April 2015. doi: 10.1051/0004-6361/201423909.
- P. C. Keenan and R. C. McNeil. The Perkins catalog of revised MK types for the cooler stars. *ApJS*, 71: 245–266, October 1989. doi: 10.1086/191373.
- T. Klocová and S. Kohl. Using molecfit with tigre data. http://www.hs.uni-hamburg.de/DE/Ins/HRT/hrt_user/telluric_line_removal_soft.html, 6 2015. Accessed: April 28th, 2017. Password required for access.
- A. Kramida, Yu. Ralchenko, J. Reader, and NIST ASD Team. NIST Atomic Spectra Database (ver. 5.3), [Online]. Available: <http://physics.nist.gov/asd> [2017, September 25]. National Institute of Standards and Technology, Gaithersburg, MD., 2015.
- W. B. Landsman. The IDL Astronomy User’s Library. In R. J. Hanisch, R. J. V. Brissenden, and J. Barnes, editors, *Astronomical Data Analysis Software and Systems II*, volume 52 of *Astronomical Society of the Pacific Conference Series*, page 246, January 1993.
- K. Lang. *The Sun from Space*. Astronomy and Astrophysics Library. Springer Berlin Heidelberg, 2008. ISBN 9783540769538. URL https://books.google.de/books?id=5vSh_XUz75IC.
- J. L. Linsky, W. McClintock, R. M. Robertson, and S. P. Worden. Stellar model chromospheres. X - High-resolution, absolute flux profiles of the CA II H and K lines in stars of spectral types F0-M2. *ApJS*, 41: 47–74, September 1979. doi: 10.1086/190607.
- Jeffrey L. Linsky, Richard G. Teske, and Carol W. Wilkinson. Observations of the infrared triplet of singly ionized calcium. *Solar Physics*, 11(3):374–383, Mar 1970. ISSN 1573-093X. doi: 10.1007/BF00153072. URL <https://doi.org/10.1007/BF00153072>.
- N. R. Lomb. Least-squares frequency analysis of unequally spaced data. *Ap&SS*, 39:447–462, February 1976. doi: 10.1007/BF00648343.
- J. Maldonado, C. Eiroa, E. Villaver, B. Montesinos, and A. Mora. Metallicity of solar-type stars with debris discs and planets. *A&A*, 541:A40, May 2012. doi: 10.1051/0004-6361/201218800.
- O. Y. Malkov, V. S. Tamazian, J. A. Docobo, and D. A. Chulkov. Dynamical masses of a selected sample of orbital binaries. *A&A*, 546:A69, October 2012. doi: 10.1051/0004-6361/201219774.
- C. B. Markwardt. Non-linear Least-squares Fitting in IDL with MPFIT. In D. A. Bohlender, D. Durand, and P. Dowler, editors, *Astronomical Data Analysis Software and Systems XVIII*, volume 411 of *Astronomical Society of the Pacific Conference Series*, page 251, September 2009.
- C. B. Markwardt. Mpfif website. <https://www.physics.wisc.edu/~craigm/idl/fitting.html>, 2009. Accessed: April 1st, 2017.
- S. C. Marsden, P. Petit, S. V. Jeffers, J. Morin, R. Fares, A. Reiners, J.-D. do Nascimento, M. Aurière, J. Bouvier, B. D. Carter, C. Catala, B. Dintrans, J.-F. Donati, T. Gastine, M. Jardine, R. Konstantinova-Antova, J. Lanoux, F. Lignières, A. Morgenthaler, J. C. Ramirez-Vélez, S. Théado, V. Van Grootel, and BCool Collaboration. A BCool magnetic snapshot survey of solar-type stars. *MNRAS*, 444:3517–3536, November 2014. doi: 10.1093/mnras/stu1663.

- J. Martin, B. Fuhrmeister, M. Mittag, T. O. B. Schmidt, A. Hempelmann, J. N. González-Pérez, and J. H. M. M. Schmitt. The Ca II infrared triplet's performance as an activity indicator compared to Ca II H and K. Empirical relations to convert Ca II infrared triplet measurements to common activity indices. *A&A*, 605:A113, September 2017. doi: 10.1051/0004-6361/201630298.
- R. Martínez-Arnáiz, J. Maldonado, D. Montes, C. Eiroa, and B. Montesinos. Chromospheric activity and rotation of FGK stars in the solar vicinity. An estimation of the radial velocity jitter. *A&A*, 520:A79, September 2010. doi: 10.1051/0004-6361/200913725.
- R. Martínez-Arnáiz, J. López-Santiago, I. Crespo-Chacón, and D. Montes. Effect of magnetic activity saturation in chromospheric flux-flux relationships. *MNRAS*, 414:2629–2641, July 2011a. doi: 10.1111/j.1365-2966.2011.18584.x.
- R. Martínez-Arnáiz, J. López-Santiago, I. Crespo-Chacón, and D. Montes. Effect of magnetic activity saturation in chromospheric flux-flux relationships. *MNRAS*, 414:2629–2641, July 2011b. doi: 10.1111/j.1365-2966.2011.18584.x.
- K. McCarthy and R. J. Wilhelm. Characterizing the AB Doradus Moving Group via High-resolution Spectroscopy and Kinematic Traceback. *AJ*, 148:70, October 2014. doi: 10.1088/0004-6256/148/4/70.
- Dermot H McLain. Drawing contours from arbitrary data points. *The Computer Journal*, 17(4):318–324, 1974.
- Dermot H McLain. Two dimensional interpolation from random data. *The Computer Journal*, 19(2):178–181, 1976.
- Nicholas Metropolis, Arianna W. Rosenbluth, Marshall N. Rosenbluth, Augusta H. Teller, and Edward Teller. Equation of state calculations by fast computing machines. *The Journal of Chemical Physics*, 21(6):1087–1092, 1953. doi: 10.1063/1.1699114. URL <http://dx.doi.org/10.1063/1.1699114>.
- N. Meunier and X. Delfosse. On the correlation between Ca and H α solar emission and consequences for stellar activity observations. *A&A*, 501:1103–1112, July 2009. doi: 10.1051/0004-6361/200911823.
- T. V. Mishenina, C. Soubiran, V. V. Kovtyukh, M. M. Katsova, and M. A. Livshits. Activity and the Li abundances in the FGK dwarfs. *A&A*, 547:A106, November 2012. doi: 10.1051/0004-6361/201118412.
- M. Mittag. *Die technische Performance des Hamburger Robotischen Teleskops*. Diploma Thesis, Universität Hamburg, 2006.
- M. Mittag. Tigre website. http://www.hs.uni-hamburg.de/DE/Ins/HRT/hrt_user/hrt_user_main_page.html, 2015. Accessed: January 31st, 2017.
- M. Mittag, A. Hempelmann, J. N. González-Pérez, and J. H. M. M. Schmitt. The Data Reduction Pipeline of the Hamburg Robotic Telescope. *Advances in Astronomy*, 2010:101502, 2010. doi: 10.1155/2010/101502.
- M. Mittag, J. H. M. M. Schmitt, and K.-P. Schröder. Ca II H+K fluxes from S-indices of large samples: a reliable and consistent conversion based on PHOENIX model atmospheres. *A&A*, 549:A117, January 2013. doi: 10.1051/0004-6361/201219868.
- M. Mittag, K.-P. Schröder, A. Hempelmann, J. N. González-Pérez, and J. H. M. M. Schmitt. Chromospheric activity and evolutionary age of the Sun and four solar twins. *A&A*, 591:A89, June 2016. doi: 10.1051/0004-6361/201527542.
- M. Mittag, J. Robrade, J. H. M. M. Schmitt, A. Hempelmann, J. N. González-Pérez, and K.-P. Schröder. Four-month chromospheric and coronal activity cycle in τ Boötis. *A&A*, 600:A119, April 2017. doi: 10.1051/0004-6361/201629156.
- A. F. J. Moffat. A Theoretical Investigation of Focal Stellar Images in the Photographic Emulsion and Application to Photographic Photometry. *A&A*, 3:455, December 1969.
- Jorge J. Moré. *The Levenberg-Marquardt algorithm: Implementation and theory*. Springer Berlin Heidelberg, Berlin, Heidelberg, 1978. ISBN 978-3-540-35972-2. doi: 10.1007/BFb0067700. URL <http://dx.doi.org/10.1007/BFb0067700>.

- J. Moré and S. Wright. *Optimization Software Guide*. Society for Industrial and Applied Mathematics, 1993. doi: 10.1137/1.9781611970951. URL <http://epubs.siam.org/doi/abs/10.1137/1.9781611970951>.
- Holger M. Müller. Limb-darkening measurements on exoplanet host stars and the sun. 2016. URL <http://ediss.sub.uni-hamburg.de/volltexte/2016/8041>.
- NASA/SDO. URL <https://sdo.gsfc.nasa.gov/gallery/>. "Courtesy of NASA/SDO and the AIA, EVE, and HMI science teams."
- H. Neckel and D. Labs. The solar radiation between 3300 and 12500 Å. *SoPh*, 90:205–258, February 1984. doi: 10.1007/BF00173953.
- F. Ochsenbein, P. Bauer, and J. Marcout. The Vizier database of astronomical catalogues. *A&AS*, 143: 23–32, April 2000. doi: 10.1051/aas:2000169.
- E. N. Parker. Hydromagnetic Dynamo Models. *ApJ*, 122:293, September 1955. doi: 10.1086/146087.
- Karl Pearson. Note on regression and inheritance in the case of two parents. *Proceedings of the Royal Society of London*, 58:240–242, 1895.
- M. I. Pérez Martínez, K.-P. Schröder, and P. Hauschildt. The non-active stellar chromosphere: Ca II basal flux. *MNRAS*, 445:270–279, November 2014a. doi: 10.1093/mnras/stu1706.
- M. I. Pérez Martínez, K.-P. Schröder, and P. Hauschildt. The non-active stellar chromosphere: Ca II basal flux. *MNRAS*, 445:270–279, November 2014b. doi: 10.1093/mnras/stu1706.
- R. C. Peterson. Abundance analyses of metal-poor stars. III - Red spectra of nine dwarfs. *ApJ*, 235:491–503, January 1980. doi: 10.1086/157651.
- A. Petz, P. H. Hauschildt, J.-U. Ness, and S. Starrfield. Modeling CHANDRA low energy transmission grating spectrometer observations of classical novae with PHOENIX. I. V4743 Sagittarii. *A&A*, 431: 321–328, February 2005. doi: 10.1051/0004-6361/20041396.
- N. E. Piskunov and J. A. Valenti. New algorithms for reducing cross-dispersed echelle spectra. *A&A*, 385: 1095–1106, April 2002. doi: 10.1051/0004-6361/20020175.
- P. Prugniel, I. Vauglin, and M. Koleva. The atmospheric parameters and spectral interpolator for the MILES stars. *A&A*, 531:A165, July 2011. doi: 10.1051/0004-6361/201116769.
- T Prusti. The promises of gaia. *Astronomische Nachrichten*, 333(5-6):453–459, 2012.
- A. Quirrenbach, P. J. Amado, J. A. Caballero, R. Mundt, A. Reiners, I. Ribas, W. Seifert, M. Abril, J. Aceituno, F. J. Alonso-Floriano, M. Ammler-von Eiff, R. Antona Jiménez, H. Anwand-Heerwart, M. Azzaro, F. Bauer, D. Barrado, S. Becerril, V. J. S. Béjar, D. Benítez, Z. M. Berdiñas, M. C. Cárdenas, E. Casal, A. Claret, J. Colomé, M. Cortés-Contreras, S. Czesla, M. Doellinger, S. Dreizler, C. Feiz, M. Fernández, D. Galadí, M. C. Gálvez-Ortiz, A. García-Piquer, M. L. García-Vargas, R. Garrido, L. Gesa, V. Gómez Galera, E. González Álvarez, J. I. González Hernández, U. Grözinger, J. Guàrdia, E. W. Guenther, E. de Guindos, J. Gutiérrez-Soto, H.-J. Hagen, A. P. Hatzes, P. H. Hauschildt, J. Hellmich, T. Henning, D. Hermann, L. Hernández Castaño, E. Herrero, D. Hidalgo, G. Holgado, A. Huber, K. F. Huber, S. Jeffers, V. Joergens, E. de Juan, M. Kehr, R. Klein, M. Kürster, A. Lamert, S. Lalitha, W. Laun, U. Lemke, R. Lenzen, M. López del Fresno, B. López Martí, J. López-Santiago, U. Mall, H. Mandel, E. L. Martín, S. Martín-Ruiz, H. Martínez-Rodríguez, C. J. Marvin, R. J. Mathar, E. Mirabet, D. Montes, R. Morales Muñoz, A. Moya, V. Naranjo, A. Ofir, R. Oreiro, E. Pallé, J. Panduro, V.-M. Passegger, A. Pérez-Calpena, D. Pérez Medialdea, M. Perger, M. Pluto, A. Ramón, R. Rebolo, P. Redondo, S. Reffert, S. Reinhardt, P. Rhode, H.-W. Rix, F. Rodler, E. Rodríguez, C. Rodríguez-López, E. Rodríguez-Pérez, R.-R. Rohloff, A. Rosich, E. Sánchez-Blanco, M. A. Sánchez Carrasco, J. Sanz-Forcada, L. F. Sarmiento, S. Schäfer, J. Schiller, C. Schmidt, J. H. M. M. Schmitt, E. Solano, O. Stahl, C. Storz, J. Stürmer, J. C. Suárez, R. G. Ulbrich, G. Veredas, K. Wagner, J. Winkler, M. R. Zapatero Osorio, M. Zechmeister, F. J. Abellán de Paco, G. Anglada-Escudé, C. del Burgo, A. Klutsch, J. L. Lizon, M. López-Morales, J. C. Morales, M. A. C. Perryman, S. M. Tulloch, and W. Xu. CARMENES instrument overview. In *Ground-based and Airborne Instrumentation for Astronomy V*, volume 9147 of *Proc. SPIE*, page 91471F, July 2014. doi: 10.1117/12.2056453.

- R. G. M. Rutten. Magnetic structure in cool stars. VII - Absolute surface flux in CA II H and K line cores. *A&A*, 130:353–360, January 1984.
- R. G. M. Rutten, C. J. Schrijver, A. F. P. Lemmens, and C. Zwaan. Magnetic structure in cool stars. XVII - Minimum radiative losses from the outer atmosphere. *A&A*, 252:203–219, December 1991.
- R. J. Rutten. Radiative Transfer in Stellar Atmospheres. Utrecht University lecture notes, 2003. 8th edition.
- T. Ryabchikova, N. Piskunov, Y. Pakhomov, V. Tsymbal, A. Titarenko, T. Sitnova, S. Alexeeva, L. Fossati, and L. Mashonkina. Accuracy of atmospheric parameters of FGK dwarfs determined by spectrum fitting. *MNRAS*, 456:1221–1234, February 2016. doi: 10.1093/mnras/stv2725.
- J. D. Scargle. Studies in astronomical time series analysis. II - Statistical aspects of spectral analysis of unevenly spaced data. *ApJ*, 263:835–853, December 1982. doi: 10.1086/160554.
- J. H. M. M. Schmitt, K.-P. Schröder, G. Rauw, A. Hempelmann, M. Mittag, J. N. González-Pérez, S. Czesla, U. Wolter, D. Jack, P. Eenens, and M. A. Trinidad. TIGRE: A new robotic spectroscopy telescope at Guanajuato, Mexico. *Astronomische Nachrichten*, 335:787, October 2014. doi: 10.1002/asna.201412116.
- C. J. Schrijver. Magnetic structure in cool stars. XI - Relations between radiative fluxes measuring stellar activity, and evidence for two components in stellar chromospheres. *A&A*, 172:111–123, January 1987.
- C. J. Schrijver and A. M. Title. The Magnetic Connection between the Solar Photosphere and the Corona. *ApJL*, 597:L165–L168, November 2003. doi: 10.1086/379870.
- C. J. Schrijver and C. Zwaan. *Solar and Stellar Magnetic Activity*. Cambridge Astrophysics. Cambridge University Press, 2008. ISBN 9781139425421. URL <https://books.google.de/books?id=Tk0nNfABUrMC>.
- C. Schröder, A. Reiners, and J. H. M. M. Schmitt. Ca II HK emission in rapidly rotating stars. Evidence for an onset of the solar-type dynamo. *A&A*, 493:1099–1107, January 2009. doi: 10.1051/0004-6361:200810377.
- M. Schwarzschild. On Noise Arising from the Solar Granulation. *ApJ*, 107:1, January 1948. doi: 10.1086/144983.
- R. A. Shine, R. W. Milkey, and D. Mihalas. Resonance Line Transfer with Partial Redistribution. V. The Solar CA II Lines. *ApJ*, 199:724–733, August 1975. doi: 10.1086/153744.
- SILSO World Data Center.
- A. Siviero, S. Dallaporta, and U. Munari. Period Change, Spot Migration and Orbital Solution for the Eclipsing Binary AR Lac. *Baltic Astronomy*, 15:387–394, 2006.
- A. Smette, H. Sana, S. Noll, H. Horst, W. Kausch, S. Kimeswenger, M. Barden, C. Szyszka, A. M. Jones, A. Gallenne, J. Vinther, P. Ballester, and J. Taylor. Molecfit: A general tool for telluric absorption correction. I. Method and application to ESO instruments. *A&A*, 576:A77, April 2015. doi: 10.1051/0004-6361/201423932.
- C. Soubiran, J.-F. Le Campion, G. Cayrel de Strobel, and A. Caillo. The PASTEL catalogue of stellar parameters. *A&A*, 515:A111, June 2010. doi: 10.1051/0004-6361/201014247.
- M. Stix. Dynamo Theory and the Solar Cycle. In V. Bumba and J. Kleczek, editors, *Basic Mechanisms of Solar Activity*, volume 71 of *IAU Symposium*, page 367, 1976.
- K.G. Strassmeier. *Aktive Sterne: Laboratorien der solaren Astrophysik*. Springer Vienna, 1997. ISBN 9783211830055. URL <https://books.google.de/books?id=0hWeAAAACAAJ>.
- Y. Takeda, B. Sato, E. Kambe, S. Masuda, H. Izumiura, E. Watanabe, M. Ohkubo, K. Yanagisawa, Y. Yasaka, S. Honda, S. Kawanomoto, W. Aoki, H. Ando, K. Sadakane, M. Takada-Hidai, and S. M. Miyama. High-Dispersion Spectra Collection of Nearby F–K Stars at Okayama Astrophysical Observatory: A Basis for Spectroscopic Abundance Standards. *Publications of the Astronomical Society of Japan*, 57:13–25, February 2005. doi: 10.1093/pasj/57.1.13.
- TIGRE Team. Tigre newsletter 2. <http://www.lsw.uni-heidelberg.de/projects/instrumentation/Heros/>, 06 2015. Accessed: July 20th, 2017.

- C. A. O. Torres, G. R. Quast, L. da Silva, R. de La Reza, C. H. F. Melo, and M. Sterzik. Search for associations containing young stars (SACY). I. Sample and searching method. *A&A*, 460:695–708, December 2006. doi: 10.1051/0004-6361:20065602.
- G. Torres, D. A. Fischer, A. Sozzetti, L. A. Buchhave, J. N. Winn, M. J. Holman, and J. A. Carter. Improved Spectroscopic Parameters for Transiting Planet Hosts. *ApJ*, 757:161, October 2012. doi: 10.1088/0004-637X/757/2/161.
- A. Uesugi and I. Fukuda. *Catalogue of rotational velocities of the stars*. 1970.
- A. H. Vaughan, G. W. Preston, and O. C. Wilson. Flux measurements of CA II H and K emission. *Publications of the Astronomical Society of the Pacific*, 90:267–274, June 1978. doi: 10.1086/130324.
- J. Eo Vernazza, E. Ho Avrett, and R. Loeser. Structure of the solar chromosphere. iii-models of the euV brightness components of the quiet-sun. *The Astrophysical Journal Supplement Series*, 45:635–725, 1981.
- G. Wallerstein. Abundances in G. Dwarfs.VI. a Survey of Field Stars. *ApJS*, 6:407, February 1962. doi: 10.1086/190067.
- Alexander Christopher Wawrzyn. *The structure and spectra of irradiated secondaries in close binaries (pre-CVs)*. PhD thesis, Universität Hamburg, Von-Melle-Park 3, 20146 Hamburg, 2009. URL <http://ediss.sub.uni-hamburg.de/volltexte/2009/4085>.
- M. Wenger, F. Ochsenbein, D. Egret, P. Dubois, F. Bonnarel, S. Borde, F. Genova, G. Jasniewicz, S. Laloë, S. Lesteven, and R. Monier. The SIMBAD astronomical database. The CDS reference database for astronomical objects. *A&AS*, 143:9–22, April 2000. doi: 10.1051/aas:2000332.
- Joseph Werne. The solar dynamo. <https://www.cora.nwra.com/~werne/eos/text/dynamo.html>, 2000. Accessed: August 14th, 2017.
- O. R. White and W. C. Livingston. Solar luminosity variation. III - Calcium K variation from solar minimum to maximum in cycle 21. *ApJ*, 249:798–816, October 1981. doi: 10.1086/159338.
- R. J. White, J. M. Gabor, and L. A. Hillenbrand. High-Dispersion Optical Spectra of Nearby Stars Younger Than the Sun. *AJ*, 133:2524–2536, June 2007. doi: 10.1086/514336.
- T. Wiecki. Mcmc sampling for dummies. <http://twiecki.github.io/blog/2015/11/10/mcmc-sampling/>, 11 2015. Accessed: April 6th, 2017.
- O. C. Wilson. Flux Measurements at the Centers of Stellar h- and K-Lines. *ApJ*, 153:221, July 1968. doi: 10.1086/149652.
- O. C. Wilson. Chromospheric variations in main-sequence stars. *ApJ*, 226:379–396, December 1978. doi: 10.1086/156618.
- O. C. Wilson and M. K. Vainu Bappu. H and K Emission in Late-Type Stars: Dependence of Line Width on Luminosity and Related Topics. *ApJ*, 125:661, May 1957. doi: 10.1086/146339.
- U. Wolter, J. Robrade, J. H. M. M. Schmitt, and J. U. Ness. Doppler imaging an X-ray flare on the ultrafast rotator BO Mic. A contemporaneous multiwavelength study using XMM-Newton and VLT. *A&A*, 478: L11–L14, January 2008. doi: 10.1051/0004-6361:20078838.
- J. M. Zobitz, A. R. Desai, D. J. P. Moore, and M. A. Chadwick. A primer for data assimilation with ecological models using markov chain monte carlo (mcmc). *Oecologia*, 167(3):599, 2011. ISSN 1432-1939. doi: 10.1007/s00442-011-2107-9. URL <http://dx.doi.org/10.1007/s00442-011-2107-9>.

Appendix A

Notes on the IDL Implementation

A.1 Measuring chromospheric excess

The procedure described in Chapter 4 is written in IDL (“Interactive Data Language”). The corresponding function to call is named `getexcesspro`. It takes the comparison spectrum and the one it should be compared to, and returns a structure that holds the determined values. It allows the user to pass a variety of keywords to setup the procedure to their needs. Below, only a fraction of all possible keywords and input is given:

<code>getexcesspro</code> ,	<code>wavem, specm, errm, waveo, speco, specerr, order, 1, rr, BV=bv, ROTVEL=rotvel, MCITER=mciter, SUBMCITER=submciter, WHATFIT=whatfit, AUTOEXCESSAREA=autoexcessarea, USEENVELOPE=useenvelope, EXCESSSIZE=excesssize, NOSHIFT=noshift, SAVEEXCESS=saveexcess, NORESAMP=noresamp, NORMALREGION=normalregion</code>
<code>wavem, specm, errm</code>	Three arrays holding the wavelength scale (in Å), flux (in physical units) and error of the comparison spectrum.
<code>waveo, speco, specerr</code>	Three arrays holding the wavelength scale (in Å), flux (in arbitrary units) and error of the spectrum under consideration.
<code>order</code>	Polynomial order to be used for normalization. Recommended value is 1.
<code>1</code>	Wavelength of the line the excess is to be obtained from.
<code>rr</code>	Two-element array of the spectral region to consider. Must include 1.
Optional input	
<code>BV</code>	$B - V$ of the star under consideration.
<code>ROTVEL</code>	The comparison spectrum is broadened by this rotational velocity of the star under consideration. See also text below.
<code>MCITER, SUBMCITER</code>	Determines how many Monte-Carlo iterations are performed. See text for details.
<code>WHATFIT</code>	Function to fit to the excess. 0: Gaussian profile (Default), 1: Voigt-profile, 2: Moffat profile.
<code>EXCESSSIZE</code>	Size of the region the excess is expected to cover. Used for integrating, if <code>/AUTOEXCESSAREA</code> is not set.
<code>NORMALREGION</code>	See text below.
Keywords	
<code>AUTOEXCESSAREA</code>	If set, the region the excess is covering is determined automatically.
<code>USEENVELOPE</code>	1: Uses the upper envelope of the spectrum for finding the continuum for both spectra, 2: Use it only for the considered spectrum, 3: Use it only for the comparison spectrum.
<code>NOSHIFT</code>	If set, performs no wavelength shift as described in Sect. 3.3
<code>SAVEEXCESS</code>	If set, an additional field is added to the struct returned by this function, which holds the average excess distribution.
<code>NORESAMP</code>	If set, no resampling of the comparison spectrum to an equidistant wavelength scale is performed.
Performs the steps outlined in Chapter 3 to obtain the chromospheric excess.	

Table A.1: Overview of the common block `FBPF_Data` used by the code.

Name	Type	Description
<code>coeffs</code>	<code>double[10, N_W, N_P]</code>	The 10 coefficients from Eq. (5.8), for each wavelength point N_W and grid point N_P .
<code>w</code>	<code>double[N_W]</code>	The wavelength scale in use.
<code>ts</code>	<code>double[N_P]</code>	The value of T_{eff} of the model at gridpoint N_P .
<code>gs</code>	<code>double[N_P]</code>	The value of $\log g$ of the model at gridpoint N_P .
<code>zs</code>	<code>double[N_P]</code>	The value of $[M/H]$ of the model at gridpoint N_P .
<code>steps</code>	<code>float[3]</code>	The values defining the scale of the partitioning. Here, we use 100, 0.2, 0.25 as given in Eq. (5.6).
<code>tetras</code>	<code>struct</code>	Holds the parameters of the tetrahedra. Details given in Table A.2.
<code>fs</code>	<code>fs[N_P, N_W]</code>	The flux of the degraded model at gridpoint N_P , for each wavelength point N_W . This value is intended for debugging and can be removed.

This procedure expects an error also for the comparison spectrum. If a model spectrum is used, this can be estimated from the errors on the stellar parameters (see Sect. 7.2.3). The value for `BV` is used to estimate a value for ϵ , as described in Sec. 3.4. If no value is passed here, a value of $\epsilon = 0.6 \pm 0.05$ is assumed, corresponding to the value found from deriving the limb darkening in the Eddington approximation (Hubeny and Mihalas [2014], pg. 517).

`ROTVEL` can be set to a two-element array. The second value in that array is then used as the error on the value on the rotational velocity. Otherwise, an error of 10% is assumed. As described above, for error determination this procedure performs Monte-Carlo iterations. The value `MCITER` gives the amount of iterations where one value for R' and $v \sin i$ is sampled, whereas `SUBMCITER` defines how many randomly chosen values from the resulting distribution of each iterations are stored. The higher this value, the more accurate the result, at the cost of a bigger memory use. The default value is 250, and is suitable for most cases. Set `NORMALREGION` to a $2N$ -element array with N as the amount of regions, to give the regions to consider when obtaining the continuum, as described in Sec. 3.2. For Ca II H- & K-lines, use `[3991.07, 4011.07, 3891.07, 3911.07]`.

This procedure calls a variety of helper routines, which can also be used on their own, such as the aforementioned `obtain_continuum` and `normalize_spectrum`¹. For degradation and rotational broadening, two more functions are available for use for either large or non-equidistantly sampled spectral regions. Since the kernel cannot be assumed to be constant to good approximation, the computationally fast approach using the FFT must not be used. Instead, `degrade_large` and `rotbroaden_large` perform the folding with the changing kernel individually for each wavelength point. These procedures are therefore much slower.

A.2 Interpolating model spectra on irregular grids

A.2.1 Using the code

This interpolation algorithm was written in the IDL programming language. It consists of several procedures and functions, which we will describe below. We also provide an overview of the common block datastructure `FBPF_Data` used by these procedures in Table A.1 and Table A.2. The actual usage of this code can be separated into two parts: Preparing the interpolation, and using the resulting partitioning to calculate spectra. All names of functions and procedures part of this code begin with either `fbpf_` or `findbestphoenixfit_`, depending on whether or not it is an internal use function or is involved in the creation of the partitioning, or if it works on a higher level, such as functions for fitting, see Sec. A.4.

¹This routine calculates the error on the result as the quadratic sum from the error on the obtained continuum and the spectrum. This is not perfectly valid, since these errors are correlated. However, this approach serves as a conservative estimation of the real error.

Table A.2: Overview of the struct `tetras` storing the tetrahedra data.

Name	Type	Description
<code>tetras</code> .—		
<code>.boundary</code>	<code>long[N_s,2]</code>	Holds the indices of tetrahedra surfaces making up the boundary of the structure. The n -th boundary surface is the <code>tetras.boundary[n,1]</code> 's surface of the <code>tetras.boundary[n,0]</code> tetrahedron.
<code>tetras.tetrahedra[N_t]</code> .—		
<code>.pts</code>	<code>long[4]</code>	The four indices of the points making up this tetrahedron.
<code>.normals</code>	<code>double[4,3]</code>	The components of the normal of the four surfaces. <code>.normals[i,j]</code> holds the j -th component of the normal of tetrahedron surface i .
<code>.distfac</code>	<code>double[4,4]</code>	The four components to use for the quick calculation of the distance to a surface via a four-dimensional dot product, according to Eq. (5.11).

Preparing the interpolation

In the process of preparing the interpolation, the model spectra must be created, loaded in and assigned a place in the grid. Afterwards, the partitioning into tetrahedra must be performed, the polynomials from Eq. (5.8) determined, and finally the distance factors from Eq. (5.11) need to be calculated. The first procedure that needs to be called is:

<code>FBPF_CreateBlock,</code>	<code>w, res, steps, NONCONVEX=nonconvex, VERBOSE=verbose, USEIDL=useidl, FASTDEGRADE=fastdegrade, NOTETRA=notetra, CAREFUL=careful</code>
<code>w</code>	An array of wavelength points the model spectra will be interpolated on.
<code>res</code>	The resolution the models will be degraded to.
<code>steps</code>	A 3-element array that holds the step sizes for T_{eff} , $\log g$ and $[M/H]$, which define the scale of this parameter. Default: <code>[100,0.2,0.25]</code> .
Keywords	
<code>NOCONVEX</code>	If set, no additional pass to ensure a convex structure is performed.
<code>VERBOSE</code>	Prints out additional information.
<code>USEIDL</code>	Uses IDL routines for the partitioning. Will not result in an ideal partition, and may find tetrahedra that overlap.
<code>FASTDEGRADE</code>	Uses a fast routine for degrading. Will introduce strong errors if the wavelength region is too large, or not equidistant.
<code>NOTETRA</code>	Does not perform the actual partitioning into tetrahedra.
<code>CAREFUL</code>	Temporarily interpolates the model spectra to a higher resolution before degrading for higher accuracy.
Finds, loads and degrades spectra data, performs further preparations and then calls the next routine for partitioning the space into tetrahedra. The result is then saved.	

This function searches for all available `ilte*.sav`-files in the current folder, assuming all of those are PHOENIX model spectra in IDL `sav`-format with (at least) two saved arrays:

`wave` An array of wavelength points.
`flux` The spectrum, one point for each in `wave`.

The resolution of this spectra is then determined, and they are then interpolated to the wavelength scale `w`, or a much finer one if `/CAREFUL` is set, in which case the spectrum is then interpolated again to the real wavelength scale `w` afterwards. The filename is then analyzed to determine the corresponding values of T_{eff} , $\log g$ and $[M/H]$. For this to work, the filename must follow the structure given: `ilteTTTTT.GGGG.ZZZZ`—`.sav`, whereas the characters T are replaced by the value of T_{eff} (five characters), G are replaced by the value of $\log g$ (four characters), and Z are replaced by the value of metallicity (five characters, including sign), and any combination of text afterwards, with a file extension of `.sav`. For example, a valid filename would be `ilte06100.3.90.+0.20.PHOENIX-ACES-AGSS-COND-2015hr.sav`.

The so determined values determine the space of the corresponding point in the grid. Then, the degraded flux is stored in `fs`, necessary for determining the polynomial coefficients later.

Afterwards, the routine stores the so obtained values, and saves them in a file called `GridTetraData_MINW-MAXWA.sav`, though with `MINW` and `MAXW` replaced by the minimum and maximum values of `w` replaced, respectively. Next, it calls the routine for dividing the layout into tetrahedra, either calling the IDL routine if `USEIDL` is set - however the resulting partition may not be ideal, and may feature overlapping tetrahedra. Otherwise, the next routine is called, and the result stored in a new file with the same name as before, but beginning with `GridTetraData`.

<code>FBPF.Tetrahedrate</code> ,	<code>x, y, z, KEEPCONCAVE=keepconcave, FILLHOLES=fillholes, DEBUG=debug, QUICKSTART=quickstart</code>
<code>x</code>	An array of x -coordinates. Usually the normalized values $T_{\text{eff}}/\Delta T_{\text{eff}}$.
<code>y</code>	An array of y -coordinates. Usually the normalized values $\log g/\Delta \log g$.
<code>z</code>	An array of z -coordinates. Usually the normalized values $[M/H]/\Delta [M/H]$.
Keywords	
<code>KEEPCONCAVE</code>	If set, no additional pass is performed to ensure a convex structure. Disregarding errors due to numerical inaccuracies, the structure created will always be convex.
<code>FILLHOLES</code>	If set, the resulting structure will be checked for holes and those will be fixed.
<code>DEBUG</code>	Prints and plots various debug related information.
<code>QUICKSTART</code>	If set, a faster approach to find the starting surface at the boundary is chosen. Otherwise, another approach ensures the smallest boundary surface is taken.
Performs the actual partitioning into tetrahedra and determines the boundary surfaces. It then returns a structure holding this data, as described in Table A.2.	

This procedure performs the actual partitioning, as described in the previous sections. Before the structure can be used, however, a few more parameters must be calculated, namely the polynomial coefficients according to Eq. (5.8) and the distance factors according to Eq. (5.11). To have this done, call the next procedure:

<code>FBPF.GenerateCoefficients</code> ,	<code>fname, RANDVAR=randvar</code>
<code>fname</code>	Name of the file that stores the result of the previous steps.
Optional Input	
<code>RANDVAR</code>	Set to a value to vary the coordinates by a random amount of this magnitude.
Calculates the coefficients for the polynomial, and the distance factors.	

The calculations are performed as described in the previous sections. The result will be saved in a file named according to the passed filename `fname` and the suffix `.coeffs.sav`. This file can then be used for the actual interpolation and calculation of spectra.

The previous process can be simplified by simply calling:

<code>FBPF.Setup</code> ,	<code>w, res</code>
<code>w</code>	An array of wavelength points the model spectra will be interpolated on.
<code>res</code>	The resolution the models will be degraded to.
A wrapper function that calls <code>FBPF.CreateBlock</code> and <code>FBPF.GenerateCoefficients</code> with default parameters.	

Calculating spectra

To calculate and create spectra using this method and an existing partition, some initialization is required. These routines rely heavily on a common block called `FBPF.Data`, which stores the required information regarding the tetrahedra, their positions, as well as the interpolation coefficients. Note that it is also possible to load the actual spectral data from the models. This has been included for debugging purposes, and can be removed from the code by removing the variable `fs` from the common block. This will heavily reduce the amount of memory needed, as well as the disk space required. To initialize, call:

FBPF_LoadBlock,	filename, RANDOM=random, WAVESCALE = wavescale
filename	Name of the file to load to initialize the common block FBPF_Data with.
Optional Input	
RANDOM	A random value that varies the tetrahedra's vertex positions (without changing the partitioning).
WAVESCALE	Set this to a named variable that will afterwards store the wavelength points corresponding to the model flux.
Initializes the common block for all subsequent calls to generate the spectra.	

filename is a required parameter, and the name of the file to load that will initialize the common block. It is possible, but not recommended, to pass a nonzero floating point value using the **RANDOM** keyword. It can be used to vary the tetrahedra's vertex positions (without changing the partitioning), for example to determine the changes in the interpolation that stem from the errors on the model's stellar parameters. However, in practice, varying these points by anything small compared to the step size does not affect the interpolation results by much². **wavescale** is an optional argument that may be passed as well. If set, the wavescale the models are calculated on is returned in this variable. If **FBPF_LoadBlock** is not called, any attempt to generate a spectrum will result in the warning to be displayed:

```
FBPF Common Block not loaded! Call FBPF_LoadBlock first!
```

With the block loaded, a spectrum can be generated using:

FBPF_GenerateSpectra,	teff, logg, met, vrot, CENTER=center, DEBUGPLOT=debugplot
teff	The value of T_{eff} for the model spectrum to calculate.
logg	The value of $\log g$ for the model spectrum to calculate.
met	The value of $[M/H]$ for the model spectrum to calculate.
vrot	The value of $v \sin i$ for the model spectrum to calculate.
Optional Input & Keywords	
CENTER	If set, this center wavelength will be used for the kernel determination for the rotational broadening. This also increases the speed greatly for the broadening, but will return wrong result across large wavelength regions.
DEBUGPLOT	If this keyword is set, plots for debugging purposes are generated.
Generates a spectrum with the given stellar parameters.	

The code will then automatically determine the point X corresponding to that set of stellar parameters, and attempt to find a tetrahedron that includes X . If found, it will use the coefficients determined for this tetrahedron's vertices to calculate the polynomial that ultimately returns the spectrum at X . If no such tetrahedron is found, it will call **FBPF_ExtrapolateSpectra**, which attempts to extrapolate using the method described in Sect. 5.3.6.

This function returns the spectrum, on the wavescale that **FBPF_LoadBlock** optionally returns, so a quick way to plot a spectrum in the Ca II IRT region is:

```
FBPF_LoadBlock,filename,WAVESCALE = wave
plot, wave, FBPF_GenerateSpectra(5700,4.4,0.0,2.2), &
  xtitle='wavelength', ytitle='flux', xr = [8490, 8560]
```

Of course, **filename** has to be replaced by the actual name of the file containing the partitioning data. In this work, this file is called:

```
GridTetraData_3500.0000-8999.9000A.sav_coeffs.sav .
```

This spectrum plotted is very solar like with parameters of $T_{\text{eff}}=5700$ K, $\log g=4.4$ and $[M/H]=0.0$, as well as being a slow rotator with a velocity of $v \sin i = 2.2 \text{ km s}^{-1}$. The resulting plot from these two lines is shown in Fig. A.1.

²In old versions of the code, problems occurred when tetrahedra were regular or the grid points arranged in a regular fashion. In that case, some of the required dot products would then become zero, but due to numerical inaccuracies a small non-zero value would be returned. In a similar vain, very small angles would also be determined incorrectly. Then, the code may determine a point to lie in a tetrahedron it did not lie in at all, resulting in wrong interpolation. This parameter can also help in such case, as it breaks the regular gridding, and avoids parallel surfaces.

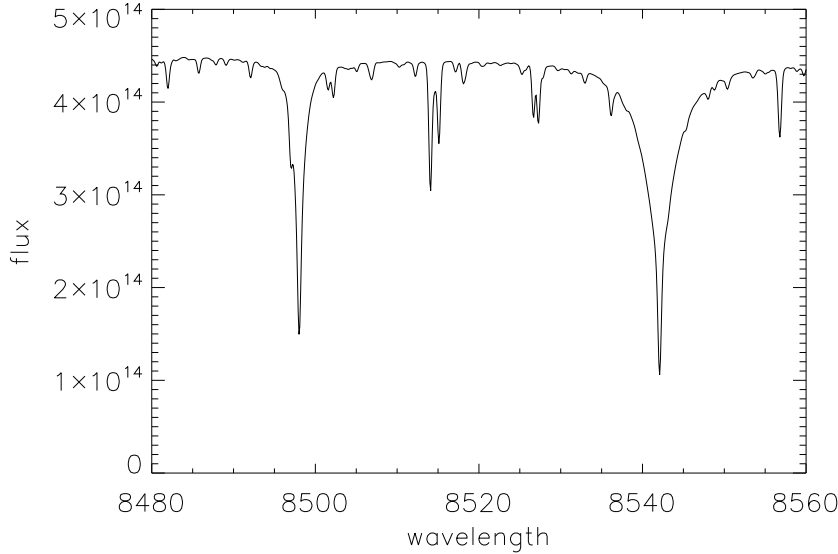


Figure A.1: **Simple Example of using this code.** Resulting plot from calling `FBPF_LoadBlock` and `FBPF_GenerateSpectra`, with additional settings for `chars` and `thick` to make this plot easier to read in the printed version.

A.3 Obtaining conversion relations

To obtain these relations, we have written code that takes as input the output of `get_correlation`, which is a procedure used to generate the correlation plots and distributions shown in Chapter 4 and Chapter 7. This routine saves the collected data in a subfolder `CorrelationsResult`. These files can directly be passed to `get_conversion`, which opens the file and performs the Monte-carlo iterations and subsequent fit according to the GS approach described above:

<code>get_conversion,</code>	<code>fname, bvstep, polydeg, NOB=nob, MLOG=mlog, MCIT = mcit, FLIP=flip, KEEPOUTLIERS=keepoutliers, NOTTHESE=notthese</code>
<code>fname</code>	File to load which holds the results of a previous call to <code>get_correlation</code> .
<code>bvstep</code>	Either an array of the $B - V$ -values used for the different segments, or a number that holds the step size for equidistant segmenting. Segments that no stars fall into are ignored.
<code>polydeg</code>	The order of the polynomials for the coefficients (as function of $B - V$).
Keywords & Optional Inputs	
<code>NOB</code>	If set, only a fit of $y = m(B - V) \cdot x$ is performed, with no intercept b .
<code>MLOG</code>	If set, not m is assumed to be polynomial in $B - V$, but rather $\log m$.
<code>MCIT</code>	Can be set to the number of iterations to be performed during the Monte Carlo process.
<code>FLIP</code>	Flips the two parameters from the <code>get_correlation</code> file, in order to find $x(y)$ instead of $y(x)$.
<code>KEEPOUTLIERS</code>	If set, no attempt is made to remove outliers or erroneous data from the fit in the segments.
<code>NOTTHESE</code>	Can be set to an array of <code>string</code> , holding the names of stars to ignore during the procedure.
<code>DEBUG</code>	Creates additional debugging plots.
Finds a conversion formula using the GS approach from output of <code>get_correlation</code> .	

On the other hand, `get_conversion_allatonce` performs the simpler linear regression. Its procedure cannot be customized as much. The signature of this procedure is explained in detail below:

<code>get_conversion.allatonce,</code>	<code>fname, polydeg, FLIP=flip, NOTTHESE=notthese</code>
<code>fname</code>	File to load which holds the results of a previous call to <code>get_correlation</code> .
<code>polydeg</code>	The order of the polynomials for the coefficients (as function of $B - V$).
Keywords & Optional Inputs	
<code>FLIP</code>	Flips the two parameters from the <code>get_correlation</code> file, in order to find $x(y)$ instead of $y(x)$.
<code>NOTTHESE</code>	Can be set to an array of <code>string</code> , holding the names of stars to ignore during the procedure.
Finds a conversion formula using the LR approach from output of <code>get_correlation</code> .	

Both of these procedures find and print the resulting relations to the terminal. Afterwards, a conversion using the same sample is performed, and various values from a comparison of these values to the original, measured ones are printed out. Among these is the residual value that 68% of residual values fall below, which we also give as an error. Another parameter printed is the “Relative deviation”, which is the median value of the residuals divided by the real value. We have given these two values for all conversion relations given. Additionally, the conversion results are plotted by these procedures. `get_conversion` additionally plots various other functions, most notably $m(B - V)$ and $b(B - V)$. If the `/DEBUG` keyword is set, then an additional file is created, which shows the fitted relation for each $B - V$ segment, and lists the stars used for it.

These procedures are ready to be used, in conjunction with `get_correlation`. They do not require much user input, and could therefore be used to automatically derive conversion relations from different large datasets, if combined with sensible segments (in `bvstep`), for the case of the GS approach. The simpler linear regression can always be used in this fashion.

A.4 Determining stellar parameters from TIGRE spectra and PHOENIX model spectra

Here, we describe the process of performing a fit using the method and interpolation stated above. First ensure that the common block is loaded using `FBPF_LoadBlock`. Then, call the following IDL function to perform a fit according to the Levenberg-Marquardt method:

<code>FindBestPhoenixFit_super,</code>	<code>wave, flux, err, Teff,logg,met,vrot, ERRORS=errors, REGIONS=regions, MASK=mask, NOPLOT=noplot, SILENT=silent, FITRESULT=fitresult, FITRESOL=fitresol, FITSHIFT=fitshift, NORMCORRECTION=normcorrection, OTHERP=otherp, OTHERE=othere, CHISQ=chisq, MPFITINFO=mpfitinfo, EXTRAVEL=extravel, IGNOREERRORS=ignoreerrors, FIXPARAMS=fixparams</code>
<code>wave</code>	An N -element array of wavelengths.
<code>flux</code>	An array of flux points. Must have N elements.
<code>err</code>	An array of errors on <code>flux</code> . Must have N elements.
<code>Teff, logg, met, vrot</code>	Named variables that hold the starting value for T_{eff} , $\log g$, $[M/H]$ and $v \sin i$ respectively, and which will hold the fitted value afterwards.
Optional Inputs	
<code>REGIONS</code>	Defines the region for the fit. See text.
<code>MASK</code>	Further defines the region for the fit. See text.
<code>FIXPARAMS</code>	Allows to fix (not fit) certain parameters. See text.
Optional Output	
<code>ERRORS</code>	This four-element array will hold the errors on the stellar parameters.
<code>OTHERP</code>	This array will hold the rest of the parameters fitted (see Table 6.3).
<code>OTHERE</code>	Same as <code>OTHERP</code> , but this array holds the error on the parameters.
<code>FITRESULT</code>	2-dimensional array that holds wavelength and flux of the fitted spectrum.
<code>CHISQ</code>	The χ^2_{ν} -value of the fit.
Keywords	
<code>NOPLOT</code>	If set, no plots to compare the fits are generated.
<code>SILENT</code>	If set, no output is given.
<code>FITRESOL</code>	If set, the resolution in each region is considered a parameter of the fit. Otherwise, the resolution is not fitted.
<code>FITSHIFT</code>	If set, a global wavelength shift is considered a parameter of the fit.
<code>NORMCORRECTION</code>	If set, a normalization correction is considered a parameter of the fit.
<code>MPFITINFO</code>	If set, the <code>/QUIET</code> -keyword for MPFit is suppressed.
<code>EXTRAVEL</code>	If set, an additional fit for just $v \sin i$ is performed after the main fit.
<code>IGNOREERRORS</code>	If set, no weighting according to <code>err</code> is performed.
Fits a spectrum using the Levenberg-Marquardt-approach.	

After this procedure is called, `Teff`, `logg`, `met` and `vrot` will store the best-fitted stellar parameters. If set, additional optional output is stored as well. If `regions` is not set, the two regions from 5100–5200 Å and 6100–6200 Å are fitted. If a different set of N regions should be fitted, pass an array with an even amount of datapoints of the form $[\lambda_{l,1}, \lambda_{u,1}, \dots, \lambda_{l,N}, \lambda_{u,N}]$, where $\lambda_{l,i}$ is the lower wavelength limit of the i -th region, and $\lambda_{u,i}$ the upper wavelength of the same region. The array to pass to `mask` follows the same structure, except that any wavelength point inside its region are ignored in the fit.

Afterwards, the code attempts to fit a number of parameters: 4 in any case, an additional one if `FITSHIFT` is set, additional N more if `FITRESOL` is set, and finally an additional $2N$ if `NORMCORRECTION` is set. For the full recommended set, $5 + 3N$ parameters are set. If desired, an array of 1's and 0's can be passed in `fixparams`. If it's i -th element is 1, then the corresponding parameter is fixed and not fitted. For example, if `fixparams[3]` is set to 1, then $v \sin i$ is fixed, whereas `fixparams[5] = 1` would fix the first normalization correction coefficient if `NORMCORRECTION` is set, or the resolution in the first region if `FITRESOL` is set and `NORMCORRECTION` is not set. The output given via `OTHERP` is following the same structure, i.e. it holds the two normalization correction coefficients of the first region if `NORMCORRECTION` is set, followed by one value for the resolution in the first region if `FITRESOL` is set, and then this set of three values for the second region, and so on. `EXTRAVEL` allows an additional fit for just $v \sin i$, which in many cases was not varied very much from

its starting value in this approach (see Fig. 6.5 and Fig. 6.7). However, tests indicate that this additional step is not enough to correct this wrong behaviour, and that this may very well be a systematic problem of the approach (Fig. 6.6).

To instead perform a fit using the MCMC approach:

<pre>FindBestPhoenixFit.mcmc, wave, flux, err, Teff, logg, Feh, vrot, ERRORS=errors, REGIONS=regions, MASK=mask, NOPLOT=noplot, SILENT=silent, FITRESULT=fitresult, FITRESOL=fitresol, FITSHIFT=fitshift, NORMCORRECTION=normcorrection, OTHERP=otherp, OTHERE=othere, V=v</pre>
See <code>FindBestPhoenixFit_super</code> for description on input & output.
Additional output
<code>V</code> A $[k,N]$ -element array that holds the N accepted values for parameter k (T_{eff} , $\log g$, ..., according to Table 6.3).
Fits a spectrum using the MCMC-approach.

The use of this procedure is almost identical, except for the use of `V`, which allows to store the trace by obtaining the list of accepted parameter values. For example, after the call, `V[0,*]` will hold the trace for the first parameter, T_{eff} . This procedure calls `mcmc.pro` by Zobitz et al. [2011] with the `/medium`-keyword, which was the best compromise of speed and accuracy. It calculates the result from 6 individual chains. By setting a different keyword to select a preset, or by passing different values for `numchains`, `numatonce`, etc. to `mcmc` (Line 164 of `FindBestPhoenixFit.mcmc`), this behaviour can be changed. Additionally, if desired, further conditions can be added into the likelihood estimator `fbpf_mcmclikelihood`.

Both these function call `fbpf_fitfuncpro`, which calculates, shifts, normalizes, broadens and degrades the model spectrum, and finally interpolates it to the correct wavelength scale.

For convenience sake, an additional wrapper `findestphoenixfit_wrapper` is provided, that can merge TI-GRE observation together until a target SNR is reached, and to then fit the result.

Appendix B

Additional Information, Figures and Tables

Chapter 4

In the following pages, we present the following tables:

- Stellar parameters for the active stars investigated in this work
- Stellar parameters for comparison stars
- List of comparison stars, and which stars were compared to them
- Relations to estimate the inactive line flux in the center of the Ca II H- & K-lines
- Relations to estimate the inactive line flux in the center of the H α -line

All of these tables are referred to and explained in the main text. We also give second-order polynomials, fitted to the results of the inactive line flux in the center of the Ca II H- & K-lines and the H α -line.

Table B.1: **Stellar parameters for the active stars investigated in this work.** Values missing were inferred from a fit to the values of other stars. References are numbered in superscript and correspond to the following sources: (1) Soubiran et al. [2010]; (2) Schröder et al. [2009]; (3) Martínez-Arnáiz et al. [2010]; (4) Marsden et al. [2014]; (5) Mishenina et al. [2012]; (6) Bernacca and Perinotto [1970]; (7) Ammler-von Eiff and Reiners [2012]; (8) Torres et al. [2006]; (9) White et al. [2007]; (10) Glebocki and Gnacinski [2005]; (11) Maldonado et al. [2012]; (12) Takeda et al. [2005]; (13) Torres et al. [2012]; (14) Uesugi and Fukuda [1970]; (15) McCarthy and Wilhelm [2014]; (16) Prugniel et al. [2011]; (17) Jenkins et al. [2011]

Name	<i>B-V</i>	log <i>g</i>	[Fe/H]	<i>v</i> sin <i>i</i>	Name	<i>B-V</i>	log <i>g</i>	[Fe/H]	<i>v</i> sin <i>i</i>
HD 88355	0.43 ⁽¹⁾	-	0.00 ⁽¹⁾	-	HD 75332	0.50 ⁽¹⁾	4.41 ⁽¹⁾	0.13 ⁽¹⁾	11.00 ⁽¹¹⁾
HD 25457	0.50 ⁽¹⁾	4.30 ⁽¹⁾	-0.03 ⁽¹⁾	20.24 ⁽³⁾	HD 179949	0.50 ⁽¹⁾	4.44 ⁽¹⁾	0.20 ⁽¹⁾	6.40 ⁽²⁾
HD 35296	0.52 ⁽¹⁾	4.28 ⁽¹⁾	-0.02 ⁽¹⁾	16.00 ⁽²⁾	HD 19019	0.52 ⁽¹⁾	4.00 ⁽¹⁾	-0.17 ⁽¹⁾	10.00 ⁽⁹⁾
HD 20367	0.52 ⁽¹⁾	4.46 ⁽¹⁾	0.13 ⁽¹⁾	-	HD 137107	0.55 ⁽¹⁾	4.22 ⁽¹⁾	-0.03 ⁽¹⁾	-
HD 100180	0.57 ⁽¹⁾	4.25 ⁽¹⁾	-0.06 ⁽¹⁾	3.59 ⁽³⁾	HD 150706	0.57 ⁽¹⁾	4.47 ⁽¹⁾	-0.03 ⁽¹⁾	10.00 ⁽⁹⁾
HD 154417	0.58 ⁽¹⁾	4.38 ⁽¹⁾	-0.01 ⁽¹⁾	8.00 ⁽³⁾	HD 206860	0.58 ⁽¹⁾	4.49 ⁽¹⁾	-0.08 ⁽¹⁾	12.81 ⁽³⁾
HD 209458	0.58 ⁽¹⁾	4.45 ⁽¹⁾	0.01 ⁽¹⁾	4.5 ⁽¹⁰⁾	HD 70573	0.59 ⁽¹⁾	4.58 ⁽¹⁾	-0.11 ⁽¹⁾	19.39 ± 4.00 ⁽⁹⁾
HD 114710	0.59 ⁽¹⁾	4.43 ⁽¹⁾	0.07 ⁽¹⁾	4.72 ⁽³⁾	HD 115383	0.59 ⁽¹⁾	4.25 ⁽¹⁾	0.13 ⁽¹⁾	7.20 ± 1.10 ⁽⁷⁾
HD 129333	0.59 ⁽¹⁾	4.47 ⁽¹⁾	0.16 ⁽¹⁾	22.01 ± 3.95 ⁽⁹⁾	HD 26913	0.60 ⁽¹⁾	4.49 ⁽¹⁾	-0.02 ⁽¹⁾	1.83 ⁽⁵⁾
HD 39587	0.60 ⁽¹⁾	4.45 ⁽¹⁾	-0.03 ⁽¹⁾	10.79 ⁽³⁾	HD 97334	0.61 ⁽¹⁾	4.35 ⁽¹⁾	0.06 ⁽¹⁾	7.74 ⁽³⁾
HD 75767	0.61 ⁽¹⁾	4.33 ⁽¹⁾	-0.04 ⁽¹⁾	4.00 ⁽⁴⁾	HD 165401	0.61 ⁽¹⁾	4.39 ⁽¹⁾	-0.41 ⁽¹⁾	13.90 ⁽³⁾
HD 190406	0.61 ⁽¹⁾	4.39 ⁽¹⁾	0.04 ⁽¹⁾	8.27 ⁽³⁾	HD 25680	0.62 ⁽¹⁾	4.52 ⁽¹⁾	0.05 ⁽¹⁾	3.20 ⁽⁵⁾
HD 72905	0.62 ⁽¹⁾	4.53 ⁽¹⁾	-0.08 ⁽¹⁾	11.21 ⁽³⁾	HD 197076	0.62 ⁽¹⁾	4.41 ⁽¹⁾	-0.11 ⁽¹⁾	10.22 ⁽⁹⁾
HD 126053	0.63 ⁽¹⁾	4.43 ⁽¹⁾	-0.38 ⁽¹⁾	3.08 ⁽³⁾	HD 181321	0.63 ⁽¹⁾	4.42 ⁽¹⁾	-0.01 ⁽¹⁾	13.00 ⁽⁸⁾
HD 30495	0.64 ⁽¹⁾	4.49 ⁽¹⁾	-0.01 ⁽¹⁾	3.57 ⁽⁵⁾	HD 38858	0.64 ⁽¹⁾	4.48 ⁽¹⁾	-0.22 ⁽¹⁾	2.61 ⁽³⁾
HD 71148	0.64 ⁽¹⁾	4.36 ⁽¹⁾	-0.00 ⁽¹⁾	12.37 ⁽³⁾	HD 146233	0.65 ⁽¹⁾	4.42 ⁽¹⁾	0.03 ⁽¹⁾	4.07 ⁽³⁾
HD 140538	0.65 ⁽¹⁾	4.47 ⁽¹⁾	0.05 ⁽¹⁾	11.01 ⁽³⁾	HD 159222	0.65 ⁽¹⁾	4.34 ⁽¹⁾	0.10 ⁽¹⁾	3.01 ⁽³⁾
HD 190771	0.65 ⁽¹⁾	4.41 ⁽¹⁾	0.14 ⁽¹⁾	4.20 ⁽⁵⁾	HD 20619	0.66 ⁽¹⁾	4.42 ⁽¹⁾	-0.24 ⁽¹⁾	3.20 ⁽³⁾
HD 28099	0.66 ⁽¹⁾	4.43 ⁽¹⁾	0.13 ⁽¹⁾	3.54 ⁽⁵⁾	HD 42618	0.66 ⁽¹⁾	4.46 ⁽¹⁾	-0.11 ⁽¹⁾	4.40 ⁽¹⁵⁾
HD 20630	0.67 ⁽¹⁾	4.49 ⁽¹⁾	0.06 ⁽¹⁾	5.86 ⁽³⁾	HD 43162	0.67 ⁽¹⁾	4.38 ⁽¹⁾	-0.05 ⁽¹⁾	9.63 ⁽³⁾
HD 73350	0.67 ⁽¹⁾	4.46 ⁽¹⁾	0.11 ⁽¹⁾	4.00 ⁽⁴⁾	HD 76151	0.67 ⁽¹⁾	4.46 ⁽¹⁾	0.08 ⁽¹⁾	3.58 ⁽³⁾
HD 145825	0.67 ⁽¹⁾	4.46 ⁽¹⁾	0.03 ⁽¹⁾	3.10 ± 1.20 ⁽⁸⁾	HD 224930	0.67 ⁽¹⁾	4.41 ⁽¹⁾	-0.77 ⁽¹⁾	4.07 ⁽³⁾
HD 42807	0.68 ⁽¹⁾	4.46 ⁽¹⁾	-0.03 ⁽¹⁾	3.80 ⁽⁵⁾	HD 6582	0.69 ⁽¹⁾	4.50 ⁽¹⁾	-0.80 ⁽¹⁾	4.17 ⁽³⁾
HD 10086	0.69 ⁽¹⁾	4.39 ⁽¹⁾	0.12 ⁽¹⁾	2.40 ⁽⁴⁾	HD 68017	0.69 ⁽¹⁾	4.46 ⁽¹⁾	-0.44 ⁽¹⁾	1.49 ⁽³⁾
HD 111395	0.69 ⁽¹⁾	4.54 ⁽¹⁾	0.10 ⁽¹⁾	2.60 ⁽⁵⁾	HD 101501	0.74 ⁽¹⁾	4.55 ⁽¹⁾	-0.07 ⁽¹⁾	3.26 ⁽³⁾
HD 103095	0.75 ⁽¹⁾	4.63 ⁽¹⁾	-1.34 ⁽¹⁾	9.28 ⁽³⁾	HD 184385	0.75 ⁽¹⁾	4.49 ⁽¹⁾	0.12 ⁽¹⁾	2.70 ⁽⁵⁾
HD 152391	0.76 ⁽¹⁾	4.47 ⁽¹⁾	-0.05 ⁽¹⁾	3.06 ⁽⁵⁾	HD 82443	0.77 ⁽¹⁾	4.45 ⁽¹⁾	-0.13 ⁽¹⁾	5.90 ⁽⁵⁾
HD 82885	0.77 ⁽¹⁾	4.49 ⁽¹⁾	0.32 ⁽¹⁾	7.22 ⁽³⁾	HD 131156A	0.77 ⁽¹⁾	4.54 ⁽¹⁾	-0.12 ⁽¹⁾	-
HD 149661	0.78 ⁽¹⁾	4.50 ⁽¹⁾	0.03 ⁽¹⁾	1.63 ⁽⁵⁾	HD 185144	0.78 ⁽¹⁾	4.49 ⁽¹⁾	-0.22 ⁽¹⁾	6.79 ⁽³⁾

Continued on next page

Table B.1 – Continued from previous page

Name	$B-V$	$\log g$	[Fe/H]	$v \sin i$	Name	$B-V$	$\log g$	[Fe/H]	$v \sin i$
HD 100623	0.81 ⁽¹⁾	4.60 ⁽¹⁾	-0.41 ⁽¹⁾	6.79 ⁽³⁾	HD 165341A	0.83 ⁽¹⁾	4.49 ⁽¹⁾	-0.04 ⁽¹⁾	16.00 ⁽¹¹⁾
HD 10476	0.84 ⁽¹⁾	4.45 ⁽¹⁾	-0.05 ⁽¹⁾	1.20 ⁽³⁾	HD 115404	0.85 ⁽¹⁾	4.45 ⁽¹⁾	-0.19 ⁽¹⁾	-
HD 17925	0.86 ⁽¹⁾	4.52 ⁽¹⁾	0.07 ⁽¹⁾	4.80 ⁽⁵⁾	HD 97658	0.86 ⁽¹⁾	4.49 ⁽¹⁾	-0.30 ⁽¹⁾	8.70 ⁽⁵⁾
HD 118972	0.86 ⁽¹⁾	4.36 ⁽¹⁾	-0.02 ⁽¹⁾	4.10 ± 1.20 ⁽⁸⁾	HD 166620	0.87 ⁽¹⁾	4.47 ⁽¹⁾	-0.17 ⁽¹⁾	4.82 ⁽³⁾
HD 75732	0.87 ⁽¹⁾	4.41 ⁽¹⁾	0.28 ⁽¹⁾	2.27 ⁽³⁾	HD 22049	0.88 ⁽¹⁾	4.53 ⁽¹⁾	-0.10 ⁽¹⁾	4.08 ⁽³⁾
HD 37394	0.90 ⁽¹⁾	4.51 ⁽¹⁾	0.08 ⁽¹⁾	2.80 ⁽⁵⁾	HD 4628	0.90 ⁽¹⁾	4.63 ⁽¹⁾	-0.27 ⁽¹⁾	1.50 ⁽⁵⁾
HD 145675	0.90 ⁽¹⁾	4.45 ⁽¹⁾	0.41 ⁽¹⁾	2.6 ⁽¹⁰⁾	HD 22468	0.92 ⁽¹⁾	-	-	-
HD 189733	0.93 ⁽¹⁾	4.49 ⁽¹⁾	-0.02 ⁽¹⁾	2.30 ⁽¹³⁾	HD 5133	0.94 ⁽¹⁾	4.66 ⁽¹⁾	-0.11 ⁽¹⁾	3.52 ⁽³⁾
HD 160346	0.96 ⁽¹⁾	4.46 ⁽¹⁾	-0.03 ⁽¹⁾	3.37 ⁽³⁾	HD 16160	0.98 ⁽¹⁾	4.54 ⁽¹⁾	-0.12 ⁽¹⁾	0.90 ⁽⁵⁾
HD 87883	0.99 ⁽¹⁾	4.47 ⁽¹⁾	0.05 ⁽¹⁾	1.20 ⁽³⁾	HD 32147	1.06 ⁽¹⁾	4.41 ⁽¹⁾	0.26 ⁽¹⁾	5.18 ⁽³⁾
HD 131977	1.11 ⁽¹⁾	4.35 ⁽¹⁾	-0.00 ⁽¹⁾	2.48 ⁽⁵⁾	HD 190007	1.12 ⁽¹⁾	4.38 ⁽¹⁾	0.16 ⁽¹⁾	2.55 ⁽⁵⁾
HD 156026	1.16 ⁽¹⁾	4.60 ⁽¹⁾	-0.20 ⁽¹⁾	4.40 ⁽²⁾	HD 201091	1.18 ⁽¹⁾	4.70 ⁽¹⁾	-0.38 ⁽¹⁶⁾	4.72 ⁽³⁾

Table B.2: Stellar parameters for the comparison stars used in this work. Same as Table B.1, but for the comparison stars.

Name	$B-V$	$\log g$	[Fe/H]	$v \sin i$	Name	$B-V$	$\log g$	[Fe/H]	$v \sin i$
HD 739	0.40 ⁽³⁾	4.27 ⁽³⁾	-0.09 ⁽³⁾	4.40 ⁽²⁾	HD 159332	0.45 ⁽³⁾	3.85 ⁽³⁾	-0.23 ⁽³⁾	5.00 ⁽⁶⁾
HD 216385	0.48 ⁽³⁾	3.95 ⁽³⁾	-0.29 ⁽³⁾	3.00 ⁽¹²⁾	HD 45067	0.53 ⁽³⁾	4.01 ⁽³⁾	-0.09 ⁽³⁾	5.00 ⁽⁶⁾
HD 187691	0.56 ⁽³⁾	4.26 ⁽³⁾	0.10 ⁽³⁾	3.00 ⁽¹²⁾	HD 100180	0.57 ⁽³⁾	4.25 ⁽³⁾	-0.06 ⁽³⁾	3.59 ⁽³⁾
HD 124570	0.58 ⁽³⁾	4.05 ⁽³⁾	0.08 ⁽³⁾	3.00 ⁽¹²⁾	HD 19373	0.59 ⁽³⁾	4.21 ⁽³⁾	0.08 ⁽³⁾	3.15 ⁽³⁾
HD 168009	0.60 ⁽³⁾	4.23 ⁽³⁾	-0.01 ⁽³⁾	3.00 ⁽¹²⁾	HD 10307	0.62 ⁽³⁾	4.32 ⁽³⁾	0.03 ⁽³⁾	4.07 ⁽³⁾
HD 34411	0.62 ⁽³⁾	4.22 ⁽³⁾	0.08 ⁽³⁾	3.15 ⁽³⁾	HD 95128	0.62 ⁽³⁾	4.30 ⁽³⁾	0.01 ⁽³⁾	3.15 ⁽³⁾
HD 157214	0.62 ⁽³⁾	4.31 ⁽³⁾	-0.40 ⁽³⁾	3.15 ⁽³⁾	HD 126053	0.63 ⁽³⁾	4.43 ⁽³⁾	-0.38 ⁽³⁾	3.08 ⁽³⁾
HD 38858	0.64 ⁽³⁾	4.48 ⁽³⁾	-0.22 ⁽³⁾	2.61 ⁽³⁾	HD 146233	0.65 ⁽³⁾	4.42 ⁽³⁾	0.03 ⁽³⁾	4.07 ⁽³⁾
HD 186427	0.65 ⁽³⁾	4.32 ⁽³⁾	0.07 ⁽³⁾	2.18 ± 0.50 ⁽⁴⁾	HD 12846	0.66 ⁽³⁾	4.38 ⁽³⁾	-0.26 ⁽³⁾	2.20 ⁽⁴⁾
HD 42618	0.66 ⁽³⁾	4.46 ⁽³⁾	-0.11 ⁽³⁾	4.40 ⁽¹⁵⁾	HD 43587	0.67 ⁽³⁾	4.29 ⁽³⁾	-0.04 ⁽³⁾	2.98 ⁽³⁾
HD 3795	0.70 ⁽³⁾	3.91 ⁽³⁾	-0.63 ⁽³⁾	1.70 ⁽¹⁷⁾	HD 115617	0.70 ⁽³⁾	4.39 ⁽³⁾	-0.01 ⁽³⁾	3.90 ± 0.90 ⁽⁷⁾
HD 178428	0.70 ⁽³⁾	4.25 ⁽³⁾	0.14 ⁽³⁾	1.50 ⁽⁵⁾	HD 117176	0.71 ⁽³⁾	3.97 ⁽³⁾	-0.06 ⁽³⁾	4.83 ⁽³⁾
HD 10700	0.72 ⁽³⁾	4.48 ⁽³⁾	-0.50 ⁽³⁾	1.60 ⁽¹⁷⁾	HD 26965	0.85 ⁽³⁾	4.51 ⁽³⁾	-0.27 ⁽³⁾	2.10 ⁽¹⁷⁾
HD 75732	0.87 ⁽³⁾	4.41 ⁽³⁾	0.28 ⁽³⁾	2.27 ⁽³⁾	HD 145675	0.90 ⁽³⁾	4.45 ⁽³⁾	0.41 ⁽³⁾	2.10 ⁽¹⁷⁾

Table B.3: **List of comparison stars and which stars were compared to them.**

Comparison	Stars compared to it
HD 739	HD 182101, HD 157856, HD 10032, HD 49933, HD 40136
HD 159332	HD 111456, HD 114378, HD 194012, HD 106516, HD 18256, HD 88355
HD 216385	HD 25998, HD 17206, HD 16673
HD 45067	HD 25457, HD 35296, HD 88737, HD 19019, HD 100563, HD 6920, HD 137107
HD 187691	HD 75332, HD 179949, HD 20367
HD 124570	HD 206860, HD 115043, HD 150706, HD 154417, HD 100180, HD 209458
HD 19373	HD 115383, HD 114710, HD 70573
HD 168009	HD 26913, HD 39587, HD 75767
HD 10307	HD 190406
HD 157214	HD 165401, HD 126053
HD 34411	HD 97334, HD 25680
HD 95128	HD 181321, HD 72905, HD 30495, HD 197076, HD 71148
HD 186427	HD 129333, HD 190771, HD 140538, HD 159222, HD 146233, HD 28099, HD 197027, HD 76151, HD 73350
HD 12846	HD 133640A, HD 38858, HD 20619, HD 42618
HD 43587	HD 43162, HD 42807, HD 145825, HD 20630
HD 115617	HD 131977, HD 149661
HD 178428	HD 111395, HD 75732, HD 184385, HD 82885, HD 145675, HD 10086
HD 3795	HD 224930, HD 6582
HD 117176	HD 82443, HD 152391, HD 101501, HD 131156A
HD 10700	HD 103095, HD 68017
HD 26965	HD 17925, HD 156026, HD 201091A, HD 118972, HD 22049, HD 201091, HD 115404, HD 165341A, HD 4628, HD 16160, HD 10476, HD 100623, HD 166620, HD 185144, HD 97658, HD 201092, HD 201091
HD 145675	HD 190007, HD 37394, HD 5133, HD 32147, HD 160346, HD 22468, HD 87883, HD 189733, HD 75732

Table B.4: **Relations to estimate the summed-up flux in a 2 Å-window in the center of both Ca II H- & K-lines for inactive objects.** v_{rot} must be entered in units of kms^{-1} . Values for $B - V$, $\log g$ and $[\text{Fe}/\text{H}]$ are taken from Soubiran et al. [2010].

Star	$B - V$	$\log g$	$[\text{Fe}/\text{H}]$	$\log R'_{\text{HK}}$	Estimated total flux in 2 \AA -bandpasses for the Ca II H- & K-lines in $10^6 \text{ erg s}^{-1} \text{ cm}^{-2}$	W_{HK} from normalized spectra in Å
HD739	0.40	4.27	-0.09	-4.91	$12.666 + 0.001 \cdot v_{\text{rot}} + 1.888 \cdot 10^{-4} \cdot v_{\text{rot}}^2$	$0.485 + 0.072 \cdot 10^{-4} \cdot v_{\text{rot}}^2$
HD159332	0.45	3.85	-0.23	-4.99	$9.501 + 1.503 \cdot 10^{-4} \cdot v_{\text{rot}}^2$	$0.452 + 0.071 \cdot 10^{-4} \cdot v_{\text{rot}}^2$
HD216385	0.48	3.95	-0.29	-4.98	$8.090 + 0.001 \cdot v_{\text{rot}} + 1.275 \cdot 10^{-4} \cdot v_{\text{rot}}^2$	$0.441 + 0.070 \cdot 10^{-4} \cdot v_{\text{rot}}^2$
HD45067	0.53	4.01	-0.09	-4.90	$6.385 + 1.132 \cdot 10^{-4} \cdot v_{\text{rot}}^2$	$0.438 + 0.078 \cdot 10^{-4} \cdot v_{\text{rot}}^2$
HD187691	0.56	4.26	+0.10	-4.89	$5.611 + 0.001 \cdot v_{\text{rot}} + 0.768 \cdot 10^{-4} \cdot v_{\text{rot}}^2$	$0.442 + 0.060 \cdot 10^{-4} \cdot v_{\text{rot}}^2$
HD100180	0.57	4.25	-0.06	-4.76	$5.698 + 0.002 \cdot v_{\text{rot}} + 0.580 \cdot 10^{-4} \cdot v_{\text{rot}}^2$	$0.470 + 0.048 \cdot 10^{-4} \cdot v_{\text{rot}}^2$
HD124570	0.58	4.05	+0.08	-5.05	$4.640 + * * * \cdot v_{\text{rot}} + 0.882 \cdot 10^{-4} \cdot v_{\text{rot}}^2$	$0.401 + 0.076 \cdot 10^{-4} \cdot v_{\text{rot}}^2$
HD19373	0.59	4.21	+0.08	-4.84	$4.928 + 0.748 \cdot 10^{-4} \cdot v_{\text{rot}}^2$	$0.445 + 0.068 \cdot 10^{-4} \cdot v_{\text{rot}}^2$
HD168009	0.60	4.23	-0.01	-4.77	$4.594 + 0.001 \cdot v_{\text{rot}} + 0.554 \cdot 10^{-4} \cdot v_{\text{rot}}^2$	$0.443 + 0.053 \cdot 10^{-4} \cdot v_{\text{rot}}^2$
HD10307	0.62	4.32	+0.03	-4.84	$4.286 + 0.001 \cdot v_{\text{rot}} + 0.599 \cdot 10^{-4} \cdot v_{\text{rot}}^2$	$0.445 + 0.062 \cdot 10^{-4} \cdot v_{\text{rot}}^2$
HD157214	0.62	4.31	-0.40	-4.80	$4.521 + 0.001 \cdot v_{\text{rot}} + 0.449 \cdot 10^{-4} \cdot v_{\text{rot}}^2$	$0.469 + 0.047 \cdot 10^{-4} \cdot v_{\text{rot}}^2$
HD34411	0.62	4.22	+0.08	-4.85	$3.957 + 0.634 \cdot 10^{-4} \cdot v_{\text{rot}}^2$	$0.410 + 0.066 \cdot 10^{-4} \cdot v_{\text{rot}}^2$
HD95128	0.62	4.30	+0.01	-4.85	$4.413 + 0.001 \cdot v_{\text{rot}} + 0.615 \cdot 10^{-4} \cdot v_{\text{rot}}^2$	$0.458 + 0.064 \cdot 10^{-4} \cdot v_{\text{rot}}^2$
HD126053	0.63	4.43	-0.38	-4.74	$4.587 + 0.001 \cdot v_{\text{rot}} + 0.438 \cdot 10^{-4} \cdot v_{\text{rot}}^2$	$0.498 + 0.048 \cdot 10^{-4} \cdot v_{\text{rot}}^2$
HD38858	0.64	4.48	-0.22	-4.79	$3.970 + 0.001 \cdot v_{\text{rot}} + 0.414 \cdot 10^{-4} \cdot v_{\text{rot}}^2$	$0.451 + 0.047 \cdot 10^{-4} \cdot v_{\text{rot}}^2$
HD146233	0.65	4.42	+0.03	-4.75	$4.050 + 0.001 \cdot v_{\text{rot}} + 0.469 \cdot 10^{-4} \cdot v_{\text{rot}}^2$	$0.482 + 0.056 \cdot 10^{-4} \cdot v_{\text{rot}}^2$
HD186427	0.65	4.32	+0.07	-4.80	$3.546 + 0.001 \cdot v_{\text{rot}} + 0.415 \cdot 10^{-4} \cdot v_{\text{rot}}^2$	$0.422 + 0.049 \cdot 10^{-4} \cdot v_{\text{rot}}^2$
HD12846	0.66	4.38	-0.26	-4.78	$3.761 + 0.001 \cdot v_{\text{rot}} + 0.386 \cdot 10^{-4} \cdot v_{\text{rot}}^2$	$0.462 + 0.047 \cdot 10^{-4} \cdot v_{\text{rot}}^2$
HD42618	0.66	4.46	-0.11	-4.74	$3.744 + 0.001 \cdot v_{\text{rot}} + 0.403 \cdot 10^{-4} \cdot v_{\text{rot}}^2$	$0.460 + 0.050 \cdot 10^{-4} \cdot v_{\text{rot}}^2$
HD43587	0.67	4.29	-0.04	-4.80	$3.769 + 0.001 \cdot v_{\text{rot}} + 0.482 \cdot 10^{-4} \cdot v_{\text{rot}}^2$	$0.485 + 0.062 \cdot 10^{-4} \cdot v_{\text{rot}}^2$
HD115617	0.70	4.39	-0.01	-4.80	$2.910 + 0.001 \cdot v_{\text{rot}} + 0.256 \cdot 10^{-4} \cdot v_{\text{rot}}^2$	$0.436 + 0.038 \cdot 10^{-4} \cdot v_{\text{rot}}^2$
HD178428	0.70	4.25	+0.14	-4.88	$2.581 + 0.001 \cdot v_{\text{rot}} + 0.358 \cdot 10^{-4} \cdot v_{\text{rot}}^2$	$0.387 + 0.054 \cdot 10^{-4} \cdot v_{\text{rot}}^2$
HD3795	0.70	3.91	-0.63	-4.83	$2.803 + 0.001 \cdot v_{\text{rot}} + 0.324 \cdot 10^{-4} \cdot v_{\text{rot}}^2$	$0.420 + 0.049 \cdot 10^{-4} \cdot v_{\text{rot}}^2$
HD117176	0.71	3.97	-0.06	-4.90	$2.373 + 0.001 \cdot v_{\text{rot}} + 0.293 \cdot 10^{-4} \cdot v_{\text{rot}}^2$	$0.372 + 0.046 \cdot 10^{-4} \cdot v_{\text{rot}}^2$
HD10700	0.72	4.48	-0.50	-4.75	$2.836 + 0.341 \cdot 10^{-4} \cdot v_{\text{rot}}^2$	$0.466 + 0.056 \cdot 10^{-4} \cdot v_{\text{rot}}^2$
HD26965	0.85	4.51	-0.27	-4.89	$1.406 + 0.158 \cdot 10^{-4} \cdot v_{\text{rot}}^2$	$0.425 + 0.048 \cdot 10^{-4} \cdot v_{\text{rot}}^2$
HD75732	0.87	4.41	+0.28	-4.84	$1.263 + 0.177 \cdot 10^{-4} \cdot v_{\text{rot}}^2$	$0.413 + 0.058 \cdot 10^{-4} \cdot v_{\text{rot}}^2$
HD145675	0.90	4.45	+0.41	-4.80	$1.111 + 0.119 \cdot 10^{-4} \cdot v_{\text{rot}}^2$	$0.417 + 0.045 \cdot 10^{-4} \cdot v_{\text{rot}}^2$

Table B.5: **Relations to estimate the summed up flux in an 1 Å-window in the center of the H α -line for inactive objects.** v_{rot} must be entered in units of km s^{-1} . Values for $B - V$, $\log g$ and $[\text{Fe}/\text{H}]$ are taken from Soubiran et al. [2010].

Star	$B - V$	$\log g$	$[\text{Fe}/\text{H}]$	Estimated total flux in 1 Å-bandpasses for the H α -line	
				$\log R'_{\text{HK}}$	W_{irr} from normalized spectra in Å
HD739	0.40	4.27	-0.09	$3.371 + 0.011 \cdot v_{\text{rot}} + 4.739 \cdot 10^{-4} v_{\text{rot}}^2$	$0.266 + 0.001 \cdot v_{\text{rot}} + 0.374 \cdot 10^{-4} v_{\text{rot}}^2$
HD159332	0.45	3.85	-0.23	$2.980 + 0.009 \cdot v_{\text{rot}} + 4.394 \cdot 10^{-4} v_{\text{rot}}^2$	$0.265 + 0.001 \cdot v_{\text{rot}} + 0.390 \cdot 10^{-4} v_{\text{rot}}^2$
HD216385	0.48	3.95	-0.29	$2.643 + 0.009 \cdot v_{\text{rot}} + 4.308 \cdot 10^{-4} v_{\text{rot}}^2$	$0.253 + 0.001 \cdot v_{\text{rot}} + 0.412 \cdot 10^{-4} v_{\text{rot}}^2$
HD45067	0.53	4.01	-0.09	$2.323 + 0.009 \cdot v_{\text{rot}} + 3.947 \cdot 10^{-4} v_{\text{rot}}^2$	$0.252 + 0.001 \cdot v_{\text{rot}} + 0.428 \cdot 10^{-4} v_{\text{rot}}^2$
HD187691	0.56	4.26	+0.10	$2.220 + 0.008 \cdot v_{\text{rot}} + 3.497 \cdot 10^{-4} v_{\text{rot}}^2$	$0.259 + 0.001 \cdot v_{\text{rot}} + 0.408 \cdot 10^{-4} v_{\text{rot}}^2$
HD100180	0.57	4.25	-0.06	$2.213 + 0.009 \cdot v_{\text{rot}} + 3.458 \cdot 10^{-4} v_{\text{rot}}^2$	$0.265 + 0.001 \cdot v_{\text{rot}} + 0.414 \cdot 10^{-4} v_{\text{rot}}^2$
HD124570	0.58	4.05	+0.08	$2.101 + 0.008 \cdot v_{\text{rot}} + 3.307 \cdot 10^{-4} v_{\text{rot}}^2$	$0.258 + 0.001 \cdot v_{\text{rot}} + 0.406 \cdot 10^{-4} v_{\text{rot}}^2$
HD19373	0.59	4.21	+0.08	$2.035 + 0.009 \cdot v_{\text{rot}} + 3.366 \cdot 10^{-4} v_{\text{rot}}^2$	$0.256 + 0.001 \cdot v_{\text{rot}} + 0.424 \cdot 10^{-4} v_{\text{rot}}^2$
HD168009	0.60	4.23	-0.01	$2.059 + 0.009 \cdot v_{\text{rot}} + 3.258 \cdot 10^{-4} v_{\text{rot}}^2$	$0.268 + 0.001 \cdot v_{\text{rot}} + 0.424 \cdot 10^{-4} v_{\text{rot}}^2$
HD10307	0.62	4.32	+0.03	$1.970 + 0.008 \cdot v_{\text{rot}} + 3.140 \cdot 10^{-4} v_{\text{rot}}^2$	$0.267 + 0.001 \cdot v_{\text{rot}} + 0.426 \cdot 10^{-4} v_{\text{rot}}^2$
HD157214	0.62	4.31	-0.40	$2.014 + 0.008 \cdot v_{\text{rot}} + 3.267 \cdot 10^{-4} v_{\text{rot}}^2$	$0.273 + 0.001 \cdot v_{\text{rot}} + 0.443 \cdot 10^{-4} v_{\text{rot}}^2$
HD34411	0.62	4.22	+0.08	$1.924 + 0.008 \cdot v_{\text{rot}} + 3.158 \cdot 10^{-4} v_{\text{rot}}^2$	$0.261 + 0.001 \cdot v_{\text{rot}} + 0.428 \cdot 10^{-4} v_{\text{rot}}^2$
HD95128	0.62	4.30	+0.01	$1.968 + 0.008 \cdot v_{\text{rot}} + 3.189 \cdot 10^{-4} v_{\text{rot}}^2$	$0.267 + 0.001 \cdot v_{\text{rot}} + 0.432 \cdot 10^{-4} v_{\text{rot}}^2$
HD126053	0.63	4.43	-0.38	$1.985 + 0.009 \cdot v_{\text{rot}} + 3.047 \cdot 10^{-4} v_{\text{rot}}^2$	$0.276 + 0.001 \cdot v_{\text{rot}} + 0.424 \cdot 10^{-4} v_{\text{rot}}^2$
HD38858	0.64	4.48	-0.22	$1.865 + 0.009 \cdot v_{\text{rot}} + 3.011 \cdot 10^{-4} v_{\text{rot}}^2$	$0.266 + 0.001 \cdot v_{\text{rot}} + 0.429 \cdot 10^{-4} v_{\text{rot}}^2$
HD146233	0.65	4.42	+0.03	$1.793 + 0.008 \cdot v_{\text{rot}} + 2.970 \cdot 10^{-4} v_{\text{rot}}^2$	$0.262 + 0.001 \cdot v_{\text{rot}} + 0.434 \cdot 10^{-4} v_{\text{rot}}^2$
HD186427	0.65	4.32	+0.07	$1.861 + 0.008 \cdot v_{\text{rot}} + 2.937 \cdot 10^{-4} v_{\text{rot}}^2$	$0.272 + 0.001 \cdot v_{\text{rot}} + 0.429 \cdot 10^{-4} v_{\text{rot}}^2$
HD12846	0.66	4.38	-0.26	$1.868 + 0.007 \cdot v_{\text{rot}} + 2.933 \cdot 10^{-4} v_{\text{rot}}^2$	$0.278 + 0.001 \cdot v_{\text{rot}} + 0.436 \cdot 10^{-4} v_{\text{rot}}^2$
HD42618	0.66	4.46	-0.11	$1.827 + 0.008 \cdot v_{\text{rot}} + 2.868 \cdot 10^{-4} v_{\text{rot}}^2$	$0.272 + 0.001 \cdot v_{\text{rot}} + 0.426 \cdot 10^{-4} v_{\text{rot}}^2$
HD43587	0.67	4.29	-0.04	$1.758 + 0.007 \cdot v_{\text{rot}} + 2.778 \cdot 10^{-4} v_{\text{rot}}^2$	$0.268 + 0.001 \cdot v_{\text{rot}} + 0.423 \cdot 10^{-4} v_{\text{rot}}^2$
HD115617	0.70	4.39	-0.01	$1.698 + 0.007 \cdot v_{\text{rot}} + 2.702 \cdot 10^{-4} v_{\text{rot}}^2$	$0.281 + 0.001 \cdot v_{\text{rot}} + 0.447 \cdot 10^{-4} v_{\text{rot}}^2$
HD178428	0.70	4.25	+0.14	$1.595 + 0.008 \cdot v_{\text{rot}} + 2.664 \cdot 10^{-4} v_{\text{rot}}^2$	$0.264 + 0.001 \cdot v_{\text{rot}} + 0.441 \cdot 10^{-4} v_{\text{rot}}^2$
HD3795	0.70	3.91	-0.63	$1.624 + 0.008 \cdot v_{\text{rot}} + 2.773 \cdot 10^{-4} v_{\text{rot}}^2$	$0.269 + 0.001 \cdot v_{\text{rot}} + 0.459 \cdot 10^{-4} v_{\text{rot}}^2$
HD117176	0.71	3.97	-0.06	$1.579 + 0.007 \cdot v_{\text{rot}} + 2.730 \cdot 10^{-4} v_{\text{rot}}^2$	$0.268 + 0.001 \cdot v_{\text{rot}} + 0.463 \cdot 10^{-4} v_{\text{rot}}^2$
HD10700	0.72	4.48	-0.50	$1.670 + 0.008 \cdot v_{\text{rot}} + 2.511 \cdot 10^{-4} v_{\text{rot}}^2$	$0.290 + 0.001 \cdot v_{\text{rot}} + 0.437 \cdot 10^{-4} v_{\text{rot}}^2$
HD26965	0.85	4.51	-0.27	$1.293 + 0.006 \cdot v_{\text{rot}} + 1.893 \cdot 10^{-4} v_{\text{rot}}^2$	$0.313 + 0.001 \cdot v_{\text{rot}} + 0.459 \cdot 10^{-4} v_{\text{rot}}^2$
HD75732	0.87	4.41	+0.28	$1.095 + 0.005 \cdot v_{\text{rot}} + 1.765 \cdot 10^{-4} v_{\text{rot}}^2$	$0.277 + 0.001 \cdot v_{\text{rot}} + 0.446 \cdot 10^{-4} v_{\text{rot}}^2$
HD145675	0.90	4.45	+0.41	$1.154 + 0.005 \cdot v_{\text{rot}} + 1.687 \cdot 10^{-4} v_{\text{rot}}^2$	$0.314 + 0.001 \cdot v_{\text{rot}} + 0.459 \cdot 10^{-4} v_{\text{rot}}^2$

We can fit a three-dimensional, second-order polynomial to the results of the inactive line flux in the Ca II H- & K-lines and H α -line, just like we did before. As described in the main text, the line flux is estimated in a 2 Å-bandpass for the Ca II H- & K-lines. The results for the flux in $\text{erg s}^{-1} \text{cm}^{-2}$ are:

$$\begin{aligned}
F_{\text{inact,H\&K}}(B - V, [\text{M}/\text{H}], v \sin i) &= 38.373 - & (\text{B.1}) \\
&86.775(B - V) - 0.699[\text{M}/\text{H}] + \\
&0.012v \sin i + 51.228(B - V)^2 - \\
&1.170[\text{M}/\text{H}]^2 + 5.950 \cdot 10^{-5}v \sin i^2 - \\
&0.397(B - V)[\text{M}/\text{H}] - 0.017(B - V)v \sin i + \\
&0.683 \cdot 10^{-3}[\text{M}/\text{H}]v \sin i,
\end{aligned}$$

$$\begin{aligned}
F_{\text{inact,H}\alpha}(B - V, [\text{M}/\text{H}], v \sin i) &= 7.554 - & (\text{B.2}) \\
&13.694(B - V) - 0.087[\text{M}/\text{H}] + \\
&0.034v \sin i + 7.490(B - V)^2 - \\
&0.167[\text{M}/\text{H}]^2 + 3.082 \cdot 10^{-4}v \sin i^2 - \\
&0.391(B - V)[\text{M}/\text{H}] - 0.041(B - V)v \sin i - \\
&0.654 \cdot 10^{-3}[\text{M}/\text{H}]v \sin i,
\end{aligned}$$

and for the line flux in continuum units:

$$\begin{aligned}
W_{\text{inact,H\&K}}(B - V, [\text{M}/\text{H}], v \sin i) &= 0.421 + & (\text{B.3}) \\
&0.092(B - V) - 0.280[\text{M}/\text{H}] + \\
&0.246 \cdot 10^{-3}v \sin i - 0.095(B - V)^2 - \\
&0.105[\text{M}/\text{H}]^2 + 0.567 \cdot 10^{-5}v \sin i^2 + \\
&0.295(B - V)[\text{M}/\text{H}] - 0.254 \cdot 10^{-3}(B - V)v \sin i + \\
&0.233 \cdot 10^{-4}[\text{M}/\text{H}]v \sin i,
\end{aligned}$$

$$\begin{aligned}
W_{\text{inact,H}\alpha}(B - V, [\text{M}/\text{H}], v \sin i) &= 0.338 - & (\text{B.4}) \\
&0.317(B - V) + 0.021[\text{M}/\text{H}] - \\
&0.193 \cdot 10^{-3}v \sin i + 0.323(B - V)^2 - \\
&0.022[\text{M}/\text{H}]^2 + 4.294 \cdot 10^{-5}v \sin i^2 - \\
&0.062(B - V)[\text{M}/\text{H}] + 2.009 \cdot 10^{-3}(B - V)v \sin i - \\
&2.417 \cdot 10^{-4}[\text{M}/\text{H}]v \sin i.
\end{aligned}$$

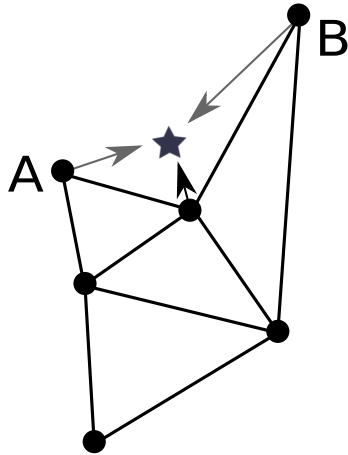


Figure B.1: **Unnecessary extrapolation in then two-dimensional case of a concave partitioning shape.** If the desired position (star) falls outside the partitioning structure, the result will be extrapolated from the known data (points). However, in this particular case of a concave shape, it is unclear whether to use the information from point *A* or point *B*. In fact, here the correct choice would be an interpolation (three arrows). Had the partitioning be continued to ensure a convex shape, an additional triangle connecting the points *A* and *B*, enclosing the position, would exist, and the algorithm would correctly interpolate the result.

Chapter 6

In the following pages, we present the following tables:

- Complete mask in use for the fit to determine stellar parameters (Complete version from Table 6.2)
- Complete results of the various fitting procedures (Levenberg-Marquardt, MCMC)

We then proceed to shortly describe the procedure where the Levenberg-Marquardt-method was used to finalize the result of the MCMC approach, including a table of the results. However, we first give the reason why it is important for the tetrahedra structure to be convex, and how to achieve this if it is not.

Guaranteeing a convex shape

Using the method described above, the structure made up of the tetrahedra is always convex. However, it is of use to create an additional function that takes a partitioning with a concave shape, and adds tetrahedra until the structure is convex. This is useful for instance when manually adding tetrahedra to an existing structure, for example after adding another point to the set. The requirement for a convex shape is necessary as any point *X* that falls inside the tetrahedra structure can then be assigned to a tetrahedron in the structure generated with the algorithm described. The vertices of a boundary surface of the structure are used when extrapolating a spectrum. In case of a concave shape, it is possible to find a point that is not included in any tetrahedron of the structure, even though it would be possible to define a suitable one that includes this point. The equivalent case in two dimensions is shown in Fig. B.1. The algorithm iterates through all tetrahedra surfaces that are not yet shared between two tetrahedra, and looks for those that share either an edge or a point. If they share an edge, the total of four points (two surfaces with three vertices each, but both share two of them, so each surface features one more vertex for a total of four) are checked to see that a tetrahedron formed from this does not intersect with any existing ones. If they share a point, two tetrahedra could be formed: The two surfaces each have three vertices, but one of those is shared, so a total of five vertices must be taken into account. Connecting the three points of the first surface with either unshared vertex from the second results in a tetrahedron, so two tetrahedra in total. These are, again, checked to not intersect any existing ones. Of all the possible tetrahedra found in this fashion, the one with the smallest volume is then added to the structure and the cycle begins anew.

Additional Tables

Table B.6: **Masks in use to ignore certain regions in the fit.** The regions given here are ignored in our fit, as the model shows different behaviour here than the observed spectra, e.g. due to wrong line profiles.

Mask region			
5117.16 – 5117.56	5117.89 – 5118.02	5120.94 – 5121.14	5123.39 – 5124.32
5124.52 – 5124.85	5125.44 – 5125.77	5126.17 – 5127.81	5130.24 – 5130.65
5132.60 – 5132.81	5135.85 – 5136.20	5140.68 – 5140.89	5142.06 – 5142.26
5142.88 – 5143.23	5146.04 – 5146.24	5150.68 – 5151.29	5151.70 – 5152.04
5152.31 – 5152.51	5153.53 – 5153.67	5154.28 – 5154.35	5154.96 – 5155.16
5155.50 – 5155.57	5159.35 – 5159.56	5159.82 – 5160.09	5162.59 – 5162.72
5163.46 – 5163.53	5163.86 – 5164.06	5166.48 – 5166.81	5168.28 – 5168.48
5169.28 – 5169.42	5169.68 – 5169.82	5170.62 – 5170.88	5171.22 – 5171.48
5174.01 – 5174.54	5176.38 – 5177.30	5178.56 – 5179.12	5179.96 – 5180.24
5181.29 – 5181.43	5181.85 – 5182.06	5184.91 – 5185.12	5187.76 – 5188.04
5188.25 – 5188.32	5188.74 – 5189.08	5189.36 – 5189.64	5189.85 – 5190.19
5190.75 – 5190.81	5191.71 – 5192.06	5194.54 – 5195.23	5195.37 – 5195.99
5197.85 – 5198.05	5199.08 – 5199.29	5199.84 – 5199.91	5100.62 – 5101.34
5102.41 – 5102.85	5103.61 – 5104.76	5111.01 – 5112.85	5113.92 – 5114.77
5115.56 – 5116.46	5129.08 – 5129.91	5131.39 – 5132.12	5134.17 – 5134.98
5143.40 – 5144.03	5144.77 – 5145.71	5146.79 – 5147.86	5148.45 – 5149.17
5149.70 – 5150.38	5156.89 – 5158.13	5175.00 – 5175.56	5177.71 – 5178.37
6103.60 – 6103.75	6106.45 – 6106.67	6107.12 – 6107.49	6112.83 – 6113.13
6120.88 – 6121.12	6131.49 – 6131.97	6142.29 – 6142.69	6144.88 – 6145.50
6159.21 – 6159.59	6189.22 – 6189.55	6104.90 – 6105.49	6123.93 – 6125.44
6125.86 – 6126.62	6128.62 – 6130.61	6133.32 – 6134.36	6145.91 – 6146.69
6157.40 – 6158.24	6156.59 – 6157.14	6154.83 – 6156.36	6163.06 – 6165.75
6166.60 – 6167.14	6183.11 – 6184.07	6185.30 – 6186.53	6189.90 – 6192.63
6194.73 – 6195.37	6195.98 – 6196.90	6199.00 – 6199.45	6523.41 – 6524.05
6527.07 – 6527.39	6538.77 – 6539.20	6543.67 – 6544.10	6549.66 – 6550.59
6551.36 – 6551.70	6552.47 – 6552.81	6553.23 – 6553.49	6556.03 – 6556.88
6557.56 – 6557.81	6558.74 – 6560.18	6564.81 – 6568.58	6569.00 – 6569.41
6569.67 – 6570.25	6561.70 – 6563.90	6530.43 – 6533.42	6536.27 – 6538.09
6540.99 – 6542.95	6546.06 – 6546.42	6546.60 – 6549.24	6571.58 – 6573.63
6577.40 – 6577.97	6561.50 – 6564.50	7746.07 – 7746.65	7758.68 – 7758.68
7758.55 – 7760.06	7796.78 – 7796.78	7796.78 – 7796.78	7798.60 – 7799.71
7799.98 – 7801.16	7810.21 – 7812.04	7816.20 – 7817.01	7821.27 – 7822.25
7826.06 – 7827.47	7832.94 – 7834.09	7837.48 – 7838.65	8519.55 – 8519.77
8496.90 – 8499.10	8481.45 – 8482.53	8485.15 – 8487.60	8490.88 – 8494.59
8501.08 – 8503.78	8504.56 – 8508.06	8509.05 – 8516.76	8517.72 – 8519.00
8553.76 – 8556.51	8557.04 – 8557.35	8635.97 – 8636.31	8540.90 – 8543.10
8534.12 – 8538.53	8525.56 – 8528.61	8560.97 – 8563.81	8580.88 – 8587.09
8603.41 – 8605.68	8609.65 – 8617.16	8625.24 – 8626.39	8630.52 – 8631.84
8621.05 – 8623.39	8637.35 – 8639.91	8642.95 – 8644.16	8646.53 – 8647.41

Table B.7: **Result of the Levenberg-Marquardt-Fit, with starting parameters searched from a grid search.** The fit has been performed as described in the text, with the regions and masked given in Table 6.1 and Table 6.2. Other parameters have been fitted that are not shown here, such as resolution and a wavelength shift, see Table 6.3. If no error is given, the statistical error has been determined to be less than the step size in the grid, or unrealistic in the case of $v \sin i$, and should then be considered to be 50 K for T_{eff} , 0.10 for $\log g$, 0.12 for $[M/H]$ and 1 km s^{-1} for $v \sin i$.

Object	T_{eff} in K	$\log g$	$[M/H]$	$v \sin i$ in km s^{-1}	Object	T_{eff} in K	$\log g$	$[M/H]$	$v \sin i$ in km s^{-1}
HD157214	5491	4.36	-0.38	8.5	HD168009	5499	4.00	-0.00	3.8
HD129333	5520	3.80	+0.00	14.4	HD184385	5570	4.56	+0.12	3.3
HD178428	5570	4.04	+0.12	3.5	HD43162	5600	4.54	+0.00	8.7
HD82885	5602	4.59	+0.33	5.5	HD111395	5603	4.55	+0.07	3.1
HD68017	5609	4.41	-0.27	9.6	HD42807	5620	4.38	-0.01	9.0
HD115617	5621	4.51	-0.00	3.4	HD140538	5629	4.45	+0.01	5.4
HD117176	5650	3.98	-0.03	3.1	HD20619	5674	4.45	-0.22	3.5
HD20630	5675	4.54	+0.01	5.5	HD115043	5684	4.31	-0.16	5.2
HD26913	5687	4.56	-0.01	8.9	HD86728	5688	4.16	+0.19	3.1
HD1461	5689	4.17	+0.20	3.2	HD73350	5700	4.38	+0.11	3.8
HD75767	5700	4.39	-0.00	8.8	HD10086	5705	4.52	+0.09	3.3
HD38858	5710	4.39	-0.22	2.7	HD89269	5712	4.47	-0.12	3.6
HD12846	5718	4.30	-0.22	3.6	HD126053	5737	4.34	-0.31	3.4
HD159222	5750	4.32	+0.11	3.3	HD190771	5756	4.58	+0.12	3.6
HD165401	5765	4.12	-0.33	1.2	HD30495	5780	4.58	-0.01	3.5
HD186427	5782	4.32	+0.10	3.3	HD106116	5784	4.33	+0.19	3.3
HD76151	5788	4.52	+0.11	3.7	HD19373	5795	4.20	+0.12	2.7
HD42618	5796	4.44	-0.10	3.6	HD150706	5800	4.40	+0.00	9.5
HD43587	5804	4.38	-0.00	8.3	HD75528	5810	3.84	+0.18	5.1
HD186408	5815	4.30	+0.10	5.3	HD95128	5828	4.29	+0.09	8.8
HD92719	5840	4.37	-0.03	9.5	HD28099	5842	4.40	+0.30	3.5
HD197027	5843	4.37	+0.05	3.2	HD25680	5847	4.59	+0.10	3.6
HD145825	5855	4.57	+0.10	3.4	HD196850	5858	4.32	-0.03	9.5
HD72905	5865	4.58	-0.01	10.3	HD197076	5869	4.54	-0.02	9.9
HD79028	5870	4.14	+0.01	5.4	HD32923	5882	4.29	-0.02	9.7
HD146233	5886	4.56	+0.08	3.5	HD70573	5894	4.44	+0.11	14.4
HD133640A	5900	4.60	-0.38	11.7	HD19019	5900	4.40	-0.12	9.6
HD181321	5912	4.45	+0.09	13.5	HD41330	5919	4.12	-0.13	5.2
HD107213	5959	3.88	+0.19	3.0	HD34411	5961	4.31	+0.13	9.9
HD71148	5967	4.52	+0.10	3.0	HD39587	5973	4.58	-0.00	10.2
HD45067	5976	3.96	-0.02	9.9	HD90508	5988	4.42	-0.14	9.6
HD143761	5995	4.49	-0.11	2.5	HD142373	5997	4.25	-0.36	2.9
HD216385	5999	4.00	-0.25	2.5	HD10307	6000	4.52	+0.10	3.3
HD154417	6003	4.59	-0.00	2.7	HD20367	6004	4.59	+0.12	2.5
HD50692	6004	4.47	-0.11	3.1	HD124570	6008	3.85	+0.06	1.2
HD206860	6010	4.60	+0.00	10.2	HD89744	6014	4.00	+0.12	10.5
HD97334	6018	4.60	+0.13	2.9	HD190406	6020	4.59	+0.12	2.7
HD88737	6051	3.85	+0.22	2.6	HD9826	6060	4.01	+0.10	10.3
HD209458	6065	4.54	-0.00	2.9	HD100180	6066	4.57	+0.00	3.7
HD114710	6074	4.53	+0.09	3.7	HD6920	6082	3.82	+0.10	9.0
HD137107	6101	4.60	-0.00	10.0	HD115383	6134	4.53	+0.14	5.4
HD106516	6152	4.57	-0.51	8.6	HD159332	6153	3.93	-0.12	10.2
HD194012	6179	4.22	-0.12	9.5	HD187691	6181	4.34	+0.22	3.6
HD100563	6182	4.17	+0.10	17.5	HD75332	6204	4.37	+0.11	10.4
HD35296	6206	4.40	+0.09	15.5	HD182101	6206	4.19	-0.02	14.4
HD16673	6222	4.35	+0.00	10.1	HD179949	6227	4.59	+0.13	5.7
HD111456	6229	4.60	-0.12	41.3	HD58855	6240	4.31	-0.25	10.7
HD25457	6255	4.42	+0.11	19.1	HD88355	6278	4.10	-0.02	18.1
HD84117	6308	4.53	-0.00	5.4	HD18256	6340	4.03	-0.01	19.2
HD76572	6359	3.85	-0.12	5.4	HD72945	6375	4.56	+0.12	5.2
HD25998	6400	4.60	+0.25	16.1	HD114378	6476	4.56	-0.13	20.0
HD157856	6477	4.03	-0.02	15.2	HD17206	6510	4.61	+0.12	23.6
HD160915	6616	4.59	-0.01	12.2					

Table B.8: **Result of the MCMC-Fit.** The fit has been performed as described in the text, with the regions and masked given in Table 6.1 and Table 6.2. Other parameters have been fitted that are not shown here, such as resolution and a wavelength shift, see Table 6.3. If no error is given, the statistical error has been determined to be less than the step size in the grid, or unrealistic in the case of $v \sin i$, and should then be considered to be 50 K for T_{eff} , 0.10 for $\log g$, 0.12 for [M/H] and 1 km s^{-1} for $v \sin i$.

Object	T_{eff} in K	$\log g$	[M/H]	$v \sin i$ in km s^{-1}	Object	T_{eff} in K	$\log g$	[M/H]	$v \sin i$ in km s^{-1}
HD82443	5398	4.60	+0.00	5.2	HD145675	5411	4.60	+0.49	1.8
HD152391	5454	4.60	-0.03	3.1	HD131156A	5467	4.60	-0.14	2.9
HD3795	5477	4.46	-0.47	0.7	HD117176	5489	4.10	-0.10	2.8 ± 1.99
HD101501	5501	4.60	-0.08	3.5	HD178428	5524	4.22	+0.07	0.7
HD82885	5525	4.61	+0.28	3.3	HD115617	5549	4.60	-0.06	2.8 ± 2.42
HD68017	5569	4.72	-0.36	0.8	HD224930	5571	4.87	-0.57	3.1
HD10700	5571	4.90	-0.27	0.6	HD6582	5571	4.90	-0.48	3.4
HD184385	5579	4.69	+0.09	2.9	HD106116	5587	4.40	+0.07	1.2
HD43162	5601	4.65	-0.06	3.0	HD140538	5628	4.59	-0.02	5.2
HD111395	5631	4.67	+0.03	1.4 ± 1.30	HD42618	5638	4.44	-0.17	0.3 ± 1.19
HD186427	5642	4.36	-0.02	1.3	HD20630	5647	4.52	-0.01	5.2
HD42807	5650	4.53	-0.09	0.2 ± 1.50	HD32923	5650	4.24	-0.18	5.2
HD197027	5653	4.41	-0.08	2.3	HD1461	5661	4.36	+0.14	2.2 ± 1.70
HD168009	5665	4.30	-0.08	1.3 ± 1.03	HD129333	5672	4.49	-0.12	13.7
HD89269	5673	4.67	-0.17	0.5 ± 1.06	HD75528	5678	3.91	+0.06	3.0
HD26913	5684	4.66	-0.10	3.5	HD157214	5686	4.61	-0.32	3.1
HD38858	5696	4.60	-0.24	2.9	HD75767	5697	4.43	-0.14	1.7 ± 1.27
HD86728	5701	4.44	+0.15	1.3	HD76151	5701	4.52	+0.05	3.4
HD28099	5704	4.47	+0.12	1.6 ± 1.25	HD126053	5717	4.73	-0.32	3.1
HD90508	5720	4.53	-0.32	5.2	HD143761	5731	4.38	-0.24	2.6
HD186408	5740	4.38	+0.02	3.0	HD73350	5746	4.55	+0.03	3.4
HD145825	5747	4.54	-0.00	2.8	HD146233	5758	4.54	-0.01	3.4
HD190771	5768	4.60	+0.07	2.9	HD10086	5769	4.66	+0.11	0.6
HD20619	5774	4.72	-0.17	1.3	HD12846	5774	4.72	-0.20	0.6
HD159222	5774	4.47	+0.07	3.1	HD142373	5775	4.20	-0.48	0.2 ± 1.34
HD41330	5777	4.30	-0.22	3.0	HD25680	5779	4.53	-0.01	1.4 ± 1.10
HD30495	5782	4.60	-0.05	1.5 ± 1.19	HD92719	5783	4.64	-0.14	5.2
HD71148	5791	4.49	-0.05	7.7	HD197076	5791	4.61	-0.14	5.2
HD70573	5794	4.57	-0.11	13.7	HD196850	5797	4.49	-0.12	5.2
HD165401	5811	4.80	-0.35	2.5	HD72905	5838	4.63	-0.10	5.2
HD133640A	5840	4.54	-0.51	9.1	HD190406	5847	4.44	-0.02	7.7
HD97334	5847	4.49	+0.03	7.6	HD43587	5848	4.38	-0.06	3.0
HD95128	5849	4.44	-0.00	1.5 ± 1.18	HD10307	5849	4.46	+0.01	2.7
HD34411	5853	4.41	+0.05	3.3	HD50692	5862	4.51	-0.19	1.1
HD181321	5872	4.60	-0.07	13.5	HD79028	5873	4.21	-0.01	5.2
HD206860	5874	4.51	-0.12	7.7	HD45067	5885	4.03	-0.15	3.9
HD39587	5896	4.60	-0.09	5.2	HD150706	5897	4.59	-0.08	3.0
HD19373	5900	4.31	+0.06	3.2	HD100180	5902	4.44	-0.08	3.2
HD114710	5910	4.46	-0.04	1.6 ± 1.27	HD154417	5927	4.46	-0.06	2.5
HD115383	5929	4.39	+0.06	4.0	HD137107	5933	4.46	-0.10	12.1
HD187691	5940	4.22	+0.02	0.3 ± 1.16	HD209458	5947	4.42	-0.08	2.2 ± 1.84
HD20367	5948	4.43	-0.02	1.4 ± 1.08	HD6920	5952	3.93	-0.04	2.3
HD75332	5959	4.28	-0.08	9.0	HD19019	5963	4.45	-0.16	5.2
HD84117	5981	4.26	-0.15	4.0	HD115043	5982	4.77	-0.05	2.6
HD124570	6015	3.99	+0.03	3.5	HD88737	6035	3.93	+0.14	2.5
HD89744	6037	3.98	+0.08	5.2	HD194012	6050	4.28	-0.20	5.1
HD107213	6050	3.98	+0.11	7.6	HD9826	6061	4.23	+0.03	5.2
HD179949	6065	4.42	+0.06	3.0	HD35296	6081	4.50	-0.08	14.8
HD159332	6093	3.91	-0.18	5.0	HD72945	6109	4.33	-0.01	5.2
HD16673	6138	4.46	-0.09	2.3 ± 1.90	HD216385	6141	4.07	-0.21	1.4 ± 1.08
HD25998	6155	4.46	+0.04	15.6	HD25457	6165	4.51	-0.02	17.4
HD111456	6191	4.48	-0.25	41.8	HD76572	6204	3.88	-0.20	3.0
HD58855	6207	4.36	-0.31	5.2	HD114378	6218	4.39	-0.29	19.8
HD88355	6222	4.17	-0.09	17.4	HD18256	6222	4.07	-0.15	15.6
HD157856	6235	3.91	-0.20	13.6	HD160915	6244	4.31	-0.21	11.9
HD17206	6249	4.38	-0.03	23.9	HD106516	6324	4.90	-0.56	7.6
HD2454	6339	4.21	-0.30	3.0	HD182101	6354	4.44	-0.14	12.1
HD100563	6371	4.43	+0.04	13.5	HD739	6404	4.35	-0.09	2.9

B.1 Combining Levenberg-Marquardt and the MCMC approach

We can use the best value for the stellar parameters, as determined by the MCMC approach, as starting values for a subsequent Levenberg-Marquardt fit, which is a more goal-oriented fit. The “random-walk” behaviour of the former ensures that we do not suffer from a final distribution of found values showing a grid-structure, whereas the optimized behaviour of the latter quickly finds a (local) minimum from the parameters provided. Of course, the final runtime is now the sum of both individual runtimes. However, since the MCMC runtime is so much larger, the relative increase is acceptable. Table B.9 shows the found parameters of such a fit, where the stellar parameters from the MCMC result have been used as starting parameters, however, shift normalization corrections and resolution have not. The χ^2 -values differ by about 4% on average, however, the resulting fit is more often slightly worse compared to the original MCMC fit. The high correlation of resolution and rotational velocity might be the reason for this. We compare the new fitted stellar parameters to the starting values in Fig. B.2. There is a tendency towards lower $\log g$, reaching up towards the grid spacing of $\Delta \log g = 0.25$. For metallicity, the values were changed to slightly higher $[M/H]$, though to a lesser degree. All in all, these changes in stellar parameters is below the uncertainty given by the grid spacing, so that we do not consider this additional Levenberg-Marquardt-fit essential.

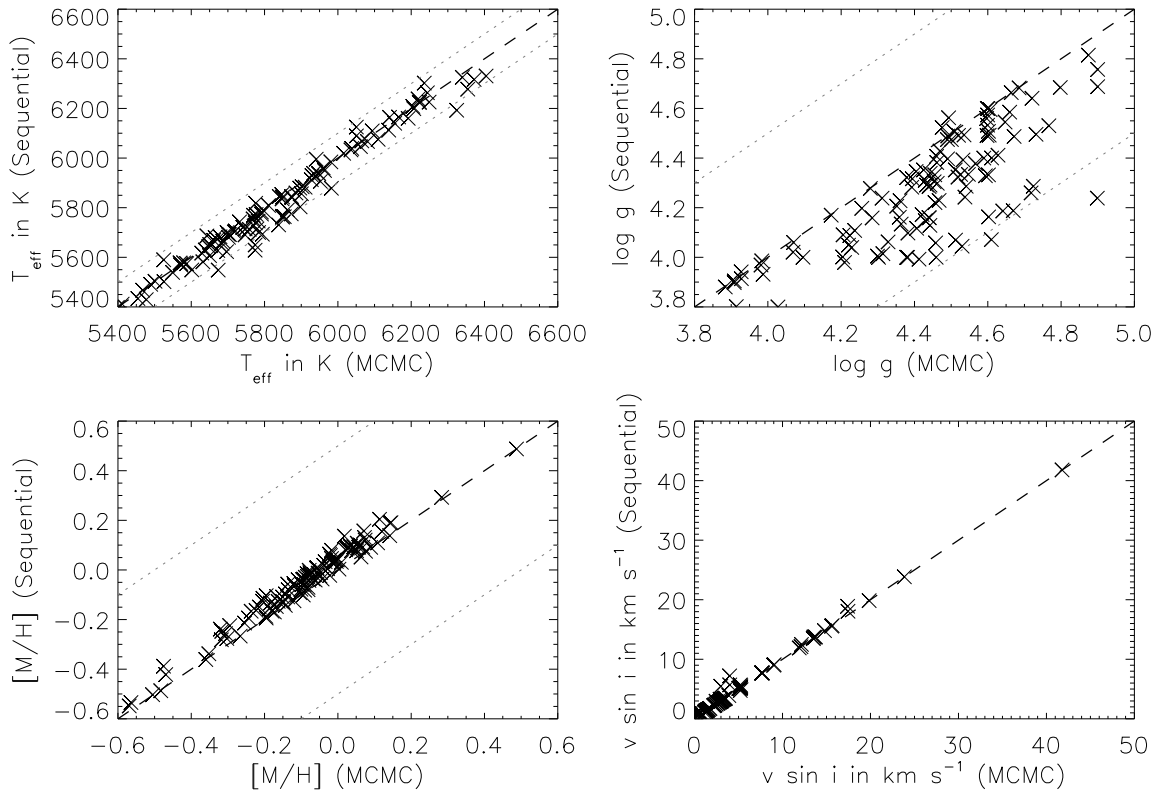


Figure B.2: Comparing the fitted stellar parameters of just the MCMC fit to the fitted stellar parameters from an additional Levenberg-Marquardt fit using the MCMC values as starting values (“Sequential”). The dashed line corresponds to the identity, the dotted lines show the typical grid-spacing, corresponding to “small changes”. Adding an additional pass of a subsequent Levenberg-Marquardt fit with the MCMC-derived stellar parameters as starting values does not change the resulting values by much. The tendency is towards lower values in $\log g$, and slightly higher $[M/H]$.

Table B.9: **Result of the Levenberg-Marquardt-fit from MCMC starting parameters.** The fit has been performed as described in the text, with the regions and masked given in Table 6.1 and Table 6.2. Other parameters have been fitted that are not shown here, such as resolution and a wavelength shift, see Table 6.3. If no error is given, the statistical error has been determined to be less than the step size in the grid, or unrealistic in the case of $v \sin i$, and should then be considered to be 50 K for T_{eff} , 0.10 for $\log g$, 0.12 for $[M/H]$ and 1 km s^{-1} for $v \sin i$.

Object	T_{eff} in K	$\log g$	$[M/H]$	$v \sin i$ in km s^{-1}	Object	T_{eff} in K	$\log g$	$[M/H]$	$v \sin i$ in km s^{-1}
HD82443	5398	4.60	+0.00	5.7	HD145675	5411	4.60	+0.49	1.8
HD3795	5429	4.00	-0.42	1.0	HD152391	5433	4.57	+0.03	3.0
HD131156A	5467	4.60	-0.14	3.3	HD117176	5490	4.00	-0.08	2.8
HD82885	5501	4.59	+0.29	3.3	HD101501	5503	4.53	-0.01	3.5
HD115617	5538	4.33	+0.01	2.8	HD89269	5548	4.19	-0.15	1.0
HD43162	5549	4.55	+0.01	3.0	HD6582	5568	4.69	-0.49	3.4
HD10700	5569	4.76	-0.27	1.0	HD224930	5573	4.81	-0.55	3.1
HD106116	5574	4.35	+0.09	1.2	HD68017	5577	4.64	-0.36	1.0
HD184385	5577	4.68	+0.09	2.9	HD111395	5581	4.49	+0.09	1.4
HD178428	5589	4.09	+0.13	1.0	HD42807	5606	4.39	-0.04	1.0
HD140538	5616	4.40	+0.06	5.2	HD38858	5622	4.16	-0.19	2.9
HD129333	5627	4.56	-0.06	13.8	HD20619	5628	4.29	-0.17	1.3
HD42618	5629	4.13	-0.11	1.0	HD20630	5642	4.49	+0.03	5.2
HD197027	5646	4.12	-0.03	2.3	HD12846	5649	4.26	-0.19	1.0
HD32923	5650	4.11	-0.17	5.1	HD26913	5655	4.58	-0.04	3.5
HD157214	5664	4.07	-0.24	3.1	HD1461	5668	4.23	+0.19	2.2
HD168009	5679	4.00	-0.00	1.3	HD76151	5680	4.32	+0.11	3.4
HD75528	5682	3.80	+0.05	3.0	HD186427	5686	4.13	+0.06	1.3
HD73350	5690	4.33	+0.10	3.4	HD28099	5691	4.43	+0.16	1.6
HD86728	5692	4.29	+0.19	1.3	HD70573	5693	4.38	-0.04	13.7
HD75767	5700	4.15	-0.06	1.7	HD92719	5700	4.19	-0.10	5.2
HD126053	5702	4.50	-0.28	3.1	HD90508	5706	4.04	-0.25	5.2
HD146233	5712	4.24	+0.04	3.4	HD145825	5714	4.29	+0.04	2.8
HD25680	5714	4.33	+0.04	1.4	HD186408	5720	4.10	+0.08	3.0
HD72905	5730	4.41	-0.06	5.4	HD159222	5738	4.23	+0.12	3.0
HD143761	5742	4.00	-0.17	2.6	HD30495	5746	4.49	-0.01	1.5
HD190771	5754	4.51	+0.16	2.9	HD43587	5761	4.00	-0.04	3.0
HD34411	5763	3.99	+0.08	3.3	HD10307	5765	4.06	+0.03	2.7
HD10086	5769	4.66	+0.11	1.0	HD41330	5772	4.00	-0.16	3.0
HD197076	5774	4.40	-0.08	5.3	HD181321	5775	4.49	-0.04	13.6
HD71148	5782	4.40	-0.01	7.7	HD196850	5788	4.49	-0.12	5.2
HD50692	5791	4.07	-0.15	1.1	HD150706	5803	4.33	-0.04	3.0
HD165401	5808	4.68	-0.34	3.0	HD142373	5818	4.00	-0.39	1.0
HD97334	5835	4.47	+0.09	7.7	HD206860	5840	4.35	-0.05	7.7
HD95128	5842	4.29	+0.03	1.5	HD79028	5844	3.98	+0.03	5.2
HD133640A	5845	4.49	-0.50	9.1	HD190406	5852	4.34	+0.05	7.7
HD19373	5856	4.01	+0.10	3.3	HD45067	5859	3.80	-0.11	3.9
HD115043	5878	4.53	-0.02	2.6 ± 1.04	HD39587	5878	4.56	-0.10	5.6
HD114710	5882	4.22	+0.02	1.6	HD100180	5884	4.16	-0.02	3.2
HD6920	5905	3.94	-0.04	2.3	HD154417	5912	4.33	-0.02	2.5
HD115383	5928	4.32	+0.10	5.7	HD20367	5935	4.31	+0.08	1.4
HD137107	5938	4.41	-0.09	12.5	HD209458	5938	4.17	-0.02	2.2
HD19019	5949	4.30	-0.13	5.2	HD75332	5960	4.28	-0.08	9.0
HD84117	5984	4.20	-0.13	7.2	HD187691	5995	4.05	+0.14	1.0
HD124570	6019	3.93	+0.10	3.5	HD88737	6032	3.91	+0.14	2.5
HD89744	6038	3.99	+0.08	4.7	HD9826	6045	4.04	+0.09	5.2
HD35296	6066	4.47	-0.07	14.8	HD179949	6069	4.35	+0.09	5.5
HD72945	6075	4.06	+0.04	5.2	HD107213	6089	3.97	+0.20	7.7
HD159332	6109	3.90	-0.13	5.1	HD16673	6112	4.30	-0.03	2.3 ± 1.66
HD194012	6125	4.16	-0.11	5.1	HD25998	6140	4.38	+0.09	15.7
HD111456	6160	4.52	-0.21	41.8	HD216385	6164	4.02	-0.15	1.4
HD25457	6165	4.51	-0.02	18.9	HD106516	6192	4.24	-0.53	7.7
HD58855	6198	4.16	-0.26	5.2	HD76572	6208	3.88	-0.19	3.0
HD88355	6223	4.17	-0.08	18.1	HD18256	6225	4.06	-0.13	15.6
HD17206	6225	4.32	+0.00	23.9	HD114378	6238	4.28	-0.22	19.8
HD160915	6263	4.24	-0.13	11.9	HD182101	6277	4.16	-0.11	12.1
HD157856	6302	3.90	-0.10	13.8	HD100563	6316	4.29	+0.08	13.5
HD2454	6325	4.09	-0.28	3.0	HD739	6330	4.21	-0.06	2.9

Appendix C

Previously published works

Here, we list the previous publications that have been derived from the results of this thesis.

Poster

I presented preliminary results as a poster contribution at the Cool Stars 19 workshop in Uppsala, Sweden:

J. Martin, M. Mittag, B. Fuhrmeister, T. O. B. Schmidt, A. Hempelmann, J. N. González-Pérez, K.-P. Schröder, J. H. M. M. Schmitt. **Determining activity and rotation periods from TIGRE Ca II observations**. Poster contribution for Cool Stars 19 workshop, June 2016.

Paper

Some of the results of this thesis were previously published in my paper entitled “**The Ca II infrared triplet’s performance as an activity indicator compared to Ca II H and K: Empirical relations to convert Ca II infrared triplet measurements to common activity indices**” [Martin et al., 2017]. Such content has been marked accordingly. This paper is reproduced here in its entirety. Permission to do so was graciously provided by Astronomy & Astrophysics.

The paper’s copyright is as follows:

Credit: J. Martin, B. Fuhrmeister, M. Mittag, T.O.B. Schmidt, A. Hempelmann, J.N. González-Pérez, and J.H.M.M. Schmitt; A&A, 605, id.A113, 2017, reproduced with permission, © ESO.

My contribution to the paper was the development of the method (as it is also described in Chapter 3), the “manual” S-Index determination and its conversion to the S_{MWO} scale, the relations to estimate inactive flux (see also Chapter 4), as well as the excess flux determination and the analysis of their correlations. I also obtained the conversion relations given.

The other authors contributed with important input on how to solve some challenges in the method, the interpretation of the results, and with the exact selection of stars to use, most of them from a subset preselected by M. Mittag, A. Hempelmann and J. H. M. M. Schmitt. All spectra in use were reduced by the automatic TIGRE pipeline, developed by M. Mittag.

The Ca II infrared triplet's performance as an activity indicator compared to Ca II H and K

Empirical relations to convert Ca II infrared triplet measurements to common activity indices

J. Martin¹, B. Fuhrmeister¹, M. Mittag¹, T. O. B. Schmidt^{1,2}, A. Hempelmann¹,
J. N. González-Pérez¹, and J. H. M. M. Schmitt¹

¹ Hamburger Sternwarte, Universität Hamburg, 21029 Hamburg, Germany
e-mail: jmartin@hs.uni-hamburg.de

² LESIA, Observatoire de Paris, CNRS, PSL Research University, Sorbonne Universités, UPMC Univ. Paris 06, Univ. Paris Diderot, Sorbonne Paris Cité, 5 place Jules Janssen, 92190 Meudon, France

Received 20 December 2016 / Accepted 19 May 2017

ABSTRACT

Aims. A large number of Calcium infrared triplet (IRT) spectra are expected from the *Gaia* and CARMENES missions. Conversion of these spectra into known activity indicators will allow analysis of their temporal evolution to a better degree. We set out to find such a conversion formula and to determine its robustness.

Methods. We have compared 2274 Ca II IRT spectra of active main-sequence F to K stars taken by the TIGRE telescope with those of inactive stars of the same spectral type. After normalizing and applying rotational broadening, we subtracted the comparison spectra to find the chromospheric excess flux caused by activity. We obtained the total excess flux, and compared it to established activity indices derived from the Ca II H and K lines, the spectra of which were obtained simultaneously to the infrared spectra.

Results. The excess flux in the Ca II IRT is found to correlate well with R'_{HK} and R^+_{HK} , as well as S_{MWO} , if the $B - V$ -dependency is taken into account. We find an empirical conversion formula to calculate the corresponding value of one activity indicator from the measurement of another, by comparing groups of datapoints of stars with similar $B - V$.

Key words. stars: activity – stars: chromospheres – stars: magnetic field – stars: atmospheres

1. Introduction

Cool stars with outer convective envelopes ubiquitously show signatures of magnetic activity. Such activity manifests itself in a plethora of observable signatures, such as spots, chromospheric emission lines, emission at X-ray and XUV wavelengths, and many others. On quite a few stars these activity phenomena are more pronounced than what we observe in the Sun, and it is therefore useful to perform activity studies on other, more active stars, both to learn about the underlying physical processes, but also to learn more about the Sun.

One of the best-known measures of activity is the so-called Mount-Wilson S -index S_{MWO} , defined as the ratio of the flux in the center of the Ca II H and K lines, where activity results in a sometimes very large excess emission, relative to the flux in the continuum on either side of the lines. As we have access to a large number of such observations dating back many years, this S -index is well-suited for long-term activity studies (Duncan et al. 1991). It has, in fact, been used to determine periods for activity cycles and/or rotation in cool stars (Baliunas et al. 1995).

Since the photosphere also contributes in the center of the Ca II H and K lines, the S -index characterizes not only chromospheric activity, and it becomes difficult to compare stars with different effective temperatures, where these photospheric contributions will vary. To overcome these shortcomings,

Linsky et al. (1979) introduced the so-called R'_{HK} -index. The photospheric flux is first subtracted from the flux measured in the Ca II H and K lines, and the remainder subsequently normalized by dividing by σT_{eff}^4 . This correction allows a direct comparison of stars of various stellar types, which have different photospheric fluxes. Given T_{eff} , it is possible to convert the measured values of S_{MWO} into R'_{HK} (Rutten 1984; Linsky et al. 1979), hence the large amount of archival data for S_{MWO} can directly be used to compare in the R'_{HK} -scale.

Both the *Gaia* mission (Prusti 2012) and CARMENES (Quirrenbach et al. 2014) are expected to provide very large numbers of spectra that can be used for activity studies of stars. The Radial Velocity Spectrometer (RVS) onboard *Gaia* has a resolution of about 11 500 with a wavelength coverage of 8470–8740 Å, and CARMENES covers the region between 5 500–17 000 Å with a resolution of 82 000. The *Gaia* RVS is expected to yield spectra down to a magnitude of about 17, which corresponds to 15–16% of the *Gaia* catalog of presently 1 142 679 769 entries (Gaia Collaboration 2016). CARMENES will yield time series of selected M dwarfs and the total number of spectra in the first three years will be approximately 15 000.

In both cases, the Ca II H and K lines at 3933.7 Å and 3968.5 Å are not covered, and thus no data to enhance temporal studies of activity can be combined with the existing S_{MWO} data. However, spectra obtained with either of these instruments

cover the calcium infrared triplet (IRT), three lines centered at 8498 Å, 8542 Å and 8662 Å. Like the Ca II H and K lines, the IRT are Ca II lines, which have been reported to be sensitive to activity as well (Martínez-Arnáiz et al. 2011). In contrast to the Ca II H and K lines, these IRT lines usually only show a smaller fill-in due to activity, rather than stronger fill-in up to a clear emission core as the Ca II H and K lines do. While the rather simple indicator of the central depression in the IRT lines correlates well with S_{MWO} (Chmielewski 2000), it is difficult to disentangle the effects from activity on the central depression from those of rotational broadening, which is also known to correlate well with activity (Andretta et al. 2005). Busà et al. (2007) presented a new indicator ΔW_{IRT} , based on the excess flux from the chromosphere, obtained by subtracting a model of the photosphere. Their new indicators turned out to correlate well with R'_{HK} , and they were able to obtain a conversion formula from this index to R'_{HK} by analyzing the spectra of 42 stars of type F5 to K3.

In this paper, we have adopted a similar approach, but have subtracted the observed spectra of an inactive object with similar stellar parameters. We performed this comparison not only for the calcium lines, but also for H α , and we also fit a Gaussian to the obtained excess flux to test the feasibility of using such a fit as an activity indicator. We used more than two thousand observations obtained with the TIGRE telescope, which simultaneously records the Ca II H and K lines, the Ca II IRT and H α (see Sect. 2.1). This means that there is no scatter from temporal variation, which can be a rather significant introduced error (Baliunas et al. 1995), and yet we are also able to more accurately quantify the expected derivation simply from inherent differences in the two activity indices.

The plan of our paper is as follows: first, we describe the TIGRE telescope and give an overview of the objects and observations used in this paper. We then describe the method used to determine the excess flux, and show the results for the measured line flux for inactive objects. Then, we show the observed correlations for the excess flux in the lines to other indicators. Finally, we give relations to convert the measured values to other indicators.

2. Observations

2.1. The TIGRE telescope

The Telescopio Internacional de Guanajuato Robótico Espectroscópico (TIGRE) is operated by a collaboration between the Hamburger Sternwarte, the University of Guanajuato and the University of Liège. TIGRE is a 1.2 m telescope stationed at the La Luz Observatory in central Mexico near Guanajuato at a height of about 2400 m. Equipped with the refurbished Heidelberg Extended Range Optical Spectrograph (HEROS), TIGRE takes spectra with a resolution of $\sim 20\,000$, covering a wavelength range of $\sim 3800\text{--}8800$ Å, with only a small gap of about 130 Å centered at 5765 Å. This wide wavelength coverage allows to obtain measurements of the Ca II IRT simultaneously with those taken of the Ca II H and K lines. TIGRE can be operated both manually and fully automatically, including the selection of the observation time for each object, based on factors such as weather, position, visibility in other nights, and the assigned priority. More detailed information about TIGRE can be found in Schmitt et al. (2014).

After every night the system automatically reduces the data, running a modified version of the REDUCE package (Piskunov & Valenti 2002), as described in Mittag et al. (2010).

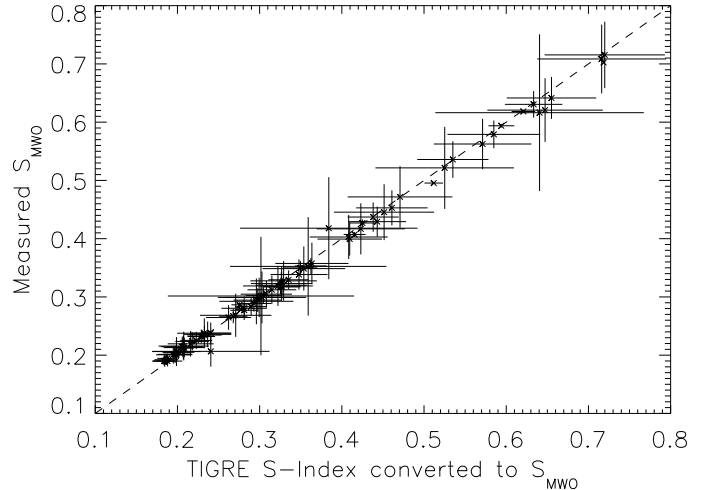


Fig. 1. Comparison of our measured value for S_{MWO} with the converted TIGRE S -Index.

This reduction pipeline includes flatfielding and the wavelength calibration. Moreover, TIGRE determines its own S -index, defined almost identically to the original Mount-Wilson S -Index S_{MWO} (Vaughan et al. 1978; Duncan et al. 1991),

$$S_{\text{MWO}} = \frac{N_{\text{H}} + N_{\text{K}}}{N_{\text{V}} + N_{\text{R}}} \alpha, \quad (1)$$

where N_{H} and N_{K} are the countrates in a bandpass with a FWHM of 1.09 Å in the center of the Ca II H and K line, respectively. In the original definition, this bandpass is triangular, whereas the TIGRE S -Index uses a rectangular bandpass. N_{V} and N_{R} are the countrates in 20 Å-wide continuum bands outside the lines, centered at 3901.07 Å and 4001.07 Å. The factor α ensures that countrates measured by different instruments are in agreement. The TIGRE S -Index can be converted to the S_{MWO} -scale (Mittag et al. 2016).

In this paper, we have measured the S -index “manually” from the spectra for every observation using the same bandpasses as given in the original definition, including the triangular shape in the center of the lines. To determine α correctly for our values, we compare our values to the corresponding TIGRE S -index values converted to S_{MWO} . As shown in Fig. 1, there is a clear linear relation between the two S -indices, allowing us to transform our values to the S_{MWO} -scale. We cannot simply always use the TIGRE-determined S -index, because older versions of the pipeline did not calculate that value. To ensure that we can also use these spectra, but do not introduce systematic errors due to a different approach in calculating the S -index, we have always calculated it manually according to the original definition.

2.2. Overview of data used

In this paper, a total of 2807 individual observations of 102 stars were analyzed. Some of these observations were not suitable for the excess flux determination (see Sect. 3.4), so that only 2274 observations of 82 stars were eventually used. The stars with observations used here were not originally selected for this paper, but rather for other science purposes. The largest part of the data was originally taken to determine stellar rotation periods of solar-like stars (Hempelmann et al. 2016). Here, we only

Table 1. Overview of the data used in this paper, categorized by spectral type.

Type	#	#	S/N	Exp. time [s]
	Obj.	Obs.	min/med/max	min/med/max
F	9	265	36.1/60.7/161.3	120/360/2578
G	46	1419	20.1/59.2/114.0	60/622/4767
K	27	590	20.4/64.3/114.8	60/799/4846
Total	82	2274	20.1/60.4/161.3	60/610/4846

look at data from main-sequence stars with $B - V$ -colors ranging from 0.4 to 1.2, corresponding to F, G and K stars. The earliest data points are from April 15, 2013, ranging up to the latest from May 4, 2016. We have excluded data points obtained between December 6th, 2014 and May 15th, 2015, since there was a different camera for the red channel in use at that time. Because these objects were observed for different projects, the signal-to-noise-ratio (S/N) and exposure time are not constant in our sample. We only analyzed observations with an average S/N of at least 20, because otherwise their noise level introduces large errors in our sample. Finally, telluric line correction was done using Molecfit (Smette et al. 2015; Kausch et al. 2015). We have used the stellar parameters given in Soubiran et al. (2010) whenever possible. Table 1 shows an overview of the number of analyzed observations for each spectral type, as well as the minimum, median and maximum values for S/N and exposure time in that class. We provide a full list of all objects, with sources for values $B - V$, $v \sin i$, $\log g$ and $[Fe/H]$ that we used, in Tables A.1 and A.2.

3. Method

3.1. Selecting comparison objects

The changes in the Ca II IRT lines due to activity are much smaller than those seen in the Ca II H and K lines. To measure this change, we compared our observations with those from an inactive star. The comparison star must be similar in its parameters to the active star in question, to ensure that the difference in the line profiles stems from activity rather than from differences in the photosphere. Whether a star is considered active or inactive is determined by its value of R'_{HK} , defined by Linsky et al. (1979) as:

$$R'_{HK} = \frac{F_{HK} - F_{HK,phot}}{\sigma T_{eff}^4}, \quad (2)$$

where F_{HK} is the flux measured in the Ca II H and K lines and $F_{HK,phot}$ the photospheric contribution to that flux. Since this index is normalized to σT_{eff}^4 , it is only marginally dependent on $B - V$, and thus, while slightly more difficult to determine, better suited for activity studies. We have used the relation given in Mittag et al. (2013) to convert our measured values for S_{MWO} to R'_{HK} . We only study stars with $\log R'_{HK} \geq -4.75$, and define those with smaller R'_{HK} as inactive, following the definition by Henry et al. (1996). This threshold value is close to the lower levels of the Sun’s activity. For each potentially active star in question, we select one inactive star as close as possible in stellar parameters and slowly rotating, so that $v \sin i \leq 5 \text{ km s}^{-1}$. These criteria have been given different weights: a similar value for $B - V$ is given the highest priority, followed by similar values for metallicity and then gravity. For each comparison object, the “best” comparison spectrum – defined as the one with the highest S/N – is selected, and visually checked to ensure that no

artifacts remain, for example from uncorrected cosmics. Every observation of the star in question is compared to that spectrum, referred to as comparison spectrum in the following.

3.2. Errors from incorrect stellar parameters

The stellar parameters are not always well-determined, and sometimes even a rather large range of possible values is given in the literature. The Ca II IRT line profiles, especially the wings, are affected quite strongly by changes in metallicity as analyses of model spectra show (Smith & Drake 1987; Erdelyi-Mendes & Barbuy 1991). In Fig. 2, we show the normalized spectra of the first Ca II IRT line from several interpolated PHOENIX models (Hauschildt et al. 1999), that are based on those from Husser et al. (2013). In these spectra, H I, He I, He II, Ca I, Ca II, Ca III, Fe I and Fe II were, among others, all calculated in Non Local Thermodynamic Equilibrium (NLTE). The plotted first Ca II IRT line shows the strongest effects, and allows us to give a “worst-case” estimate. It is obvious that the lines are not very sensitive to gravity, but show a strong dependence on metallicity, confirming the result by Andretta et al. (2005). Temperature also affects the line profile, but values for T_{eff} tend to be determined more reliably.

Most of the stellar parameters we have used are taken from Soubiran et al. (2010), where the authors have compiled the stellar parameters from the literature. The average discrepancy in metallicity for stars that have more than one set of stellar parameters available is given there as 0.08 dex, and the discrepancy in T_{eff} as 1.3%. For our rough determination on the errors introduced in the final excess flux, we ignored the low discrepancy on T_{eff} , as we can confidently say from Fig. 2 that a deviation of $\sim 10 \text{ K}$ will have negligible effects compared to those from the deviation in metallicity. We then considered the conservative case of template and active star to both have incorrectly determined metallicity, and that the real difference between the two is $\Delta [M/H] = 0.25 \text{ dex}$. We took two model spectra with $T_{eff} = 5700 \text{ K}$, $\log g = 4.40$ and $[M/H] = 0.25$ and $[M/H] = 0$, respectively, and integrated the flux of those two spectra numerically, across a 1 \AA -wide bandpass in the center of the first Ca II IRT line. The results differ by less than 3%. We therefore conclude that the error from incorrect stellar parameters will not strongly affect our results.

3.3. Comparing active stars to inactive template stars

The Ca II H and K lines, the Ca II IRT lines, and $H\alpha$ were checked individually with a procedure (written in IDL) that worked as follows: for each line, a region was defined that encompasses the line and continuum on either side. Both observation and comparison spectrum were then normalized in this region by finding a linear fit to the upper envelope in small regions defined as continuum. Observation and comparison spectrum were then shifted on top of each other by cross-correlation. In this way, any potential wavelength-shift, no matter the cause, is corrected. Afterwards, the comparison is rotationally broadened to the rotational velocity of the actual star, following the procedure described by Gray (2005), with a limb-darkening coefficient interpolated from the figure given there (their Fig. 17.6, p. 437). As a local normalization, a fit was performed to match the photospheric wings. This can be done, since only the core of the line should be affected by chromospheric activity (Busà et al. 2007). Finally, we subtracted the comparison spectrum from the spectrum, and ended up with the excess flux, thought to

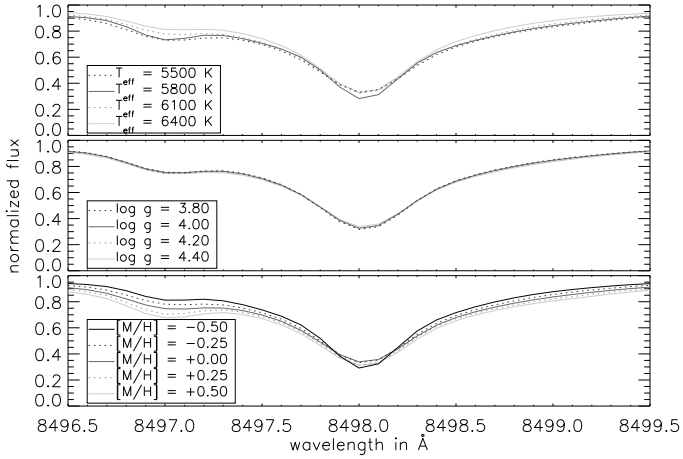


Fig. 2. Effects of stellar parameters on the Ca II IRT lines. Shown here are PHOENIX spectra, degraded to the resolution of TIGRE spectra, with T_{eff} varied in the top plot, $\log g$ in the middle, and metallicity in the bottom plot. Unless varied in that plot, stellar parameters were set to $T_{\text{eff}} = 5700$ K, $\log g = 4.40$ and $[M/H] = 0.0$.

come from chromospheric activity. We integrated this excess curve in an 1 Å-wide region for the Ca II IRT lines and H α , and a 2 Å-wide region for Ca II H and K to obtain the resulting excess flux F_{Exc} . The larger bandpass for the Ca II H and K-lines has been purposefully selected to be larger than the expected width of ~ 1 Å according to the Wilson-Bappu-effect (Wilson & Vainu Bappu 1957), to ensure that all of the flux is included in these rather wide lines.

In Fig. 3 we show the result of such a comparison for three objects with different levels of activity, i.e., for a star with low activity ($S_{\text{MWO}} = 0.19$), medium activity ($S_{\text{MWO}} = 0.23$) and high activity ($S_{\text{MWO}} = 0.36$). Figure 3 also shows that the observed excess flux in the lines is increased for the more active objects. The excess fluxes shown here correspond to $0.1 \times 10^5 \text{ erg s}^{-1} \text{ cm}^{-2}$, $2.0 \times 10^5 \text{ erg s}^{-1} \text{ cm}^{-2}$ and $4.4 \times 10^5 \text{ erg s}^{-1} \text{ cm}^{-2}$ respectively. In order to assess the error of the excess flux, we use Gaussian error propagation where possible, for example propagation of the errors on the normalization fit, or a Monte Carlo approach, for example by broadening the line 150 times with the values for $v \sin i$ varying within its error; in those cases where no error is given, we have assumed a 10% error. The resulting distribution of the values for the integrated excess flux are Gaussian in almost every case, so that we interpret the resulting error as a 1σ -error; see Sect. 3.4 for a description of objects for which the distribution is not Gaussian. A typical example for our procedure is shown in Fig. 4. Since the spectra are normalized to unity, this implies that this excess flux is given in units of the continuum flux. To convert this to a stellar surface flux in units of $\text{erg cm}^{-2} \text{ s}^{-1} \text{ \AA}^{-1}$, we use the relation from Hall (1996) for the continuum flux at different wavelength points. We also fit Gaussians or Lorentzians to the resulting excess flux distribution using the MPFIT routine (Markwardt 2009). These fit parameters can in principle also be used as activity indicators (see Sect. 4.4). The equivalent width has also been determined, but gives less reliable results than the integrated flux. We present a formula to determine the flux of inactive objects in Sect. 4.1, which can be subtracted from a measured flux to estimate the excess flux.

In some cases, we obtain a negative value for the excess flux, implying that the comparison star was more active than the star under investigation. Indeed, this only occurred for observations that also feature a low value for established activity indicators,

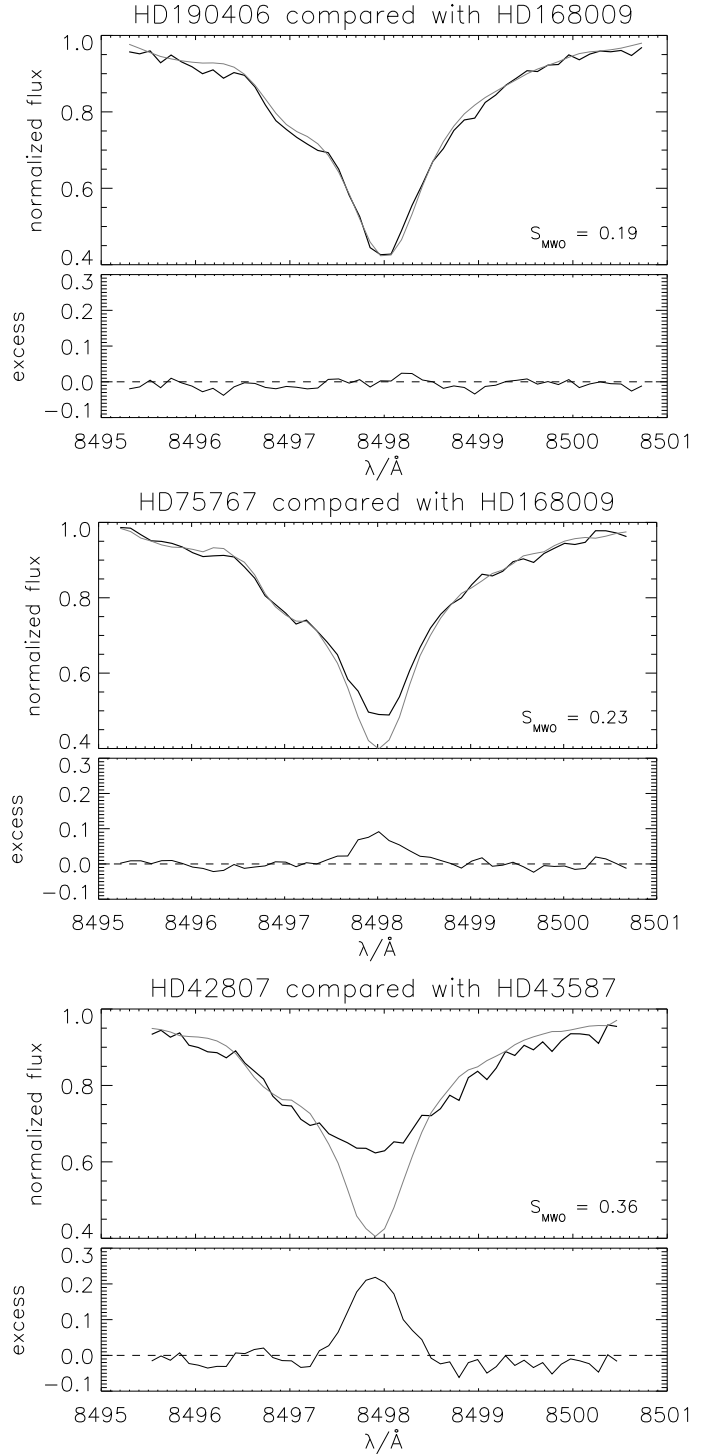


Fig. 3. Comparison of different stars' spectra (black) with the spectra of inactive stars (gray). For the lowest-activity stars (top), no excess flux can be seen, whereas for higher activity, the observed fill-in increases with activity. The determined excess flux in the first Ca II line in these three cases are $0.1 \times 10^5 \text{ erg s}^{-1} \text{ cm}^{-2}$, $2.0 \times 10^5 \text{ erg s}^{-1} \text{ cm}^{-2}$ and $4.4 \times 10^5 \text{ erg s}^{-1} \text{ cm}^{-2}$.

as well as a higher noise level. Our procedure is not well suited for these objects, because the change in the line that stems from activity is smaller than the errors introduced from the line profile differences as the stellar parameters of the two objects do not match exactly. A future study that compares the spectra to models will hopefully resolve this.

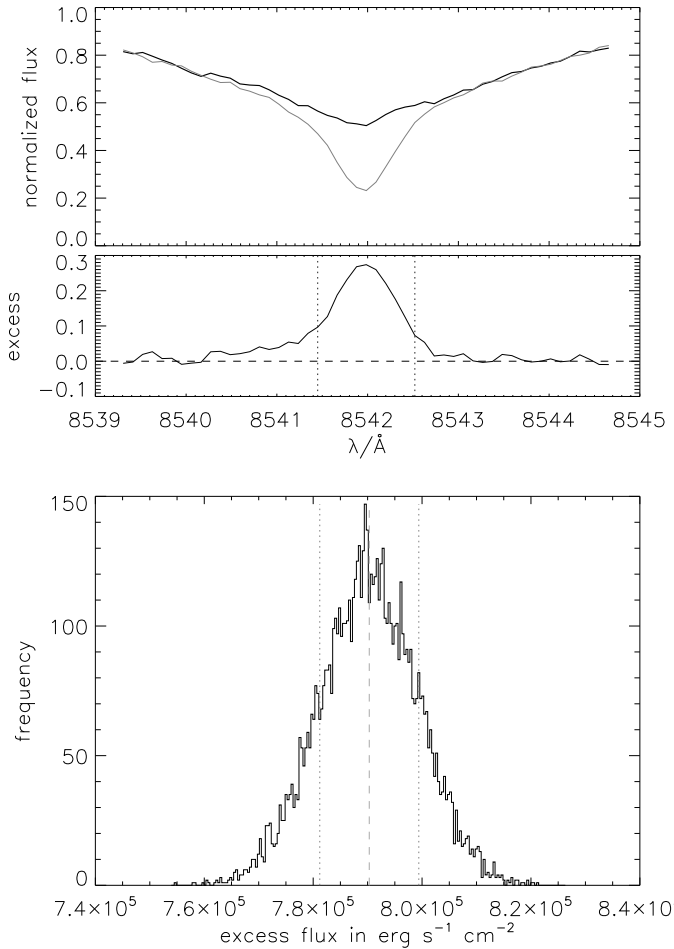


Fig. 4. Determination of the excess flux measured for HD 152391 in the second Ca II IRT line at 8542 Å and resulting distribution of the integrated excess flux after performing the Monte-Carlo-iterations. *Top:* comparison of the observation (black) with the rotationally broadened comparison spectrum (gray). The resulting excess flux, shifted to find an agreement in the wings, is shown in the lower plot. The dotted vertical lines show the 1 Å-region used for integrating. *Bottom:* histogram resulting from performing the excess flux determination 150 times, varying rotation and other parameters within their errors. The gray dashed line shows the average excess flux, the gray dotted lines the found 1σ values. Here, we found an excess flux of $(7.9 \pm 0.09) \times 10^5 \text{ erg s}^{-1} \text{ cm}^{-2}$.

As mentioned earlier, Busà et al. (2007) introduced a new activity index ΔW_{IRT} , which is obtained in a similar fashion. Two objects studied by Busà et al. (2007) are also in our sample: HD 25998 and HD 82443. A slight change in our calculation allows us to also obtain this parameter from our data. For both objects and all three lines, the values agree to within 1σ .

In our approach we have chosen to make use of the large sample of available stellar TIGRE spectra, and to compare the spectra of active stars to the spectra of inactive stars. This approach requires no further assumptions on the formation of the spectrum. One advantage of this approach compared to the one of subtracting a model spectrum, as is the case in Busà et al. (2007), is that we remove the basal flux level as well, leaving only the “true” activity related excess flux. An additional advantage is that we avoid errors due to incorrect parameters in the line list, or incomplete or otherwise erroneous line profiles. This error is hard to quantify and likely to be systematic in nature. On

the other hand, the observed spectra of inactive stars will have a certain degree of noise in them, which introduces some scatter as well. However, across a large sample, these errors are statistically distributed, and average out.

Since the comparison star has slightly different parameters to the star we compare to, some scatter is introduced as a systematic offset to the determined excess fluxes of that star (see also Sect. 3.2). In fairness, such scatter will also be introduced from an incorrect set of stellar parameters when using a model. It is possible to vary the stellar parameters in use to fit the model spectra so both spectra agree in the wings, this approach can not eliminate those errors completely. The best way to handle these errors is to use as many stars as possible, as those errors will then broaden the distribution, but should not affect the resulting fit by much.

3.4. Outliers

Fifteen objects for which observations were available had to be removed from further analysis as they could not be handled adequately with our approach.

- HD 114378: the comparison shows that the line shape differs to the one from the comparison spectrum, resulting in what appears to be a well-defined excess flux. However, this object has been found to be a binary star (Malkov et al. 2012). The observed line in the spectrum is then a combination of two (shifted) line profiles with different degrees of fill-in depending on their individual activity. The approach used here – comparing with a spectrum of a single, main-sequence star – is not appropriate for double stars and thus cannot be expected to yield correct results. For the same reason, we rejected results from other binary systems, such as HD 106516 and HD 133640.
- HD 6920: this object is often listed as an F8V star (e.g., Hillen et al. 2012), but has also been classified as sub-giant, for example Abt (1986), Fuhrmann (1998), Gray et al. (2001), Anderson & Francis (2012). Should the latter classification be correct, it appears reasonable that the line profile differs from that of a main-sequence star to some degree. We have therefore excluded this object from further analysis.
- HD 25998, HD 111456, HD 115043: these objects all have both a comparatively low value for $B - V$, as well as a high rotational velocity. The latter causes the excess flux to be smeared out across a wider spectral region than normal, which requires a high resolution and a very high S/N to disentangle the chromospheric excess flux from the photospheric contributions. Checking these spectra by eye shows that this could not be done reliably, so we excluded results from these stars. To determine their excess flux, follow-up observations with higher S/N are needed.

Removing these objects and an additional five stars with observations featuring too-low S/N in the lines of interest leaves us with a sample of 82 objects with a total of 2274 observations that are used to determine the conversion. Unfortunately, this leaves a rather small number of F-stars (nine objects with 265 observations in total). The other spectral types are not affected as much, with 46 G-stars (1419 observations) and 27 K-stars (590 observations). The lowest value of $B - V$ in the sample is changed to 0.43, the highest value is 1.18. See Table 1 for full details.

Table 2. Formulae to estimate the summed up flux in an 1 Å-window in the center of all three Ca II IRT lines for inactive objects.

Object	$B - V$	$\log g$	[Fe/H]	$\log R'_{\text{HK}}$	Estimated total flux in 1 Å-bandpasses in all Ca II IRT lines	
					in $10^6 \text{ erg s}^{-1} \text{ cm}^{-2}$	from normalized spectra in Å
HD 739	0.40	4.27	-0.09	-4.91	$8.645 + 0.026 \times v_{\text{rot}} + 6.106 \times 10^{-4} v_{\text{rot}}^2$	$1.371 + 0.004 \times v_{\text{rot}} + 0.972 \times 10^{-4} v_{\text{rot}}^2$
HD 159332	0.45	3.85	-0.23	-4.99	$7.326 + 0.024 \times v_{\text{rot}} + 5.770 \times 10^{-4} v_{\text{rot}}^2$	$1.250 + 0.004 \times v_{\text{rot}} + 0.987 \times 10^{-4} v_{\text{rot}}^2$
HD 216385	0.48	3.95	-0.29	-4.98	$7.318 + 0.025 \times v_{\text{rot}} + 5.791 \times 10^{-4} v_{\text{rot}}^2$	$1.309 + 0.005 \times v_{\text{rot}} + 1.039 \times 10^{-4} v_{\text{rot}}^2$
HD 45067	0.53	4.01	-0.09	-4.90	$6.323 + 0.025 \times v_{\text{rot}} + 4.679 \times 10^{-4} v_{\text{rot}}^2$	$1.224 + 0.005 \times v_{\text{rot}} + 0.909 \times 10^{-4} v_{\text{rot}}^2$
HD 187691	0.56	4.26	+0.10	-4.89	$5.862 + 0.022 \times v_{\text{rot}} + 4.432 \times 10^{-4} v_{\text{rot}}^2$	$1.190 + 0.004 \times v_{\text{rot}} + 0.903 \times 10^{-4} v_{\text{rot}}^2$
HD 100180	0.57	4.25	-0.06	-4.76	$6.134 + 0.020 \times v_{\text{rot}} + 4.188 \times 10^{-4} v_{\text{rot}}^2$	$1.265 + 0.004 \times v_{\text{rot}} + 0.866 \times 10^{-4} v_{\text{rot}}^2$
HD 124570	0.58	4.05	+0.08	-5.05	$5.504 + 0.023 \times v_{\text{rot}} + 4.536 \times 10^{-4} v_{\text{rot}}^2$	$1.153 + 0.005 \times v_{\text{rot}} + 0.953 \times 10^{-4} v_{\text{rot}}^2$
HD 19373	0.59	4.21	+0.08	-4.84	$5.698 + 0.021 \times v_{\text{rot}} + 4.367 \times 10^{-4} v_{\text{rot}}^2$	$1.213 + 0.004 \times v_{\text{rot}} + 0.931 \times 10^{-4} v_{\text{rot}}^2$
HD 168009	0.60	4.23	-0.01	-4.77	$5.711 + 0.019 \times v_{\text{rot}} + 4.289 \times 10^{-4} v_{\text{rot}}^2$	$1.242 + 0.004 \times v_{\text{rot}} + 0.935 \times 10^{-4} v_{\text{rot}}^2$
HD 10307	0.62	4.32	+0.03	-4.84	$5.635 + 0.019 \times v_{\text{rot}} + 3.969 \times 10^{-4} v_{\text{rot}}^2$	$1.257 + 0.004 \times v_{\text{rot}} + 0.888 \times 10^{-4} v_{\text{rot}}^2$
HD 157214	0.62	4.31	-0.40	-4.80	$5.922 + 0.018 \times v_{\text{rot}} + 3.963 \times 10^{-4} v_{\text{rot}}^2$	$1.321 + 0.004 \times v_{\text{rot}} + 0.886 \times 10^{-4} v_{\text{rot}}^2$
HD 34411	0.62	4.22	+0.08	-4.85	$5.458 + 0.021 \times v_{\text{rot}} + 3.975 \times 10^{-4} v_{\text{rot}}^2$	$1.218 + 0.005 \times v_{\text{rot}} + 0.890 \times 10^{-4} v_{\text{rot}}^2$
HD 95128	0.62	4.30	+0.01	-4.85	$5.888 + 0.018 \times v_{\text{rot}} + 4.288 \times 10^{-4} v_{\text{rot}}^2$	$1.312 + 0.004 \times v_{\text{rot}} + 0.957 \times 10^{-4} v_{\text{rot}}^2$
HD 38858	0.64	4.48	-0.22	-4.79	$5.798 + 0.017 \times v_{\text{rot}} + 3.754 \times 10^{-4} v_{\text{rot}}^2$	$1.335 + 0.004 \times v_{\text{rot}} + 0.868 \times 10^{-4} v_{\text{rot}}^2$
HD 146233	0.65	4.42	+0.03	-4.75	$5.380 + 0.018 \times v_{\text{rot}} + 3.774 \times 10^{-4} v_{\text{rot}}^2$	$1.258 + 0.004 \times v_{\text{rot}} + 0.885 \times 10^{-4} v_{\text{rot}}^2$
HD 186427	0.65	4.32	+0.07	-4.80	$5.166 + 0.019 \times v_{\text{rot}} + 3.785 \times 10^{-4} v_{\text{rot}}^2$	$1.208 + 0.004 \times v_{\text{rot}} + 0.888 \times 10^{-4} v_{\text{rot}}^2$
HD 12846	0.66	4.38	-0.26	-4.78	$5.875 + 0.015 \times v_{\text{rot}} + 3.984 \times 10^{-4} v_{\text{rot}}^2$	$1.391 + 0.004 \times v_{\text{rot}} + 0.946 \times 10^{-4} v_{\text{rot}}^2$
HD 43587	0.67	4.29	-0.04	-4.80	$5.528 + 0.018 \times v_{\text{rot}} + 3.879 \times 10^{-4} v_{\text{rot}}^2$	$1.327 + 0.004 \times v_{\text{rot}} + 0.933 \times 10^{-4} v_{\text{rot}}^2$
HD 115617	0.70	4.39	-0.01	-4.80	$4.934 + 0.017 \times v_{\text{rot}} + 3.450 \times 10^{-4} v_{\text{rot}}^2$	$1.248 + 0.004 \times v_{\text{rot}} + 0.874 \times 10^{-4} v_{\text{rot}}^2$
HD 178428	0.70	4.25	+0.14	-4.88	$4.659 + 0.018 \times v_{\text{rot}} + 3.663 \times 10^{-4} v_{\text{rot}}^2$	$1.178 + 0.005 \times v_{\text{rot}} + 0.929 \times 10^{-4} v_{\text{rot}}^2$
HD 3795	0.70	3.91	-0.63	-4.83	$5.331 + 0.015 \times v_{\text{rot}} + 4.096 \times 10^{-4} v_{\text{rot}}^2$	$1.347 + 0.004 \times v_{\text{rot}} + 1.037 \times 10^{-4} v_{\text{rot}}^2$
HD 117176	0.71	3.97	-0.06	-4.90	$4.584 + 0.018 \times v_{\text{rot}} + 3.628 \times 10^{-4} v_{\text{rot}}^2$	$1.177 + 0.005 \times v_{\text{rot}} + 0.934 \times 10^{-4} v_{\text{rot}}^2$
HD 10700	0.72	4.48	-0.50	-4.75	$5.163 + 0.014 \times v_{\text{rot}} + 3.325 \times 10^{-4} v_{\text{rot}}^2$	$1.347 + 0.004 \times v_{\text{rot}} + 0.869 \times 10^{-4} v_{\text{rot}}^2$
HD 26965	0.85	4.51	-0.27	-4.89	$3.944 + 0.012 \times v_{\text{rot}} + 2.855 \times 10^{-4} v_{\text{rot}}^2$	$1.265 + 0.004 \times v_{\text{rot}} + 0.919 \times 10^{-4} v_{\text{rot}}^2$
HD 75732	0.87	4.41	+0.28	-4.84	$3.372 + 0.014 \times v_{\text{rot}} + 2.740 \times 10^{-4} v_{\text{rot}}^2$	$1.110 + 0.005 \times v_{\text{rot}} + 0.905 \times 10^{-4} v_{\text{rot}}^2$
HD 145675	0.90	4.45	+0.41	-4.80	$3.150 + 0.013 \times v_{\text{rot}} + 2.729 \times 10^{-4} v_{\text{rot}}^2$	$1.087 + 0.005 \times v_{\text{rot}} + 0.944 \times 10^{-4} v_{\text{rot}}^2$

Notes. v_{rot} must be entered in units of km s^{-1} . To obtain the best fit, it is recommended to compare the values from normalized spectra and to subtract an additional 20 mÅ, as described in the text. Values for $B - V$, $\log g$ and [Fe/H] are taken from Soubiran et al. (2010).

4. Results

4.1. Flux of inactive stars

Determining the excess flux requires a comparison spectrum to subtract the line flux of an inactive star. However, an observer may not always have a suitable spectrum at hand. In this case an estimate of the excess flux can still be performed, by calculating the inactive line flux. Table 2 shows a list of inactive ($\log R'_{\text{HK}} \leq 4.75$), slowly-rotating stars, which we used as comparison. In this paper, we always directly subtracted their normalized spectra from the normalized spectra of the object under investigation, which also allows an independent check on the quality of the comparison by the spectra's alignment in the wings. However, to determine the excess flux, only the (rotationally broadened) flux in the center of the line is of importance. In Fig. 5, we show the resulting values for the summed-up stellar surface flux $F_{\text{IRT},1 \text{ Å}}$ in 1 Å-bandpasses for all three lines for the different inactive objects with varying simulated rotational

broadening. We provide empirically derived formulae for the summed-up flux in 1 Å-wide bandpasses in the center of all the three Ca II IRT lines for these inactive objects as a function of rotational velocity $v \sin i$. The rotational broadening was performed according to Gray (2005). The relations are second-order polynomials fitted to the artificially rotationally broadened TIGRE spectra with a resolution of roughly 20 000. To use these relations for determining the excess flux in a spectrum with a very different resolution, the “bleeding” of the flux from within the wings due to the finite resolution must be taken into account. These relations can be used to estimate the inactive line flux, and therefore to determine a value for the Ca II IRT excess flux from the spectrum of an active star. To determine this value from a spectrum, a suitable comparison star from Table 2 must first be found. Then, the value of $v \sin i$ of the observed star should be plugged into the relation given there. The result will be the summed up flux $F_{\text{Inactive,IRT},1 \text{ Å}}$ of all three Ca II IRT lines of this best-fitting inactive star broadened by the $v \sin i$ of the star under

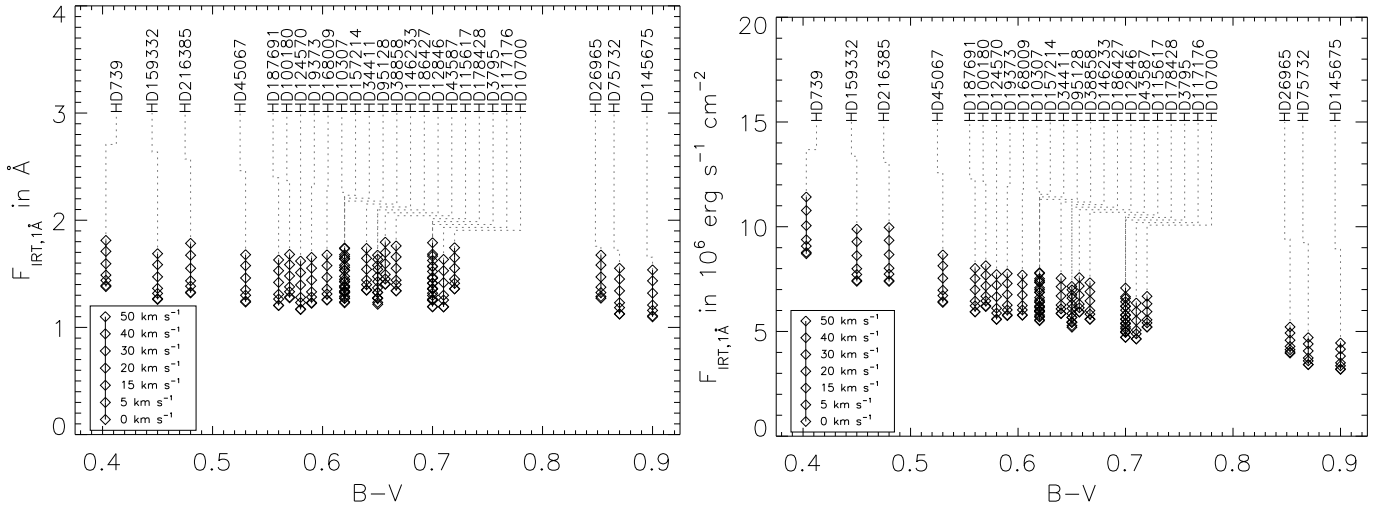


Fig. 5. Comparison of the obtained values for the summed-up Flux $F_{\text{IRT},1 \text{ \AA}}$ for rotational velocities 0, 5, 15, 20, 30, 40, and 50, all in km s^{-1} (flux increases with higher rotational velocity). Dotted lines connect to the name of the inactive object in question. *Left*: flux in continuum units, or equivalent width in \AA . *Right*: flux converted to $\text{erg s}^{-1} \text{cm}^{-2}$.

consideration, or in other words, the line flux expected if the star under consideration was inactive. This value must then be subtracted from the value obtained from an observation of an active star. We give both a relation for the converted flux $F_{\text{Inactive,IRT},1 \text{ \AA}}$ in $10^6 \text{ erg s}^{-1} \text{cm}^{-2}$, as well as for the flux in “continuum units”, which is the integrated flux of a normalized spectrum in units of \AA . Subtracting the flux in continuum units yields an excess flux value that can be compared to ΔW_{IRT} of Busà et al. (2007). Alternatively, this resulting value in \AA can then be converted to physical units ($\text{erg s}^{-1} \text{cm}^{-2}$), for example using the relation in Hall (1996), which tends to be more reliable than directly comparing values in $\text{erg s}^{-1} \text{cm}^{-2}$, as no error is introduced due to different values for $B - V$ of comparison and analyzed object.

Figure 6 shows a comparison of the values measured for the excess flux using the method described in this paper against the value obtained from simply subtracting the value calculated from Table 2 from the measured line flux (in continuum units) for the 42 active stars with observations where $R'_{\text{HK}} \geq 3 \times 10^{-5}$. On average, the discrepancy is about 20 m\AA , determined as the median of the residuals (68% of points differ less than 45 m\AA). It should be noted that the actual measured value is on the order of 1.5 \AA , so this error is only about 1.3%. Since the excess flux is the comparatively small difference of two larger values, the relative error is dramatically increased. The calculated values tend to be lower than the measured ones. The likely reason for this is the additional correction of shifting the observed spectrum to reach an agreement in the line wings to the comparison spectrum, and could thus be interpreted as the result of an additional correction for photospheric effects. Adding the aforementioned 20 m\AA to the subtracted value would be a possibility to fix this.

4.2. Measured flux in the Ca II H and K lines

The procedure mentioned was also carried out for the Ca II H and K lines. While they exhibit strong changes in excess flux amplitude, the shape of these lines is very broad and contaminated by other lines, making the determination of the excess flux more difficult. Nevertheless, we obtain a measured excess flux in the center of the Ca II H and K lines, by integrating over a 2 \AA -wide region. This value can be compared against the flux in the

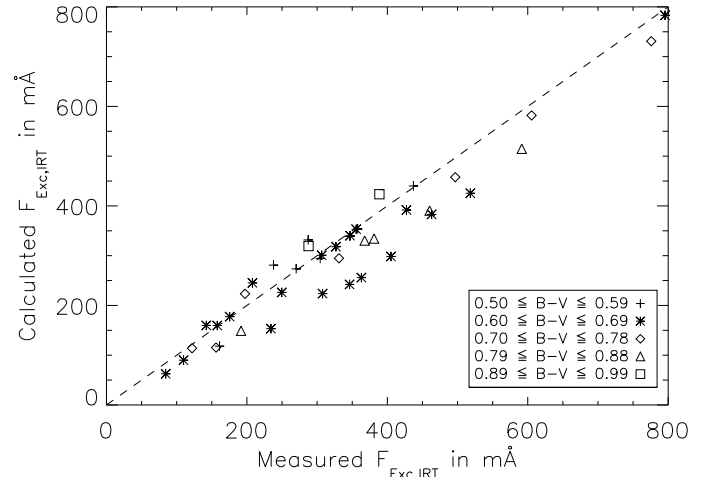


Fig. 6. Comparison of the excess flux in continuum units determined using the method described in Sect. 3.3 to the excess flux determined from subtracting the resulting value from a fitting relation from Table 2 to the measured line flux, for the 42 objects with observations displaying a level of activity exceeding $R'_{\text{HK}} = 3 \times 10^{-5}$. The dashed line corresponds to the identity relation.

Ca II H and K lines, which can be calculated from S_{MWO} using one of several available relations in the literature. In the top plot in Fig. 7, we compare our measured excess flux with the one calculated from the relation in Mittag et al. (2013) for the 82 stars in our sample. There, the authors present a relation for the total flux in the Ca II H and K lines, but they also give relations for just the photospheric flux as well as chromospheric basal flux contribution. Subtracting these from the total flux should in theory result in just the excess flux. Our values are lower than the calculated ones. As a second test, we can correct the fluxes calculated according to Rutten (1984) using the same relations for photospheric and basal flux contributions and compare our measurements to that result. In that comparison, the measured values are higher than the calculated ones. In Mittag et al. (2013), the authors used PHOENIX-models to convert to fluxes in $\text{erg s}^{-1} \text{cm}^{-2}$, whereas in Rutten (1984), the calibration is done using the measured solar flux. It is likely that the discrepancy

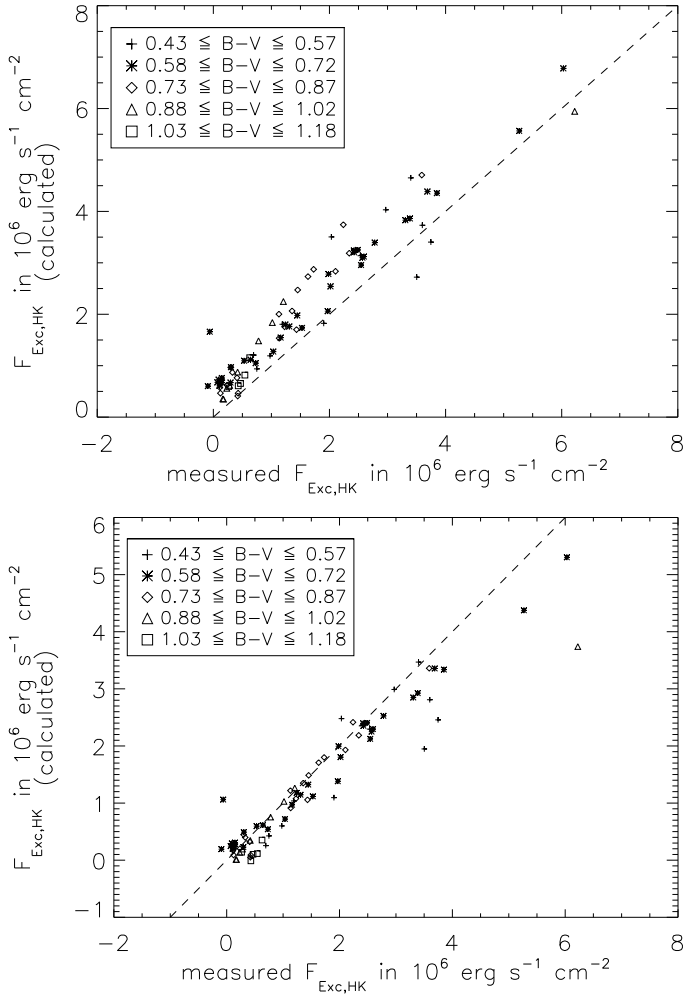


Fig. 7. Comparison of the measured chromospheric excess flux in the Ca II H and K-lines to the one calculated from various sources. The dashed line corresponds to the identity relation. *Top*: comparing to the chromospheric excess flux according to [Mittag et al. \(2013\)](#) for 82 objects. *Bottom*: comparing for these same stars to the flux given in [Rutten \(1984\)](#) but corrected for photospheric and basal flux contribution, also according to [Mittag et al. \(2013\)](#).

originates in the different approaches of calibrating the values to physical units. To test this, we compared the total flux in the lines calculated according to [Mittag et al. \(2013\)](#) with the relation in [Rutten \(1984\)](#). We find that the latter relation yields lower values, consistent with [Fig. 7](#). Our measurements and the relations from the literature for the total stellar flux in the Ca II H and K-lines can be used to find a relation for the photospheric and basal flux for a star of given $B - V$. The relations describe a value for the total flux in the Ca II H and K-lines, including the photospheric and basal component, as well as the flux from activity, which we measure as excess flux: $F_{\text{HK}} = F_{\text{phot,HK}} + F_{\text{basal,HK}} + F_{\text{Exc,HK}}$, as a function of S_{MWO} . Since our measured value is $F_{\text{Exc,HK}}$, subtracting the measured from the calculated value leaves us with just the photospheric and basal flux contributions to the line flux. We performed this determination using the relation from [Rutten \(1984\)](#) for the total line flux (shown in [Fig. 8](#)). We could then perform a linear fit to the resulting values, and compare this relation to the one in [Mittag et al. \(2013\)](#). While our relation yields lower values, the difference is not significant compared to the scatter in the datapoints for most of the covered range in $B - V$. Only for values $B - V > 1.0$ do the two relations differ from one

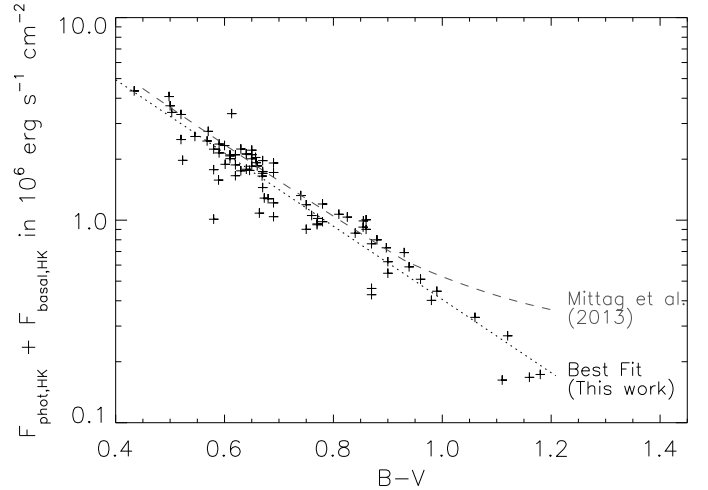


Fig. 8. Comparison of the determined photospheric and basal flux from this work to the relation given in [Mittag et al. \(2013\)](#). Shown are the average measured values for the 82 stars left after removal of the outliers described in [Sect. 3.4](#).

another. The relation given in [Mittag et al. \(2013\)](#) is defined in a step-wise fashion, and the relation changes for $B - V > 0.94$. From [Fig. 8](#), it appears as if a linear extrapolation of the previous relation would result in a better fit. However, we note that our sample does not reach much further beyond this threshold value in $B - V$. The relation found is:

$$\log(F_{\text{phot,HK}} + F_{\text{basal,HK}}) = 7.42 - 1.81 \times (B - V). \quad (3)$$

4.3. Comparing measured excess fluxes of different lines

We obtained 2274 values from 82 stars for the measured chromospheric flux in the Ca II H, K and IRT lines, as well as $H\alpha$, converted to real physical units by interpolating the relations in [Hall \(1996\)](#). The determined excess fluxes do not include any photospheric or chromospheric basal flux contributions, as those have been removed by subtraction of the comparison spectrum. The resulting plots for the three individual lines in the Ca II IRT, as well as the sum of all three lines, compared to the measured flux in the Ca II H and K lines are shown in [Fig. 9](#). The second Ca II IRT line shows both a strong correlation, as well as the largest fill-in, implying that it is the most sensitive line of the three. We obtain a very obvious correlation. We determined the Spearman's correlation value ρ to be largest ($\rho \approx 0.908$) for the correlation between the summed-up excess flux in all three Ca II IRT lines and the excess flux in the Ca II H and K lines.

$H\alpha$, another often-used indicator, also shows a correlation ([Fig. 10](#)), but the scatter is larger, and therefore we obtain a lower value with $\rho \approx 0.824$. It has been shown previously that $H\alpha$ does not always correlate with the Ca II H and K line indicators ([Cincunegui et al. 2007](#); [Meunier & Delfosse 2009](#); [Gomes da Silva et al. 2014](#)). Many stars in our sample show less variation in the excess fluxes than the errors on the individual measurements, so that they cannot be used to reliably estimate the correlation for an individual star. Using only the 68 stars with five or more observations for which the errors on the excess fluxes are significantly lower than their variation, we found the Spearman correlation to cover the entire range from -1.0 for some stars to 1.0 for others. The median correlation between the two excess fluxes is only $\rho \approx 0.24$. In contrast, performing the same analysis for Ca II excess fluxes, the median correlation

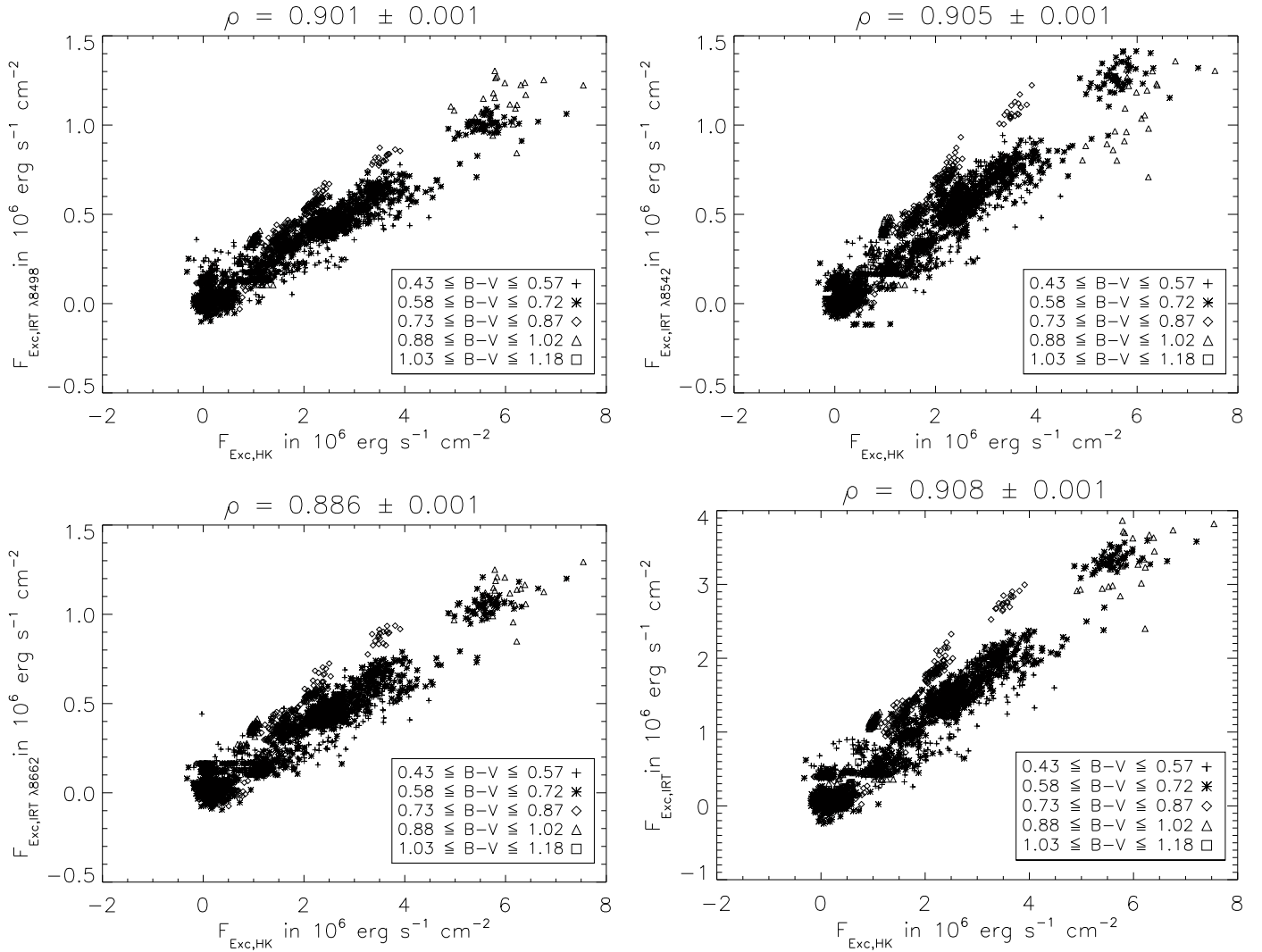


Fig. 9. Measured chromospheric excess flux in the Ca II H and K lines compared with the excess flux in the individual Ca II IRT lines, as well as the sum of all Ca II IRT lines (*bottom right*). These plots include data from 2274 observations of 82 stars.

is $\rho \approx 0.54$, significantly higher. Additionally, the number of stars with a negative correlation between the two excess fluxes is much lower.

The obtained excess fluxes in the Ca II H and K line correlate very well with each other ($\rho \approx 0.95$), and the measured flux in the K line is about 33% higher than in the H line. This is similar to the value of 27% observed by [Wilson \(1968\)](#).

4.4. Fits to the excess

For each observation, we fit Gaussians to the excess flux. We then checked if parameters obtained in this way showed any correlation to known activity indices. The amplitudes of the fitted Gaussians do show a correlation to the integrated flux in the Ca II H and K lines with $\rho \approx 0.7$ after removal of obvious outliers, yet the determined amplitudes have very large errors and are thus less suited for conversion than the integrated flux. Additionally, this method suffers more strongly from high noise in the spectra, as single spikes from noise can dominate the fit. This is the reason for the larger number of outliers. The width of the fitted Gaussian shows no correlation to the integrated flux in the Ca II H and K lines, or any of the established activity indicators.

5. Conversion relations

Because the excess fluxes in the Ca II lines and the indices derived from them are well-correlated, we can make use of our comparatively large sample size and find relations to convert one parameter into another. We assume that the two indices we wish to convert into one another follow a linear relation. We do however, allow the coefficients in the conversion to depend on stellar parameters. Here, we use $B - V$, but equivalently T_{eff} could also be used. Letting x be the index to be converted into another index y , we then set out to find the relation:

$$y = m(B - V) \times x + b(B - V). \quad (4)$$

If we assume m and b to be a polynomial, we can perform a regression to determine the coefficients. However, our data is not equally sampled in $B - V$. Therefore, if we perform the regression without taking this fact into consideration, we might find the resulting polynomial to just be optimized for the regions in $B - V$ where many stars of our sample lie in. To avoid this, we selected subsets of all datapoints. For fifteen different values of $B - V$, we select only observations of stars close to that value, and then fit Eq. (4) only for the datapoints from that subset of stars, which yields the values m , b only for that specific $B - V$. Since our objects are not evenly distributed in $B - V$, our sampling in

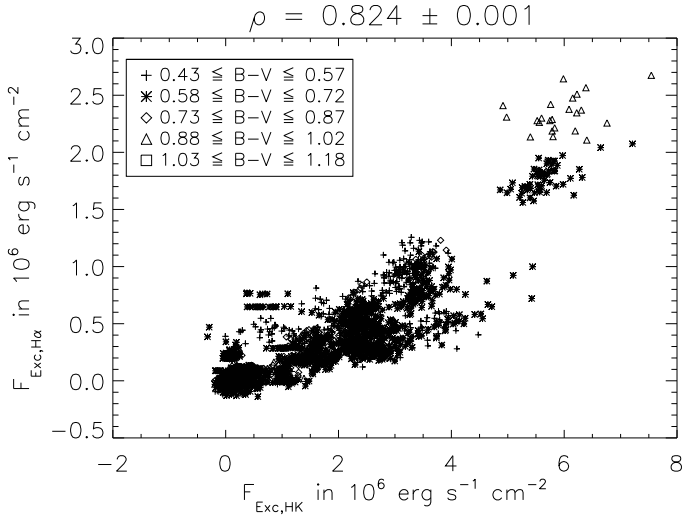


Fig. 10. Measured chromospheric excess flux from 2274 observations of 82 stars in the Ca II H and K lines compared with the excess flux in H α . Fluxes given in $\text{erg s}^{-1} \text{cm}^{-2}$.

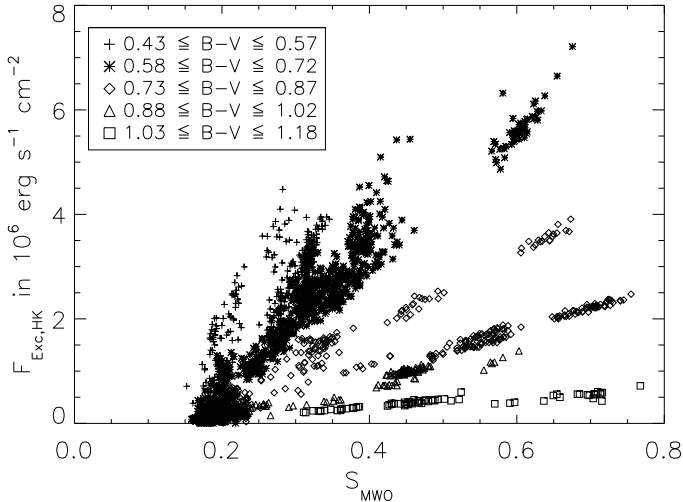


Fig. 11. Measured excess flux in the Ca II H and K lines as a function of S_{MWO} . This plot shows data from 2154 observations of 80 stars. For reasons of clarity, we have removed HD 22468 from this plot, as it contributes a number of datapoints clustering around a value of $S_{\text{MWO}} \approx 1.25$, as well as some observations with a negative value of $F_{\text{Exc,HK}}$ that is consistent with zero considering its error.

$B - V$ is not equidistant. Instead, we selected the different values for $B - V$ for which we perform this fit so there are datapoints of at least three stars for each subset. On average, a subset includes ~ 190 observations and seven stars. Finally, we fit a polynomial to the found values m and b , or their logarithm, for each $B - V$ sampled to obtain the relations $m(B - V)$ and $b(B - V)$. For completeness' sake, we have determined the coefficients with regression as well. The values converted by that approach are of similar quality. In the following, we will discuss the relations found in more detail for some specific pairs of observed indicators.

5.1. Excess flux in the Ca II H and K lines computed from S_{MWO}

Figure 11 shows our measured excess flux compared with the corresponding value for S_{MWO} , with different symbols again

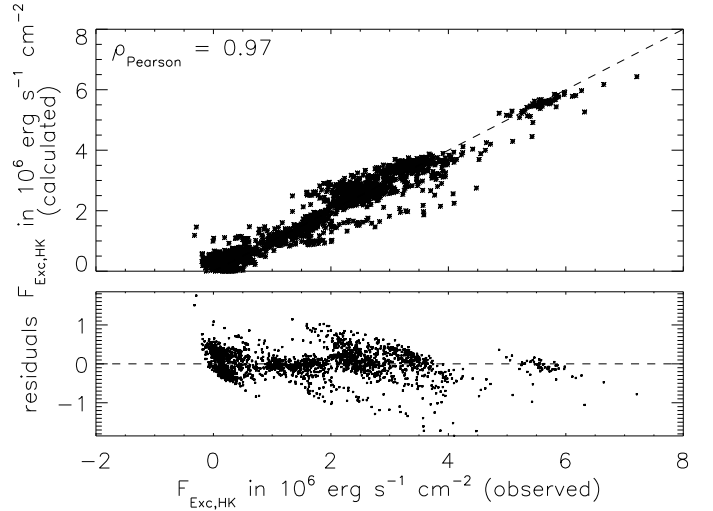


Fig. 12. Comparison of the measured excess flux in the Ca II H and K lines to the one converted from S_{MWO} using Eq. (5). The dashed line is the identity (top), or the zero-level (bottom). This plot shows data from 2137 observations of 79 stars. After conversion, the Pearson correlation coefficient is 0.97, indicating a strong linear correlation.

corresponding to different values of $B - V$. It appears that the relation between the two parameters is linear, yet the exact values of the linear fit coefficients depend on $B - V$. As previously described, we obtained relations for slope (m) and intercept (b) for individual values of $B - V$, after removal of 120 observations that were either clearly inaccurate (e.g., negative excess flux values), or too noisy with a strong influence on any linear fit performed (HD 22468), to not have the fit dominated by noisy data. We found a second-order polynomial fit for $\log m$ and b respectively to give good results:

$$F_{\text{Exc,HK}} = (m \times S_{\text{MWO}} + b) \times 10^6 \text{ erg s}^{-1} \text{ cm}^{-2}, \quad \text{with} \quad (5)$$

$$\log m = 1.027 + 1.718 \times (B - V) - 2.440 \times (B - V)^2$$

$$b = -2.908 - 0.667 \times (B - V) + 3.249 \times (B - V)^2$$

As this formula was found using data from only F, G and K main sequence stars, it is only valid for those, with a valid $B - V$ ranging from ~ 0.5 to ~ 1.0 . Figure 12 compares the converted value from S_{MWO} to the measured value. We can estimate the error of the converted values from the average of the residuals to be $3.0 \times 10^5 \text{ erg s}^{-1} \text{ cm}^{-2}$. This value is not a true 1σ -value, however, as the distribution is not Gaussian (68% lie within $3.0 \times 10^5 \text{ erg s}^{-1} \text{ cm}^{-2}$, 95% within $7.0 \times 10^5 \text{ erg s}^{-1} \text{ cm}^{-2}$). The stated error corresponds to an average relative error of about 11%. The quality of the conversion can be estimated from the Pearson correlation coefficient, which is a measure on the linear correlation. Here, we find $\rho_{\text{Pearson}} = 0.97$, indicating that the conversion worked well, as expected.

5.2. Flux conversion

As shown in Sect. 4.3, the excess flux in the Ca II IRT lines is strongly correlated with the one seen in the Ca II H and K lines (Fig. 9). From definition of those values, it is apparent that no intercept b is needed here. We find a dependence of the logarithm of the slope m to $B - V$ in our dataset. First, due to the different temperatures, the surface flux ratio at the different lines introduces a rather strong dependence, towards higher excess fluxes in the Ca II H and K lines for lower values of $B - V$. However,

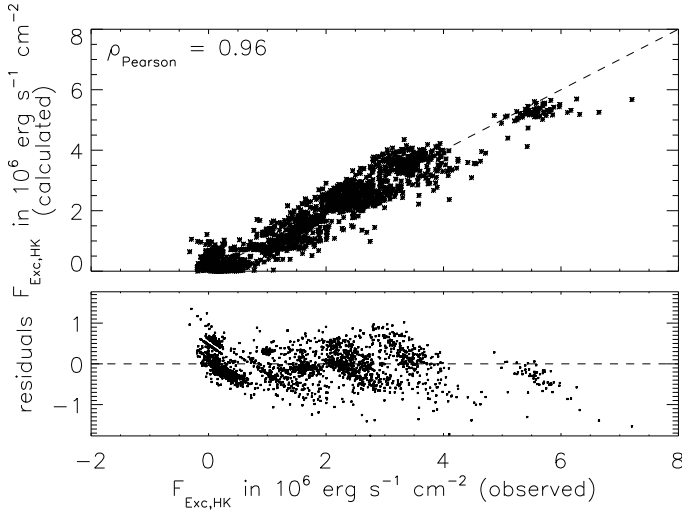


Fig. 13. Comparison of the measured values of the excess flux in the Ca II H and K lines with the one converted from the excess flux in the Ca II IRT lines using Eq. (7). This plot includes data from 2234 observations of 80 stars. The dashed line corresponds to the identity relation (top), or the zero-level (bottom).

when using the excess flux in continuum units, this effect disappears. The resulting $B - V$ -dependence now results in the opposite direction, and there is a trend towards higher excess fluxes for higher $B - V$, evident from the different sign in the slope relation below (Eqs. (7) and (8)). Of those two effects, the surface flux ratio at the different points in the continuum is larger and thus dominates. For our sample of stars, relations linear in $B - V$ result in a good fit. To convert fluxes in $\text{erg s}^{-1} \text{cm}^{-2}$:

$$F_{\text{Exc,HK}} = 10^{1.095-0.587 \cdot (B-V)} \times F_{\text{Exc,IRT } \lambda 8498} \quad (6)$$

$$F_{\text{Exc,HK}} = 10^{1.036-0.631 \cdot (B-V)} \times F_{\text{Exc,IRT } \lambda 8542}$$

$$F_{\text{Exc,HK}} = 10^{1.137-0.663 \cdot (B-V)} \times F_{\text{Exc,IRT } \lambda 8662}$$

$$F_{\text{Exc,HK}} = 10^{0.606-0.612 \cdot (B-V)} \times F_{\text{Exc,IRT}}. \quad (7)$$

And to convert normalized fluxes in continuum units:

$$F_{\text{Exc,HK}} = (-0.085 + 1.402 \times (B - V)) \times F_{\text{Exc,IRT}}. \quad (8)$$

As before, these relations are, by nature of how they were determined, only valid for F, G and K main-sequence stars with $B - V$ ranging from ~ 0.5 to ~ 1.0 . The Pearson correlation coefficient of the converted to observed values is larger than 0.95 in all cases.

The errors of such a conversion have been estimated from the residuals to be about $4 \times 10^5 \text{ erg s}^{-1} \text{cm}^{-2}$ and $60 \text{ m}\text{\AA}$, respectively. In Fig. 13, we compare the converted values from Eq. (7) to the measured values.

We note that the Ca II IRT lines are well correlated with each other. Therefore, measuring the excess flux in just one allows estimating it in the others from a linear relation. Equations for such a conversion are shown in Table 3. From these parameters, it is evident that the second line is the most sensitive of them, with the largest fill-in observed.

5.3. Converting Ca II IRT measurements to known activity indices

We have already shown the activity indices S_{MWO} and R'_{HK} , which are both widely used. In Mittag et al. (2013), the authors define an additional index that does not include basal flux

contributions:

$$R_{\text{HK}}^+ = \frac{F_{\text{HK}} - F_{\text{HK,phot}} - F_{\text{HK,basal}}}{\sigma T_{\text{eff}}^4} = \frac{F_{\text{Exc,HK}}}{\sigma T_{\text{eff}}^4}, \quad (9)$$

with $F_{\text{HK,basal}}$ as the basal chromospheric flux contribution.

Both R'_{HK} and R_{HK}^+ show a strong correlation ($\rho \geq 0.9$) to our excess flux obtained here.

Since we have already provided relations to convert Ca II IRT measurements to $F_{\text{Exc,HK}}$, converting them to R_{HK}^+ is simply a matter of dividing by σT_{eff}^4 . This parameter can be estimated from $B - V$, so it could be included in the fit.

Here, we find the conversion from Ca II IRT-measurements to the indices in Eqs. (2) and (9), calculated from S_{MWO} using the relation in Mittag et al. (2013). This allows us to compare the equations to convert to R'_{HK} and R_{HK}^+ in a more consistent fashion than if we used the measured value $F_{\text{Exc,HK}}$, as we have not measured a $F_{\text{HK,chrom}}$ that still includes a basal flux contribution. However, $F_{\text{Exc,HK}}/\sigma T_{\text{eff}}^4$ and R_{HK}^+ are very close to identical, except for an offset already discussed in Sect. 4.2. We find similar parameters for the formulae when using a value for R_{HK}^+ determined using our measured $F_{\text{Exc,HK}}$. Applying the method described in Sect. 5 yields:

$$R'_{\text{HK}} = m \cdot F_{\text{Exc,IRT}} + b, \quad \text{with} \quad (10)$$

$$\log m = -10.014 - 1.815 \cdot (B - V) + 1.501 \cdot (B - V)^2$$

$$b = -0.277 \times 10^{-4} + 1.069 \times 10^{-4} (B - V) - 0.586 \times 10^{-4} (B - V)^2,$$

$$R_{\text{HK}}^+ = m \cdot F_{\text{Exc,IRT}} + b, \quad \text{with} \quad (11)$$

$$\log m = -10.257 - 1.127 \cdot (B - V) + 1.033 \cdot (B - V)^2$$

$$b = -0.459 \times 10^{-4} + 1.334 \times 10^{-4} (B - V) - 0.753 \times 10^{-4} \cdot (B - V)^2,$$

with $F_{\text{Exc,IRT}}$ in $\text{erg s}^{-1} \text{cm}^{-2}$. The error is again estimated from residuals and is roughly 5.5×10^{-6} for both R'_{HK} and R_{HK}^+ , corresponding to an average error of $\sim 10\%$. The relations for slope and intercept are very similar in shape, and in case of the slope m also the actual function values. However, the intercepts b shows a clear offset that stems from the small chromospheric basal flux correction that forms the difference in the two indices. For the determination of this conversion, we have removed 198 data-points with very different S/N in the red and blue channels. The Pearson correlation coefficient between the converted and observed values is 0.97. Figure 14 compares the converted to the measured values.

To convert Ca II IRT measurements into S_{MWO} , the following relation can be used:

$$S_{\text{MWO}} = m \times F_{\text{Exc,IRT}} + b, \quad \text{with} \quad (12)$$

$$\log m = -6.500 - 2.165 \times (B - V) + 2.264 \times (B - V)^2$$

$$b = 0.044 + 0.202 \times (B - V) - 0.013 \times (B - V)^2,$$

where $F_{\text{Exc,IRT}}$ has to be entered in $\text{erg s}^{-1} \text{cm}^{-2}$. We estimate the errors from the residuals to be 0.03, a relative error of about 6%. We find a Pearson correlation coefficient of $\rho_{\text{Pearson}} = 0.97$. The converted values are compared to the measured ones in Fig. 15.

Table 3. Relations to estimate the excess flux in a Ca II IRT line from measurements of another.

Source line	Target line		
	Ca II IRT $\lambda 8498$	Ca II IRT $\lambda 8542$	Ca II IRT $\lambda 8662$
Ca II IRT $\lambda 8498$		$F_{\text{Exc,IRT } \lambda 8542} = 1.232 \times F_{\text{Exc,IRT } \lambda 8498}$	$F_{\text{Exc,IRT } \lambda 8662} = 1.006 \times F_{\text{Exc,IRT } \lambda 8498}$
Ca II IRT $\lambda 8542$	$F_{\text{Exc,IRT } \lambda 8498} = 0.801 \times F_{\text{Exc,IRT } \lambda 8542}$		$F_{\text{Exc,IRT } \lambda 8662} = 0.808 \times F_{\text{Exc,IRT } \lambda 8542}$
Ca II IRT $\lambda 8662$	$F_{\text{Exc,IRT } \lambda 8498} = 0.976 \times F_{\text{Exc,IRT } \lambda 8662}$	$F_{\text{Exc,IRT } \lambda 8542} = 1.210 \times F_{\text{Exc,IRT } \lambda 8662}$	

Notes. The errors of such a conversion are about $30\,000 \text{ erg s}^{-1} \text{ cm}^{-2}$.

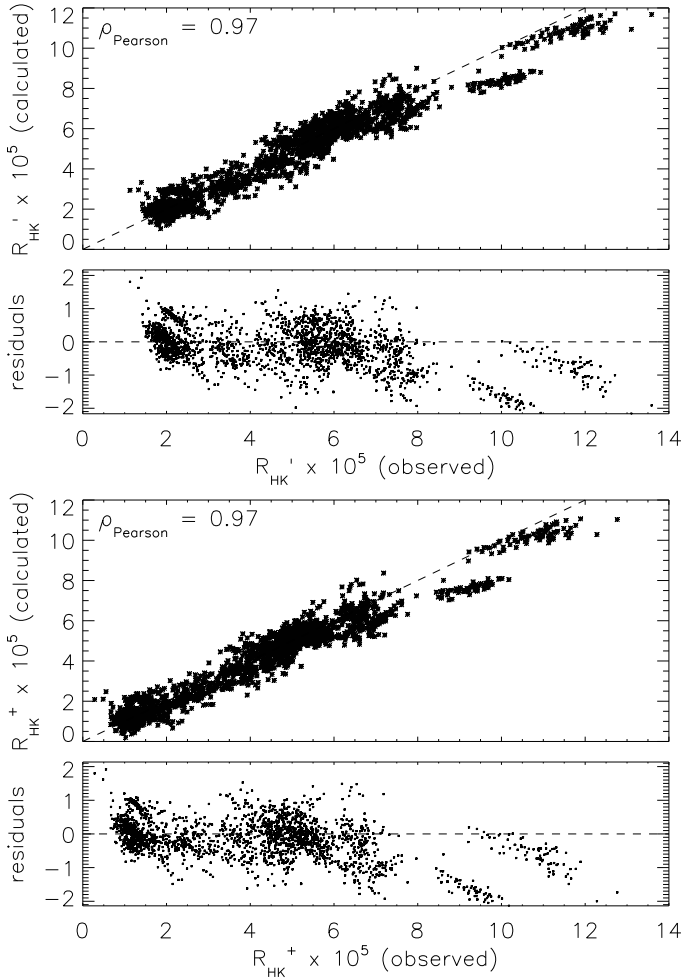


Fig. 14. Comparison of the measured value for R'_{HK} (top), resp. R^+_{HK} (bottom) to the one converted from the excess flux in the Ca II IRT lines, using Eqs. (10) and (11). These plots include data from 2076 observations of 76 stars. The dashed line corresponds to the identity relation (top), or the zero-level (bottom). The Pearson correlation coefficient of converted to observed values is 0.97 in both cases, indicating a good conversion.

6. Conclusions

We have analyzed more than two thousand spectra of almost a hundred main-sequence stars of type F, G and K obtained by the TIGRE telescope, which simultaneously records the spectral range of the Ca II H and K-lines, as well as $H\alpha$ and the Ca II IRT. By carefully selecting an inactive comparison star of similar spectral type as the target star and artificially broadening the comparison star's spectrum to the target star's rotational velocity, we are able to derive a purely-activity related excess flux in the center of these chromospheric lines without any photospheric or basal flux contributions. This excess flux is obtained

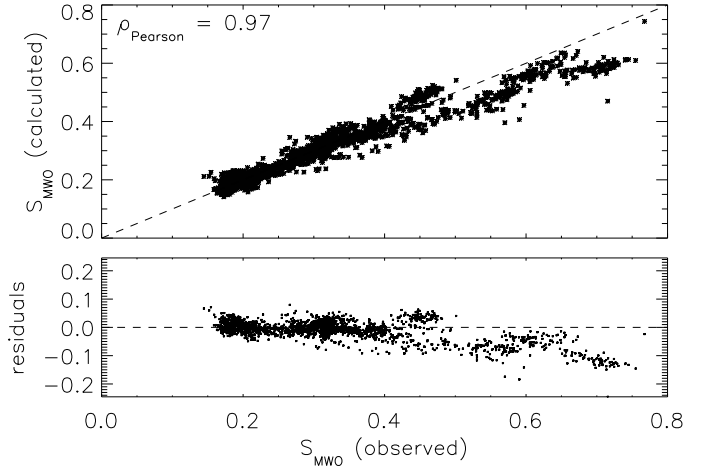


Fig. 15. Comparison of the measured value for S_{MWO} to the one converted from the excess flux in the Ca II IRT lines, using Eq. (12). This plot includes data from 2076 observations of 76 stars. The dashed line corresponds to the identity relation (top), or the zero-level (bottom). The Pearson correlation coefficient of converted to observed values is 0.97, indicating a good conversion.

both in terms of fraction of the continuum and in physical units (i.e., as a flux in $\text{erg s}^{-1} \text{ cm}^{-2}$), and it is free from any scatter from temporal variations.

This large sample of data shows that the excess flux in these lines are well correlated, with the Spearman correlation coefficients exceeding $\rho = 0.9$ for the Ca II lines, and $\rho \approx 0.8$ for the correlation of $H\alpha$ and the Ca II lines. Due to this strong correlation, it is possible to convert the observed excess flux of the Ca II IRT lines into the corresponding excess flux of the other lines, or into activity indices derived from them, despite the lower excess flux and subsequently lower sensitivity.

We provide such conversion relations and the errors on them, estimated directly from the residuals. The relations have been obtained by fitting the relations individually for stars with similar $B - V$, in order to remove any sampling bias. The given relations are valid for stars with $0.5 \leq B - V \leq 1.0$; they can be used to indirectly obtain values for activity indicators such as R'_{HK} or S_{MWO} from infrared spectra, for example, those expected from the *Gaia* mission. This makes it possible to compare these new measurements with the large amount of archival data available for these activity indices, which in turn allows new studies in the temporal behavior of these indices. To obtain the excess flux without an available comparison spectrum, we give empirically derived relations to estimate the photospheric and basal flux in the Ca II IRT lines in Table 2. Subtracting the value calculated from these relations from the flux measured in the Ca II IRT lines of the active star in question returns the excess flux value, which can subsequently be converted into other quantities, if so desired.

We hope to increase the $B - V$ validity range of the relations when more M-dwarfs have been observed by TIGRE, assuming

that the strong correlations between the lines still hold for later types. Spectra taken by CARMENES could then also be used to obtain a value of the activity indices derived from the Ca II H and K-lines, despite these lines falling outside the spectral range of CARMENES.

Acknowledgements. Part of this work was supported by the *Deutsche Forschungsgemeinschaft*, DFG project number RTG 1351. This research has made use of the SIMBAD database, operated at CDS, Strasbourg, France. This research has made use of NASA's Astrophysics Data System. We thank our anonymous referee for helpful suggestions that improved the quality of this paper.

References

- Abt, H. A. 1986, *ApJ*, **309**, 260
- Ammeler-von Eiff, M., & Reiners, A. 2012, *A&A*, **542**, A116
- Anderson, E., & Francis, C. 2012, *Astron. Lett.*, **38**, 331
- Andretta, V., Busà, I., Gomez, M. T., & Terranegra, L. 2005, *A&A*, **430**, 669
- Baliunas, S. L., Donahue, R. A., Soon, W. H., et al. 1995, *ApJ*, **438**, 269
- Bernacca, P. L., & Perinotto, M. 1970, *Contributi dell'Osservatorio Astrofisica dell'Universita di Padova in Asiago*, 239
- Busà, I., Aznar Cuadrado, R., Terranegra, L., Andretta, V., & Gomez, M. T. 2007, *A&A*, **466**, 1089
- Chmielewski, Y. 2000, *A&A*, **353**, 666
- Cincunegui, C., Díaz, R. F., & Mauas, P. J. D. 2007, *A&A*, **469**, 309
- Duncan, D. K., Vaughan, A. H., Wilson, O. C., et al. 1991, *ApJS*, **76**, 383
- Erdelyi-Mendes, M., & Barbuy, B. 1991, *A&A*, **241**, 176
- Fuhrmann, K. 1998, *A&A*, **338**, 161
- Gaia Collaboration (Brown, A. G. A., et al.) 2016, *A&A*, **595**, A2
- Glebocki, R., & Gnacinski, P. 2005, *VizieR Online Data Catalog*, **III**, 244
- Gomes da Silva, J., Santos, N. C., Boisse, I., Dumusque, X., & Lovis, C. 2014, *A&A*, **566**, A66
- Gray, D. F. 2005, *The observation and analysis of stellar photospheres*, 3rd edn. (Cambridge University Press)
- Gray, R. O., Napier, M. G., & Winkler, L. I. 2001, *AJ*, **121**, 2148
- Hall, J. C. 1996, *PASP*, **108**, 313
- Hauschildt, P. H., Allard, F., & Baron, E. 1999, *ApJ*, **512**, 377
- Hempelmann, A., Mittag, M., Gonzalez-Perez, J. N., et al. 2016, *A&A*, **586**, A14
- Henry, T. J., Soderblom, D. R., Donahue, R. A., & Baliunas, S. L. 1996, *AJ*, **111**
- Hillen, M., Verhoelst, T., Degroote, P., Acke, B., & van Winckel, H. 2012, *A&A*, **538**, L6
- Husser, T.-O., Wende-von Berg, S., Dreizler, S., et al. 2013, *A&A*, **553**, A6
- Jenkins, J. S., Murgas, F., Rojo, P., et al. 2011, *A&A*, **531**, A8
- Kausch, W., Noll, S., Smette, A., et al. 2015, *A&A*, **576**, A78
- Linsky, J. L., McClintock, W., Robertson, R. M., & Worden, S. P. 1979, *ApJS*, **41**, 47
- Maldonado, J., Eiroa, C., Villaver, E., Montesinos, B., & Mora, A. 2012, *A&A*, **541**, A40
- Malkov, O. Y., Tamazian, V. S., Docobo, J. A., & Chulkov, D. A. 2012, *A&A*, **546**, A69
- Markwardt, C. B. 2009, in *Astronomical Data Analysis Software and Systems XVIII*, eds. D. A. Bohlender, D. Durand, & P. Dowler, *ASP Conf. Ser.*, **411**, 251
- Marsden, S. C., Petit, P., Jeffers, S. V., et al. 2014, *MNRAS*, **444**, 3517
- Martínez-Arnáiz, R., Maldonado, J., Montes, D., Eiroa, C., & Montesinos, B. 2010, *A&A*, **520**, A79
- Martínez-Arnáiz, R., López-Santiago, J., Crespo-Chacón, I., & Montes, D. 2011, *MNRAS*, **414**, 2629
- McCarthy, K., & Wilhelm, R. J. 2014, *AJ*, **148**, 70
- Meunier, N., & Delfosse, X. 2009, *A&A*, **501**, 1103
- Mishenina, T. V., Soubiran, C., Kovtyukh, V. V., Katsova, M. M., & Livshits, M. A. 2012, *A&A*, **547**, A106
- Mittag, M., Hempelmann, A., González-Pérez, J. N., & Schmitt, J. H. M. M. 2010, *Adv. Astron.*, **2010**, 101502
- Mittag, M., Schmitt, J. H. M. M., & Schröder, K.-P. 2013, *A&A*, **549**, A117
- Mittag, M., Schröder, K.-P., Hempelmann, A., González-Pérez, J. N., & Schmitt, J. H. M. M. 2016, *A&A*, **591**, A89
- Piskunov, N. E., & Valenti, J. A. 2002, *A&A*, **385**, 1095
- Prugniel, P., Vauglin, I., & Koleva, M. 2011, *A&A*, **531**, A165
- Prusti, T. 2012, *Astron. Nachr.*, **333**, 453
- Quirrenbach, A., Amado, P. J., Caballero, J. A., et al. 2014, in *Ground-based and Airborne Instrumentation for Astronomy V*, *Proc. SPIE*, **9147**, 91471F
- Rutten, R. G. M. 1984, *A&A*, **130**, 353
- Schmitt, J. H. M. M., Schröder, K.-P., Rauw, G., et al. 2014, *Astron. Nachr.*, **335**, 787
- Schröder, C., Reiners, A., & Schmitt, J. H. M. M. 2009, *A&A*, **493**, 1099
- Smette, A., Sana, H., Noll, S., et al. 2015, *A&A*, **576**, A77
- Smith, G., & Drake, J. J. 1987, *A&A*, **181**, 103
- Soubiran, C., Le Campion, J.-F., Cayrel de Strobel, G., & Caillo, A. 2010, *A&A*, **515**, A111
- Takeda, Y., Sato, B., Kambe, E., et al. 2005, *PASJ*, **57**, 13
- Torres, C. A. O., Quast, G. R., da Silva, L., et al. 2006, *A&A*, **460**, 695
- Torres, G., Fischer, D. A., Sozzetti, A., et al. 2012, *ApJ*, **757**, 161
- Uesugi, A., & Fukuda, I. 1970, *Catalogue of rotational velocities of the stars*
- Vaughan, A. H., Preston, G. W., & Wilson, O. C. 1978, *PASP*, **90**, 267
- White, R. J., Gabor, J. M., & Hillenbrand, L. A. 2007, *AJ*, **133**, 2524
- Wilson, O. C. 1968, *ApJ*, **153**, 221
- Wilson, O. C., & Vainu Bappu, M. K. 1957, *ApJ*, **125**, 661

Appendix A: Stellar parameters used

Here, in Tables A.1 and A.2 we list the stellar parameters that we used in this work, and give their source.

Table A.1. Stellar parameters for the stars investigated in this work.

Name	$B - V$	$\log g$	[Fe/H]	$v \sin i$	Name	$B - V$	$\log g$	[Fe/H]	$v \sin i$
HD 88355	0.43 ⁽¹⁾	–	0.00 ⁽¹⁾	–	HD 75332	0.50 ⁽¹⁾	4.41 ⁽¹⁾	0.13 ⁽¹⁾	11.00 ⁽¹¹⁾
HD 25457	0.50 ⁽¹⁾	4.30 ⁽¹⁾	–0.03 ⁽¹⁾	20.24 ⁽³⁾	HD 179949	0.50 ⁽¹⁾	4.44 ⁽¹⁾	0.20 ⁽¹⁾	6.40 ⁽²⁾
HD 35296	0.52 ⁽¹⁾	4.28 ⁽¹⁾	–0.02 ⁽¹⁾	16.00 ⁽²⁾	HD 19019	0.52 ⁽¹⁾	4.00 ⁽¹⁾	–0.17 ⁽¹⁾	10.00 ⁽⁹⁾
HD 20367	0.52 ⁽¹⁾	4.46 ⁽¹⁾	0.13 ⁽¹⁾	–	HD 137107	0.55 ⁽¹⁾	4.22 ⁽¹⁾	–0.03 ⁽¹⁾	–
HD 100180	0.57 ⁽¹⁾	4.25 ⁽¹⁾	–0.06 ⁽¹⁾	3.59 ⁽³⁾	HD 150706	0.57 ⁽¹⁾	4.47 ⁽¹⁾	–0.03 ⁽¹⁾	10.00 ⁽⁹⁾
HD 154417	0.58 ⁽¹⁾	4.38 ⁽¹⁾	–0.01 ⁽¹⁾	8.00 ⁽³⁾	HD 206860	0.58 ⁽¹⁾	4.49 ⁽¹⁾	–0.08 ⁽¹⁾	12.81 ⁽³⁾
HD 209458	0.58 ⁽¹⁾	4.45 ⁽¹⁾	0.01 ⁽¹⁾	4.5 ⁽¹⁰⁾	HD 70573	0.59 ⁽¹⁾	4.58 ⁽¹⁾	–0.11 ⁽¹⁾	19.39 ± 4.00 ⁽⁹⁾
HD 114710	0.59 ⁽¹⁾	4.43 ⁽¹⁾	0.07 ⁽¹⁾	4.72 ⁽³⁾	HD 115383	0.59 ⁽¹⁾	4.25 ⁽¹⁾	0.13 ⁽¹⁾	7.20 ± 1.10 ⁽⁷⁾
HD 129333	0.59 ⁽¹⁾	4.47 ⁽¹⁾	0.16 ⁽¹⁾	22.01 ± 3.95 ⁽⁹⁾	HD 26913	0.60 ⁽¹⁾	4.49 ⁽¹⁾	–0.02 ⁽¹⁾	1.83 ⁽⁵⁾
HD 39587	0.60 ⁽¹⁾	4.45 ⁽¹⁾	–0.03 ⁽¹⁾	10.79 ⁽³⁾	HD 97334	0.61 ⁽¹⁾	4.35 ⁽¹⁾	0.06 ⁽¹⁾	7.74 ⁽³⁾
HD 75767	0.61 ⁽¹⁾	4.33 ⁽¹⁾	–0.04 ⁽¹⁾	4.00 ⁽⁴⁾	HD 165401	0.61 ⁽¹⁾	4.39 ⁽¹⁾	–0.41 ⁽¹⁾	13.90 ⁽³⁾
HD 190406	0.61 ⁽¹⁾	4.39 ⁽¹⁾	0.04 ⁽¹⁾	8.27 ⁽³⁾	HD 25680	0.62 ⁽¹⁾	4.52 ⁽¹⁾	0.05 ⁽¹⁾	3.20 ⁽⁵⁾
HD 72905	0.62 ⁽¹⁾	4.53 ⁽¹⁾	–0.08 ⁽¹⁾	11.21 ⁽³⁾	HD 197076	0.62 ⁽¹⁾	4.41 ⁽¹⁾	–0.11 ⁽¹⁾	10.22 ⁽⁹⁾
HD 126053	0.63 ⁽¹⁾	4.43 ⁽¹⁾	–0.38 ⁽¹⁾	3.08 ⁽³⁾	HD 181321	0.63 ⁽¹⁾	4.42 ⁽¹⁾	–0.01 ⁽¹⁾	13.00 ⁽⁸⁾
HD 30495	0.64 ⁽¹⁾	4.49 ⁽¹⁾	–0.01 ⁽¹⁾	3.57 ⁽⁵⁾	HD 38858	0.64 ⁽¹⁾	4.48 ⁽¹⁾	–0.22 ⁽¹⁾	2.61 ⁽³⁾
HD 71148	0.64 ⁽¹⁾	4.36 ⁽¹⁾	–0.00 ⁽¹⁾	12.37 ⁽³⁾	HD 146233	0.65 ⁽¹⁾	4.42 ⁽¹⁾	0.03 ⁽¹⁾	4.07 ⁽³⁾
HD 140538	0.65 ⁽¹⁾	4.47 ⁽¹⁾	0.05 ⁽¹⁾	11.01 ⁽³⁾	HD 159222	0.65 ⁽¹⁾	4.34 ⁽¹⁾	0.10 ⁽¹⁾	3.01 ⁽³⁾
HD 190771	0.65 ⁽¹⁾	4.41 ⁽¹⁾	0.14 ⁽¹⁾	4.20 ⁽⁵⁾	HD 20619	0.66 ⁽¹⁾	4.42 ⁽¹⁾	–0.24 ⁽¹⁾	3.20 ⁽³⁾
HD 28099	0.66 ⁽¹⁾	4.43 ⁽¹⁾	0.13 ⁽¹⁾	3.54 ⁽⁵⁾	HD 42618	0.66 ⁽¹⁾	4.46 ⁽¹⁾	–0.11 ⁽¹⁾	4.40 ⁽¹⁵⁾
HD 20630	0.67 ⁽¹⁾	4.49 ⁽¹⁾	0.06 ⁽¹⁾	5.86 ⁽³⁾	HD 43162	0.67 ⁽¹⁾	4.38 ⁽¹⁾	–0.05 ⁽¹⁾	9.63 ⁽³⁾
HD 73350	0.67 ⁽¹⁾	4.46 ⁽¹⁾	0.11 ⁽¹⁾	4.00 ⁽⁴⁾	HD 76151	0.67 ⁽¹⁾	4.46 ⁽¹⁾	0.08 ⁽¹⁾	3.58 ⁽³⁾
HD 145825	0.67 ⁽¹⁾	4.46 ⁽¹⁾	0.03 ⁽¹⁾	3.10 ± 1.20 ⁽⁸⁾	HD 224930	0.67 ⁽¹⁾	4.41 ⁽¹⁾	–0.77 ⁽¹⁾	4.07 ⁽³⁾
HD 42807	0.68 ⁽¹⁾	4.46 ⁽¹⁾	–0.03 ⁽¹⁾	3.80 ⁽⁵⁾	HD 6582	0.69 ⁽¹⁾	4.50 ⁽¹⁾	–0.80 ⁽¹⁾	4.17 ⁽³⁾
HD 10086	0.69 ⁽¹⁾	4.39 ⁽¹⁾	0.12 ⁽¹⁾	2.40 ⁽⁴⁾	HD 68017	0.69 ⁽¹⁾	4.46 ⁽¹⁾	–0.44 ⁽¹⁾	1.49 ⁽³⁾
HD 111395	0.69 ⁽¹⁾	4.54 ⁽¹⁾	0.10 ⁽¹⁾	2.60 ⁽⁵⁾	HD 101501	0.74 ⁽¹⁾	4.55 ⁽¹⁾	–0.07 ⁽¹⁾	3.26 ⁽³⁾
HD 103095	0.75 ⁽¹⁾	4.63 ⁽¹⁾	–1.34 ⁽¹⁾	9.28 ⁽³⁾	HD 184385	0.75 ⁽¹⁾	4.49 ⁽¹⁾	0.12 ⁽¹⁾	2.70 ⁽⁵⁾
HD 152391	0.76 ⁽¹⁾	4.47 ⁽¹⁾	–0.05 ⁽¹⁾	3.06 ⁽⁵⁾	HD 82443	0.77 ⁽¹⁾	4.45 ⁽¹⁾	–0.13 ⁽¹⁾	5.90 ⁽⁵⁾
HD 82885	0.77 ⁽¹⁾	4.49 ⁽¹⁾	0.32 ⁽¹⁾	7.22 ⁽³⁾	HD 131156A	0.77 ⁽¹⁾	4.54 ⁽¹⁾	–0.12 ⁽¹⁾	–
HD 149661	0.78 ⁽¹⁾	4.50 ⁽¹⁾	0.03 ⁽¹⁾	1.63 ⁽⁵⁾	HD 185144	0.78 ⁽¹⁾	4.49 ⁽¹⁾	–0.22 ⁽¹⁾	6.79 ⁽³⁾
HD 100623	0.81 ⁽¹⁾	4.60 ⁽¹⁾	–0.41 ⁽¹⁾	6.79 ⁽³⁾	HD 165341A	0.83 ⁽¹⁾	4.49 ⁽¹⁾	–0.04 ⁽¹⁾	16.00 ⁽¹¹⁾
HD 10476	0.84 ⁽¹⁾	4.45 ⁽¹⁾	–0.05 ⁽¹⁾	1.20 ⁽³⁾	HD 115404	0.85 ⁽¹⁾	4.45 ⁽¹⁾	–0.19 ⁽¹⁾	–
HD 17925	0.86 ⁽¹⁾	4.52 ⁽¹⁾	0.07 ⁽¹⁾	4.80 ⁽⁵⁾	HD 97658	0.86 ⁽¹⁾	4.49 ⁽¹⁾	–0.30 ⁽¹⁾	8.70 ⁽⁵⁾
HD 118972	0.86 ⁽¹⁾	4.36 ⁽¹⁾	–0.02 ⁽¹⁾	4.10 ± 1.20 ⁽⁸⁾	HD 166620	0.87 ⁽¹⁾	4.47 ⁽¹⁾	–0.17 ⁽¹⁾	4.82 ⁽³⁾
HD 75732	0.87 ⁽¹⁾	4.41 ⁽¹⁾	0.28 ⁽¹⁾	2.27 ⁽³⁾	HD 22049	0.88 ⁽¹⁾	4.53 ⁽¹⁾	–0.10 ⁽¹⁾	4.08 ⁽³⁾
HD 37394	0.90 ⁽¹⁾	4.51 ⁽¹⁾	0.08 ⁽¹⁾	2.80 ⁽⁵⁾	HD 4628	0.90 ⁽¹⁾	4.63 ⁽¹⁾	–0.27 ⁽¹⁾	1.50 ⁽⁵⁾
HD 145675	0.90 ⁽¹⁾	4.45 ⁽¹⁾	0.41 ⁽¹⁾	2.6 ⁽¹⁰⁾	HD 22468	0.92 ⁽¹⁾	–	–	–
HD 189733	0.93 ⁽¹⁾	4.49 ⁽¹⁾	–0.02 ⁽¹⁾	2.30 ⁽¹³⁾	HD 5133	0.94 ⁽¹⁾	4.66 ⁽¹⁾	–0.11 ⁽¹⁾	3.52 ⁽³⁾
HD 160346	0.96 ⁽¹⁾	4.46 ⁽¹⁾	–0.03 ⁽¹⁾	3.37 ⁽³⁾	HD 16160	0.98 ⁽¹⁾	4.54 ⁽¹⁾	–0.12 ⁽¹⁾	0.90 ⁽⁵⁾
HD 87883	0.99 ⁽¹⁾	4.47 ⁽¹⁾	0.05 ⁽¹⁾	1.20 ⁽³⁾	HD 32147	1.06 ⁽¹⁾	4.41 ⁽¹⁾	0.26 ⁽¹⁾	5.18 ⁽³⁾
HD 131977	1.11 ⁽¹⁾	4.35 ⁽¹⁾	–0.00 ⁽¹⁾	2.48 ⁽⁵⁾	HD 190007	1.12 ⁽¹⁾	4.38 ⁽¹⁾	0.16 ⁽¹⁾	2.55 ⁽⁵⁾
HD 156026	1.16 ⁽¹⁾	4.60 ⁽¹⁾	–0.20 ⁽¹⁾	4.40 ⁽²⁾	HD 201091	1.18 ⁽¹⁾	4.70 ⁽¹⁾	–0.38 ⁽¹⁶⁾	4.72 ⁽³⁾

References. References are numbered in superscript and given below. Values missing were inferred from a fit to the values of other stars. (1) Soubiran et al. (2010); (2) Schröder et al. (2009); (3) Martínez-Arnáiz et al. (2010); (4) Marsden et al. (2014); (5) Mishenina et al. (2012); (6) Bernacca & Perinotto (1970); (7) Ammler-von Eiff & Reiners (2012); (8) Torres et al. (2006); (9) White et al. (2007); (10) Glebocki & Gnacinski (2005); (11) Maldonado et al. (2012); (12) Takeda et al. (2005); (13) Torres et al. (2012); (14) Uesugi & Fukuda (1970); (15) McCarthy & Wilhelm (2014); (16) Prugniel et al. (2011).

Table A.2. Stellar parameters for the comparison stars used.

Name	$B - V$	$\log g$	[Fe/H]	$v \sin i$	Name	$B - V$	$\log g$	[Fe/H]	$v \sin i$
HD 739	0.40 ⁽¹⁾	4.27 ⁽¹⁾	-0.09 ⁽¹⁾	4.40 ⁽⁹⁾	HD 159332	0.45 ⁽¹⁾	3.85 ⁽¹⁾	-0.23 ⁽¹⁾	5.00 ⁽⁶⁾
HD 216385	0.48 ⁽¹⁾	3.95 ⁽¹⁾	-0.29 ⁽¹⁾	3.00 ⁽⁴⁾	HD 45067	0.53 ⁽¹⁾	4.01 ⁽¹⁾	-0.09 ⁽¹⁾	5.00 ⁽⁶⁾
HD 187691	0.56 ⁽¹⁾	4.26 ⁽¹⁾	0.10 ⁽¹⁾	3.00 ⁽⁴⁾	HD 100180	0.57 ⁽¹⁾	4.25 ⁽¹⁾	-0.06 ⁽¹⁾	3.59 ⁽¹⁾
HD 124570	0.58 ⁽¹⁾	4.05 ⁽¹⁾	0.08 ⁽¹⁾	3.00 ⁽⁴⁾	HD 19373	0.59 ⁽¹⁾	4.21 ⁽¹⁾	0.08 ⁽¹⁾	3.15 ⁽¹⁾
HD 168009	0.60 ⁽¹⁾	4.23 ⁽¹⁾	-0.01 ⁽¹⁾	3.00 ⁽⁴⁾	HD 10307	0.62 ⁽¹⁾	4.32 ⁽¹⁾	0.03 ⁽¹⁾	4.07 ⁽¹⁾
HD 34411	0.62 ⁽¹⁾	4.22 ⁽¹⁾	0.08 ⁽¹⁾	3.15 ⁽¹⁾	HD 95128	0.62 ⁽¹⁾	4.30 ⁽¹⁾	0.01 ⁽¹⁾	3.15 ⁽¹⁾
HD 157214	0.62 ⁽¹⁾	4.31 ⁽¹⁾	-0.40 ⁽¹⁾	3.15 ⁽¹⁾	HD 126053	0.63 ⁽¹⁾	4.43 ⁽¹⁾	-0.38 ⁽¹⁾	3.08 ⁽¹⁾
HD 38858	0.64 ⁽¹⁾	4.48 ⁽¹⁾	-0.22 ⁽¹⁾	2.61 ⁽¹⁾	HD 146233	0.65 ⁽¹⁾	4.42 ⁽¹⁾	0.03 ⁽¹⁾	4.07 ⁽¹⁾
HD 186427	0.65 ⁽¹⁾	4.32 ⁽¹⁾	0.07 ⁽¹⁾	2.18 ± 0.50 ⁽⁵⁾	HD 12846	0.66 ⁽¹⁾	4.38 ⁽¹⁾	-0.26 ⁽¹⁾	2.20 ⁽⁵⁾
HD 42618	0.66 ⁽¹⁾	4.46 ⁽¹⁾	-0.11 ⁽¹⁾	4.40 ⁽⁸⁾	HD 43587	0.67 ⁽¹⁾	4.29 ⁽¹⁾	-0.04 ⁽¹⁾	2.98 ⁽¹⁾
HD 3795	0.70 ⁽¹⁾	3.91 ⁽¹⁾	-0.63 ⁽¹⁾	1.70 ⁽²⁾	HD 115617	0.70 ⁽¹⁾	4.39 ⁽¹⁾	-0.01 ⁽¹⁾	3.90 ± 0.90 ⁽³⁾
HD 178428	0.70 ⁽¹⁾	4.25 ⁽¹⁾	0.14 ⁽¹⁾	1.50 ⁽⁷⁾	HD 117176	0.71 ⁽¹⁾	3.97 ⁽¹⁾	-0.06 ⁽¹⁾	4.83 ⁽¹⁾
HD 10700	0.72 ⁽¹⁾	4.48 ⁽¹⁾	-0.50 ⁽¹⁾	1.60 ⁽²⁾	HD 26965	0.85 ⁽¹⁾	4.51 ⁽¹⁾	-0.27 ⁽¹⁾	2.10 ⁽²⁾
HD 75732	0.87 ⁽¹⁾	4.41 ⁽¹⁾	0.28 ⁽¹⁾	2.27 ⁽¹⁾	HD 145675	0.90 ⁽¹⁾	4.45 ⁽¹⁾	0.41 ⁽¹⁾	2.10 ⁽²⁾

References. References are numbered in superscript and given below. (1) [Martínez-Arnáiz et al. \(2010\)](#); (2) [Jenkins et al. \(2011\)](#); (3) [Ammler-von Eiff & Reiners \(2012\)](#); (4) [Takeda et al. \(2005\)](#); (5) [Marsden et al. \(2014\)](#); (6) [Bernacca & Perinotto \(1970\)](#); (7) [Mishenina et al. \(2012\)](#); (8) [McCarthy & Wilhelm \(2014\)](#); (9) [Schröder et al. \(2009\)](#).